

Faculty of Resource Science and Technology

Design and Evaluation of Vanillin Derivatives as Dual Inhibitors of Neuraminidase of *Streptococcus pneumoniae* and FtsZ of *Staphylococcus aureus*

Law Woon Yi

Doctor of Philosophy
2025

Design and Evaluation of Vanillin Derivatives as Dual Inhibitors of Neuraminidase of *Streptococcus pneumoniae* and FtsZ of *Staphylococcus aureus*

Law Woon Yi

A thesis submitted

In fulfillment of the requirements for the degree of Doctor of Philosophy

(Chemistry)

Faculty of Resource Science and Technology
UNIVERSITI MALAYSIA SARAWAK
2025

DECLARATION

I declare that the work in this thesis was carried out in accordance with the regulations of Universiti Malaysia Sarawak. Except where due acknowledgements have been made, the work is that of the author alone. The thesis has not been accepted for any degree and is not concurrently submitted in candidature of any other degree.



……

Signature

Name: Law Woon Yi

Matric No.: 22010257

Faculty of Resource Science and Technology

Universiti Malaysia Sarawak

Date : 03 October 2025

ACKNOWLEDGEMENT

First and foremost, I would like to express my gratitude to my supervisor, Associate Professor Dr. Mohd Razip bin Asaruddin, and to my co-supervisor, Associate Professor Dr. Showkat Ahmad Bhawani for all the guidance and support throughout my period of study. The accomplishment of the research is greatly contributed by the help from Associate Professor Dr. Mohd Razip bin Asaruddin and Associate Professor Dr. Showkat Ahmad Bhawani.

Consequently, I would also like to convey my sincerest gratitude to the Centre for Graduate Studies, for all the support, seminars and advice to the completion of my thesis. On top of that, I would like to thank my laboratory partners for all the help throughout my research study.

Furthermore, I would like to express my uttermost gratitude to my parents, Mr. Law Joon Chiew and Madam Thian Li Moi for the support, care and love throughout my period of study. I would also like to thank my siblings and my family members for always standing behind me. Moreover, I would like to express my appreciation to my husband, Dr. Sim Song-Lin for being my strongest pillar of strength. Most importantly, I would like to thank my children, Ashton Sim Chu Hao and Astrid Sim Rui Yee for being my strongest reason to fight all the way through. I hope you all are proud of mummy. Thank you.

ABSTRACT

Majority pneumonia cases were caused by two types of bacterial strains: *Streptococcus pneumoniae* and *Staphylococcus aureus*. Despite the fact that vaccines and antibiotics were available, the problem continue to arise due to the increasing emergence of strains that exhibit significant resistance to the available drugs. Based on reported research, neuraminidase of *S. pneumoniae* and FtsZ of *S. aureus* played imperative role in facilitating the pneumococcal infection. Schiff base vanillin derivatives were reported to exhibit wide range of biological activity, including antibacterial activity against various bacterial strains. As a whole, this research study focuses on the study of Schiff base vanillin derivatives targeting neuraminidase of *S. pneumoniae* and FtsZ of *S. aureus* by performing computational methods and antibacterial assay. A total of 21 vanillin derivatives were evaluated. Based on the results of the study as potential *S. pneumoniae* neuraminidase inhibitors, all 21 vanillin derivatives were able to show pharmacophore fit values and matching features more than half of the training sets. The fit values ranged from 64.25 to 81.50, together with 6 to 8 matching features in ligand-based pharmacophore modelling. In structure-based pharmacophore modelling and molecular docking, 15 out of 21 derivatives were successfully aligned with the 4 out of 6 key active site residues of oseltamivir carboxylate ligand of 2YA8, including ARG332, ARG648, ARG706 and ASP357. Simultaneously, the derivatives were able to show binding affinity values lower than –6.00 kcal/mol, indicating strong docking interaction to the protein pocket of 2YA8. For analysis as potential inhibitors of *S. aureus* FtsZ, the 21 derivatives showed pharmacophore fit values ranging from 66.45 to 104.06, depicting 6 to 10 out of 17 pharmacophore features. Only 17 out of 21 showed fit values more than half of the training sets. In structure-based pharmacophore modelling and molecular docking, 19 out of 21 derivatives were able to

matched with 4 to 6 out of 6 key active site residues of the PC190723 ligand of 3VOB, including VAL297, VAL203, THR309, LEU200, LEU209 and ASN263. Similarly, the derivatives possessed strong binding affinity values less than –6.00 kcal/mol in the protein pocket of 3VOB, suggesting strong interaction to the active site. In combination of the all results, 10 out of 21 vanillin derivatives showed satisfactory results as potential inhibitors of both *S. pneumoniae* and *S. aureus*, which were compounds (5), (8), (9), (10), (12), (15), (16), (17), (19) and (21). By fulfilling all rules in Lipinski's Rule of 5, this provided further support to their role as orally active drugs. A total of 6 out of 10 vanillin derivatives were successfully synthesized and characterized by Fourier-Transform-Infrared spectroscopy (FT-IR) and Nuclear Magnetic Resonance Spectroscopy (NMR). On top of that, the derivatives also depicted significant antibacterial activity against Gram-positive bacteria by agar diffusion antibacterial assay. Average diameter of inhibition zone ranging from 9.78 mm to 20.40 mm were shown in comparison with the controls. Schiff base vanillin derivatives were concluded to possess potential dual inhibitory activity against both neuraminidase of *S. pneumoniae* and FtsZ of *S. aureus via in silico*. With support from their druglikeness in Lipinski's Rule of 5, and their agar diffusion antibacterial activity against Gram-positive bacteria, the derivatives serve as promising drug candidates for futuristic development *via in vivo* or *in vitro*.

Keywords: Antibacterial, docking, pharmacophore, pneumonia, vanillin

***Pemodelan dan Kajian Antibakteria Derivatif Vanilin Menyasarkan Neuraminidase* Streptococcus pneumoniae *dan FtsZ* Staphylococcus aureus**

ABSTRAK

Kebanyakan kes pneumonia adalah disebabkan oleh dua jenis bakteria: Streptococcus pneumoniae *dan* Staphylococcus aureus*. Walaupun vaksin dan antibiotik adalah tersedia, masalah ini terus timbul disebabkan oleh kemunculan strain yang semakin meningkat yang mempunyai rintangan kuat terhadap perubatan yang sedia ada. Berdasarkan kajian dilaporkan, neuraminidase* S. pneumoniae *dan FtsZ* S. aureus *memainkan peranan penting dalam memudahkan jangkitan pneumokokus. Derivatif vanilin bes Schiff dilaporkan untuk menunjukkan pelbagai aktiviti biologi, termasuk aktiviti antibakteria terhadap pelbagai strain bakteria. Secara keseluruhan, penyelidikan ini memberi fokus kepada kajian derivatif vanilin bes Schiff menyasarkan neuraminidase* S. pneumoniae *dan FtsZ* S. aureus *dengan kaedah pengiraan dan ujian aktiviti antibakteria. Sebanyak 21 derivatif vanilin telah dinilai. Berdasarkan keputusan penyelidikan sebagai perencat berpotensi neuraminidase* S. pneumoniae*, semua 21 derivatif vanilin mampu menunjukkan nilai kesesuaian farmakofor dan ciri sepadan melebihi separuh daripada set latihan. Nilai kesesuaian berlingkung daripada 64.25 hingga 81.50, dengan 6 hingga 8 ciri sepadan dalam pemodelan farmakofor berasaskan ligan. Dalam pemodelan farmakofor dan dok molekul berasaskan struktur, 15 daripada 21 derivatif berjaya berjajar dengan 4 daripada 6 residu tapak aktif penting ligan oseltamivir karboksilat 2YA8, termasuk ARG332, ARG648, ARG706, dan ASP357. Secara serentak, semua derivatif mampu menunjukkan nilai tenaga pengikatan lebih rendah daripada –6.00 kcal/mol, menunjukkan interaksi pengikatan yang kuat dengan poket protein 2YA8. Untuk analisis sebagai perencat berpotensi FtsZ* S. aureus*, 21 derivatif menunjukkan nilai kesesuaian farmakofor dalam lingkungan 66.45 hingga 104.06, menggambarkan 6*

hingga 10 daripada 17 ciri farmakofor. Hanya 17 daripada 21 derivatif menunjukkan nilai kesesuaian lebih daripada separuh nilai set latihan. Dalam pemodelan farmakofor dan dok molekul berasaskan struktur, 19 daripada 21 derivatif berjaya memadan dengan 4 hingga 6 daripada 6 residu tapak aktif penting ligan PC190723 3VOB, termasuk VAL297, VAL203, THR309, LEU200, LEU209, dan ASN263. Begitu juga, derivatif ini menunjukkan nilai tenaga pengikatan kurang daripada –6.00 kcal/mol dalam poket protein 3VOB, mencadangkan interaksi kuat dengan tapak aktif. Secara keseluruhan, 10 daripada 21 derivatif vanilin bes Schiff menunjukkan keputusan yang memuaskan sebagai perencat berpotensi bagi kedua-dua S. pneumoniae *dan* S. aureus*, iaitu sebatian (5), (8), (9), (10), (12), (15), (16), (17), (19), dan (21). Dengan memenuhi semua kriteria dalam lima aturan Lipinski, ini memberikan sokongan tambahan terhadap peranan sebagai ubat aktif oral. Sebanyak 6 daripada 10 derivatif vanillin berjaya disintesis dan dicirikan menggunakan spektroskopi Inframerah Transformasi Fourier (FT-IR) dan Spektroskopi Resonans Magnetik Nuklear (NMR). Selain itu, derivatif ini juga menunjukkan aktiviti penghambatan yang ketara terhadap bakteria Gram-positif melalui ujian penyebaran agar. Purata diameter zon perencatan yang ditunjukkan adalah antara 9.78 mm hingga 20.40 mm berbanding dengan kawalan. Derivatif vanilin bes Schiff disimpulkan mempunyai potensi aktiviti perencatan dwi terhadap neuraminidase* S. pneumoniae *dan FtsZ* S. aureus *melalui kaedah* in silico*. Dengan sokongan daripada sifat seperti ubat mengikut lima aturan Lipinski serta aktiviti antibakteria melalui ujian penyebaran agar terhadap bakteria Gram-positif, derivatif tersebut berfungsi sebagai calon ubat yang menjanjikan untuk perkembangan pada masa depan melalui kajian* in vivo *atau* in vitro*.*

Kata kunci: *Antibakteria, dok, farmakofor, pneumonia, vanilin*

TABLE OF CONTENTS

		Page
DECLARATION		i
ACKNOWLEDGEMENT		ii
ABSTRACT		iii
ABSTRAK		v
TABLE OF CONTENTS		vii
LIST OF TABLES		xi
LIST OF FIGURES		xiii
LIST OF ABBREVIATIONS		xxiv
CHAPTER 1: INTRODUCTION		1
1.1	General Introduction	1
1.2	Problem Statement	7
1.3	Objectives	9
CHAPTER 2: LITERATURE REVIEW		10
2.1	Vanillin	10
2.2	Schiff Base Vanillin Derivatives	12
2.3	Pneumonia	15
2.3.1	Types and Symptoms of Pneumonia, and Groups at Higher Risk	15

2.3.2 Etiology and Epidemiology of Pneumonia 17

2.3.3 Histopathology of Pneumonia 19

2.3.4 Treatment, Vaccination and Management of Pneumonia 20

2.4 *S. pneumoniae* 22

2.4.1 Introduction of *S. pneumoniae* 22

2.4.2 Pathogenesis of *S. pneumoniae* 23

2.4.3 Virulence Factors of *S. pneumoniae* 27

2.4.4 Neuraminidase and Inhibitors 30

2.5 *S. aureus* 33

2.5.1 Introduction of *S. aureus* 33

2.5.2 Life Cycle of *S. aureus* 35

2.5.3 FtsZ and Inhibitors 41

2.6 Computational-aided Drug Design 47

2.6.1 Ligand-based Pharmacophore Modelling 52

2.6.2 Structure-based Pharmacophore Modelling and Molecular Docking 57

2.6.3 Lipinski's Rule of 5 63

2.7 Antibacterial Assay by Broth Dilution and Agar Disk-Diffusion Method 65

2.8 Research Summary 68

CHAPTER 3: MATERIALS AND METHODS 69

3.1 Overview of Computer-Aided Drug Design (CADD) 69

3.2 Computational Evaluations of Schiff Base Vanillin Derivatives against *S. pneumoniae* Bacterial Neuraminidase 70

3.2.1 Ligand-Based Pharmacophore Modelling 70

3.2.2 Structure-based Molecular Docking 83

3.3 Computational Evaluations of Schiff Base Vanillin Derivatives against *S. aureus* FtsZ Protein 94

3.3.1 Ligand-based Pharmacophore Modelling 94

3.3.2 Structure-Based Molecular Docking 98

3.4 Synthesis of Schiff Base Vanillin Derivatives 101

3.5 Characterization of Schiff Base Vanillin Derivatives 102

3.5.1 Thin Layer Chromatography (TLC) 102

3.5.2 Fourier Transform-Infrared Spectroscopy 103

3.5.3 Nuclear Magnetic Resonance Spectroscopy 103

3.6 Antibacterial Assay 104

CHAPTER 4: RESULTS AND DISCUSSION 106

4.1 CADD Results of Schiff Base Vanillin Derivatives Targeting Neuraminidase of *S. pneumoniae* 106

4.1.1 Ligand-based Approach 106

4.1.2 Structure-Based Approach 138

4.2 CADD Results of Schiff Base Vanillin Derivatives Targeting FtsZ of *S. aureus* 159

4.2.1 Ligand-Based Approach 159

4.2.2 Structure-Based Approach 189

4.3 Conclusion of Schiff Base Vanillin Derivatives as Potential Inhibitors of Neuraminidase of *S. pneumoniae* and FtsZ of *S. aureus* 208

4.4 Lipinski's Rule of 5 211

4.5 Schiff Base Synthesis Reaction 213

4.6 Characterizations of Synthesized Schiff Base Vanillin Derivatives 216

4.6.1 Fourier Transform Infrared Spectroscopy 216

4.6.2 Nuclear Magnetic Resonance Spectroscopy 231

4.7 Antibacterial Assay 257

CHAPTER 5: CONCLUSION AND RECOMMENDATIONS 264

5.1 Conclusion 264

5.2 Recommendations 268

REFERENCES 270

APPENDICES 302

LIST OF TABLES

		Page
Table 2.1:	Examples of types of pharmacophore features with the interaction types and structural examples (Seidel et al., 2020)	54
Table 3.1:	Training sets used to generate pharmacophore model	71
Table 3.2:	Test sets used to validate the generated pharmacophore model	72
Table 3.3:	List of primary amines and the chemical structures of the Schiff base vanillin derivatives	78
Table 3.4:	Training sets to generate pharmacophore model	94
Table 3.5:	Test sets to validate the generated pharmacophore model	96
Table 4.1:	3D chemical structures of training sets	106
Table 4.2:	3D chemical structures of test sets for validation of pharmacophore model	108
Table 4.3:	Pharmacophore fit values and matching features of training sets and test sets in the generated pharmacophore model	109
Table 4.4:	RMSD-based evaluation of test sets alignment to the pharmacophore model	119
Table 4.5:	Cosine similarities of test sets and the pharmacophore model	120
Table 4.6:	3D chemical structures of Schiff base vanillin derivatives	121
Table 4.7:	Pharmacophore fit values and matching features of Schiff base vanillin derivatives in the generated pharmacophore model	124
Table 4.8:	Binding affinity values of Schiff base vanillin derivatives in the active site of 2YA8	156
Table 4.9:	3D chemical structures of training sets	159
Table 4.10:	3D chemical structures of test sets for validation of pharmacophore model	160
Table 4.11:	Pharmacophore fit values and matching features of training sets and test sets in the generated pharmacophore model	162

Table 4.12:	RMSD-based evaluation of test sets alignment to the pharmacophore model	171
Table 4.13:	Cosine similarities of test sets and the pharmacophore model	172
Table 4.14:	Pharmacophore fit values and matching features of Schiff base vanillin derivatives in the generated pharmacophore model	174
Table 4.15:	Binding affinity values of Schiff base vanillin derivatives in the active site of 3VOB	206
Table 4.16:	Conclusion of Schiff base vanillin derivatives as neuraminidase inhibitors of *S. pneumoniae* and FtsZ inhibitors of *S. aureus*	209
Table 4.17:	Lipinski's Rule of 5 of Schiff base vanillin derivatives	212
Table 4.18:	General synthetic route of Schiff base vanillin derivatives	213
Table 4.19:	^{1}H NMR of compound (8)	231
Table 4.20:	^{1}H NMR of compound (9)	236
Table 4.21:	^{1}H NMR of compound (12)	240
Table 4.22:	^{1}H NMR of compound (15)	245
Table 4.23:	^{1}H NMR of compound (17)	249
Table 4.24:	^{1}H NMR of compound (21)	253
Table 4.25:	Antibacterial assay results of positive control, negative control, empty control and Schiff base vanillin derivatives against *S. aureus*	258
Table 4.26:	Summary of overall CADD and agar diffusion assay results	262

LIST OF FIGURES

		Page
Figure 1.1	Highest mortality rate of children due to pneumonia infection recorded in the southern Asia and sub-Saharan Africa (Institute for Health Metrics and Evaluation, 2024)	1
Figure 2.1	Chemical structure of vanillin	10
Figure 2.2	General synthetic route of Schiff base vanillin derivative	13
Figure 2.3	Inflammation of lungs caused by pneumonia (Cleveland Clinic, 2022)	15
Figure 2.4	Structure of *S. pneumoniae* (Fleck, 2019)	23
Figure 2.5	*S. pneumoniae* and host factors affecting pneumococcal shedding (Weiser et al., 2018)	24
Figure 2.6	Transmission, colonization and invasion of *S. pneumoniae* (Weiser et al., 2018)	26
Figure 2.7	Graphical representation of virulence factors of *S. pneumoniae* (Negi and Das, 2017)	27
Figure 2.8	Chemical structure of artocarpin from *Artocarpus heterophyllus* (Walther et al., 2015)	31
Figure 2.9	Mulberry root bark	32
Figure 2.10	Chemical structure of sanggenon G from mulberry root bark	32
Figure 2.11	Chemical structure of sanggenol A from mulberry root bark	32
Figure 2.12	Chemical structure of chlorogenic acid	33
Figure 2.13	Structure of *S. aureus* (CDC, 2024)	34
Figure 2.14	General schematic outline of the life cycle of *S. aureus* (Barbuti et al., 2023)	35
Figure 2.15	General model of cytokinesis of *S. aureus* (Monteiro et al., 2018)	41
Figure 2.16	Crystal structure of FtsZ of *S. aureus* (Carro, 2019)	42
Figure 2.17	General outline of the domains in FtsZ (Pradhan et al., 2021)	42
Figure 2.18	General insight of polymerization of FtsZ (Pradhan et al., 2021)	42

Figure 2.19	Chemical structure of madurahydroxylactone	43
Figure 2.20	Chemical structure of silibinin from *Silybum marianum* (Basak et al., 2014)	43
Figure 2.21	Chemical structure of 3-methoxybenzamide	44
Figure 2.22	Chemical structure of PC190723	44
Figure 2.23	Chemical structure of TXA707	45
Figure 2.24	Chemical structure of DS01750413	45
Figure 2.25	Chemical structure of C109	45
Figure 2.26	Traditional process of drug design and discovery (Surabhi and Singh, 2018)	47
Figure 2.27	Schematic representation of drug discovery process (Schaduangrat et al., 2020)	49
Figure 2.28	General principles of drug design by CADD (Surabhi and Singh, 2018)	50
Figure 2.29	General idea of LBDD (Hoque et al., 2017)	50
Figure 2.30	General steps in SBDD (Surabhi and Singh, 2018)	51
Figure 2.31	Pharmacophore features and depiction in LigandScout 4.4.9	53
Figure 2.32	Example of shared feature pharmacophore model (Seidel et al., 2010)	56
Figure 2.33	Crystal structure of Zika virus NS2B-NS3 protease in complex with boronate inhibitor (Lei et al., 2016)	59
Figure 2.34	Boronate inhibitor ligand structure in the active site of 5LC0 (Lei et al., 2016)	59
Figure 2.35	Pharmacophore model of boronate inhibitor	59
Figure 2.36	Rigid-body (A) and flexible-rigid molecular docking (Fan et al., 2019)	62
Figure 2.37	Disk-diffusion method of a microbial extract against *Candida albicans* (Balouiri et al., 2016)	66
Figure 2.38	Broth microdilution of plant extract against *Bacillus subtilis* (Balouiri et al., 2016)	67
Figure 3.1	General overview of CADD workflow (Asaruddin, 2016)	69

Figure 3.2	ChemDraw Ultra 12.0 to draw chemical structures	70
Figure 3.3	Minimising MMFF94 energies of training sets and test sets	74
Figure 3.4	Generation of conformations by using FAST settings	75
Figure 3.5	Clustering of ligand sets based on pharmacophore RDF-code similarity and average cluster distance calculation	75
Figure 3.6	Creation of ligand-based pharmacophore model based on pharmacophore fit scoring function	76
Figure 3.7	Generation of pharmacophore model based on merged pharmacophore feature, and evaluation based on the matching features, model scores and pharmacophore fit values	76
Figure 3.8	General synthetic route of Schiff base vanillin derivatives	77
Figure 3.9	Crystal structure of *S. pneumoniae* neuraminidase A in complex with oseltamivir carboxylate (2YA8)	84
Figure 3.10	Pharmacophore model of the ligand, oseltamivir carboxylate	84
Figure 3.11	Oseltamivir carboxylate ligand and pharmacophore model copied to the alignment perspective	85
Figure 3.12	Conversion of MDL-mol files of Schiff base vanillin derivatives to MDL-sdf files by using Open Babel GUI 2.3.1	86
Figure 3.13	Successful alignment between oseltamivir carboxylate ligand and vanillin derivative	87
Figure 3.14	Shared feature pharmacophore, merged pharmacophores and interpolated overlapping features	87
Figure 3.15	Interactions depicted by the vanillin derivative in the active site of 2YA8 in in comparison with oseltamivir carboxylate ligand	88
Figure 3.16	Import of 2YA8 in AutoDock 4.2	89
Figure 3.17	Import of MDF-sdf file of vanillin + salicyl hydrazide in PyMOL to be converted to PDB file format	90
Figure 3.18	Import of PDB file of vanillin + salicyl hydrazide in AutoDock 4.2 to be converted to PDBQT file format	90
Figure 3.19	PDB file format of 2YA8 and vanillin + salicyl hydrazude in AutoDock 4.2	91
Figure 3.20	Grid box of 2YA8	92

Figure 3.21	Information in configuration text	92
Figure 3.22	Command prompt that successfully show binding affinity value of vanillin + salicyl hydrazide in the active site of 2YA8	93
Figure 3.23	*S. aureus* with PC190723 (3VOB)	98
Figure 3.24	Pharmacophore model of the ligand, PC190723	99
Figure 3.25	PC190723 ligand and pharmacophore model copied to the alignment perspective	99
Figure 3.26	Import of 3VOB in AutoDock 4.2	100
Figure 3.27	Synthetic route of Schiff base vanillin derivatives	102
Figure 3.28	General illustration of thin layer chromatography (TLC)	103
Figure 4.1	Generated pharmacophore model by training sets	109
Figure 4.2	Interaction, pharmacophore fit value and matching features of DANA and pharmacophore model	111
Figure 4.3	Interaction, pharmacophore fit value and matching features of NANA and pharmacophore model	112
Figure 4.4	Interaction, pharmacophore fit value and matching features of zanamivir and pharmacophore model	112
Figure 4.5	Interaction, pharmacophore fit value and matching features of 9N3Neu5Ac2en and pharmacophore model	113
Figure 4.6	Interaction, pharmacophore fit value and matching features of artocarpin and pharmacophore model	114
Figure 4.7	Interaction, pharmacophore fit value and matching features of chlorogenic acid and pharmacophore model	115
Figure 4.8	Interaction, pharmacophore fit value and matching features of sanggenon G and pharmacophore model	116
Figure 4.9	Interaction, pharmacophore fit value and matching features of sanggenol A and pharmacophore model	117
Figure 4.10	Interaction, pharmacophore fit value and matching features of kaempferol and pharmacophore model	117
Figure 4.11	Interaction, pharmacophore fit value and matching features of katsumadain A and pharmacophore model	118

Figure 4.12	Interaction, pharmacophore fit value and matching features of compound (1) and pharmacophore model	126
Figure 4.13	Interaction, pharmacophore fit value and matching features of compound (2) and pharmacophore model	127
Figure 4.14	Interaction, pharmacophore fit value and matching features of compound (3) and pharmacophore model	127
Figure 4.15	Interaction, pharmacophore fit value and matching features of compound (4) and pharmacophore model	128
Figure 4.16	Interaction, pharmacophore fit value and matching features of compound (5) and pharmacophore model	129
Figure 4.17	Interaction, pharmacophore fit value and matching features of compound (6) and pharmacophore model	129
Figure 4.18	Interaction, pharmacophore fit value and matching features of compound (7) and pharmacophore model	130
Figure 4.19	Interaction, pharmacophore fit value and matching features of compound (8) and pharmacophore model	130
Figure 4.20	Interaction, pharmacophore fit value and matching features of compound (9) and pharmacophore model	131
Figure 4.21	Interaction, pharmacophore fit value and matching features of compound (10) and pharmacophore model	132
Figure 4.22	Interaction, pharmacophore fit value and matching features of compound (11) and pharmacophore model	132
Figure 4.23	Interaction, pharmacophore fit value and matching features of compound (12) and pharmacophore model	133
Figure 4.24	Interaction, pharmacophore fit value and matching features of compound (13) and pharmacophore model	133
Figure 4.25	Interaction, pharmacophore fit value and matching features of compound (14) and pharmacophore model	134
Figure 4.26	Interaction, pharmacophore fit value and matching features of compound (15) and pharmacophore model	134
Figure 4.27	Interaction, pharmacophore fit value and matching features of compound (16) and pharmacophore model	135
Figure 4.28	Interaction, pharmacophore fit value and matching features of compound (17) and pharmacophore model	135

Figure 4.29	Interaction, pharmacophore fit value and matching features of compound (18) and pharmacophore model	136
Figure 4.30	Interaction, pharmacophore fit value and matching features of compound (19) and pharmacophore model	136
Figure 4.31	Interaction, pharmacophore fit value and matching features of compound (20) and pharmacophore model	137
Figure 4.32	Interaction, pharmacophore fit value and matching features of compound (21) and pharmacophore model	137
Figure 4.33	Pharmacophore model of oseltamivir carboxylate ligand in 2YA8	139
Figure 4.34	Alignment of compound (1) with oseltamivir carboxylate ligand and the matching interactions with the pharmacophore model	140
Figure 4.35	Alignment of compound (2) with oseltamivir carboxylate ligand and the matching interactions with the pharmacophore model	141
Figure 4.36	Alignment of compound (3) with oseltamivir carboxylate ligand and the matching interactions with the pharmacophore model	141
Figure 4.37	Alignment of compound (4) with oseltamivir carboxylate ligand and the matching interactions with the pharmacophore model	142
Figure 4.38	Alignment of compound (5) with oseltamivir carboxylate ligand and the matching interactions with the pharmacophore model	143
Figure 4.39	Alignment of compound (6) with oseltamivir carboxylate ligand and the matching interactions with the pharmacophore model	143
Figure 4.40	Alignment of compound (7) with oseltamivir carboxylate ligand and the matching interactions with the pharmacophore model	144
Figure 4.41	Alignment of compound (8) with oseltamivir carboxylate ligand and the matching interactions with the pharmacophore model	145
Figure 4.42	Alignment of compound (9) with oseltamivir carboxylate ligand and the matching interactions with the pharmacophore model	145
Figure 4.43	Alignment of compound (10) with oseltamivir carboxylate ligand and the matching interactions with the pharmacophore model	146
Figure 4.44	Alignment of compound (11) with oseltamivir carboxylate ligand and the matching interactions with the pharmacophore model	147
Figure 4.45	Alignment of compound (12) with oseltamivir carboxylate ligand and the matching interactions with the pharmacophore model	148

Figure 4.46	Alignment of compound (13) with oseltamivir carboxylate ligand and the matching interactions with the pharmacophore model	149
Figure 4.47	Alignment of compound (14) with oseltamivir carboxylate ligand and the matching interactions with the pharmacophore model	149
Figure 4.48	Alignment of compound (15) with oseltamivir carboxylate ligand and the matching interactions with the pharmacophore model	150
Figure 4.49	Alignment of compound (16) with oseltamivir carboxylate ligand and the matching interactions with the pharmacophore model	150
Figure 4.50	Alignment of compound (17) with oseltamivir carboxylate ligand and the matching interactions with the pharmacophore model	151
Figure 4.51	Alignment of compound (18) with oseltamivir carboxylate ligand and the matching interactions with the pharmacophore model	152
Figure 4.52	Alignment of compound (19) with oseltamivir carboxylate ligand and the matching interactions with the pharmacophore model	153
Figure 4.53	Alignment of compound (21) with oseltamivir carboxylate ligand and the matching interactions with the pharmacophore model	153
Figure 4.54	Failure of compound (20) to align with oseltamivir carboxylate ligand and the pharmacophore model	154
Figure 4.55	Key active site residues of catalytic domain of 2YA8	154
Figure 4.56	Generated pharmacophore model by training sets	162
Figure 4.57	Interaction, pharmacophore fit value and matching features of TXA707 and pharmacophore model	164
Figure 4.58	Interaction, pharmacophore fit value and matching features of TXH9179 and pharmacophore model	165
Figure 4.59	Interaction, pharmacophore fit value and matching features of PC190723 and pharmacophore model	165
Figure 4.60	Interaction, pharmacophore fit value and matching features of TXA6101 and pharmacophore model	166
Figure 4.61	Interaction, pharmacophore fit value and matching features of silibinin and pharmacophore model	167
Figure 4.62	Interaction, pharmacophore fit value and matching features of arbutin and pharmacophore model	168

Figure 4.63 Interaction, pharmacophore fit value and matching features of diaporthalasin and pharmacophore model 169

Figure 4.64 Interaction, pharmacophore fit value and matching features of gliotoxin and pharmacophore model 169

Figure 4.65 Interaction, pharmacophore fit value and matching features of baicalein and pharmacophore model 170

Figure 4.66 Interaction, pharmacophore fit value and matching features of 5-methoxydihydrosterigmatocystin and pharmacophore model 170

Figure 4.67 Interaction, pharmacophore fit value and matching features of compound (13) and pharmacophore model 176

Figure 4.68 Interaction, pharmacophore fit value and matching features of compound (12) and pharmacophore model 177

Figure 4.69 Interaction, pharmacophore fit value and matching features of compound (1) and pharmacophore model 177

Figure 4.70 Interaction, pharmacophore fit value and matching features of compound (9) and pharmacophore model 178

Figure 4.71 Interaction, pharmacophore fit value and matching features of compound (19) and pharmacophore model 179

Figure 4.72 Interaction, pharmacophore fit value and matching features of compound (6) and pharmacophore model 179

Figure 4.73 Interaction, pharmacophore fit value and matching features of compound (5) and pharmacophore model 180

Figure 4.74 Interaction, pharmacophore fit value and matching features of compound (8) and pharmacophore model 181

Figure 4.75 Interaction, pharmacophore fit value and matching features of compound (7) and pharmacophore model 181

Figure 4.76 Interaction, pharmacophore fit value and matching features of compound (17) and pharmacophore model 182

Figure 4.77 Interaction, pharmacophore fit value and matching features of compound (21) and pharmacophore model 182

Figure 4.78 Interaction, pharmacophore fit value and matching features of compound (20) and pharmacophore model 183

Figure 4.79 Interaction, pharmacophore fit value and matching features of compound (10) and pharmacophore model 184

Figure 4.80 Interaction, pharmacophore fit value and matching features of compound (14) and pharmacophore model 184

Figure 4.81 Interaction, pharmacophore fit value and matching features of compound (18) and pharmacophore model 185

Figure 4.82 Interaction, pharmacophore fit value and matching features of compound (15) and pharmacophore model 185

Figure 4.83 Interaction, pharmacophore fit value and matching features of compound (16) and pharmacophore model 186

Figure 4.84 Interaction, pharmacophore fit value and matching features of compound (2) and pharmacophore model 187

Figure 4.85 Interaction, pharmacophore fit value and matching features of compound (4) and pharmacophore model 187

Figure 4.86 Interaction, pharmacophore fit value and matching features of compound (11) and pharmacophore model 188

Figure 4.87 Interaction, pharmacophore fit value and matching features of compound (3) and pharmacophore model 188

Figure 4.88 Pharmacophore model of PC190723 ligand in 3VOB 190

Figure 4.89 Alignment of compound (1) with PC190723 ligand and the matching interactions with the pharmacophore model 191

Figure 4.90 Alignment of compound (2) with PC190723 ligand and the matching interactions with the pharmacophore model 192

Figure 4.91 Alignment of compound (3) with PC190723 ligand and the matching interactions with the pharmacophore model 192

Figure 4.92 Alignment of compound (4) with PC190723 ligand and the matching interactions with the pharmacophore model 193

Figure 4.93 Alignment of compound (5) with PC190723 ligand and the matching interactions with the pharmacophore model 194

Figure 4.94 Alignment of compound (6) with PC190723 ligand and the matching interactions with the pharmacophore model 194

Figure 4.95 Alignment of compound (7) with PC190723 ligand and the matching interactions with the pharmacophore model 195

Figure 4.96 Alignment of compound (8) with PC190723 ligand and the matching interactions with the pharmacophore model 195

Figure 4.97	Alignment of compound (9) with PC190723 ligand and the matching interactions with the pharmacophore model	196
Figure 4.98	Alignment of compound (10) with PC190723 ligand and the matching interactions with the pharmacophore model	197
Figure 4.99	Alignment of compound (11) with PC190723 ligand and the matching interactions with the pharmacophore model	197
Figure 4.100	Alignment of compound (12) with PC190723 ligand and the matching interactions with the pharmacophore model	198
Figure 4.101	Alignment of compound (13) with PC190723 ligand and the matching interactions with the pharmacophore model	199
Figure 4.102	Alignment of compound (14) with PC190723 ligand and the matching interactions with the pharmacophore model	199
Figure 4.103	Alignment of compound (15) with PC190723 ligand and the matching interactions with the pharmacophore model	200
Figure 4.104	Alignment of compound (16) with PC190723 ligand and the matching interactions with the pharmacophore model	201
Figure 4.105	Alignment of compound (17) with PC190723 ligand and the matching interactions with the pharmacophore model	202
Figure 4.106	Alignment of compound (19) with PC190723 ligand and the matching interactions with the pharmacophore model	202
Figure 4.107	Alignment of compound (20) with PC190723 ligand and the matching interactions with the pharmacophore model	203
Figure 4.108	Alignment of compound (21) with PC190723 ligand and the matching interactions with the pharmacophore model	203
Figure 4.109	Failure of compound (18) to align with oseltamivir carboxylate ligand and the pharmacophore model	204
Figure 4.110	Synthesized Schiff base vanillin derivatives	216
Figure 4.111	FT-IR spectrum of vanillin (Reusch, 2013)	217
Figure 4.112	FT-IR spectrum of compound (8)	220
Figure 4.113	FT-IR spectrum of compound (9)	222
Figure 4.114	FT-IR spectrum of compound (12)	224
Figure 4.115	FT-IR spectrum of compound (15)	226

Figure 4.116 FT-IR spectrum of compound (17) 228

Figure 4.117 FT-IR spectrum of compound (21) 230

Figure 4.118 ^{1}H NMR of compound (8) 234

Figure 4.119 Expansion of several sections of ^{1}H NMR of compound (8) 235

Figure 4.120 ^{1}H NMR of compound (9) 238

Figure 4.121 Expansion of several sections of ^{1}H NMR of compound (9) 239

Figure 4.122 ^{1}H NMR of compound (12) 243

Figure 4.123 Expansion of several sections of ^{1}H NMR of compound (12) 244

Figure 4.124 ^{1}H NMR of compound (15) 247

Figure 4.125 Expansion of several sections of ^{1}H NMR of compound (15) 248

Figure 4.126 ^{1}H NMR of compound (17) 251

Figure 4.127 Expansion of several sections of ^{1}H NMR of compound (17) 252

Figure 4.128 ^{1}H NMR of compound (21) 255

Figure 4.129 Expansion of several sections of ^{1}H NMR of compound (21) 256

Figure 4.130 Agar disk diffusion antibacterial assay of positive control, negative control and empty control against *S. aureus* 257

Figure 4.131 Agar disk diffusion antibacterial assay of compounds (8), (9) and (12) against *S. aureus* 259

Figure 4.132 Agar disk diffusion antibacterial assay of compounds (15), (17) and (21) against *S. aureus* 260

LIST OF ABBREVIATIONS

^{1}H NMR	Proton Nuclear Magnetic Resonance
2D	2 Dimensional
3D	3 Dimensional
AR	Aromatic Ring
CADD	Computational-aided Drug Design
CDC	Centers For Disease Control And Prevention
DANA	2-deoxy-2,3-dehydro-N-acetyl-neuraminic acid
DMSO	Dimethyl Sulfoxide
FT-IR	Fourier Transform-Infrared Spectroscopy
HBA	Hydrogen Bond Acceptor
HBD	Hydrogen Bond Donor
HI	Hydrophobic Interaction
LBDD	Ligand-Based Drug Design
NANA	N-acetyl-alpha-neuraminic acid
NI	Negative Ionizable Area
PDB	Protein Data Bank
PI	Positive Ionizable Area
RMSD	Root Mean Square Deviation
RO5	Lipinski's Rule of 5
SBDD	Structure-Based Drug Design
TLC	Thin Layer Chromatography
WHO	World Health Organization

CHAPTER 1

INTRODUCTION

1.1 General Introduction

Pneumonia is recorded as one of the greatest killer all over the world, especially children. More than 725,000 children were reported dead due to pneumonia infection, and among these death cases, 190,000 were newborns who possess weak immunity towards the infection (UNICEF, 2024). UNICEF (2024) also reported that the statistics of death due to pneumonia infection is recorded as one death case every 43 seconds. WHO (2022) reported that in 2019, 14% of deaths of children below 5 years old and 22% of deaths of children between 1 to 5 years old were due to pneumonia infection, with highest mortality rate recorded in the southern Asia and sub-Saharan Africa as depicted in Figure 1.1.

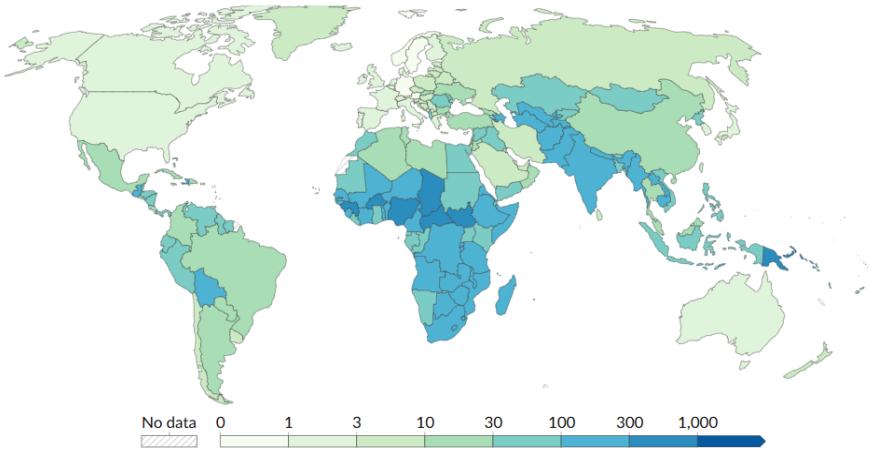


Figure 1.1: Highest mortality rate of children due to pneumonia infection recorded in the southern Asia and sub-Saharan Africa (Institute for Health Metrics and Evaluation, 2024)

Apart from children, senior citizens aged 70 and above are also susceptible to pneumonia, such that pneumonia infection was reported as the second highest reason of hospitalizations, which is responsible for more than 600,000 hospitalizations annually

(Bauer et al., 2000). Aged patients who were subjected to hospitalizations were more susceptible to severe complications and require more time to be monitored, and the mortality rate recorded was as high as 20% (Fein and Niederman, 1994; Mandel et al., 2007). Generally, pneumonia is defined as infection of lung, particularly the lower respiratory tract in the alveolar spaces of either one for both lungs (Sattar et al., 2024). Most pneumonia cases were due to infection caused by *Streptococcus pneumoniae* and *Staphylococcus aureus*.

S. pneumoniae, or known as pneumococcus, is a gram-positive, lancet-shaped bacterium, usually found in pairs and with more than 100 serotypes, which commonly reside human's upper respiratory tract, nasal cavity and sinuses (WHO, 2022). Being a pathogenic bacterium, it has led to significant level of morbidity and mortality worldwide, especially among the children and elder people in developing areas (Lv et al., 2020). *S. pneumoniae* is alpha-hemolytic, which means that it is able to produce hydrogen peroxide, H_2O_2 and causing the haemolysis of erythrocytes. The presence of H_2O_2 may led to destruction of DNA and apoptosis of lung cells (Oliver, 2019). On top of that, for inhabiting human nasopharynx asymptomatically, it has led to numerous invasive pneumococcal infections, aside from pneumonia, other include meningitis, otitis media and bacteremia (Nguyen and Bhattacharya, 2022).

S. aureus is also Gram-positive bacterium, but spherical-shaped and discovered in cocci-shaped in clusters (CDC, 2024). By possessing its ability to grow and survive with or without oxygen at temperatures between 18°C and 40°C, it is also a common cause of pneumonia by inhabiting upper respiratory tract just like the activity of *S. pneumoniae* (Taylor and Unakal, 2023). Similarly, this resulted in high level of morbidity and mortality all over the world.

Being an urgent public health concern, developments and discoveries of therapeutic agents and vaccines have been done to overcome the bacterial infection. Antibiotics have been prescribed as the main treatment for *S. pneumoniae* infections. The commonly used antibiotics include penicillin, macrolides, clindamycin, cephalosporin, rifampin, vancomycin, and trimethoprim-sulfamethoxazole, which were utilized until the 70s (Sanchez and Perloff, 2023). Pneumococcal vaccinations were also given as a step of prevention of pneumococcal disease, which include pneumococcal conjugate vaccines (PCV13, PCV15, and PCV20) and pneumococcal polysaccharide vaccine (PPSV23) (CDC, 2023). Other than that, amoxicillin is given to patients with pneumonia, otitis media and sinusitis (Musher, 2019).

Despite significant studies, developments and availability of effective therapeutic agents and vaccines, the mortality rate has remained high due to the increasing number of strains that are resistant to the available antibiotics which complicates the medications (Lv et al., 2020). Due to antibiotic abusage in hospitals, multidrug-resistant and vancomycin-resistant strains have drastically increased (Lui and Lai, 2025). It was reported by Centers of Disease Control and Prevention (CDC) (2022) that up to 40% of the pneumococcal infections until 2000 were due to resistance of pneumococcal bacteria to at least one type of antibiotic. Particularly for *S. aureus*, presence of Methicillin-Resistant *S. aureus* (MRSA) and Vancomycin-resistant *S. aureus* (VRSA) further complicates the condition (Saber et al., 2022). Vaccines may depict great effectivity, but the loopholes of a few vaccine strain serotypes may result in frequent cases of pneumonia (Micoli et al., 2023). For the increasing emergence of antibiotic-resistance *S. pneumoniae* and *S. aureus* isolates, the greater increase of more serious and risky complications may be a possible concern in the future. Therefore,

the development of more drugs or novel inhibitors against infections caused by *S. pneumoniae* and *S. aureus* is crucially necessary in different fields.

Neuraminidase A of *S. pneumoniae*, NanA, played an imperative role by catalyzing the release and removal of terminal sialic acid residues from cell membrane glycostructures, hence decreasing the binding of complement regulator factor H to cell surfaces (Parker et al., 2009). FtsZ of *S. aureus* played its essential role by facilitating cell division of the bacteria, which undergoes polymerization to form Z ring, thus initiates recruitment of conserved proteins and mediates bacteria division (Adams and Errington, 2009). For these reasons, neuraminidase of *S. pneumoniae* and FtsZ of *S. aureus* serve as attractive target for the design, development and discovery of chemical of drug compounds to inhibit the bacterial activity.

Particularly, Schiff base vanillin derivatives, chemical compounds derived from Schiff base synthesis reactions between vanillin and a series of primary amines, were reported for possessing wide range of biological activities (Ngaini and Mortadza, 2019). Previously, a research has reported that neuraminidase of influenza virus was able to be inhibited by Schiff base vanillin derivatives, compounds derived from the Schiff base synthesis mechanism between vanillin and primary amines, by *in silico* pharmacophore modelling, virtual screening and molecular docking, as well as *via* 2′-(4-Methylumbelliferyl)-α-D-N-acetylneuraminic acid (MUNANA) assay (Asaruddin, 2016). As a result, Schiff base vanillin derivatives are considered potential neuraminidase inhibitors, but research related to their inhibitory activity against neuraminidase of *S. pneumoniae* are considered highly potential but very limited. At the same time, Sun et al. (2014), reported the potential inhibitory activity of Schiff base vanillin derivatives against

FtsZ of *Escherichia coli* by performing antibacterial assay and docking simulation. Despite that, research related to Schiff base vanillin derivatives against FtsZ of particularly *S. aureus* is also highly potential but deficient. Simultaneously, most the the methods employed in antibacterial studies are either *in vitro* or *in vivo*, hence methods of study are not sufficient too. *In silico* studies, which are computer-aided drug design methods are potential and limited field to investigate the antibacterial activity of Schiff base vanillin derivatives against neuraminidase of *S. pneumoniae* and FtsZ of *S. aureus*.

Pharmacophore modelling is a CADD approach which is successful in hit identification, lead optimization to clinical candidates and rational design of novel drugs (Qing et al., 2014). The IUPAC definition of pharmacophore is "an ensemble of steric and electronic features that is necessary to ensure the optimal supramolecular interactions with a specific biological target and to trigger (or block) its biological response" (Wermuth et al., 1998). Structural information about the molecular interactions shared by the set of active molecules can be obtained from a pharmacophore model. Based on the IUPAC definition of pharmacophore, the 3D arrangement of abstract features that show interaction types represent the interaction patterns of bioactive molecules with their biological targets (Kaserer et al., 2015).

Pharmacophore modelling can be performed in the presence of a set of active ligand structures of similar or different scaffolds, even if the target protein is unknown or absent. First of all, a set structurally diverse molecules are selected and imported as training sets which will be used to develop a pharmacophore model. Consequently, conformational analysis is performed, in which a set of low energy conformations is generated, whereby there’s high probability that the bioactive conformation is in the list of generated

conformations. After conformational analysis, the conformations of the molecules are aligned and superimposed, where similar functional groups are fitted together, for instance carboxylic acid groups or phenyl rings. The superimposed molecules are then converted to an abstract description, or pharmacophore model, whereby the superimposed functional groups are referred to as pharmacophore features, for instance, phenyl rings are referred as 'aromatic rings', hydroxyl groups are referred as 'hydrogen bond donors/acceptors' (Qing et al., 2014).

Molecular docking is a computational simulation method of a candidate ligand in a receptor. The method analyses the binding mode of ligand to the active site of receptor and the quality of interaction based on free energy of binding based on scoring functions (Kitchen et al., 2004). On top of that, the preferred orientation of the ligand molecule can also be evaluated, which will determine the strength of binding affinity between the ligand molecule and the receptor to form a stable complex (Lengauer and Rarey, 1996). In structure-based drug design, molecular docking is the most common method applied *via* evaluation of the binding mode and ability of ligand molecules to target proteins.

Molecular docking can be illustrated as the 'lock and key' concept, whereby the 'key' represents the ligand molecule, and 'lock' represents the target protein. Only the 'key' with the best fit orientation can fit in the 'lock', therefore only the ligand with the best conformation and orientation can bind to the active site of receptor (Jorgensen, 1991). In CADD, simulation of molecular recognition is the key to molecular docking process, as the final aim is to achieve optimum conformation and orientation for the ligand-substrate complex, which means with minimized free energy. However, the docking process *via in silico* is complicated, challenging and expensive which requires large energy landscape,

hence pharmacophores play an important role to enrich and assist the molecular docking process, subsequently the analysis of the biological activity of ligands against the target protein. The combination of pharmacophore modelling and molecular docking is computationally efficient method, for example, it was reported that the evaluation of poly (ADP-ribose) polymerase-1 (PARP-1) inhibitors *via* pharmacophore modelling and molecular docking is performed due to more accurate, rapid and convenient results (Zhou et al., 2019).

Pharmacophores are abstract representation of chemical features; hence pharmacophore model can be generated from PDB target protein in complex with the ligand. The pharmacophore model generated will be utilised to screen and test candidate ligands based on the alignment perspective. The imported candidate ligands can be aligned with the pharmacophore model and docked in the active site of target protein for evaluation based on their interaction with the active sites of the PDB protein structure. A single alignment is based on alignment of candidate molecule with the chemical features of the pharmacophore model and determine the total shared and aligned features based on scoring, whereas docking evaluates the protein-ligand interaction in the active site. By applying pharmacophore-based molecular docking instead of only molecular docking, the filtering and discovery process of lead candidates will be easier, faster and more precise. On top of that, together with the facilitation of ligand-based pharmacophore modelling, the outcome of the result will be optimally accurate and valid.

1.2 Problem Statement

Despite the fact that efficient therapeutic agents and vaccinations are available for the treatment of pneumonia, more strains of *S. pneumoniae* and *S. aureus* have acquired

significant resistance towards the available antibiotics, not only complicating the medication process, but also depicting ineffective in reducing the mortality rate of pneumonia infections. The possible consequence of the situation may lead to outbreak of epidemic or pandemic, such that the community may possess zero resistance due to the lack of medications for the treatment of resistant strains of *S. pneumoniae* and *S. aureus*. Therefore, the development of new drugs of inhibitors against *S. pneumoniae* and *S. aureus* infections is a highly necessary field of study from time to time. Furthermore, the neuraminidase of *S. pneumoniae* and FtsZ of *S. aureus* possess significant contribution in pathogenesis. However, research related to the search and discovery of inhibitors against particularly neuraminidase of *S. pneumoniae* and FtsZ of *S. aureus* is highly inadequate despite their greatly important role in the bacterial infection. Simultaneously, Schiff base vanillin derivatives were reported in past literature for their potential in various biological activity, including antibacterial activity (Khan et al., 2024). Despite the great potential, research reporting Schiff base vanillin derivatives' potential as neuraminidase inhibitors of *S. pneumoniae* and FtsZ inhibitors of *S. aureus* were also considered limited but with appreciable potential. In comparison to the previous studies, methods specifically based on computational study of Schiff base vanillin derivatives as potential dual inhibitors *S. pneumoniae* neuraminidase and *S. aureus* FtsZ are not being studies yet while being clinically promising. As a result, the research is uniquely novel in terms of *in silico* method of study, which is the combination of ligand-based and structure based pharmacophore modeling and molecular docking against dual targets. Hypothetically, Schiff base vanillin derivatives are able to show significant antibacterial activity, specifically dual inhibitory activity against both *S. pneumoniae* neuraminidase and *S. aureus* FtsZ *via in silico*, simultaneously exhibiting druglikeness as orally active drugs.

1.3 Objectives

In general, the main objective of the research is to evaluate the potential antibacterial activity of Schiff base vanillin derivatives against Gram-positive, pneumonia-related bacterial strains, which are *S. pneumoniae* and *S. aureus*. The elaborations of the objectives are as follow:

i. To analyse the potential of Schiff base vanillin derivatives as dual target inhibitors, particularly against the neuraminidase of *S. pneumoniae* and FtsZ of *S. aureus* by performing ligand-based pharmacophore modelling, structure-based pharmacophore modelling, structure-based molecular docking using two computational software: LigandScout 4.4.9 and AutoDock 4.2, as well as to evaluate the druglikeness by Lipinski's Rule of 5.

ii. To synthesise the Schiff base vanillin derivatives which depict satisfying results in CADD methods by Schiff base synthesis reactions.

iii. To characterize the synthesized Schiff base vanillin derivatives by performing thin layer chromatography (TLC), Fourier transform infrared spectroscopy (FTIR) and nuclear magnetic resonance spectroscopy (NMR).

iv. To further affirm the antibacterial activity of Schiff base vanillin derivatives against Gram-positive bacterium by performing agar diffusion method on Schiff base vanillin derivatives against *S. aureus* to provide stronger fundamental support to the CADD results.

CHAPTER 2

LITERATURE REVIEW

2.1 Vanillin

Vanillin, or 4-hydroxy-3-methoxybenzaldehyde is one of the most common food-grade additive and widely utilised flavourings in preparation of various type of food such as cakes, ice creams, soft drink, chocolate etc. It is the major chemical compound of vanilla which is vanilla bean or pod extracted from various Vanilla species, including *Vanilla planifolia* Andrews and *Vanilla tahitensis* Moore (Ramachandra and Ravishankar, 2000). On top of that, it was also reported to be discovered in other plant species that are not from the Vanilla genus, which are *Oryza sativa* (Chou et al., 2010), *Bruguiera gymnorhiza* (Sadeer et al., 2020), *Melia azedarach* (Han et al., 1991) etc. It has been reported that there are many types of volatile compounds discovered and extracted from vanilla, which are *p*-anisaldehyde and guaiacol, but vanillin is still the major component of vanilla (Anuradha et al., 2013). It is an organic compound of phenolic aldehyde with chemical formula of $C_8H_8O_3$, which is composed of three functional groups: aldehyde, hydroxyl and ether group, attached to an aromatic ring. The chemical structure of vanillin is as depicted in Figure 2.1.

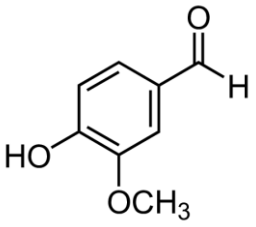


Figure 2.1: Chemical structure of vanillin

Aside from the significance of vanillin as food flavourings, in the pharmaceutical industry, cosmetic field etc., vanillin is also important for possessing diverse crucial

biological activities such as anticancer (Kurma et al., 2012), antidiabetic (Olatunde et al., 2022), antioxidant (Karathanos et al., 2007, antimicrobial (Fuqua and Greenberg, 2002) and antidepressant properties (Dhingra and Sharma, 2005). For its importance and high demand not only as food flavourings, but as well as in the pharmaceutical field, cosmetic industries etc., about 20,000 tons of vanillin are manufactured worldwide every year (Ma et al., 2022). Despite this fact, vanillin naturally extracted from natural vanilla is only about 1% of the total vanillin manufactured (Walton et al., 2003). This is because the extraction process of vanillin requires great amount of manpower while the yield is non-satisfactory (Vijayalakshmi et al., 2019). The traditional method of extraction of vanillin requires extraction from plant by using solvent, followed by chemical synthesis, and hence being inefficient and protracted (Pérez-Rodríguez et al., 2016).

As a consequence, most of the vanillin are synthesised through chemical processes in laboratories which is relatively cheaper and more convenient (Walton et al., 2003). Converti et al. (2010) have reported that about 95% of vanillin is synthesised by electing lignin and guaiacol as main material. Lignin is hydrolysed and oxidised to obtain about 10% yield (Converti et al., 2010), while guaiacol and glyoxylic acid are reacted together to yield 3-methoxy-4-hydroxymandelate sodium, followed by subsequent oxidation and acidification to yield vanillin, known as the Riedel reaction (Fache et al., 2016). To encounter and improve the loopholes and disadvantages of various synthesis methods, more methods have been developed to fulfil the increasing demands for vanillin, such as the bioconversion methods which involve the usage of microbial catalysts and cheap natural substrates (Mathew and Abraham, 2006). Methods like these are safe, greatly efficient, requires low energy and little pollution. In a nutshell, for being easily synthesised at low cost, thus conveniently available and simultaneously depicting great potential biological activities,

vanillin possesses exceptional interest by different fields of research. It has been proven in significant number of researches that chemical compounds obtained from natural sources possess promising potential upon subject to chemical alteration as this improved their biological activities by enhancing their interactions with biological targets (Ngaini and Mortadza, 2019). Therefore, a lot of studies focused on the chemical modification of the chemical structure of vanillin to improve its biological activities.

2.2 Schiff Base Vanillin Derivatives

Schiff bases, named after Hugo Schiff, are responsible for a broad spectrum of increased and improved biological activities due to the presence of C=N linkage (Vhanale et al., 2022). They are utilised as pigments, dyes, catalysts, intermediates in organic synthesis, polymer stabilisers and luminescence chemosensors (Ceramella et al., 2022). For exhibiting a wide range of biological activities due to the important C=N bond, they are discovered as potent drug in various fields of studies in pharmaceutical industries. On top of that, due to their strong coordinative strength by intra-hydrogen bonding, they were utilised as ligands to form metal complexes with transition metal ions (Vhanale et al., 2022).

Schiff bases have been reported in a number of research for their significant biological activities. For example, a few Schiff bases are reported for their potential antimalarial activity against ancistrocladidine, a secondary metabolite found in the *Ancistrocladaceae* and *Dioncophyllaceae* family plants (da Silva et al., 2011). Furthermore, Schiff bases in combination with moiety of 2,4-dichloro-5-fluorophenyl was reported for their potential inhibitory activity against fungus, such as *Aspergillus fumigatus*, *Aspergillus flavus*, *Trichophyton mentagrophytes*, and *Penicillium marneffei*, thus demonstrating potential antifungal activity (da Silva et al., 2011). Salicylaldehyde Schiff bases of 1-amino-

3-hydroxyguanidine tosylate were also reported to show antiviral activity against coronaviruses (Wang et al., 1990). Moreover, a few phenolic Schiff base derivatives synthesised by combining with one or more halo groups were successfully discovered for their antioxidant activity by using DPPH and hydroxyl radical scavenging assay, as well as antibacterial assay against *S. aureus*, *Bacillus licheniformis* and *E. coli* (Vhanale et al., 2022).

Out of all notable research, one of the most significant class of compounds derived from vanillin is the Schiff base vanillin derivatives. Schiff base vanillin derivatives are derived from the Schiff base synthesis reaction between vanillin and primary amine molecules through formation of imine linkage (C=N), thus resulting in formation of azomethine or imine compounds. The general workflow of synthesis of Schiff base vanillin derivatives are as illustrated in Figure 2.2.

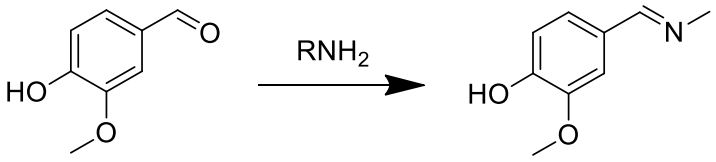


Figure 2.2: General synthetic route of Schiff base vanillin derivative

Schiff base vanillin derivatives have been developed and discovered for their greater range of biological activities in different field of research. Satpati et al. (2020) reported the adsorption and anti-corrosion activities of two Schiff base vanillin derivatives by performing electrochemical impedance spectroscopy, potentiodynamic polarization and weight loss methods. Schiff base vanillin derivatives derived from dopamine, histamine, 2-aminophenol, 4-aminophenol and 4-aminomorpholine were synthesised and tested for their neuroprotective and antidiabetic properties by their inhibitory activity against cholinesterase

(AChE and BChE), as well as against the α-glycosidase and α-amylase enzyme (Yuldasheva et al., 2022). Afterwards, Schiff base vanillin derivatives were also reported for their potential antidepressant activity by comparison with the clorgiline inhibitor (Yuldasheva et al., 2022). Furthermore, Schiff base vanillin derivatives with anthranilic acid and its ortho isomer were evaluated and discovered for possessing antifungal and antiviral activity (Prakash, 2017). Another Schiff base ligand was found out for its cytotoxic and apoptotic activity against breast cancer cells by carrying out the 3-(4,5-Dimethylthiazol-2-yl)-2,5-diphenyltetrazolium bromide (MTT)-test, such that the compound was able to reduce the growth of tumour cell and causing low toxicity to other organs simultaneously (Li et al., 2021). Due to presence of imine bond, Schiff base vanillin derivatives were also discovered for their antiviral activity against severe acute respiratory syndrome coronavirus-2 by means of computational aided drug design methods (Law et al., 2020). On top of that, the antibacterial activity of Schiff base vanillin derivatives was also studied such that the derivatives showed promising antibacterial activity against *E. coli*, *S. aureus*, *Bacillus subtilis* and *Candida albicans*, depending on the properties of aldehyde moiety combined to Schiff base ligands (Sobola, 2018). In addition to this research, a newly derived Schiff base vanillin derivative known as 5-((1E,15E)-16-(3-methoxy-4-hydroxyphenyl)hexadeca-1′,15′-di-imine)-2-methoxyphenol was synthesized and discovered for its antibacterial activity against other bacteria strains, such as *B. cereus*, *Klebsiella pneumoniae* and *Pseudomonas aeruginosa* (Celik et al., 2021).

The antibacterial activity of Schiff base vanillin derivatives was widely analysed and possess great potential to be further studied in other various fields. However, the number of bacterial strains being studied, particularly those that are related to pneumonia infections are very limited. Additionally, most research focus on methods *via in vitro* and *in vivo*, with

very limited studies related to *in silico* methods. As a result, the research focuses on the antibacterial study of Schiff base vanillin derivatives against pneumonia-related bacterial strains by performing computational methods.

2.3 Pneumonia

2.3.1 Types and Symptoms of Pneumonia, and Groups at Higher Risk

The term “pneumonia” originates from the ancient Greek work *pneumon*, thus can be considered as a “lung disease” (Kazmi, 2022). Pneumonia is an inflammatory condition of the lungs, which is a severe acute lower respiratory tract infection that inflames the lung parenchyma and alveolar spaces of one or both lungs as illustrated in Figure 2.3 (Sattar et al., 2024). Fluid or pus might fill up the air sacs in the lungs, resulting in coughing with phlegm, fever, chills and breathing problem (Mayo Foundation for Medical Education and Research, 2020).

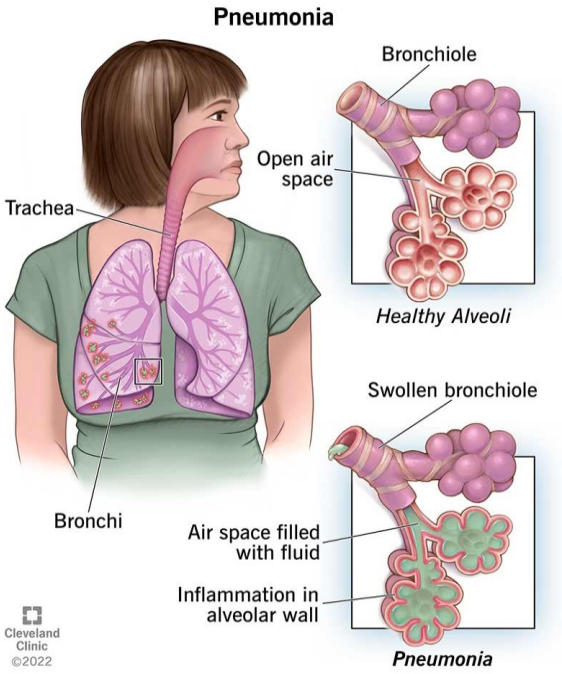


Figure 2.3: Inflammation of lungs caused by pneumonia (Cleveland Clinic, 2022)

Being reported by Chief Statistician Datuk Seri Dr Mohd Uzir Mahidin as the leading mortality cause in Malaysia in 2023 with 18,181 deaths recorded, pneumonia was responsible for 15.2% of medically certified deaths in the same year, overriding ischemic heart disease (The Star, 2024). Furthermore, more than 95% of pneumonia cases were recorded in low and middle income countries, such that pneumonia was the second leading cause of death among kids under 5 other than diarrhea and malaria (WHO, 2022). While being the sixth major cause of death, also the only infectious disease listed in the top ten killer in the United States, pneumonia is considered as a very severe infectious disease responsible for a great percentage of morbidity and mortality worldwide (Pahal et al., 2023).

Pneumonia is classified into 2 classes depending on the mode of infection, which is how the patient acquires the infection: community-acquired pneumonia (CAP) and nosocomial pneumonia, further separated into 3 types of pneumonia known as hospital-acquired pneumonia (HAP), ventilator-associated pneumonia (VAP) and healthcare-associated pneumonia (HCAP) (Pahal et al., 2023). CAP is the most common type of pneumonia, being acquired from the community, which is outside the health care facilities (Sattar et al, 2024). HAP is a type of pneumonia that develops after 48 hours being admitted to hospital, which can be very severe as the bacteria that leads to HAP has great possibility possessing significant resistance to the antibiotics (Mayo Foundation for Medical Education and Research, 2020). VAP may infect patients' lung tissues who requires mechanical ventilation for breathing, with endotracheal intubation after more than 48 hours (Pahal et al., 2023). Lastly, HCAP may cause infection to patients who are not hospitalized but requires extensive healthcare or requires treatment in outpatient clinics such as dialysis center. Similar to HAP, HCAP is caused by bacteria that is more resistant to the available antibiotics (Mayo Foundation for Medical Education and Research, 2020).

Signs and symptoms of pneumonia are different depending on several factors, including the severity of condition from mild to serious, the cause of infection, age and health condition (Mayo Foundation for Medical Education and Research, 2020). Generally, symptoms include chest pain when breathing or coughing, cough with phlegm, confused mental status, fatigue, fever, chills, nausea, vomiting, diarrhea and breathing difficulty (CDC, n.d.). Groups of people who are at higher risk of being infected include elder people aged 65 and above, children younger than 2, patients with underlying heath condition, patients with weakened immune system, or people who are under chemotherapy or and other treatments that aimed to suppress the immune system (Mayo Foundation for Medical Education and Research, 2020). In addition, people with lung and heart problems such as cystic fibrosis, asthma, chronic obstructive pulmonary disease, emphysema etc., neurological conditions such as Parkinson's disease, stroke or dementia, people who smoke, pregnant women, hospitalized patients or those require long-term treatment at hospital are also at greater risk of getting infection (Cleveland Clinic, 2022).

2.3.2 Etiology and Epidemiology of Pneumonia

Being the most common type of pneumonia, CAP is caused by various possible factors such as bacteria, viruses, fungi and parasites (Sattar et al., 2024). Out of all, bacteria are the major cause of most of the cases. Bacterial strains which lead to pneumonia include *S. pneumoniae*, *S. aureus*, *K. pneumoniae*, *Haemophilus influenzae*, *Moraxella catarrhalis*, anaerobes, and gram-negative organisms (Pahal et al., 2023). Other bacteria-like strains include *Mycoplasma pneumoniae*, *Chlamydia pneumoniae*, and *Chlamydia psittaci* (Sattar et al., 2024). The primary and main cause of CAP all over the world is *S. pneumoniae*, causing not only pneumonia, but also other pneumococcal infection, for instance meningitis, bacteremia, otitis media and sinusitis (CDC, n.d.). *S. aureus*, particularly methicillin-

resistant *S. aureus* (MRSA), is one of the predominant bacterial strain that leads to pneumonia infection, including HAP, VAP and HCAP (Sattar et al., 2024).

Viral pneumonia is caused by viral strains such as the severe acute respiratory syndrome coronavirus 2 (SARS-CoV-2) and influenza virus, whereas respiratory syncytial virus (RSV) is the most popular viral agent leading to viral pneumonia especially among children (American Lung Association, 2024). Viral pneumonias are not as severe as bacterial pneumonia, whereby they last for shorter period compared to bacterial pneumonia (American Lung Association, 2024). As for fungal pneumonia, the infection usually affects patients with chronic health conditions or weakened immune systems, for examples patients undergoing chemotherapy or organ transplant (Mayo Foundation for Medical Education and Research, 2020). As an example, Pneumocystis pneumonia is caused by *Pneumocystis jirovecii*, and other fungus strains include *Coccidioidomycosis*, *Histoplasmosis* and *Cryptococcus* (American Lung Association, 2024).

The worldwide recorded CAP every year was about 450 million cases, whereby about 95% occurring cases in developing countries, resulting in 4 million deaths every year (Sattar et al., 2024). The epidemiology of pneumonia depends on factors such as age, countries etc. In Europe countries, the number of pneumonia cases were about 206 to 470 over 100,000 patients per year (Bjarnason et al., 2018). In the United States, out of 10,000 adults, 24.8 to 26.7 CAP cases were reported, whereas out of 10,000 children below 18, 15.7 to 22.5 CAP cases were reported (Jain et al., 2015). In Malaysia, pneumonia is considered as the third leading cause of deaths among kids below 5, accounting for 12.7% of deaths in 2017 and 11.8% of deaths in 2018 (Diah and Aziz, 2021).

2.3.3 Histopathology of Pneumonia

When pneumonia develops, the illness progresses into four distinct stages, namely congestion, red hepatisation, grey hepatisation and resolution, where each stage differ from the way infection develops as time passes (Sattar et al., 2024). Stage 1 is known as congestion or consolidation which occurs 24 hours after infection takes place in the lungs, and lasts around 24 hours as well (Lee, 2022). During this stage, the lungs are inflamed, become red, heavy and boggy, as well as strongly congested due to accumulation of fluid in the alveoli (Gupta, 2023). The fluid is serous exudates which include pathogens, neutrophils and macrophages (Sattar et al., 2024).

Stage 2 is known as red hepatisation or early consolidation which happens about 2 to 3 days after infection takes place and lasts for about 2 to 4 days (Lee, 2022). At this stage, red blood cells and immune cells accumulate at the alveoli to fight the infection, as a result the lungs appear to be red due to presence of more red blood cells (Lee, 2022). The lungs also become very firm which resembles the texture of liver, dry, airless and granular (Pahal et al., 2023). This results in difficulty for alveoli to work, while at the same time, capillaries are blocked, and walls of alveoli become thick (Sattar et al., 2024). Fibrin, serous exudates, pathogens, neutrophils, macrophages, leakage of red blood cells and epithelial cells being peeled off are observed microscopically in the alveoli (Pahal et al., 2023).

During the third stage, known as grey hepatisation or late consolidation which takes place 2 to 3 days after red hepatisation, and lasts for about 4 to 8 days, lungs appear grey and firm which is akin to the liver too (Pahal et al., 2023). This is due to the exudation of fibrinopurulent followed by breakdown of red blood cells and accumulation of hemosiderin proteins which function to store iron in the blood, causing the discolouration of lungs from

red to grey (Pahal et al., 2023). Macrophages begin to enter the lungs, thus trying to protect the lungs and body (Lee, 2022).

Last but not least, the final stage which is resolution takes place around the 8th to 10th day of pneumonia infection, whereby the stage is the recovery period of pneumonia (Lee, 2022). The inflammation begins to resolve by enzymatic action, in which enzyme starts working from centre and spreads peripherally to liquefy the solid fibrin as well as to fix the aeration in the lungs (Pahal et al., 2023). Exudates are cleared by macrophages with or without leaving scar tissues (Pahal et al., 2023). By resolving the inflammation, alveoli begin to work better.

2.3.4 Treatment, Vaccination and Management of Pneumonia

Treatment and management of pneumonia patients greatly depend on how serious is the infection, thus whether the treatment received by patient is as inpatient or outpatient (Pahal et al., 2023). As a result, clinical evaluation is done by using the CURB-65 score which is composed of C = Confusion, U = Uremia (BUN more than 20 mg/dL), R = Respiratory rate (more than 30 breaths/min), B = Blood pressure (less than 90/60 mm Hg) and age 65 and above (Pahal et al., 2023). For 1 point equals to every positive criterion, if the CURB-65 score is from 0 to 1, the patients receives treatment as an outpatient, whereby 2 and above requires hospitalization, and 3 and above requires ICU admission (Sattar et al., 2024).

Medications and treatment methods depends on the severity of condition, such that for outpatients or patients who do not require hospitalization, monotherapy with antibiotics such as azithromycin and clarithromycin is necessary. Fluoroquinolones such as levofloxacin, gemifloxacin or moxifloxacin can also be utilized (Pahal et al., 2023). For hospitalized patients, treatment is given by prescribing fluoroquinones with or without

combining with beta-lactam or cephalosporin and a macrolide (Pahal et al., 2023). For patients admitted to ICU, which is when infection moves to red or grey hepatisation stages, ampicillin-sulbactam or ertapenem is added if risk of aspiration is present. For patients infected by MRSA, vancomycin or linezolid can be included in prescription (Pahal et al., 2023). Most importantly, when the infection becomes very severe, supplemental oxygen, as well as intravenous antibiotics and fluids must be provided (Gupta, 2023).

Despite the fact that different antibiotics are available, problems with pneumonia continue to arise due to presence of antibiotic-resistant bacterial strains which possess resistance towards the available antibiotics, thus showing low improvement rate despite upon treatment. Multidrug-resistant gram-negative bacteria (MDR-GNB) has led to pneumonia that possess great threat (Gao et al., 2019). It was reported that *S. pneumoniae* show strong resistance towards erythromycin, azithromycin and clindamycin, whereas *S. aureus* also shows significant resistance towards penicillin, erythromycin, tetracycline and clindamycin. On top of that, *E. coli* is resistant to ampicillin, gentamicin, and ciprofloxacin, also *K. pneumoniae* displays resistance towards gentamicin and ampicillin (Jalil et al., 2022). Similarly, *S. pneumoniae* and *S. aureus* showed 100% resistance towards cotrimoxazole (Shrestha et al., 2013).

Vaccination is given to obtain specifically serotype-protection and to prevent infection of not only pneumonia, but all pneumococcal infections. Generally, pneumococcal vaccines are divided into 2 different types, which are pneumococcal conjugate vaccine (PCV) and pneumococcal polysaccharide vaccine (PPSV). There are only 2 types of PCV utilized in Malaysia, known as PCV-10 and PCV-13. PCV-10 is composed of 10 serotypes of capsular polysaccharides, whereas PCV-13 is composed of 13 serotypes of capsular

polysaccharides (Malaysian Society of Infectious Diseases & Chemotherapy, 2023). Initially, the first PCV for infants developed in 2000 was made up of 7 pneumococcal serotypes, thus known as PCV-7 (Golos et al., 2019). It was soon replaced by PCV-10 and PCV-13 in 2010 due to additional serotypes to be targeted (Grabenstein and Klugman, 2012). Other types of PCV include PCV-15 and PCV-20, composing of 15 and 20 serotypes of capsular polysaccharides respectively (Savoy, 2024). The PPSV given in Malaysia is known as PPSV-23, which contains antigens from the 23 most virulent subtypes, developed in 1983 and replaces PPSV-14 (Golos et al., 2019).

Despite available vaccines, contraindications exist in all vaccines, such that PCV-15, PCV-20 and PPSV-23 were reported for severe allergic reactions (Savoy, 2024). On top of that, PPSV showed strong efficiency against pneumonia from all causes as reported in an analysis but only in low income countries. The efficiency is lower in adults associated with chronic illnesses (Malaysian Society of Infectious Diseases & Chemotherapy, 2023). As a whole, treatments and vaccinations that are currently available may be effective but still with loopholes. The importance of this research is to discover more alternatives as treatments and medications against pneumonia infection.

2.4 S. pneumoniae

2.4.1 Introduction of *S. pneumoniae*

S. pneumoniae, or known as pneumococcus is a member of the *Bacillota phylum*, a Gram-positive, lancet-shaped and encapsulated bacteria as shown in Figure 2.4, and the major cause of pneumonia, particularly CAP (Dion and Ashurst, 2023). The bacteria usually colonize the mucus surface of human upper respiratory tract (URT), as well as nasopharynx and nasal cavity, thus being a major cause of CAP as well as other pneumococcal infections,

including meningitis, otitis media, sepsis, bacteremia and more (Weiser et al., 2018). *S. pneumoniae* usually inhabits asymptomatically, showing no symptoms or signs, in healthy people, such that it was reported to be carried by 16.6% of healthy children in Shanghai, and about 70% of healthy children in Xinjiang (Hu et al., 2016). The highly affected groups of people include young kids and elder people, whereby an estimation of about one million deaths happened to kids annually. Because of the high carriage rates, ability to adapt to different genetic condition and strength to shift from commensalism to pathogenic interaction with the host, *S. pneumoniae* remains being eminent (Weiser et al., 2018).

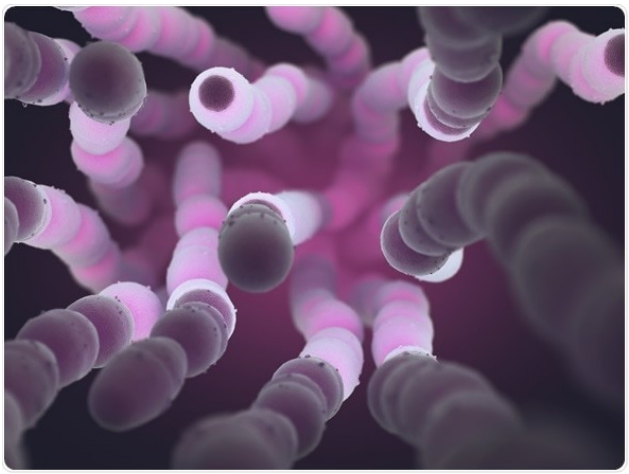


Figure 2.4: Structure of *S. pneumoniae* (Fleck, 2019)

2.4.2 Pathogenesis of *S. pneumoniae*

Generally, the pathogenesis pathway of *S. pneumoniae* is classified into 3 stages: transmission, colonization and invasion.

Stage 1 begins from transmission, such that *S. pneumoniae* was spread through close contact with carriers (Weiser et al., 2018). In most situations, the transmission stage takes place together with viral co-infection of the upper respiratory tract (Musher, 2003). The rate of transmission increases when in conjunction with viral co-infection, close contact as well as among younger age groups (Weiser et al., 2018). The transmission can move towards the

lungs, causing inflammation of alveoli and air sacs to be filled with liquid, thus resulting in breathing difficulty as elaborated earlier (Brooks and Mias, 2018).

The second stage is known as colonization or adhesion, whereby *S. pneumoniae* colonizes the epithelial barrier of upper respiratory tract and possess stable adhesion. This affects the pneumococcal shedding, such that when neutrophils are produced, which indicates inflammation occurs due to presence of pneumolysin, secretions are produced and this increases shedding. If the infection is in conjunction with influenza viral co-infection, shedding increases, too. On top of that, in the presence of agglutinating antibodies. for example, anticapsule immunoglobulin G (IgG) and immunoglobulin A1 (IgA1), shedding may decrease (Weiser et al., 2018). The illustration is as shown in Figure 2.5.

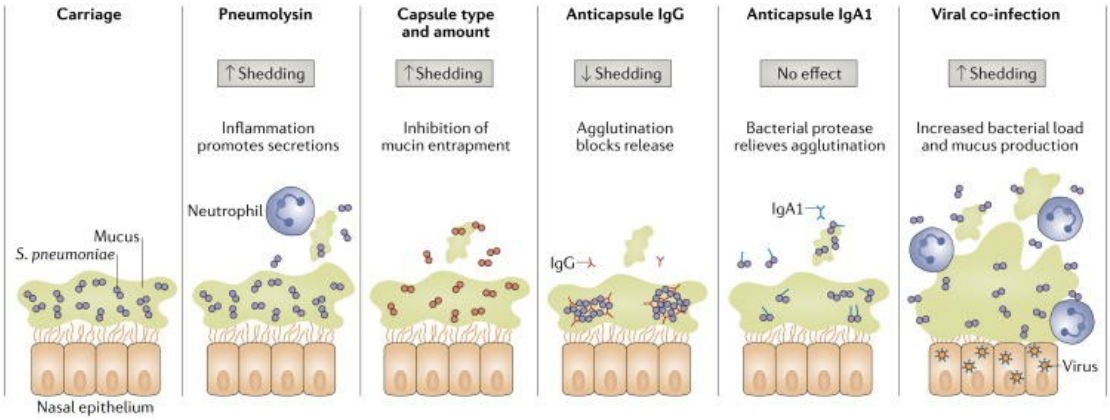


Figure 2.5: *S. pneumoniae* and host factors affecting pneumococcal shedding (Weiser et al., 2018)

The main key that allows *S. pneumoniae* to colonize upper respiratory tract is the first adhesion with epithelium, interaction with nasopharyngeal microbiota, degradation of mucus, and escaping from clearance by mucociliary flow (Weiser et al., 2018). When *S. pneumoniae* colonizes the upper respiratory tract, various proteins and polysaccharide structures known as the virulence factors begin their respective roles in evading immune attacks and facilitating the pathogenesis. The capsule is composed of polysaccharides

located around the cell wall. It plays a crucial role in pathogenesis as it is able to facilitate the bacteria to dodge phagocytosis by avoiding granulocytes from entering the underlying cell wall. The polysaccharides are important to determine the serotypes of bacteria, whereby serotypes 6, 14, 18, 19 and 23 are the usual ones that results in infection (Dion and Ashurst, 2023).

With mediation from significant roles of *S. pneumoniae* virulence factors, *S. pneumoniae* is able to invade the host cells by going through a series of mechanisms. For instance, surface protein such as pneumococcal surface protein C, PspC is important to air the entry of bacteria into the cells by its interaction with the host cells (CUSABIO, n.d.). Other example includes the crucial role of pneumococcal surface adhesin A (PsaA) to transport magnesium and zinc into the cell, thus facilitating *S. pneumoniae*'s cell adhesion and invasion (Brooks and Mias, 2018). Non-classical surface proteins (NCSPs), also known as moonlighting proteins, facilitate cell invasion by working as adhesins to bind to host molecules (Pérez-Dorado et al., 2012). Figure 2.6 shows the general life cycle and pathogenesis of *S. pneumoniae* including the transmission, colonization and invasion stages.

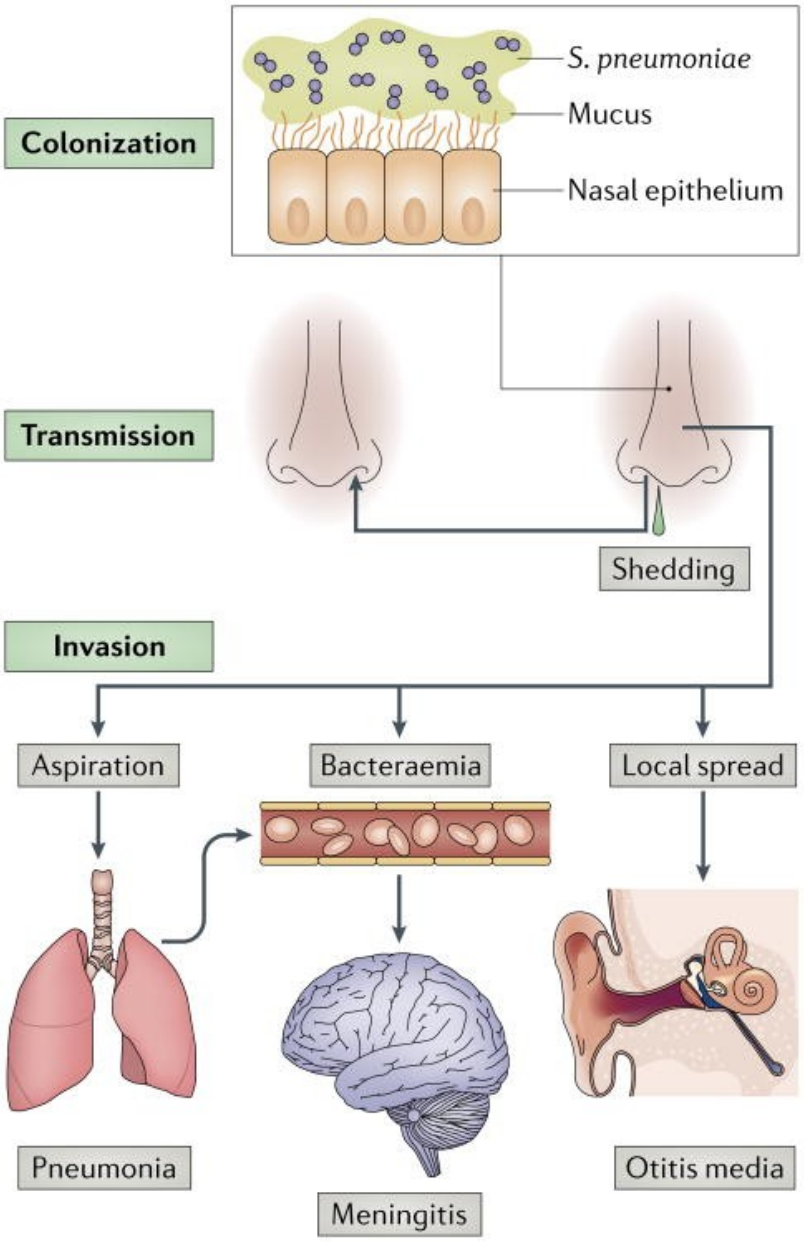


Figure 2.6: Transmission, colonization and invasion of *S. pneumoniae* (Weiser et al., 2018)

As a whole, the important characteristics of *S. pneumoniae* in pathogenesis is the capability to adhere and colonize the upper respiratory tract, nasal cavity and nasopharynx of human, the evasion ability to resist and interfere phagocytosis process of neutrophils and macrophages, as well as the strength of invasion to host cells and tissues. All the important characteristics for pathogenesis are greatly facilitated and attributed by the important roles of virulence factors.

2.4.3 Virulence Factors of *S. pneumoniae*

Virulence factors of *S. pneumoniae* significantly contribute to pathogenesis with their respective dominant roles. The virulence factors are mostly surface proteins which work in 2 ways, either directly attack or interact with host cells, or evade bacteria from host defense mechanisms (Jedrzejas, 2001). Initially, the polysaccharide capsule was known to be the main virulence factor of pathogenesis of *S. pneumoniae*, but upon more discoveries and research, more proteins are found to be essential virulence factors to mediate pathogenesis and as targets to discover inhibitors (Jedrzejas, 2001). Figure 2.7 shows the graphical representation of significant virulence factor which mediates pathogenesis and immune evasion of *S. pneumoniae*.

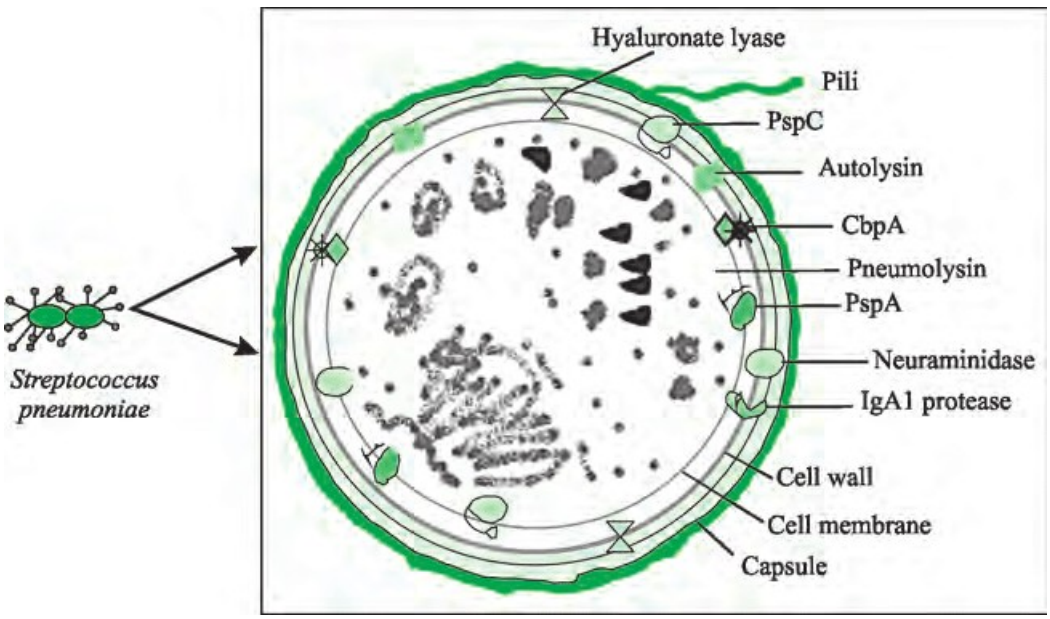


Figure 2.7: Graphical representation of virulence factors of *S. pneumoniae* (Negi and Das, 2017)

Polysaccharide capsule is located at the layer of polysaccharides on cell wall. The main function of polysaccharide capsule is to aid evasion of *S. pneumoniae* from immune attack by escaping nasal mucus and prevent phagocytosis by immune cells, thus promoting colonization and adhesion of the bacteria in the nasopharynx (Mitchell and Mitchell, 2010).

Pneumolysin is located in the cytoplasmic toxin which is important to initiate inflammation reaction, induce breakdown of cell structure and facilitate transmission from host to host (van der Poll and Opal, 2009). Autolysin is found in the intracellular enzyme, which facilitates pathogenesis by initiating cell degradation that lead to release of virulence factor, thus mediating the colonization stage (Kadioglu et al., 2008).

A significant number of pneumococcal surface proteins are present as virulence factors of *S. pneumoniae*, namely pneumococcal surface protein A (PspA), pneumococcal surface protein C (PspC) or known as choline-binding protein, pneumococcal surface adhesion A (PsaA), as well as other choline-binding proteins such as LytA, LytB, LytC, CbpC and CbpG. PspA is discovered on the cell wall of bacteria by phosphorylcholine moiety, which is essential by helping the colonization of bacteria to epithelial cell surface, as well as reducing deposition of the complement (Kadioglu et al., 2008). PspC on the cell wall also plays an imperative role in colonization and invasion of bacteria in the nasopharynx through binding to receptors, for instance human polymeric immunoglobulin A (IgA) (Kadioglu et al., 2008). PsaA is able to transport magnesium ions and zinc ions into the cytoplasm of the bacteria, thereby facilitate the adhesion and invasion of bacteria in epithelial cell surface (Negi and Das, 2017). The function of other choline-binding proteins aids bacterial colonization by modification of protein on cell surfaces and initiate binding to host cell receptors, thus crucial for recognition by host cells (van der Poll and Opal, 2009). On the surface of cell wall, there are also presence of non-classical surface proteins which serve as adhesins to assist evasion of bacteria by immune system (Brooks and Mias, 2018).

Other important virulence factors include hyaluronidase, neuraminidase, IgA1 protease and pili. Hyaluronidase and neuraminidase are found not only in bacteria, but in

viruses as well with similar function. Hyaluronidase is important in pathogenesis by disintegrating extracellular matrix of host cell and aid the dispersion of bacteria (Negi and Das, 2017). Neuraminidase is a fundamental virulence factor which cleaves terminal sialic acid residues, thus facilitate the spread of bacteria (Negi and Das, 2017). IgA1 protease functions to degrade IgA, whereas pili promote adhesion and colonization of bacterial in the epithelial cell surface (Negi and Das, 2017).

The pathogenicity of *S. pneumoniae* greatly rely on activity of virulence factors. As a result, numerous research circulates on the search, discovery and development of chemical compounds from natural and synthetic source, as well as novel compounds to inhibit the activity of these virulence factors, thereby to inhibit the pathogenesis of *S. pneumoniae*. A research reported the study of inhibitory activity of honeys from Malaysia against hyaluronidase of *S. pneumoniae*, such that the flavonoid and phenolic content of honey Kelulut displayed 18% inhibitory activity. The research also suggested that the greater the phenolic content of honey, the stronger the inhibition against hyaluronidase of *S. pneumoniae*, proving that honeys from Malaysia origin are potential hyaluronidase inhibitors to be further studied (Yusof, 2020). On top of that, a novel inhibitor isorhamnetin was shown to depict inhibitory activity against pneumolysin of *S. pneumoniae via in vivo* and *in vitro* (Zou et al., 2023). Shafaghi et al. (2023) presented their research about the inhibitory activity of novel peptide-based vaccine candidates targeting PspA and pneumococcal histidine triad protein D (PhtD) of *S. pneumoniae* by performing computational methods. Furthermore, hyaluronan-binding protein 1 (HABP1/p32/gC1qR) was reported to be highly specific and show inhibitory activity against hyaluronidase of *S. pneumoniae* by performing docking simulations (Yadav et al., 2008).

2.4.4 Neuraminidase and Inhibitors

Neuraminidase is a surface protein structure found in microorganisms and animals, performing the essential role which is to catalyze the release of terminal sialic acid residues found in O-linked and N-linked glycans (Gualdi et al., 2012). Neuraminidase is more commonly found in influenza virus which is prominent to assist viral spread by cleaving terminal sialic acid, thus served as target of drugs and inhibitors including influenza vaccine, zanamivir and oseltamivir to prevent the activity of viral infection (von Itzstein, 2007). Generally, the pneumococcal neuraminidases are important in pathogenesis by initiating modification of host glycoconjugates, uncover potential binding receptors, as well as being supply of carbohydrates for metabolism of bacteria and cleavage of sugars (Parker et al., 2009). There are three different homologous structures of neuraminidase encoded by the genomes of *S. pneumoniae*, known as NanA, NanB and NanC (Parker et al., 2009). NanA and NanB are more commonly discovered, with NanA being discovered in 100% of all pneumococcal strains, NanB found in 96% of the bacterial strains, but NanC only discovered in about 51% of the bacterial strains (Pettigrew et al., 2006). The roles of the three distinct neuraminidases are different based on the analysis of their structure, such that NanA is the key factor to cleave and remove sialic acid residues, NanB is important for sialic acid's metabolic activity, and NanC is able to form and remove intermediate metabolic compound as inhibitor of sialidase (Xu et al., 2008). As a whole, NanA was concluded to have greater expression level and possess stronger enzymatic activity that NanB and NanC in the pathogenesis of *S. pneumoniae*. The search, discovery and development of drugs, inhibitors or novel compounds against the activity of NanA become highly potential and interesting in order to inhibit pathogenesis of *S. pneumoniae* due to the highly essential role of the neuraminidase.

A vast number of research reported the discovery of chemical compounds, particularly flavonoids from natural products, as potential inhibitors of neuraminidase of *S. pneumoniae* through different methods and fields. An isoprenylated flavone artocarpin from *Artocarpus heterophyllus* (jackfruit) as shown in Figure 2.8 was reported to exhibit strong inhibitory activity against neuraminidase of *S. pneumoniae* by reducing the adhesion strength of bacteria to pulmonary epithelial cells, as well as results from biofilm formation, pneumococcal growth and viability (Walther et al., 2015).

(a)  (b)

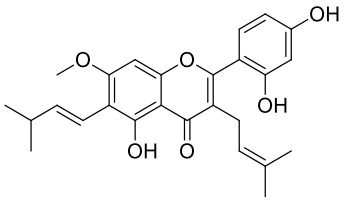


Figure 2.8: (a) *Artocarpus heterophyllus* (jackfruit) (b) Chemical structure of artocarpin from *Artocarpus heterophyllus* (Walther et al., 2015)

Another two prenylated flavonoid derivatives known as sanggenon G and sanggenol A, extracted from a traditional Chinese herbal drug mulberry root bark as depicted in Figure 2.9, were also reported for their inhibitory effect against pneumococcal neuraminidase (Grienke et al., 2016). The chemical structures of sanggenon G and sanggenol A extractred from the mulberry root bark were as illustrated in Figure 2.10 and 2.11 respectively.



Figure 2.9: Mulberry root bark

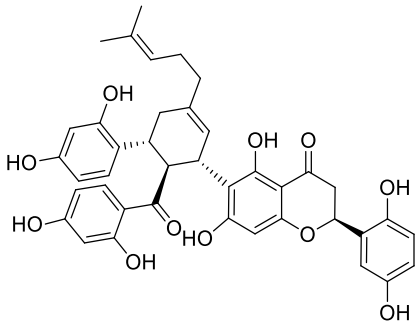


Figure 2.10: Chemical structure of sanggenon G from mulberry root bark

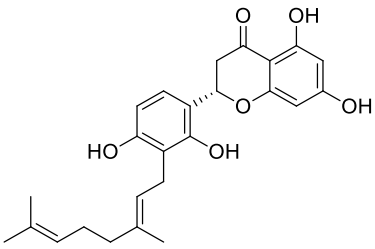


Figure 2.11: Chemical structure of sanggenol A from mulberry root bark

Chlorogenic acid, a phenolic compound found in coffee beans, potatoes and eggplants was also discovered for being able to depict potential inhibitory activity against the neuraminidase of *S. pneumoniae* by possessing strong binding potential with neuraminidase evaluated from the binding energy calculation in molecular simulation (Guan et al., 2020). Figure 2.12 portrayed the chemical structure of chlorogenic acid.

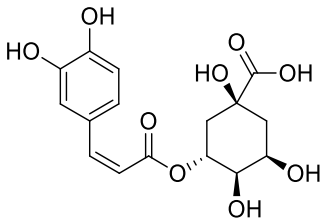


Figure 2.12: Chemical structure of chlorogenic acid

Thus, as a whole, a great number of research has reported the potential inhibitory activity of a few chemical compounds, mostly from natural products, against neuraminidase of *S. pneumoniae*. However, research related to findings about synthesized compounds or novel compounds against neuraminidase is still considered very limited compared to the findings on other virulence factors of *S. pneumoniae*, despite its great importance in pathogenesis. As elaborated earlier, Schiff base vanillin derivatives possess a broad range of biological activities due to modification of chemical structure of vanillin. Schiff base vanillin derivatives have been previously proven for their inhibitory activity against neuraminidase of influenza virus by performing computational methods as well as 20-(4-methylumbelliferyl)-a-D-N-acetylneuraminic acid (MUNANA) assay (Asaruddin, 2016). Therefore, the research focuses on the study of Schiff base vanillin derivatives against neuraminidase of *S. pneumoniae*.

2.5 S. aureus

2.5.1 Introduction of *S. aureus*

S. aureus is a Gram-positive spherical shaped bacterium which is stained purple, also a member of the *Bacillota phylum*, as well as cocci-shaped found in clusters similar to grapes, illustrated in Figure 2.13. *S. aureus* are discovered to be able to show growth in a maximum of 10% salt, whereby the colonies are large and round, usually golden or yellow, as "*aureus*" represents golden or yellow (Taylor and Unakal, 2023). About 21% to 30% of

the human population are reported to be carriers of *S. aureus*, such that the bacterial is found in nostrils or skin microbiota (Tong et al., 2015). Being a main bacterial pathogen which is able to grow and survive aerobically or anaerobically at temperatures between 18°C and 40°C (Taylor and Unakal, 2023), *S. aureus* is common in CAP and HAP infection by inhabiting upper respiratory tract similar to *S. pneumoniae*, but with challenging medication methods due to presence of multi-drug resistant strains including MRSA (Methicillin-Resistant *S. aureus*) (Boucher and Corey, 2008) and VRSA (Vancomycin-resistant *S. aureus*) (Tacconelli et al., 2017). This is due to the expression of a protein, known as the penicillin-binding protein 2a (PBP-2a), which is prominent to produce peptidoglycan in the cell wall of bacteria. As a result, *S. aureus* strains that are able to produce PBP-2a are able to survive through great number of antibiotics, including methicillin, nafcillin, oxacillin and cephalosporins (Rasigade and Vandenesch, 2014). It was recorded that in the United States, about 500,000 hospitalizations were caused by staphylococcal infection due to *S. aureus* annually, whereby out of these, 50,000 cases were reported as deaths (Schlecht et al., 2015).

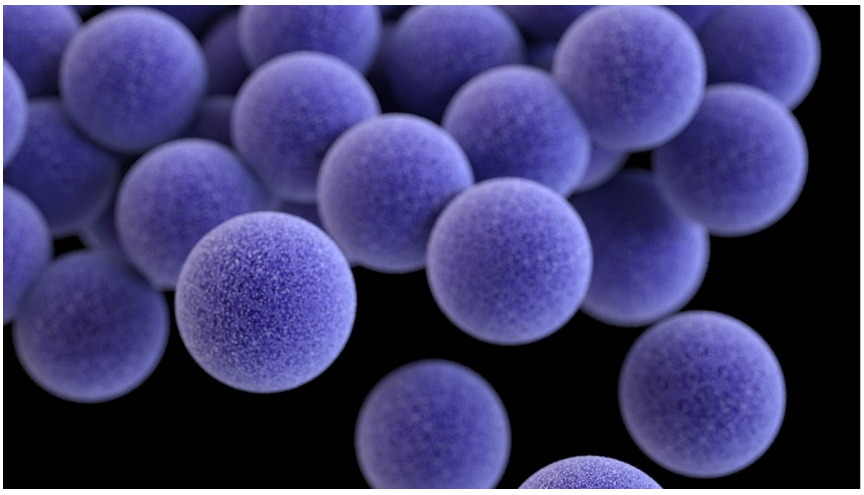


Figure 2.13: Structure of *S. aureus* (CDC, 2024)

2.5.2 Life Cycle of *S. aureus*

The fundamental of life cycle of *S. aureus* is a greatly essential and necessary field to be studied in order to exploit promising targets by synthesized or novel compounds. Figure 2.14 represents the general schematic outline of life cycle of *S. aureus,* beginning with chromosome replication and segregation, biosynthesis of staphylococcal cell wall, followed by distinct phases of cell division, and lastly regulation and coordination mechanisms of different cell cycle processes such as morphogenesis (Barbuti et al., 2023).

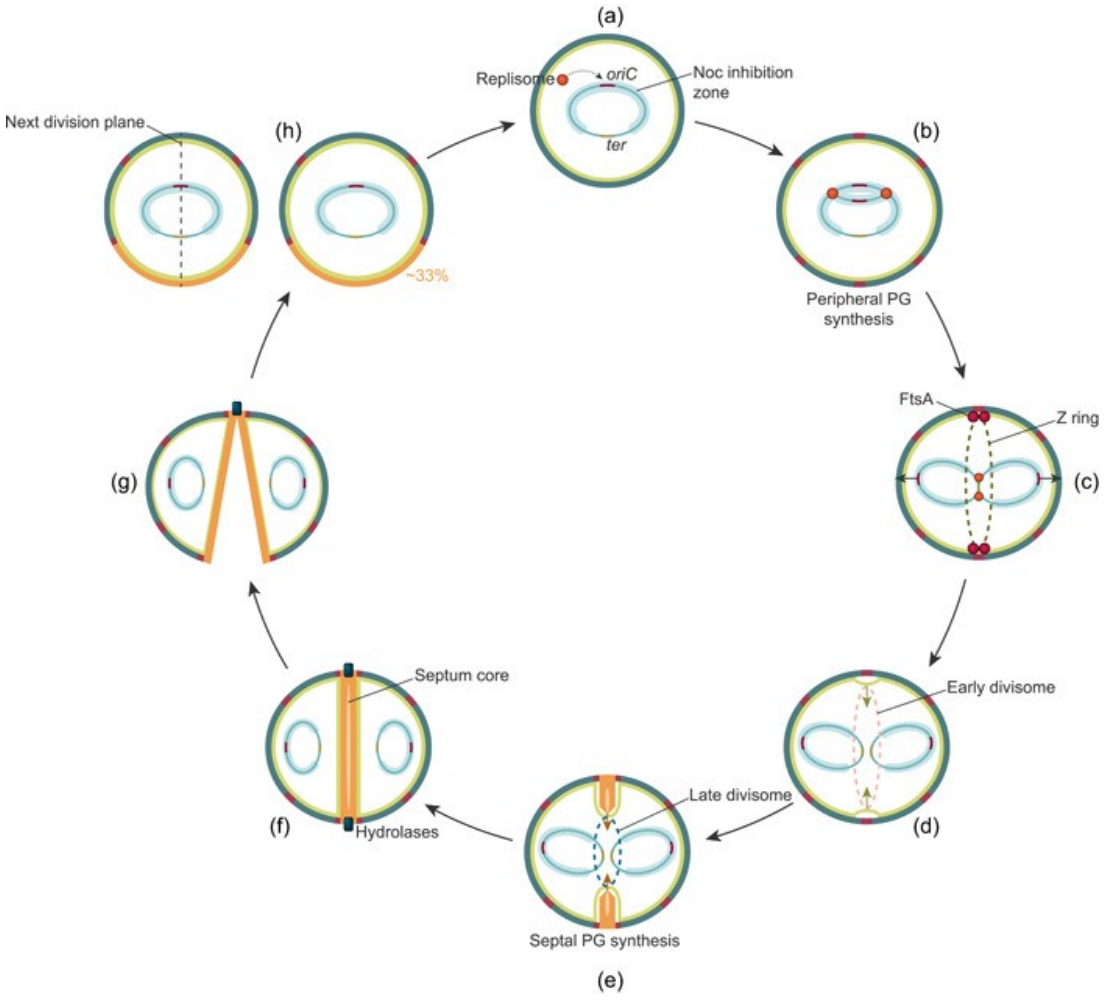


Figure 2.14: General schematic outline of the life cycle of *S. aureus* (Barbuti et al., 2023)

2.5.2.1 Chromosome Replication and Segregation

The genome of *S. aureus* contains a single circular chromosome about 2.8 Mb, such that the life cycle of *S. aureus* begins with replication of the chromosomal DNA (Młynarczyk et al., 1998). The replication is initiated when the replication initiation factor (DnaA) is bound to the adenine-thymine rich (AT-rich) sequences (DnaA-boxes) at the single origin of replication, *oriC*, as shown in (a) of Figure 2.14. DNA unravels, followed by the assembly of replisomes, which are the replication machineries, to produce two replication forks (Briggs et al., 2012). From here, the new DNA strands are formed in two directions originated from *oriC* until the end of replication terminus, followed by dissolving of replisomes, as depicted in (b) of Figure 2.14 (Hajduk et al., 2016). By the end of the replication process, the recombinase system XerCD/*dif* played its dominant role to resolve the chromosome dimers (Midonet and Barre, 2014).

Upon completion of chromosomal replication, the two sister chromosomes undergo segregation to form two sister cell compartments as shown in (c) of Figure 2.14. Essential mechanisms for proper segregation of chromosomes in *S. aureus* are the ParB/*parS*-system and structural maintenance of chromosomes (SMC) complex (Chan et al., 2020). The probable chromosome-partitioning protein, ParB shows specific binding to pseudoautosomal regions, *parS* sequences in the *oriC*-proximal region (Chan et al., 2020), whereas the SMC protein plays an imperative role in initiating condensation and organization of the chromosomes (Britton et al., 1998). The assembly and cooperation of ParB and SMC is highly important to ensure proper chromosome segregation in *S. aureus* (Chan et al., 2020). As illustrated in (d) of Figure 2.14, upon segregation of the sister chromosomes, a Noc-free zone is formed in the middle of the cell.

2.5.2.2 Biosynthesis of Staphylococcal Cell Wall

The staphylococcal cell wall is composed of peptidoglycan and teichoic acids which give structural support to the cell by withstanding the high internal turgor pressure of the cell, thus sustain cell shape throughout the cell cycle (Whatmore and Reed, 1990).

Peptidoglycan are composed of glycan chains of different lengths combined together by formation of peptide bridges. The synthetases and hydrolases of peptidoglycan work together to incorporate new peptidoglycan into existing mesh of peptidoglycan for the synthesis of septal cross wall, thus to ensure the cell structure and integrity remains during cell growth and cell division (Barbuti et al., 2023). Generally, the biosynthesis of peptidoglycan is initiated by conversion of uridine diphosphate (UDP)-linked sugar precursors in cytoplasm to lipid II, and further converted to lipid II-Gly_5 (Rohrer and Berger-Bächi, 2003). MurJ protein is a protein functions to control the synthesis of peptidoglycan to be performed in the midcell, hence to signal the synthesis of septum, (Monteiro et al., 2018). Upon directing peptidoglycan synthesis in the midcell, lipid flippase of the lipid II-Gly_5 to the outer part of cytoplasmic membrane is performed, proceeded by elongation of glycan chains by transglycosylation and transpeptidation on the cytoplasmic surface membrane (Sham et al., 2014). By this last stage, penicillin-binding proteins (PBPs) attributed important roles for growth and cross-link of glycan strains, which include the bifunctional PBP2, monofunctional TPases PBP1 as well as PBP3 and PBP4 (Barbuti et al., 2023).

Besides the synthetases, the peptidoglycan hydrolases are highly significant in the growth of cell wall, recycling, as well as segregation of daughter cell (Barbuti et al., 2023). The enzymes of peptidoglycan played their respective enzymatic roles, such that

glucosaminidases and muramidases break the bonds in the glycan chain, amidases break the bond in between the stem peptide and glycan chain, endopeptidases cut the inner part of the stem peptide, and carboxypeptidases cleave the terminal amino acid from the stem peptide (Vollmer et al., 2008). Activity of hydrolases requires appropriate control to prevent occurrence of uncontrolled cell lysis and to balance hydrolysis of enzymes on peptidoglycan, in which the stages include transcriptional regulation, interactions with proteins, proteolysis, and localization control by interactions with teichoic acid (Jensen et al., 2019).

Teichoic acids are negatively-charged glycopolymers which form covalent bonds with the peptidoglycan to form wall teichoic acid (WTA), or directly with the membrane to form lipoteichoic acid (LTA), thus possess significant effect on the cell cycle progression and cell shape of *S. aureus* (Barbuti et al., 2023). WTA is composed of about 11 to 40 unit chains of ribitol-phosphate linked to MurNAc in the peptidoglycan, synthesized by enzymes in the cytoplasm and delivered across the membrane (Neuhaus and Baddiley, 2003; Brown et al., 2013). LTA is composed of glycerol-phosphate (GroP) which bind to the plasma membrane through a lipid anchor during the formation process of enzymes UgtP, LtaA and LtaS (Schneewind and Missiakas, 2019). WTA has a greater possibility to be knocked out from production in *S. aureus*, but the synthesis of LTA cannot be compromised simultaneously (Oku et al., 2009). For depicting different cell morphologies, LTA has greater significance than WTA in staphylococcal viability (Oku et al., 2009).

2.5.2.3 Stages of Cell Division

After the replication and segregation of sister chromosomes, followed by biosynthesis of staphylococcal cell wall, *S. aureus* bacteria undergoes cytokinesis, which is a process whereby parental cell undergoes division to produce two identical daughter cells.

The process is divided into three stages, beginning with assembly of the Z ring and divisome, followed by synthesis, constriction and closure of division septum, and lastly cell splitting (Barbuti et al., 2023).

The tubulin homolog known as the Filamenting temperature sensitive mutant Z (FtsZ) proteins undergo polymerization to produce a dynamic structure Z ring, which is important to stimulate the production of the division septum (Whitley et al., 2021). Polymerization of FtsZ is an important control factor in the bacterial cell cycle, whereby the Z ring plays a crucial role to serve as a platform to assemble all other conserved proteins which combine together to form a large complex of proteins, known as divisome (Adams and Errington, 2009).

The divisome proteins are divided into two groups based on the methods of recruitment, including the early division proteins and late division proteins. The Z ring is controlled and stabilized by the early division proteins, whereas the late division proteins are important to synthesize new septal cell wall as well as constriction of the cytoplasmic membrane (Errington et al., 2003). Other than FtsZ, EzrA and SepF are proteins which controls the Z ring formation as well as being part of the early divisomes (Levin et al., 1999). EzrA is crucial for regulating cell size by controlling homeostasis (Jorge et al., 2011), whereas SepF is important for to bundle FtsZ protofilaments and to resist the GTPase activity of FtsZ (Singh et al., 2008). As for late-division proteins, examples include GpsB, FtsL, DivIB and DivIC, which strongly rely on interactions with FtsZ proteins to localize to the division site (Daniel et al., 2006), as well as PBP1-4, RodA and FtsW. All proteins which compose the divisome possess significant role in synthesizing new peptidoglycan or regulating these processes with cell division (Booth and Lewis, 2019).

After assembly of Z ring and divisome proteins, FtsZ undergoes treadmilling, a significant dynamic movement of Z ring and divisome as patches all over the division plane caused by FtsZ polymerization and depolymerization (Bisson-Filho et al., 2017). Treadmilling is important at the early phase of cell division, which is to drive the force for the beginning and processive slow step of cytokinesis (Barbuti et al., 2023). Peptidoglycan is first embodied into the lateral cell wall, followed by recruitment of lipid II flippase MurJ to the divisome by DivIB-DivIC-FtsL subcomplex at a checkpoint of cytokinesis to synthesize new peptidoglycan (Bottomley et al., 2014). Upon recruitment of MurJ, the constriction rate of Z ring increases while simultaneously, the initial treadmilling phase starts to slow down (Monteiro et al., 2018). The synthesis and rebuilding of peptidoglycan are considered as the initiator of cytokinesis from septum formation to cell segregation.

The septum is composed of several layers, which is the inner core of ordered peptidoglycan between two layers of mesh-like peptidoglycan (Pasquina-Lemonche wt al., 2020). During the production of septum, several peptidoglycan-synthesizing enzymes possess different functions, such as PBP1 and PBP2 to form initial peptidoglycan (Turner et al., 2010; Monteiro et al., 2018), FtsW-PBP1 complex to form the ordered peptidoglycan in the inner septum core, and additionally, PBP2 and PBP4 to facilitate the formation of mesh like outer layers (Wacnik et al., 2022). During septal synthesis, septum is initially thinner at the edge, and becomes thicker once it combines (Lund et al., 2018).

Up until this stage, a new peptidoglycan should be synthesized which forms a septum wall that separates the cell into two compartments. The cell undergoes splitting to produce two daughter cells, and this process is mediated by hydrolases which hydrolyze the

peptidoglycan “bridge” between the two daughter cells (Zhou et al., 2015). A general model of cytokinesis of *S. aureus* is as shown in Figure 2.15.

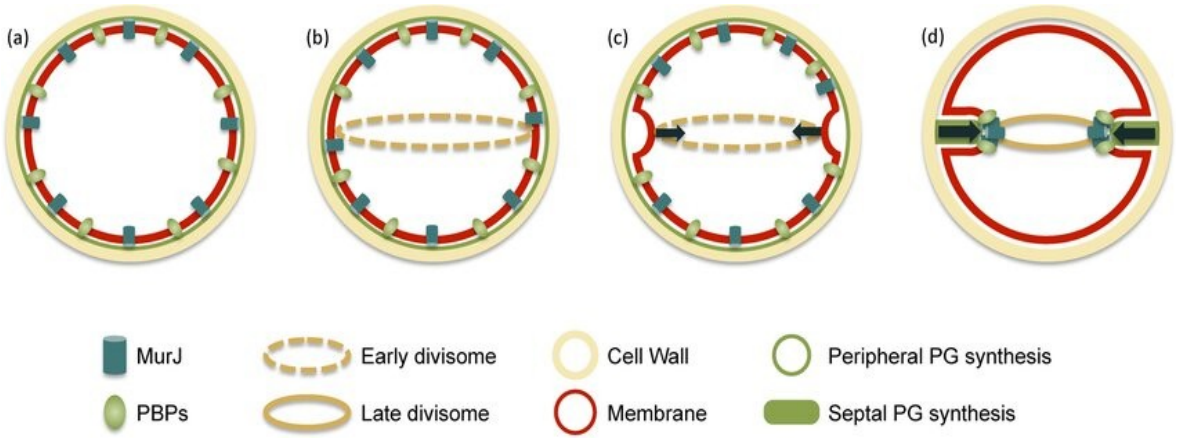


Figure 2.15: General model of cytokinesis of *S. aureus* (Monteiro et al., 2018)

2.5.3 FtsZ and Inhibitors

As elaborated earlier, FtsZ is the main protein structure important for cell division of *S. aureus*. It is a highly conserved tubulin homolog which undergoes polymerization to produce the Z ring, thus ultimately functions to recruit different conserved proteins, including peptidoglycan-synthesizing enzymes (Adams and Errington, 2009). By initiating the treadmilling process at the division site, FtsZ facilitates the separation and segregation of mother cell to produce daughter cells, hence mediates bacterial fission. This results in FtsZ being an attractive and potential drug target to inhibit the activity of cell division, thus bacterial activity of *S. aureus*.

FtsZ is composed of N-terminal domain, a core helix, a spacer loop, and a C-terminal domain, connected by a flexible unstructured linker, with the crystal structure as as illustrated in Figure 2.16 (Carro, 2019) and the general outline of domains in FtsZ as shown in Figure 2.17 (de Boer et al., 1992). In the presence of GTP, FtsZ first combine to produce short protofilaments composed of about 30 subunits, which later coalesce again to form the

Z ring (Erickson et al., 2010). The general insight of polymerization of FtsZ is as depicted in Figure 2.18.

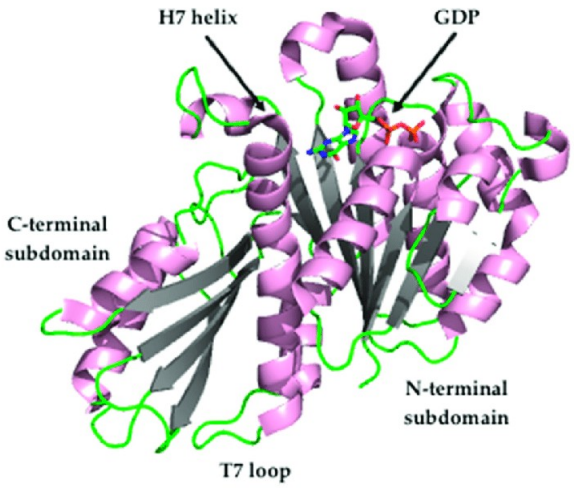


Figure 2.16: Crystal structure of FtsZ of *S. aureus* (Carro, 2019)

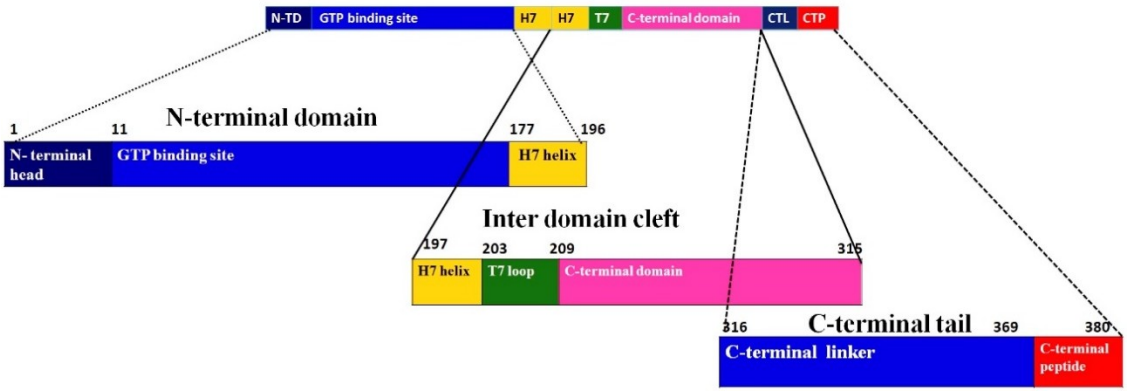


Figure 2.17: General outline of the domains in FtsZ (Pradhan et al., 2021)

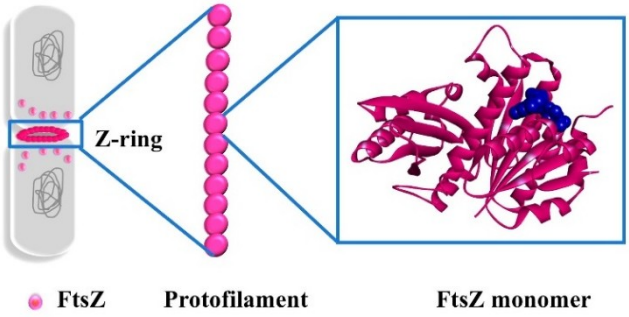


Figure 2.18: General insight of polymerization of FtsZ (Pradhan et al., 2021)

A vast number of research have been conducted to search, discover and develop inhibitors against FtsZ protein of *S. aureus*, which include chemical compounds extracted from natural products, synthesized compounds, and as well as novel compounds. Madurahydroxylactone, illustrated in Figure 2.19, and its derivatives extracted from *Nonomuraea* sp. AN100570 were reported to show inhibitory activity against FtsZ by depicting IC_{50} value of 53.4 µM, thus showing potential antibacterial activity against not only *S. aureus*, but as well as MRSA (Kim et al., 2017).

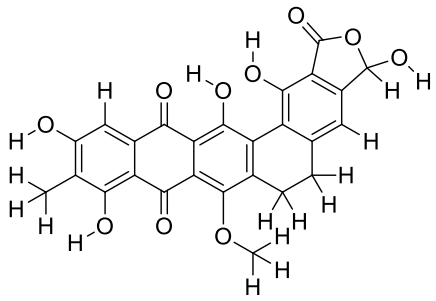


Figure 2.19: Chemical structure of madurahydroxylactone

Furthermore, silibinin, a natural flavonolignan rich extract from *Silybum marianum* with chemical structure being shown in Figure 2.20, was also reported by Basak et al. (2024) to depict strong affinity towards the GTP binding site of FtsZ, thus inhibiting GTPase activity, polymerization of FtsZ, as well as avoid growth of biofilms. These findings suggested the highly potential inhibitory activity of silibinin against FtsZ of *S. aureus*.



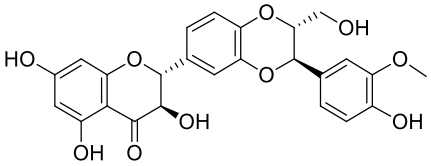


Figure 2.20: Chemical structure of silibinin from *S. marianum* (Basak et al., 2014)

A benzamide derivative known as 3-methoxybenzamide, as depicted in Figure 2.21, which is more commonly known as an ADP-ribosyltransferase inhibitor, was discovered to be able to show potential inhibitory activity against FtsZ (Ohashi et al., 1999).

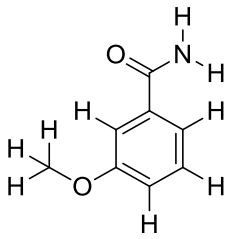


Figure 2.21: Chemical structure of 3-methoxybenzamide

Another chemical compound portrayed in Figure 2.22, PC190723 which is composed of thiazolopyridine moiety that combines with benzamide through ether bond potentiates the anti-FtsZ activity more than 3-methoxybenzamide (Pradhan et al., 2021). By reducing the GTPase activity, PC190723 promotes FtsZ polymer stabilization, thus reduce treadmilling dynamics and bacterial fission (Andreu et al., 2010).

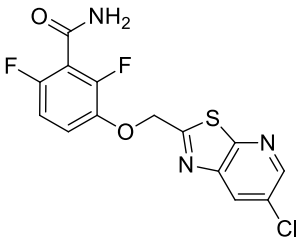


Figure 2.22: Chemical structure of PC190723

Due to presence of *S. aureus* strains which possess significance resistance to PC190723, by modulation of its chemical structure such that chlorine atom of the pyridyl ring is replaced with CF_3 group, another derivative known as TXA707, with chemical

structure being shown in Figure 2.23, possess greater stability and inhibitory activity (Pradhan et al., 2021).

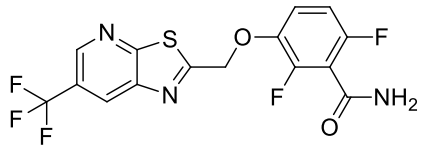


Figure 2.23: Chemical structure of TXA707

Another derivative of PC190723, which is DS01750413, is another novel inhibitor of FtsZ proven *in vitro* and *in vivo* against particularly MRSA (Kumar et al., 2021). Chemical structure of DS01750413 is as depicted in Figure 2.24.

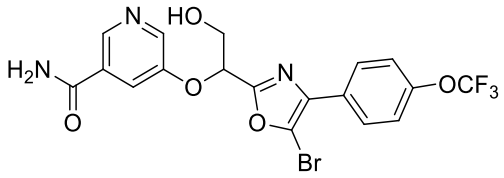


Figure 2.24: Chemical structure of DS01750413

Trespidi et al. (2021) reported another potential inhibitor of *S. aureus* FtsZ, which is a newly synthesized benzothiadiazole molecule, C109 as shown in Figure 2.25, also confirming that the benzothiadiazole molecular scaffold improves the potential of antistaphylococcal activity.

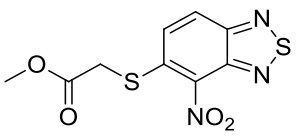


Figure 2.25: Chemical structure of C109

Despite great number of chemical compounds developed as potential inhibitors of *S. aureus* FtsZ, emergence of bacterial strains which possess notable resistance against the available drugs and inhibitors continue to arise. The increasing number of MRSA strains has reduced the number of therapeutic options, decreasing the efficiency of current available antibiotics, thus continue to be a major problem worldwide.

Aforementioned earlier, Schiff base vanillin derivatives are chemical compounds which possess a wide range of biological activities, including antibacterial activity. Sun et al. (2014), have reported a list of Schiff base vanillin derivatives as potential FtsZ inhibitors by performing antibacterial assay and docking simulation. Despite that, the research focuses more on *E. coli*, such that research related to Schiff base vanillin derivatives as FtsZ inhibitors of particularly *S. aureus* is still considered greatly limited. Apart from that, the continuous and increasing presence of multidrug-resistant strains, not only *S. aureus* but also *S. pneumoniae*, results in the necessity to continuously discover and develop more alternative chemical compounds for futuristic preparation. The dual target inhibitory activity of Schiff base vanillin derivatives is highly imperative, as simultaneous inhibition of neuraminidase and FtsZ not only enhances antibacterial efficacy against pneumonia-related bacterial strains, but also reduces the possibility of resistance development. This offers a novel mechanistic approach compared to conventional single-target antibiotics. On top of that, computational studies of Schiff base vanillin derivatives against FtsZ inhibitors are considered highly significant but also inadequate in terms of number of methods. As a whole, the research concentrates on the study of dual target antibacterial activity of Schiff base vanillin derivatives against neuraminidase of *S. pneumoniae* and FtsZ of *S. aureus* by performing computational methods.

2.6 Computational-aided Drug Design

In the ancient times, treatments and cure of diseases and sicknesses were done by using natural products from organic compounds. Following the development and advancement of science and technology, a great deal of research had been done in the discovery, design, development and synthesis of vast number of novel bioactive chemical compounds which are more advantageous, effective and safer than chemical compounds from natural products. However, the conventional and traditional method of drug design and discover to be marketed is far more challenging, exhaustive and cost-intensive which requires great load of manpower, time and cost. It was previously reported by the US Food and Drug Administration that the costing for drug design and discovery between the year 2009 and 2018 was approximately 2.8 billion dollars (Wouters et al., 2020). The drug design and discovery process was greatly serendipitous based on trial-and-error concepts, highly time-consuming, utilizing great amount of resource and simultaneously possessing great failure rate and may not bring out guaranteed results (Niazi and Mariam, 2023). As reported by Surabhi and Singh (2018), the process requires about 10 to 14 years and about 1 billion dollars to produce just 1 drug as illustrated in Figure 2.26.

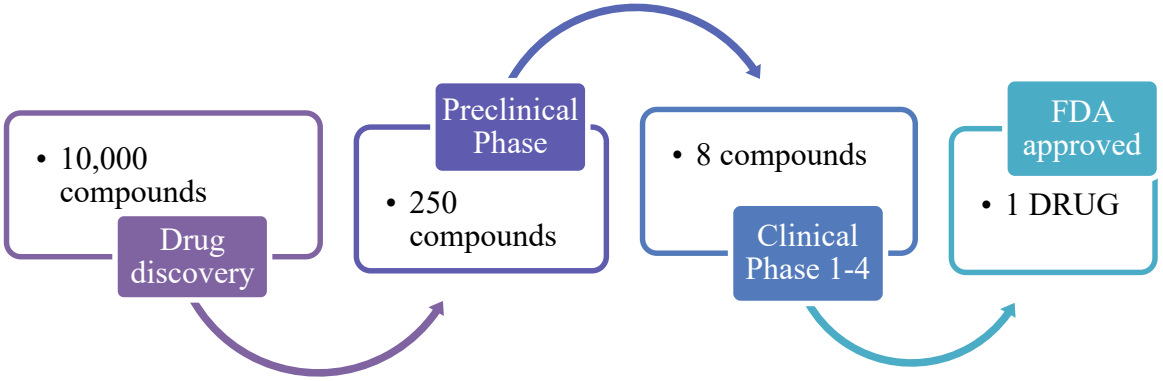


Figure 2.26: Traditional process of drug design and discovery (Surabhi and Singh, 2018)

Additionally, the rising presence of drug or chemical compounds which possess significant resistance towards their respective targets further increase the necessity to discover and design more alternative drug compounds to overcome the problem. As a result, the drug design and discovery process greatly requires new methods and approaches to proceed while being able to overcome the challenges aforementioned.

Consequently, introduction of computational aided drug design (CADD), or *in silico* drug design, begins to develop to overcome these challenges. CADD is a valuable method which comes into the limelight by utilizing the great power of computational tools, software and algorithms to study the chemical and biological data of drug molecules and targets. This allows the discovery, screening and optimization activity of chemical or drug compound against the target to be more efficient. The general concept is to evaluate and analyze the interactions between drug compounds and the target, which is usually a protein molecule of DNA sequence (Niazi and Mariam, 2023). Aside from evaluation of interactions, other analyses such as prediction of the chemical properties, the binding affinity, structural modulations, studying of binding pockets of protein structure etc. can also be done by CADD. As a result of the great functionality, CADD is widely utilized and applied in various fields of study including pharmaceutical, biotechnology, educational field etc. Among all discoveries, one of the earliest and most influential study is the design and development of an anti-influenza drug known as zanamivir (Niazi and Mariam, 2023). In comparison to the traditional drug and discovery method, CADD is faster, cheaper, more efficient, easier to use, and the rate of success is much greater. On top of that, the side effects due to drug compounds further necessitate CADD by performing screening of ADMET properties, which include adsorption, distribution, metabolism, excretion and toxicity properties of drug

compounds to further improve the rate of success in drug discovery and development within the shortest period of time (Ogu and Maxa, 2000).

Basically, CADD begins with identification of target and hit compound by performing wet-lab experiments, followed by high-throughput screening (HTS) (Schaduangrat et al., 2020). The main objective is to screen through large library of compounds towards the target, and subsequently narrowing down the candidate molecules with greater potential against the target molecule into smaller groups (Fox et al., 2006). Hit compounds are converted to lead compounds for optimization, which are later subjected to pre-clinical trials and lastly clinical trials to evaluate their pharmacokinetic properties as well as their safety, efficiency and adverse effects (Schaduangrat et al., 2020). The general schematic diagram is as shown in Figure 2.27, whereas the general principles are explained in Figure 2.28.



Figure 2.27: Schematic representation of drug discovery process (Schaduangrat et al., 2020)

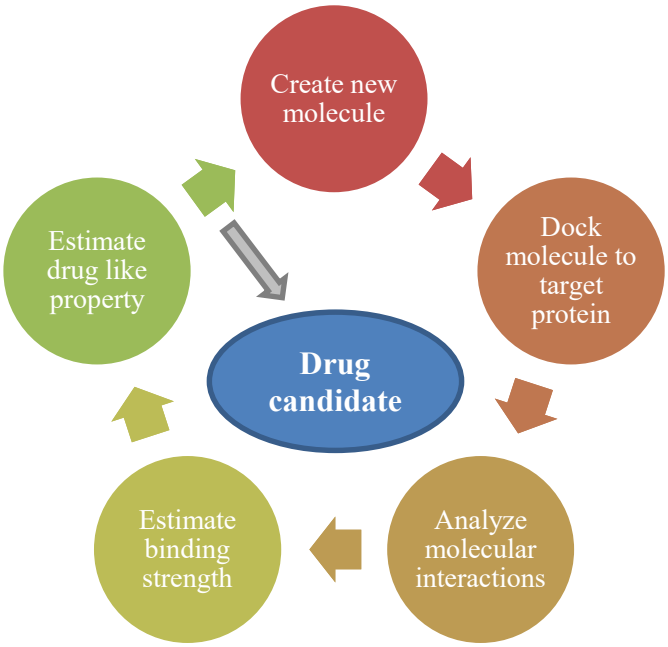


Figure 2.28: General principles of drug design by CADD (Surabhi and Singh, 2018)

CADD is generally divided into two main categories: ligand-based drug design (LBDD) and structure-based drug design (SBDD) (Niu and Lin, 2023). In ligand-based drug design, similar chemical compounds have high probability of possessing similar chemical properties and biological interactions towards biological targets (Vemula et al., 2023). Therefore, the approach focuses on the biological activity, pharmacophore profiles and experimental nature of ligands without prior knowledge of target macromolecule as well as mechanism of action (Ece, 2023). The general idea is as shown in Figure 2.29.

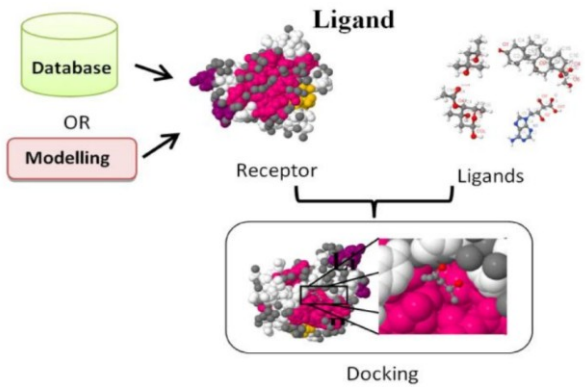


Figure 2.29: General idea of LBDD (Hoque et al., 2017)

The quantitative structure-activity relationship (QSAR) is an example of LBDD, which is a method of development of co-relationship between physicochemical properties of chemical compounds and their biological activities to get a statistical model, on purpose of prediction of the compound activities based on their structure (Verma et al., 2010). By generating a relationship equation in which the biological activity is set as the function of predicted parameters of the ligand, the activity of the compound can be predicted (Ece, 2023). Pharmacophore study is another example of LBDD which focuses on the structural alignment based on common pharmacophore molecular features of ligands, followed by prediction activity and utilized as 3D query for database screening, thus mediate the discovery of drug candidate molecules to be further optimized and evaluated (Ece, 2023).

SBDD approach is the discovery and design of drug or chemical compounds based on the fundamental knowledge of three-dimensional structure of biological target. The candidate molecules are either evaluated by their direct interaction, known as molecular docking, with the active sites of the biological target, or direct design of chemical compounds based on the active site pocket (Niazi and Mariam, 2023). Information that are obtained from SBDD include the structural features of ligand which are required to best fit in the active site of target molecule, the most optimized protein-ligand interaction (Acharya et al., 2011). The general idea in SBDD is as depicted in Figure 2.30.

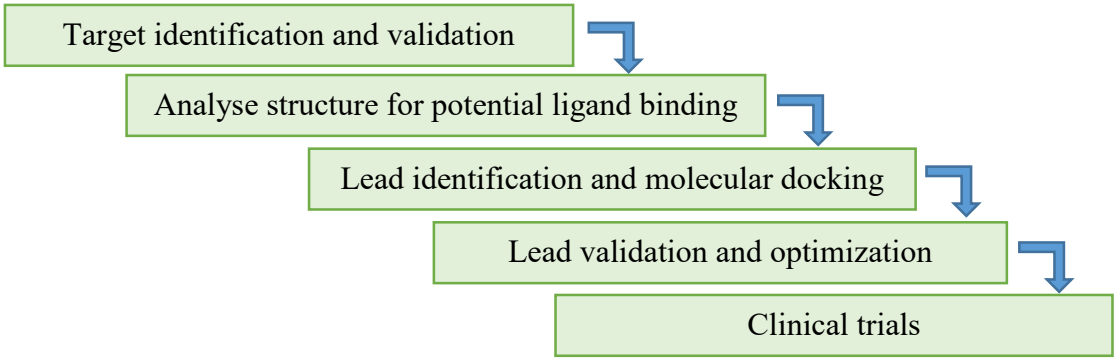


Figure 2.30: General steps in SBDD (Surabhi and Singh, 2018)

In virtual screening, large libraries of drug of chemical compounds are screened towards the biological target, such that the chemical compounds that show significant potential and binding interaction in the active site of target can be identified (Lavecchia and Giovanni, 2013). The method is advantageous not only for being able to determine more potential biological activities of existing chemical compounds, but as well as being able to determine chemical compounds which can serve as scaffold for the design and modification to produce more derivatives. However, this method is only applicable for previously synthesized compounds. which means novel compound cannot be designed by virtual screening. As a result, *de novo* drug design is another SBDD approach which utilizes the morphology of active site of target molecule to design structurally novel compounds.

2.6.1 Ligand-based Pharmacophore Modelling

The definition of pharmacophore based on The International Union of Pure and Applied Chemistry (IUPAC) is "an ensemble of steric and electronic features that is necessary to ensure the optimal supramolecular interactions with a specific biological target and to trigger (or to block) its biological response" (Wermuth et al., 1998). Alternatively, it is defined as the common functional and structural capacity depicted by a list of chemical compounds which possess specific characteristics and biological activity towards biological target (Seidel et al., 2020). Chemical compounds of diverse chemical structures but possess similar pharmacophore features and functionalities are said to be able to bind and show interactions towards target molecule, therefore showing similar biological activity (Seidel et al., 2020). These diverse chemical compounds will be subjected to alignment based on common key set of pharmacophore features required in interaction with protein target molecule, resulting in generation and development of a pharmacophore model (Tiwari and Singh, 2022). Pharmacophore model are greatly used in *de novo* drug design, as well as

virtual screening to search and discover chemical compounds that possess great probability to bind to the same receptor. Examples of essential pharmacophore features including hydrogen bond donors (HBD), hydrogen bond acceptors (HBA), aromatic groups (AR), positive ionizable area (PI), negatively ionizable area (NI), hydrophobic interactions (H), as well as metal binding locations, with their depictions in a CADD software, LigandScout 4.4.9 as portrayed in Figure 2.31 (Giordano et al., 2022).

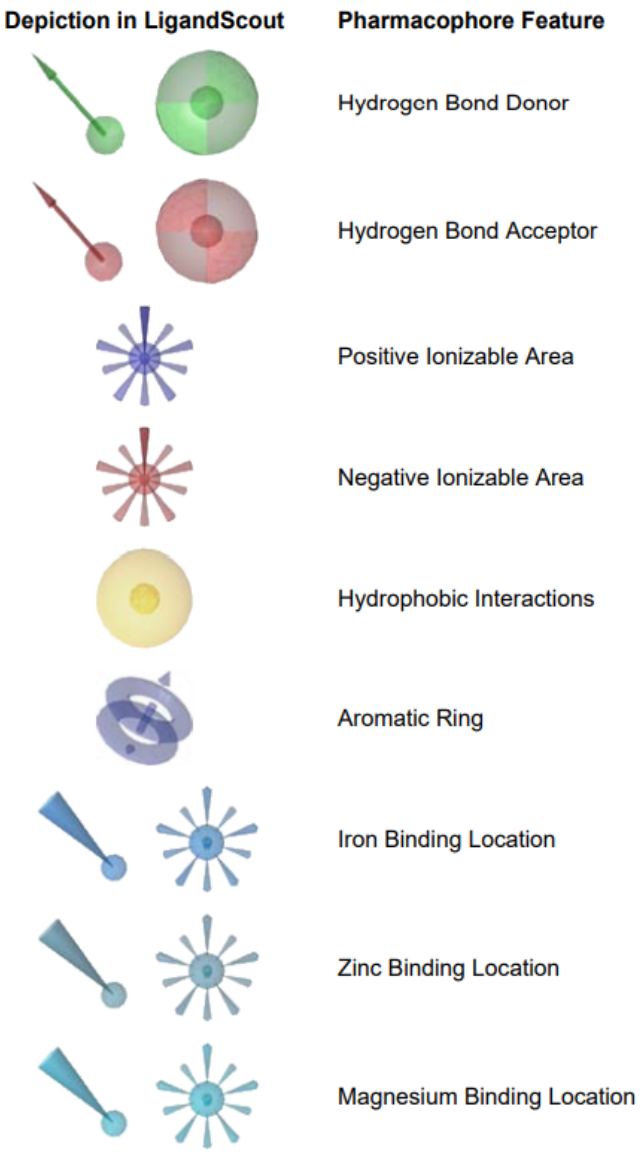


Figure 2.31: Pharmacophore features and depiction in LigandScout 4.4.9

To generate the best pharmacophore model, the functional groups, structural types and non-bonding interactions of chemical compounds are highly significant to determine the possessed pharmacophore features (Seidel et al., 2020). Table 2.1 shows a few examples of the most important types of pharmacophore feature in complementary with their non-bonding interactions and structural types that are more commonly observed in biological interactions.

Table 2.1: Examples of types of pharmacophore features with the interaction types and structural examples (Seidel et al., 2020)

Types of pharmacophore features	Interaction types	Structural examples
Hydrogen bond acceptor (HBA)	Hydrogen bonding	Amines, carboxylates, ketones, alcohols, fluorine substituents etc.
Hydrogen bond donor (HBD)	Hydrogen bonding	Amines, amides, alcohols etc.
Aromatic ring (AR)	π-Stacking, cation-π	Any aromatic rings
Positive ionizable area (PI)	Ionic, cation-π	Ammonium ion, metal cations etc.
Negative ionizable area (NI)	Ionic	Carboxylates
Hydrophobic interactions (HI)	Hydrophobic contact	Halogen substituents, alkyl groups, alicycles, weak or non-polar aromatic rings etc.

Another important consideration to be taken into account in generation of pharmacophore model is the spatial constraints of the shape at the active site. This is highly

important as a chemical compound might show good pharmacophore fit value in the generated pharmacophore model, but not in the receptor due to sterical hindrance, because pharmacophore model is only a set of key pharmacophore features which does not represent all biological activities (Seidel et al., 2020). As a whole, exclusion volumes are included to represent receptor area which do not allow ligand to occupy upon alignment with pharmacophore (Wolber et al., 2006). Pharmacophore features can be defined based on two types of constraints: distance constraints and direction constraints.

Ligand-based pharmacophore modelling begins with selection of a list of training sets. The training sets are chemical compounds, active or inactive compounds of diverse chemical structures, theoretically with similar biological activity to develop a pharmacophore model. Consequently, different conformations of training sets are generated such that low energy conformations are given priority. Upon conformational analysis, the low energy conformations of training sets are subjected to superimposition, which is alignment of similar functional groups. The set of conformations which possess the best fit is presumed as the active conformation. The superimpositions are later converted to an abstract representation of pharmacophore feature. For instance, phenyl rings that are superimposed may be represented as AR, whereas superimposed hydroxyl groups may be represented as HBA or HBD. Up until this stage, a pharmacophore model is readily available which requires validation to affirm its reliability for evaluation (Kutlushina et al., 2018). Figure 2.23 shows an example of pharmacophore model generated from the superimposition of pharmacophore features of 3 chemical compounds, whereby yellow spheres represent H interactions, red arrows represent HBA, and green arrows represent HBD (Seidel et al., 2010).

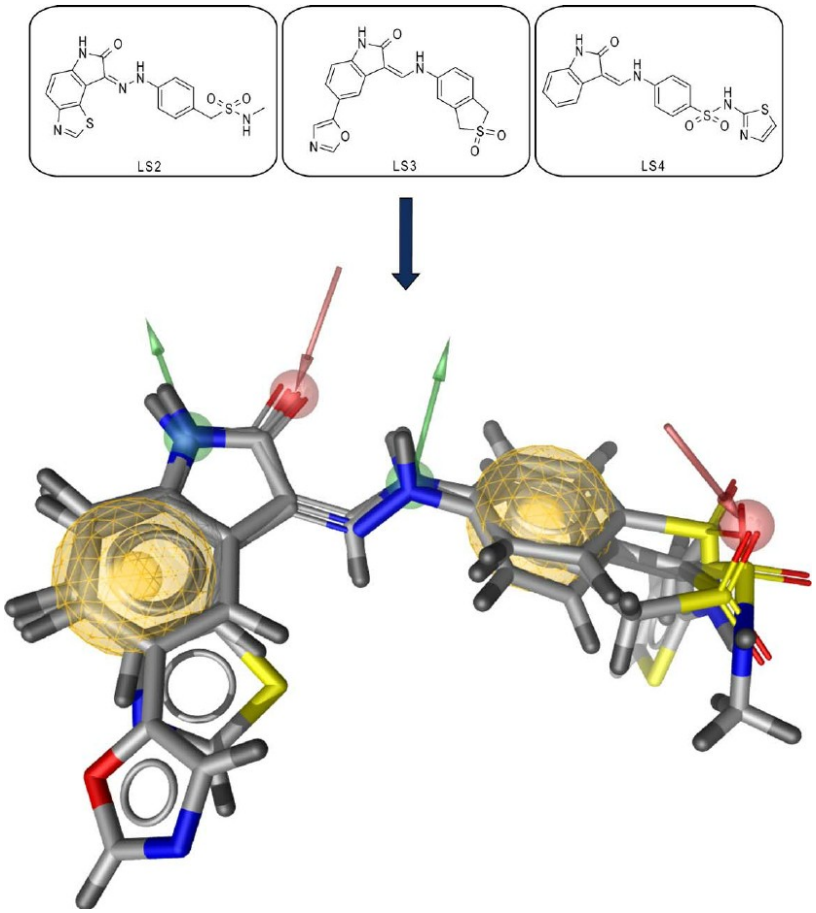


Figure 2.32: Example of shared feature pharmacophore model (Seidel et al., 2010)

Among great number of computational software that can be utilized to perform ligand-based pharmacophore modelling, LigandScout is one of the most useful, rapid and essential computational software, fully integrated and developed by Inte:Ligand. LigandScout experts in the creation of three dimensional pharmacophore models, for example, from protein-ligand complex structures, as well as generated from training or test sets. The generated pharmacophore model is defined by pharmacophore features such as HBA, HBD, PI, NI etc., which indicates the types of interactions depicted by ligands at the active sites of protein macromolecule (Wolber and Langer, 2005). For the expertise in pharmacophore modelling, it is useful for both ligand-based and structure-based pharmacophore modelling, as well as performance in virtual screening to search and discover

potential scaffold or even novel compounds against particular biological target with the best prediction quality as well as at higher speed (Wolber and Langer, 2005).

2.6.2 Structure-based Pharmacophore Modelling and Molecular Docking

As elaborated earlier, structure-based drug design requires the basic knowledge of three dimensional structure of macromolecule target. In structure-based pharmacophore modelling, the selected three-dimensional structure of a biological target or in complex with a ligand is needed at the beginning (Giordano et al., 2022). The concept of structure-based pharmacophore modelling is the generation of a pharmacophore model based on the ligand-binding site or based on the ligand in the active site of the ligand-target complex (Giordano et al., 2022).

The RCSB Protein Data Bank (PBD) deposits more than thousands of protein structures obtained by X-ray crystallography or NMR spectroscopy, either alone or in complex with a ligand. For cases where ligand is not available in the pocket of biological target, the ligand-binding site is first required to be identified and elucidated by searching and discovering areas in the biological target suggested to possess important biological role based on experimental data (Giordano et al., 2022). This can be performed by bioinformatics tools based on different methodologies to evaluate throughout the protein surface to search for highly potential ligand-binding sites, such as GRID and LUDI (Xie and Hwang, 2015). GRID utilizes grid pockets to map different molecules or functional groups on particular protein regions to search for grid points which produce the optimum favorable interactions (Goodford, 1985). LUDI is performed based on distributions of non-bonded interactions in chemical structures to identify greatly potential ligand-binding sites (Böhm, 1992). Upon identification of ligand-binding site, one or more pharmacophore hypotheses can be

generated, such that the pharmacophore model describes the type of interactions, spatial arrangements and pharmacophore features a ligand should compose to depict the required bioactivity against the biological target (Giordano et al., 2022).

In cases where the active ligand molecule is available in the biological target, the three-dimensional of the ligand molecule in its bioactive conformation provides a direct information about the pharmacophore features and interactions in the active site of the target molecule. This can be done by direct generation of pharmacophore model of the ligand, thus gives information about the pharmacophore features in complementary with the functional groups of the ligands, therefore the bioactive interactions with the target molecule. Thus, when ligand is present in the ligand-binding site, pharmacophore features of active site can be evaluated and analyzed with greater accuracy and efficiency, producing pharmacophore model of better quality (Giordano et al., 2022). Chemical compounds to be evaluated can be directly analyzed based on this pharmacophore model generated by looking into their pharmacophore scores and fit values, or in other words, to evaluate their complementary features that a chemical compound must fit in to depict great potential to show binding affinity. Structure-based pharmacophore modelling can also be evaluated by using LigandScout 4.4.9 aforementioned. Figure 2.33 shows an example of ligand-target complex, which is the crystal structure of Zika virus NS2B-NS3 protease in complex with its inhibitor ligand, known as a boronate inhibitor, retrieved from PDB encoded as 5LC0 (Lei et al., 2016). The boronate inhibitor ligand structure is illustrated in Figure 2.34, and the pharmacophore model generated from the ligand as shown in Figure 2.35.

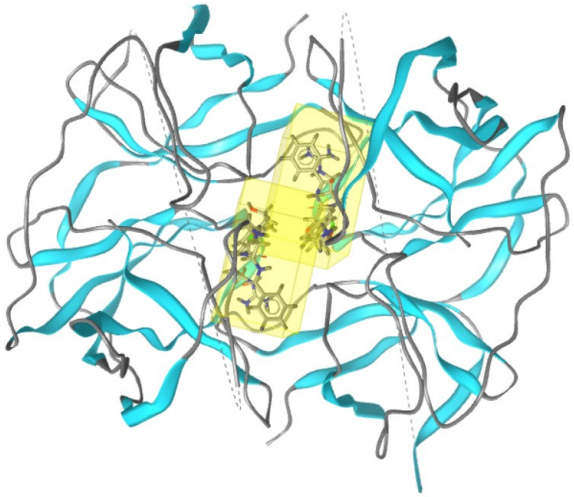


Figure 2.33: Crystal structure of Zika virus NS2B-NS3 protease in complex with boronate inhibitor (Lei et al., 2016)

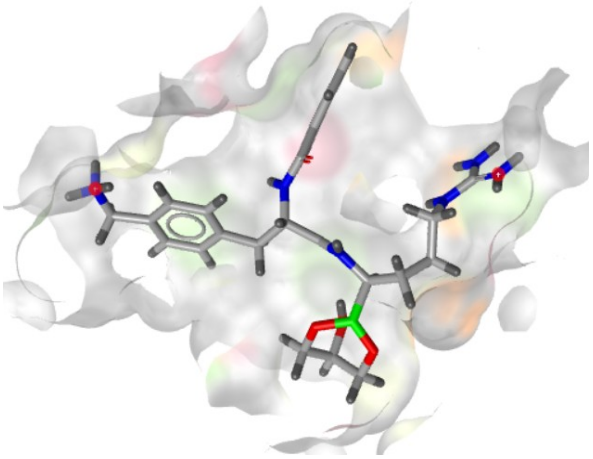


Figure 2.34: Boronate inhibitor ligand structure in the active site of 5LC0 (Lei et al., 2016)

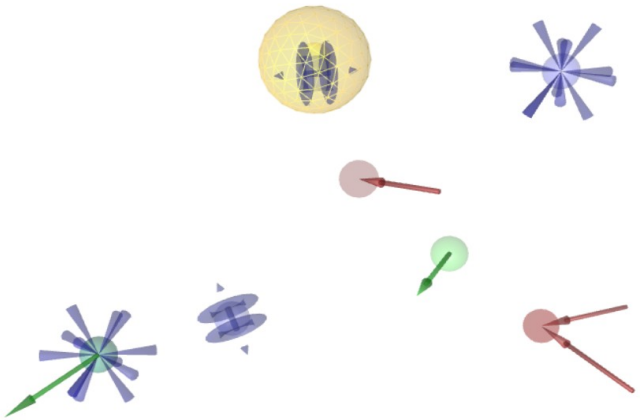


Figure 2.35: Pharmacophore model of boronate inhibitor

By performing ligand-based and structure-based pharmacophore modelling, structure-based molecular docking is usually proceeded to further evaluate and affirm the bioactivity of the tested chemical compounds. The molecular docking method is the simulation of interactions between the evaluated small molecules directly into the binding pocket of protein macromolecule at atomic level without generation of any pharmacophore model (McConkey et al., 2002). Molecular docking is considered as the most widely utilized and efficient method in SBDD since the early 80s, with many programs being developed to perform molecular docking, thus resulting in the important increment of the method (Kuntz et al., 1982). The main purpose of molecular docking is to estimate the activity of ligand-receptor complex based on computational methods. The general method of molecular docking is divided into two stages, beginning from sampling of different conformations and poses of ligand in the binding site and ranking by scoring function, followed by evaluation of the binding mode and affinity. A few sampling algorithms are developed and utilized in molecular docking computational tools to discover various conformations and binding modes, including matching algorithms (MA), incremental construction (IC), Multiple Copy Simultaneous Search (MCSS), LUDI, Monte Carlo (MC), genetic algorithms (GA) and molecular dynamics (MD) (Meng et al., 2011). A scoring function is a mathematical description to predict binding affinity value, as well as strength of ligand-receptor interactions (Kumar and Kumar, 2019). Scoring functions are essential to describe the optimum orientation and position of chemical compounds within the rightful computation time based on estimation, and can be categorized into force-field-based, empirical and knowledge-based scoring functions (Kitchen et al., 2004). Out of these three scoring functions, empirical scoring function is deduced to depict the greatest prediction of ligand-receptor complex interactions, thus utilized to discover the descriptors in the ligand-receptor

interactions such as hydrogen bonds with desolvation, van der Waals, and hydrophobic effects (Cheng et al., 2009). As a result, it is utilized to calculate the binding affinity values.

The binding affinity of chemical compounds towards the binding site of target macromolecule is defined as the strength of interaction between the ligand and protein target which can be calculated by using different scoring functions (Seo et al., 2021). The evaluation of binding affinity is greatly essential to allow efficient development of novel chemical compounds, discovery of promising candidates, as well as to enhance the biological properties (Spassov, 2024). The stronger the binding interactions, the greater the effect of ligand towards the physiological function of target protein molecule, thus the greater the potential of the ligand to serve as potential drug candidate (Li et al., 2008). Binding affinity is measured and reported by equilibrium dissociation constant (K_D), such that the smaller the K_D value, the greater the binding affinity of the ligand in the binding site of the target (Yartsev, 2017). A good binding affinity value should be less than –6 kcal/mol or IC_{50} value less than 250 nM (Carlson et al., 2008).

The performance of molecular docking simulation depends on the flexibility of receptor and ligand, which is categorized into flexible or rigid-body docking (Kumar and Kumar, 2019). Rigid-body molecular docking, alternatively known as the “lock-and-key model”, is a docking method which involves rigid conformation of ligand and receptor, thus highly focus on geometric complementary and depends on scoring function to gain the best binding orientation and position of ligand into the binding site (Chen et al., 2003). Due to the inability to allow conformational modulations in both ligand and receptors, binding affinity of ligand is difficult and challenging to be predicted (Fan et al., 2019). This results in the development of flexible-rigid docking, or known as induced-fit model. This is another

docking technique that involves flexible conformational changes of the receptor structure, particularly rotatable bonds, thus being able to depict more accurate binding affinity prediction (Agnihotry el al., 2020). Figure 2.36 illustrates the first two types of molecular docking simulations, which are rigid-body and flexible-rigid molecular docking.

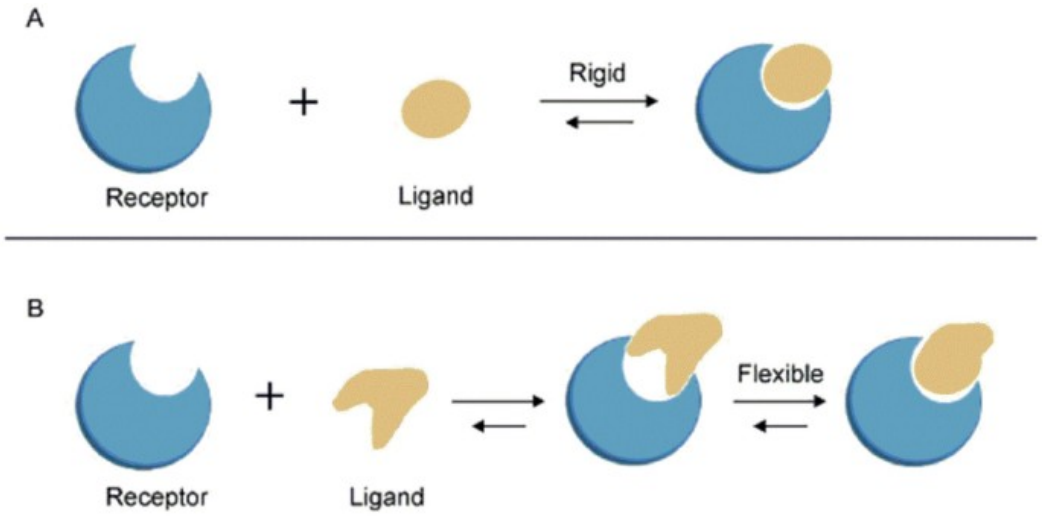


Figure 2.36: Rigid-body (A) and flexible-rigid molecular docking (Fan et al., 2019)

Flexible or soft docking technique involves flexible conformational changes of both ligand and receptor structures, resulting in enhancement to accuracy compared to rigid and flexible-rigid docking techniques (Fan et al., 2019). The method has great requirements on computational software, hardware and conformational accuracy, and also more complicated calculations (Fan et al., 2019). Despite that, accuracy of results from flexible docking is greater.

With the increasing number of computational methods to perform molecular docking, AutoDock 4.2 is one of the most efficient and suitable computational software to perform molecular docking to evaluate binding affinity. The software provides great number of functionality, whereby the most important function is to dock small molecules into binding site of receptor, thus illustrating the binding affinity prediction. Apart from that,

AutoDock 4.2 also allows virtual screening of libraries of potential compounds, discovery of new compounds with specific binding properties as well as evaluations on modulations of existing chemical compounds (Rizvi et al., 2013). AutoDock 4.2 was reported to be able to outperform another molecular docking software known as GOLD in flexible docking simulations with a dataset of 76 complexed (Ouyang et al., 2013).

Despite Schiff base vanillin derivatives being greatly studied in various *in vivo* and *in vitro* fields, the number of studies in computational-aided fields, particularly pharmacophore modelling and molecular docking are highly inadequate while showing promosing capabilities. Simultaneously, the computational studies exhibit major relevance as significant support to other fields of studies. Therefore, as mentioned earlier, the main objective of the research is to study the dual target antibacterial activity of Schiff base vanillin derivatives against neuraminidase of *S. pneumoniae* and FtsZ of *S. aureus*. As a whole, ligand-based and structure-based pharmacophore modelling, as well as molecular docking of Schiff base vanillin derivatives as ligands against neuraminidase of *S. pneumoniae* and FtsZ of *S. aureus* are planned to be performed. CADD methods are performed by using LigandScout 4.4.9 and AutoDock 4.2. With this flow, Schiff base vanillin derivatives that are both pharmacophore-compliant and geometrically compatible to neuraminidase and FtsZ can be determined and analysed.

2.6.3 Lipinski's Rule of 5

Upon evaluation of potential antibacterial activity of Schiff base vanillin derivatives by CADD methods, the chemical compounds should also be evaluated in terms of their drugability to be potential orally active drugs in human. Lipinski's rule of 5 (RO5) is a set of rules which a chemical compound must fulfill to possess druglikeness, hence to possess

great potential as orally active drugs (Lipinski et al., 2001). RO5 suggested that for a chemical compound to depict strong drugability, the chemical compound must have not more than 5 HBD, not more than 10 HBA, molecular mass less than 500 g/mol and partition coefficient value not more than 5 (Lipinski et al., 2001). The name of RO5 derived from the fact that all conditions in the rules are of multiples of five as the determinant conditions (Lipinski et al., 2001). RO5 is crucial for describing a chemical compound's pharmacokinetics in human body, which includes their "ADME" properties: absorption, distribution, metabolism and excretion.

Despite having strong functionality in evaluating drugability of most chemical compounds, RO5 was reported for having limitations. Most of the natural products and substrates of biological transporters were still reported as effective orally active drugs despite their violation to RO5. Explanations include possessing complex chemical structures with molecular weight more than 500 g/mol as well as greater number of HBA and HBD (Zhang and Wilkinson, 2007). On top of that, RO5 only applies for drugs that are oral bioavailability, which implies that drugs administered intravenously, topically, or by inhalation are not relevant to RO5. This further elaborated the bioactivity of natural products while violating RO5, as most natural products are based on non-oral administration (Zhang and Wilkinson, 2007). Subsequent to this, biological factors such as efflux, metabolism, and target specificity are not taken into consideration in RO5. Consequently, this lead to the occurrence of a few issues such as chemical compounds possess high efflux, metabolism, and low passive permeability (Doak and Kihlberg, 2016).

Regardless of the limitations of RO5 reported, the rules are still significant to analysie the druglikeness of specifically orally active drugs to be absorbed by human body,

particularly the Schiff base vanillin derivatives as dual target inhibitor of neuraminidase and FtsZ in this research study. However, fulfilling the rules in RO5 does not define being a pharmacologically active drug, but a promising drug candidate which can be utilized for clinical trials and other research fields to be further analyzed and evaluated (Lipinski, 2004).

2.7 Antibacterial Assay by Broth Dilution and Agar Disk-Diffusion Method

Antibacterial assays are *in vitro* methods to be done in laboratory to evaluate the antibacterial activity of chemical compounds (Balouiri et al., 2016). The method is employed to provide further affirmation and stronger support to the results obtained from CADD. The most accepted standards in antibacterial assay are recorded by the Clinical & Laboratory Standards Institute (CLSI) (2020) in Performance Standards for Antimicrobial Susceptibility Testing. Out of all standards recorded, the most fundamental, common and widely utilized methods include broth dilution method and disk-diffusion method (Balouiri et al., 2016).

Agar disk-diffusion method is considered as the most flexible susceptibility testing method. The method involves the usage of a paper disk saturated with antimicrobial compounds of known concentration placed on a Mueller-Hinton (MH) agar plate, with incubation overnight, followed by the evaluation and measurement of the rate of diffusion of the compound throughout the agar. The rate of diffusion depends on the solubility properties, diffusion movement and the molecular weight of the drug compound, such that compounds with larger molecular weight possess lower rate of diffusion that compounds with smaller molecular weight (Hudzicki, 2009). Initially introduced by Kirby and Bauer, the method has been further developed and enhanced by CLSI as well as other international societies such as the European Union Committee for Antimicrobial Susceptibility Testing (EUCAST) and the British Society for Antimicrobial Chemotherapy (Tenover, 2009). The

method is advantageous in terms of being simple, cheap, possessing great ability to analyze large classes of microorganisms and antimicrobial compounds, as well as easy to analyze results obtained. Figure 2.37 shows an example of disk-diffusion method of an extract against a fungus known as *C. albicans*, such that the microbial extract showed a significant zone of inhibition around the disk, suggesting the antifungal potency of the microbial extract.

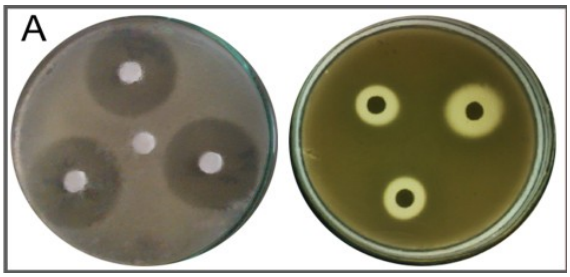


Figure 2.37: Disk-diffusion method of a microbial extract against *C. albicans* (Balouiri et al., 2016)

Despite the advantages of disk-diffusion method, the method is not suitable to measure the minimum inhibitory concentration (MIC) and minimum bactericidal concentration (MBC) as the amount of antimicrobial compounds diffuse in the agar cannot be calculated (Nijs et al., 2003). Consequently, dilution method is most suitable to predict and identify the MIC, which is the lowest concentration of antimicrobial agent to depict inhibitory activity against the visible growth of the tested microorganisms, typically expressed in µg/mL or mg/L. Similarly, the lowest concentration of antimicrobial agent that kills the bacteria, which is MBC can also be depicted. The method provides different concentration of the assayed antimicrobial agent in agar or broth medium to measure the antibacterial activity against the tested microorganisms (Balouiri et al., 2016). MIC methods are essential for resistance surveillance, comparative testing of new chemical compounds, analysis of susceptibility of organisms to show ambiguous results in disc tests (European Committee for Antimicrobial Susceptibility Testing of the European Society of Clinical

Microbiology and Infectious Diseases, 2003). Broth micro- or macro-dilution methods are assays which involve two-fold dilutions of the antimicrobial agents in liquid growth medium. An example of broth microdilution of plant extract against *B. subtilis* by using resazurin as growth indicator is as portrayed in Figure 2.38.



Figure 2.38: Broth microdilution of plant extract against *B. subtilis* (Balouiri et al., 2016)

By means of literature reviews, both agar diffusion and broth dilution method are widely accepted established methods documented in the CLSI guidelines. In comparison of both methods, broth dilution method focused on quantitative measurement of the MIC and MBC values. This increases the precision and reproducibility of the results as compared to agar diffusion method which focused on measurement of diameter inhibition zone. Despite that, broth dilution is more labour intensive, whereas agar diffusion method is simpler, more rapid and more cost effective. In this research study, the main aim is to confirm the antibacterial activity of the synthesized Schiff base vanillin derivatives against Gram-positive bacteria. In order to achieve this aim, quantitative measurement such as MIC and MBC are not necessary. As a result, agar diffusion method is selected as a fundamental support and evidence to strengthen the confidence of computational results.

2.8 Research Summary

Based on literature reviews that have been previously studied, it was discovered that Schiff base vanillin derivatives possess a wide range of biological activities which were being studied and reported by a vast number of research. Out of all, research related to the antibacterial activity of Schiff base vanillin derivatives is greatly potential but considered deficient in terms of the bacterial strains being evaluated as well as the methods being employed. Simultaneously, due to the increasing emergence of *S. pneumoniae* and *S. aureus* strains that possess significant resistance towards the available drug compounds, research related to the discovery and development of new and alternative chemical compounds against the activity of these bacteria strains is highly necessary from time to time for futuristic preparation. As a whole, the main aim of the research is to study the antibacterial activity of Schiff base vanillin derivatives targeting neuraminidase of *S. pneumoniae* and FtsZ of *S. aureus*. As CADD methods on Schiff base vanillin derivatives are limited in various research fields, the aim of this research is done by performing CADD methods, particularly ligand-based pharmacophore modelling, as well as structure-based pharmacophore modelling and molecular docking of Schiff base vanillin derivatives against neuraminidase of *S. pneumoniae* and FtsZ of *S. aureus.* Upon Schiff base synthesis reactions and characterizations to obtain the Schiff base vanillin derivatives compounds, antibacterial assay, particularly the agar diffusion method is also aimed to be performed to provide fundamental support to CADD results.

CHAPTER 3

MATERIALS AND METHODS

3.1 Overview of Computer-Aided Drug Design (CADD)

CADD methods used in this research are ligand-based pharmacophore modelling and structure-based molecular docking. All CADD works were performed by using LigandScout 4.4.9, AutoDock 4.2 and PyMOL. The general workflow of CADD is as depicted in Figure 3.1:

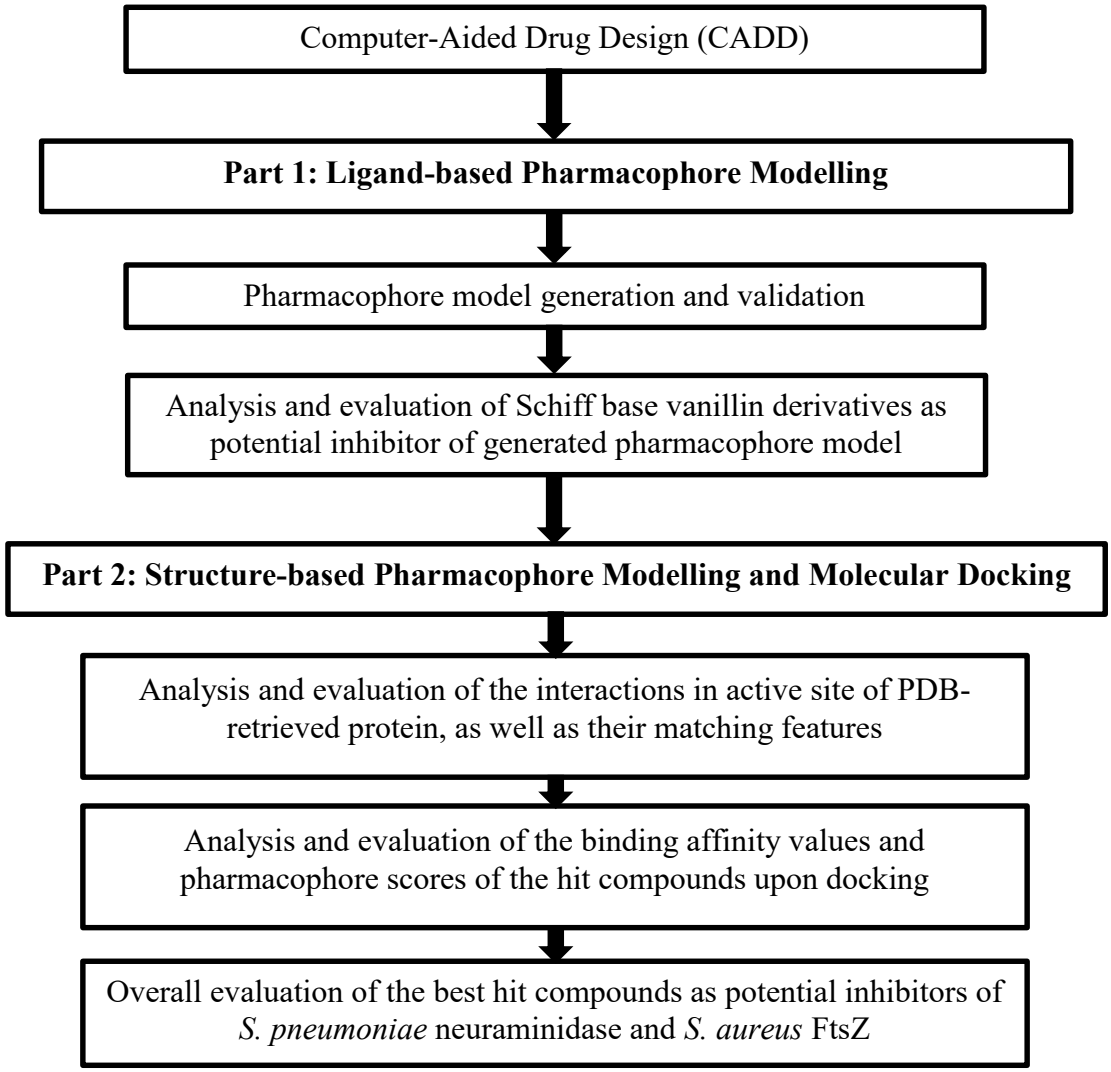


Figure 3.1: General overview of CADD workflow (Asaruddin, 2016)

3.2 Computational Evaluations of Schiff Base Vanillin Derivatives against *S. pneumoniae* Bacterial Neuraminidase

3.2.1 Ligand-Based Pharmacophore Modelling

3.2.1.1 Generation and Validation of Pharmacophore Model

A list of chemical compounds of diverse chemical structures which were reported in previous literature for their inhibitory activity against *S. pneumoniae* neuraminidase were selected as training sets. The 2D structures of these training sets were drawn by using ChemDraw Ultra 12.0 as shown in Figure 3.2, and downloaded in the MDL-mol file format.

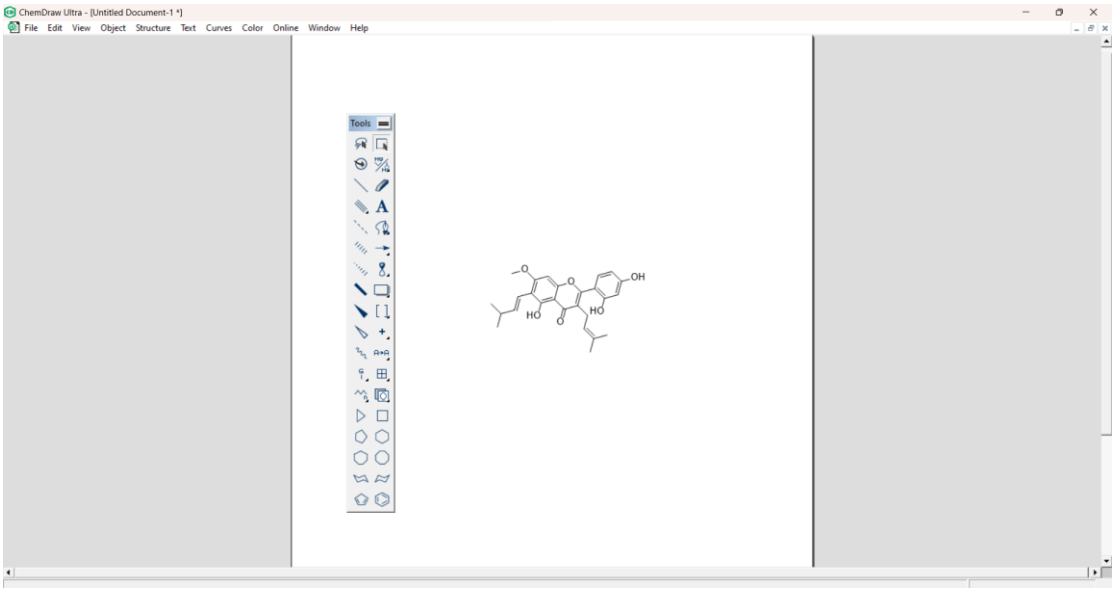


Figure 3.2: ChemDraw Ultra 12.0 to draw chemical structures

The MDL-mol files of the training sets were later imported into the ligand-based perspective of LigandScout 4.4.9 and used to generate a pharmacophore model. The generation of pharmacophore model was based on common feature hypotheses related to the activity of the compounds, with partial matching of only essential features of the training sets. Based on the results of literature review, a total of 5 chemical compounds were selected as training sets to generate the pharmacophore model. The training sets include NANA (N-acetyl-alpha-neuraminic acid) (Hsiao et al., 2009), 9N3Neu5Ac2en (5-acetamido-2,6-

anhydro-3,5,9-trideoxy-9-triazan-1-yl-D-glycero-D-galacto-non-2-enonic acid), artocarpin (Walther et al., 2015), zanamivir (Gut et al., 2011) and DANA (2-deoxy-2,3-dehydro-N-acetyl-neuraminic acid) (Owen et al., 2015). The chemical structures of the training sets are as shown in Table 3.1.

Table 3.1: Training sets used to generate pharmacophore model

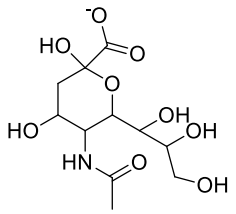
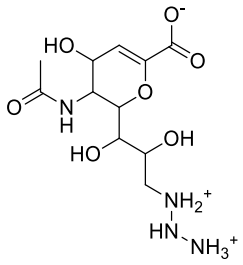
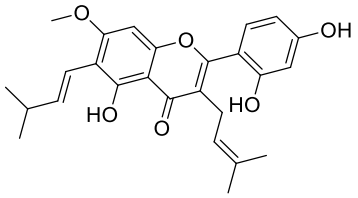
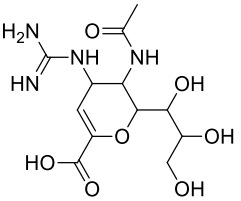
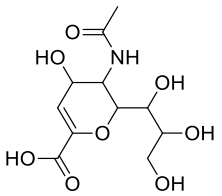
Name of training sets	Chemical structures
NANA (N-acetyl-alpha-neuraminic acid)	
9N3Neu5Ac2en (5-acetamido-2,6-anhydro-3,5,9-trideoxy-9-triazan-1-yl-D-glycero-D-galacto-non-2-enonic acid)	
Artocarpin	
Zanamivir	

Table 3.1 continued

DANA (2-deoxy-2,3-dehydro-N-acetyl-neuraminic acid)	

Test sets are a list of datasets imported to analyse and validate the reliability of the pharmacophore model generated from the training sets. In order to achieve the validation, chemical compounds from natural products which were previously reported to exhibit inhibitory activity against *S. pneumoniae* neuraminidase were selected as test sets. Similarly, the 2D structure of the chemical compounds were drawn by using ChemDraw Ultra 12.0, downloaded in the MDL-mol file format and imported into the ligand-based perspective of LigandScout 4.4.9 together with the list of training sets. The test sets selected based on literature study include kaempferol (Xu et al., 2023), sanggenol A, sanggenon G (Grienke et al., 2016), katsumadain A (Walther et al., 2015) and chlorogenic acid (Guan et al., 2020) as shown in Table 3.2.

Table 3.2: Test sets used to validate the generated pharmacophore model

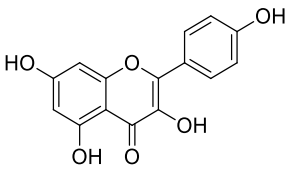
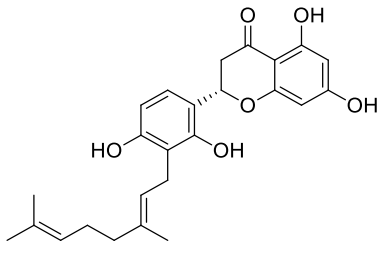
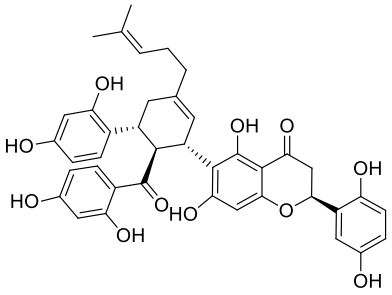
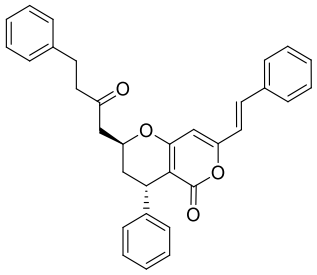
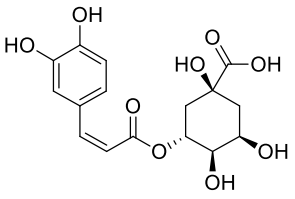
Name of test sets	Chemical structures
Kaempferol	

Table 3.2 continued

Sanggenol A	
Sanggenon G	
Katsumadain A	
Chlorogenic acid	

After all MDL-mol files of training sets and test sets were imported into the ligand-based perspective of LigandScout 4.4.9, the MMFF94 energy of the chemical structures were

minimised to reach the closest local minimum. Subsequently, conformations of the ligand sets were generated by using the FAST settings. FAST settings allow generation of pharmacophore hypotheses to be efficiently done with the shortest time consumption and minimum computational resources consumption due to large class of training sets and test sets. The ligand sets were clustered based on pharmacophore RDF-code similarity and average cluster distance calculation. Ligand-based pharmacophore modelling was run based on pharmacophore fit scoring function, and the pharmacophore model was generated based on merged pharmacophore feature. The evaluation of the generated model was based on the matching pharmacophore features, model scores and pharmacophore fit values depicted by training sets and test sets. All training sets should be able to show high matching features and pharmacophore fit values in the generated model. If the test sets were able to depict more than half of the matching features and fit values of the training sets, then the generated pharmacophore model is said to be reliable for evaluation of potential inhibitory activity against *S. pneumoniae* neuraminidase. Thus, the general workflows of ligand-based pharmacophore modelling are as shown in Figure 3.3 to 3.7.

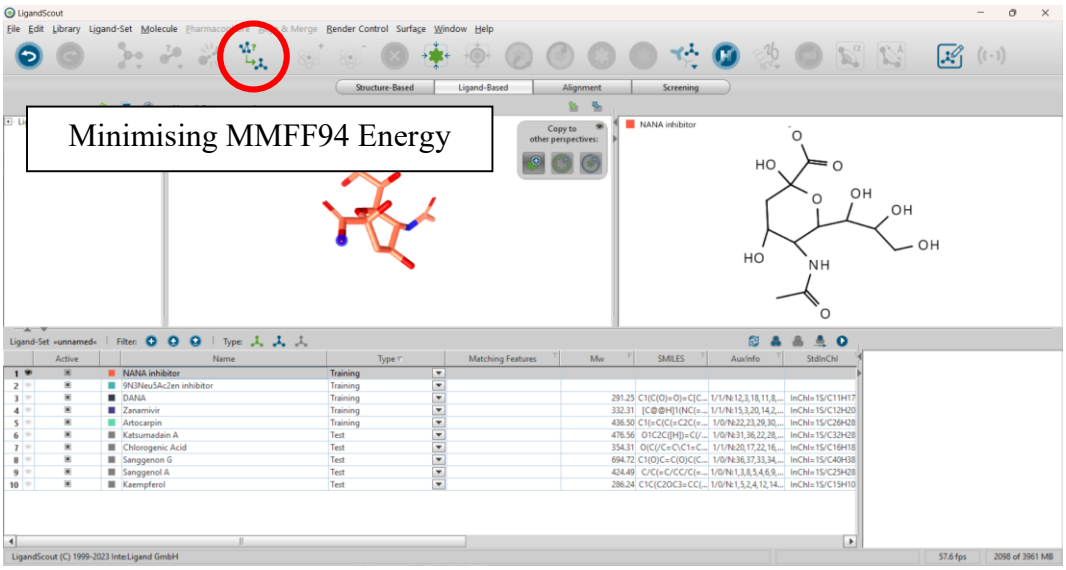


Figure 3.3: Minimising MMFF94 energies of training sets and test sets

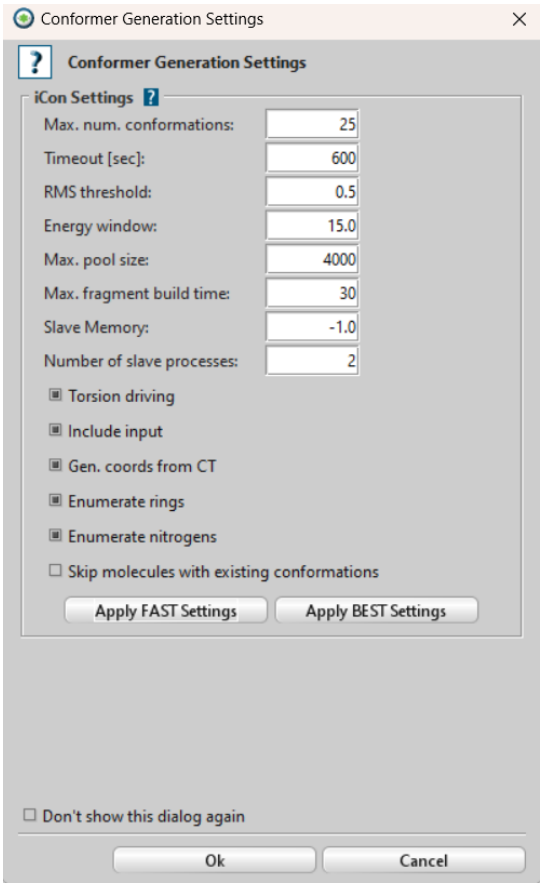


Figure 3.4: Generation of conformations by using FAST settings

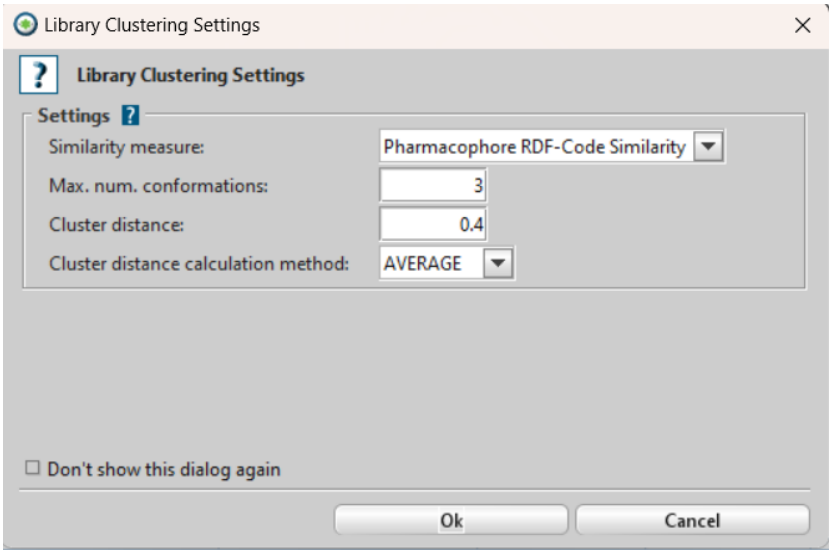


Figure 3.5: Clustering of ligand sets based on pharmacophore RDF-code similarity and average cluster distance calculation

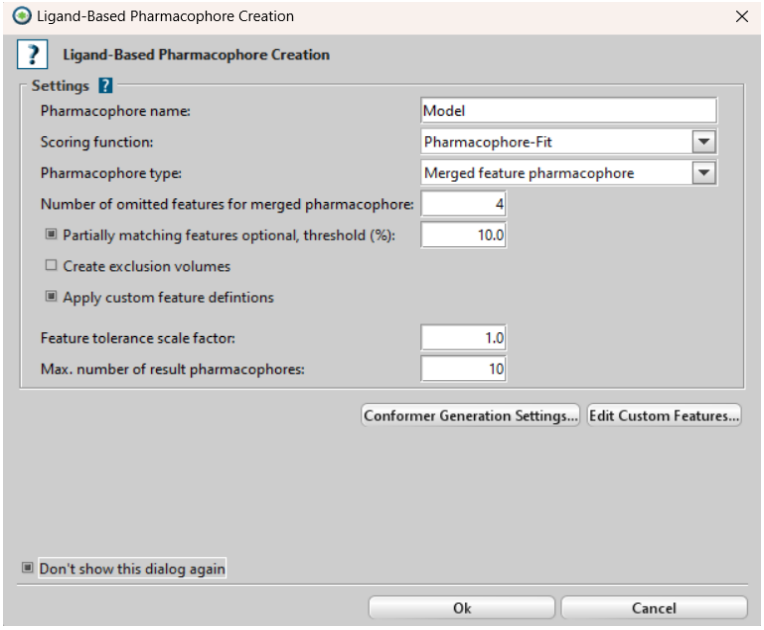


Figure 3.6: Creation of ligand-based pharmacophore model based on pharmacophore fit scoring function

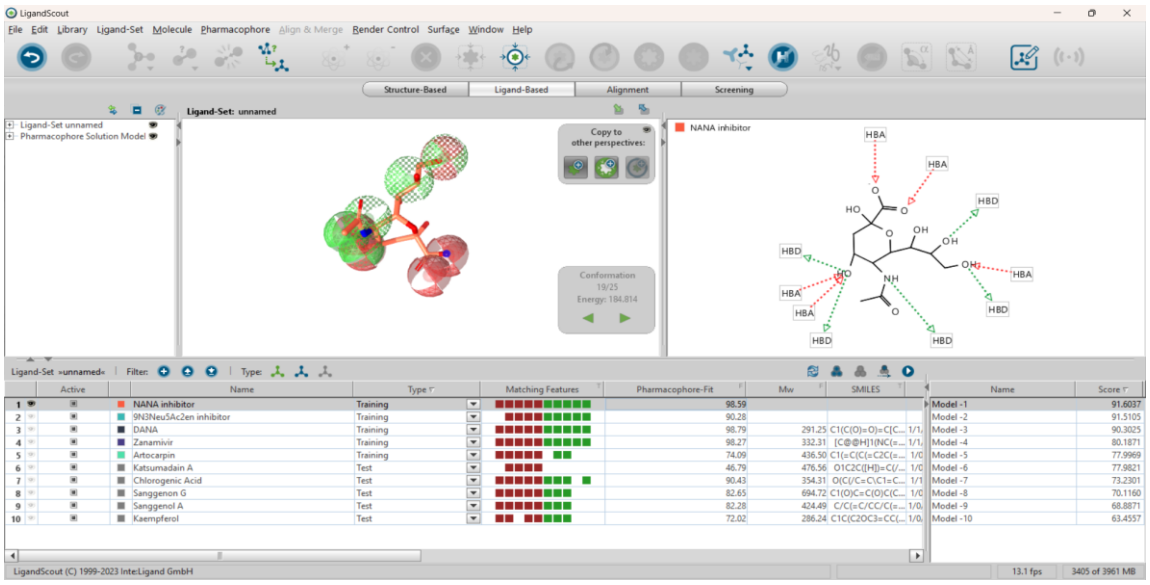


Figure 3.7: Generation of pharmacophore model based on merged pharmacophore feature, and evaluation based on the matching features, model scores and pharmacophore fit values

Additionally, the root mean square deviation (RMSD) values of the test sets in the generated pharmacophore model were evaluated to determine their binding agreement with the model, thus to further affirm the reliability of the pharmacophore model. Theoretically, an RMSD value less than 2 Å is considerably good, but the lower the RMSD value, the better

the agreement of the pharmacophore model with the actual binding pose (Al-Shar'i & Musleh, 2020). On top of that, cosine similarity is a mathematical method utilized to measure the similarity values between two vectors. The reliability of the pharmacophore model was further assessed by measuring the similarity values between a pharmacophore model and the pharmacophore features of the test sets. Based on the values ranging from -1 to 1, cosine similarities from 0 to 1 indicate strong similarity between the pharmacophore model and the test sets (Neela & Peram, 2025). Cosine similarities were calculated by using the formula as shown:

$$\cos\theta = \frac{A \cdot B}{\|A\| \cdot \|B\|} \qquad \text{Equation 3.1}$$

where A·B is the dot product of vectors A and B, A is the magnitude of vector A (pharmacophore model), and B is the magnitude of vector B (test set).

3.2.1.2 Analysis of Schiff Base Vanillin Derivatives as Potential Inhibitors of Generated Pharmacophore Model

Subsequently after the creation and validation of the generated pharmacophore model, the 2D structures of a list of 21 Schiff base vanillin derivatives were drawn by using ChemDraw Ultra 12.0 and downloaded in the MDL-mol file format. The general synthetic route of the Schiff base vanillin derivatives is as illustrated in Figure 3.8, which was by reacting primary amine (RNH_2) with vanillin to obtain the Schiff base vanillin derivative through formation of imine linkage.

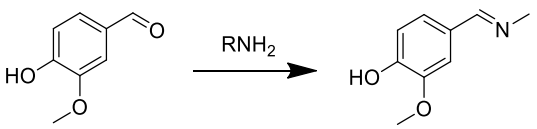


Figure 3.8: General synthetic route of Schiff base vanillin derivatives

Table 3.3 illustrates the list of primary amines involved in the drawing of Schiff base vanillin derivatives, and the resulting chemical structures.

Table 3.3: List of primary amines and the chemical structures of the Schiff base vanillin derivatives

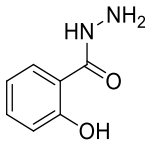
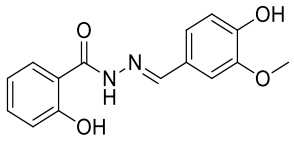
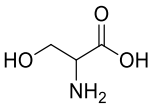
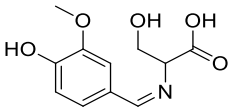
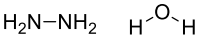
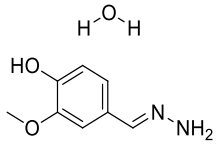
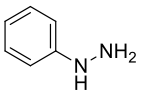
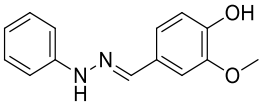
Name of primary amines	Chemical structures of primary amine	Schiff base vanillin derivatives
(1) Salicyl hydrazide		 2-hydroxy-(4-hydroxy-3-methoxybenzylidene)benzohydrazide
(2) Serine		 3-hydroxy-2-((4-hydroxy-3-methoxybenzylidene)amino)propanoic acid
(3) Hydrazide hydrate		 4-(hydrazonomethyl)-2-methoxyphenol hydrate
(4) Phenylhydrazine		 2-methoxy-4-((2-phenylhydrazono)methyl)phenol

Table 3.3 continued

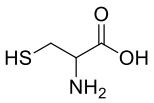
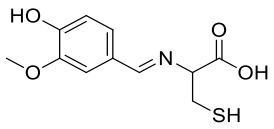
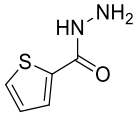
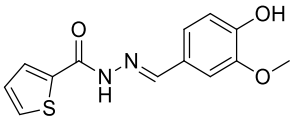
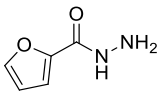
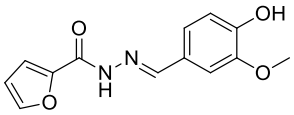
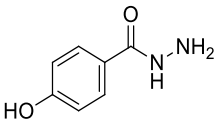
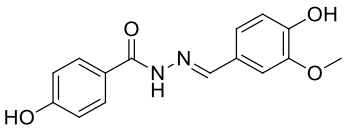
(5) Cysteine		 2-((4-hydroxy-3-methoxybenzylidene)amino)-3-mercaptopropanoic acid
(6) 2-thiophene carboxylic acid hydrazide		 N'-(4-hydroxy-3-methoxybenzylidene)thiophene-2-carbohydrazide
(7) 2-furoic acid hydrazide		 N'-(4-hydroxy-3-methoxybenzylidene)furan-2-carbohydrazide
(8) 4-hydroxybenzhydrazide		 4-hydroxy-N'-(4-hydroxy-3-methoxybenzylidene)benzohydrazide

Table 3.3 continued

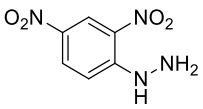
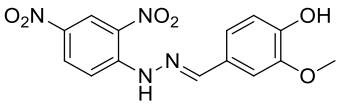
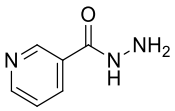
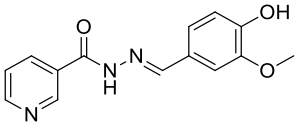
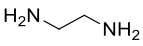
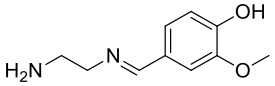
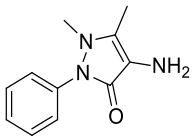
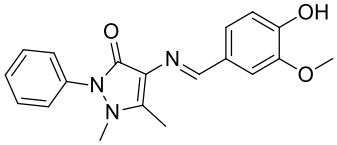
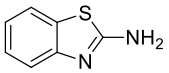
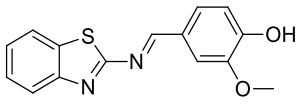
(9) 2,4-dinitrophenylhydrazine		 4-((2-(2,4-dinitrophenyl)hydrazono)methyl)-2-methoxyphenol
(10) Nicotinic hydrazide		 N'-(4-hydroxy-3-methoxybenzylidene)nicotinohydrazide
(11) Ethylenediamine		 4-(((2-aminoethyl)imino)methyl)-2-methoxyphenol
(12) 4-aminoantipyrine		 4-((4-hydroxy-3-methoxybenzylidene)amino)-1,5-dimethyl-2-phenyl-1H-pyrazol-3(2H)-one
(13) 2-aminobenzothiazole		 4-((benzo[*d*]thiazol-2-ylimino)methyl)-2-methoxyphenol

Table 3.3 continued

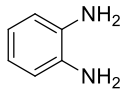
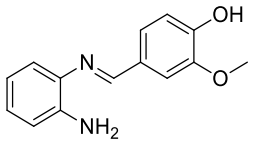
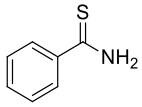
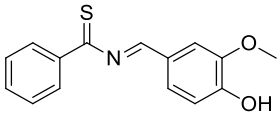
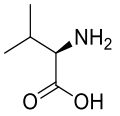
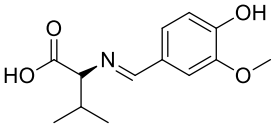
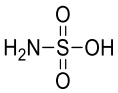
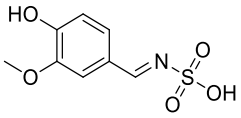
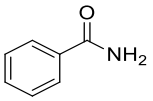
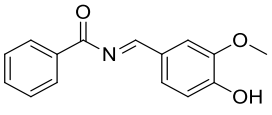
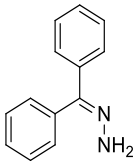
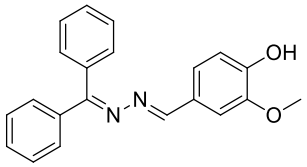
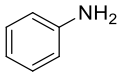
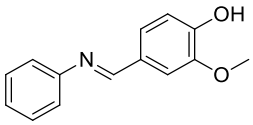
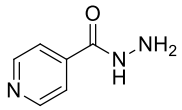
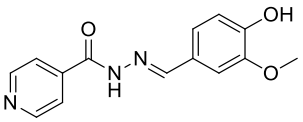
(14) O-phenyldiamine		 4-(((2-aminophenyl)imino)methyl)-2-methoxyphenol
(15) Thiobenzamide		 N-(4-hydroxy-3-methoxybenzylidene)benzothioamide
(16) L-valine		 2-((4-hydroxy-3-methoxybenzylidene)amino)-3-methylbutanoic acid
(17) Sulfamic acid		 (E)-(4-hydroxy-3-methoxybenzylidene)sulfamic acid
(18) Benzamide		 N-(4-hydroxy-3-methoxybenzylidene)benzamide

Table 3.3 continued

(19) Benzophenone hydrazone		 4-(((diphenylmethylene)hydrazono)methyl)-2-methoxyphenol
(20) Aniline		 2-methoxy-4-((phenylimino)methyl)phenol
(21) Isonicotinic acid hydrazide		 N'-(4-hydroxy-3-methoxybenzylidene)isonicotinohydrazide

In the ligand-based perspective of LigandScout 4.4.9, the Schiff base vanillin derivatives were imported as test sets after importing the training sets. Similarly, MMFF94 energies of all datasets were minimised. Conformations of the ligand sets were generated by using the FAST settings, and the ligand sets were clustered based on pharmacophore RDF-code similarity and average cluster distance calculation. Ligand-based pharmacophore modelling was run and the Schiff base vanillin derivatives were evaluated for their potential inhibitory activity against *S. pneumoniae* neuraminidase based on their matching

pharmacophore features and fit values with the generated pharmacophore model. Schiff base vanillin derivatives that were able to depict satisfied results in ligand-based pharmacophore modelling were later subjected to structure-based molecular docking for further assessment.

3.2.2 Structure-based Molecular Docking

3.2.2.1 Analysis and Alignment Evaluation of Schiff Base Vanillin Derivatives with Oseltamivir Carboxylate Inhibitor of 2YA8 against neuraminidase of *S. pneumoniae*

In structure-based molecular docking, the crystal structure of *S. pneumoniae* neuraminidase A, NanA (TIGR4) in complex with oseltamivir carboxylate, encoded as 2YA8, was first retrieved from Protein Data Bank (PDB), and imported into the structure-based perspective of LigandScout 4.4.9. The oseltamivir carboxylate is the ligand in the active site of the crystal structure, which is able to inhibit the activity of neuraminidase of *S. pneumoniae*. Thus, analysis and evaluations were done based on the alignment and matching pharmacophore features of candidate molecules with the pharmacophore model of the oseltamivir carboxylate ligand, the protein-ligand interaction and binding affinity values in the active site of 2YA8 *via* molecular docking of candidate molecule. The crystal structure of *S. pneumoniae* neuraminidase A in complex with oseltamivir carboxylate is as depicted in Figure 3.9.

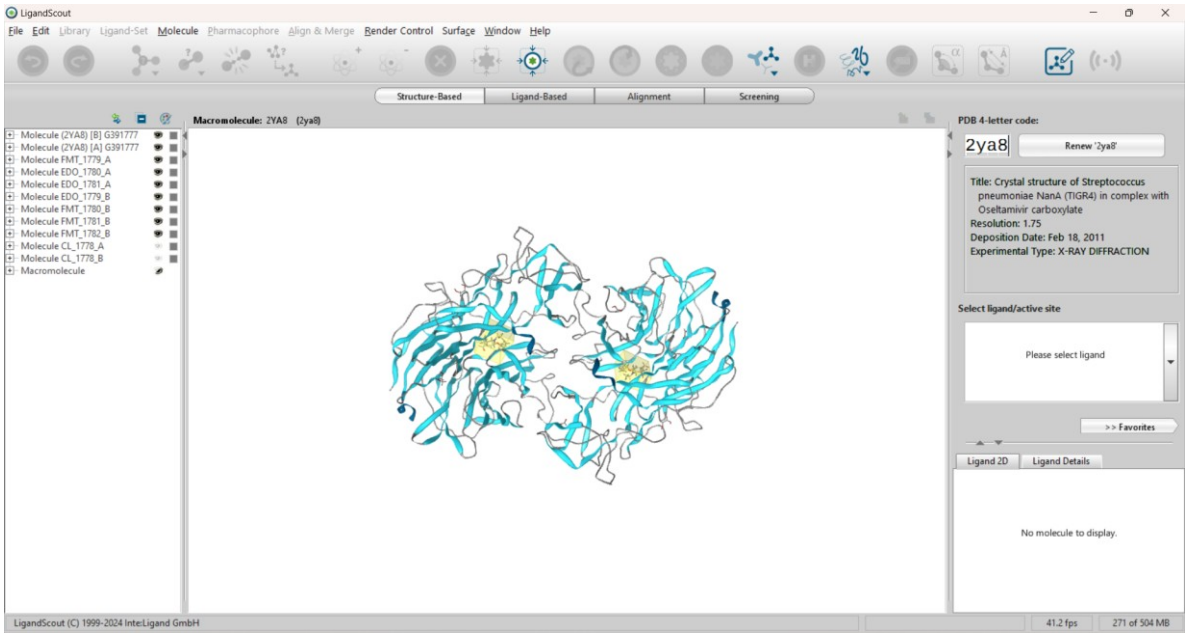


Figure 3.9: Crystal structure of *S. pneumoniae* neuraminidase A in complex with oseltamivir carboxylate (2YA8)

From the structure-based perspective, the oseltamivir carboxylate ligand was first selected and pharmacophore model was first generated, as shown in Figure 3.10. Both ligand and pharmacophore model were copied to the alignment perspective, as shown in Figure 3.11.

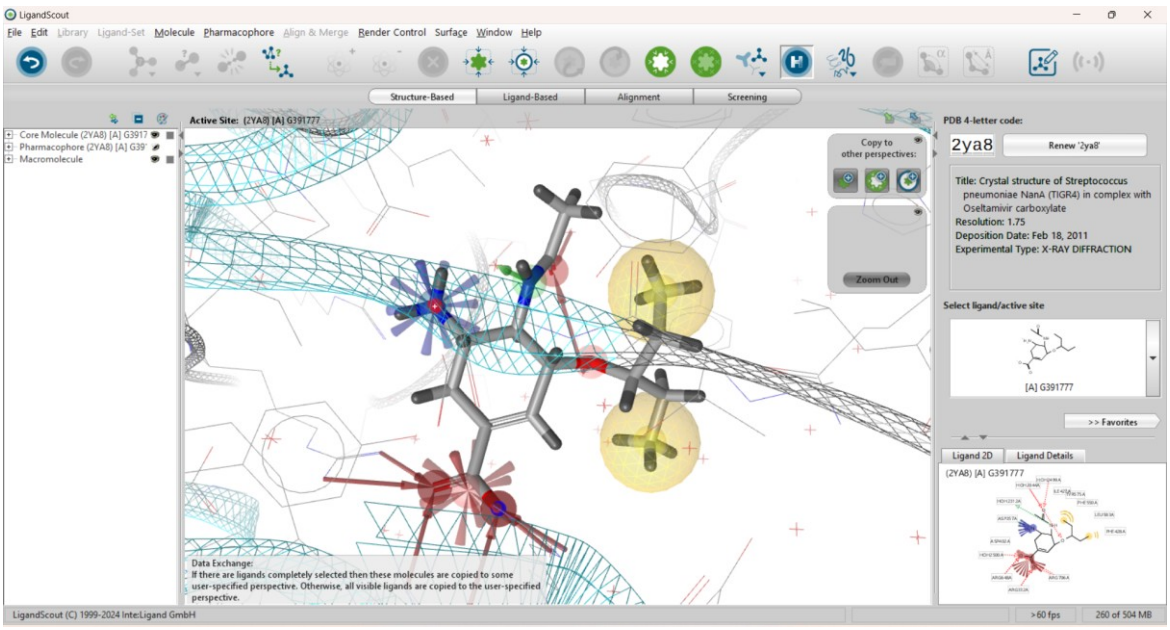


Figure 3.10: Pharmacophore model of the ligand, oseltamivir carboxylate

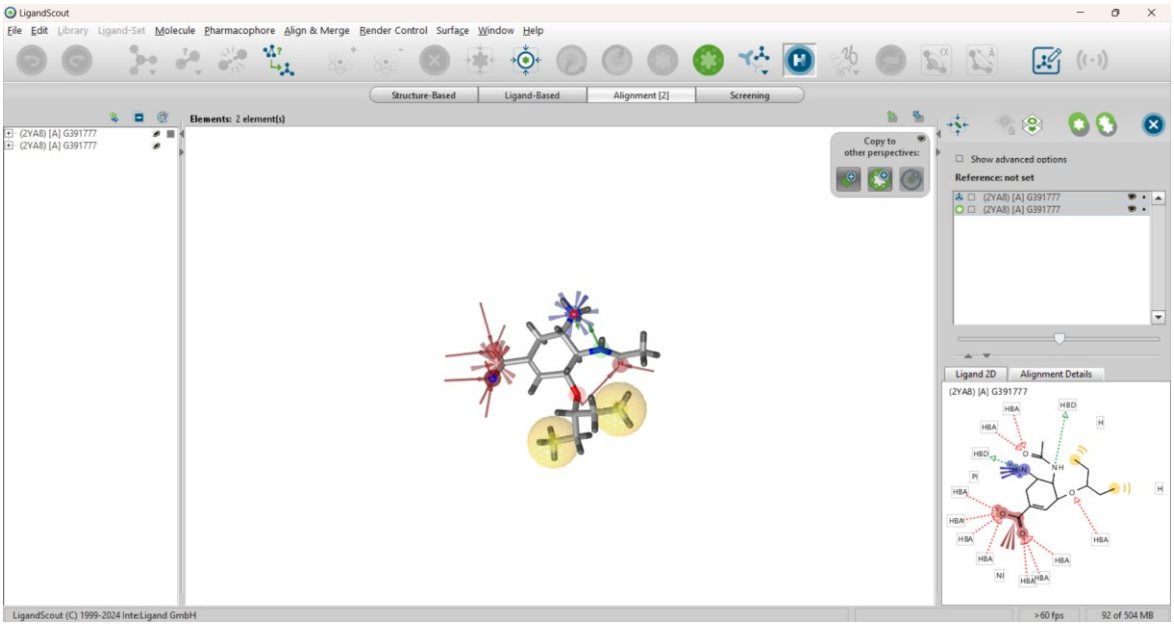


Figure 3.11: Oseltamivir carboxylate ligand and pharmacophore model copied to the alignment perspective

The list of Schiff base vanillin derivatives that satisfied ligand-based pharmacophore modelling were selected to be analysed for their potential as *S. pneumoniae* neuraminidase inhibitors in structure-based molecular docking. The MDL-mol files of the vanillin derivative were first converted to MDL-sdf formats by using Open Babel GUI 2.3.1, as shown in Figure 3.12.

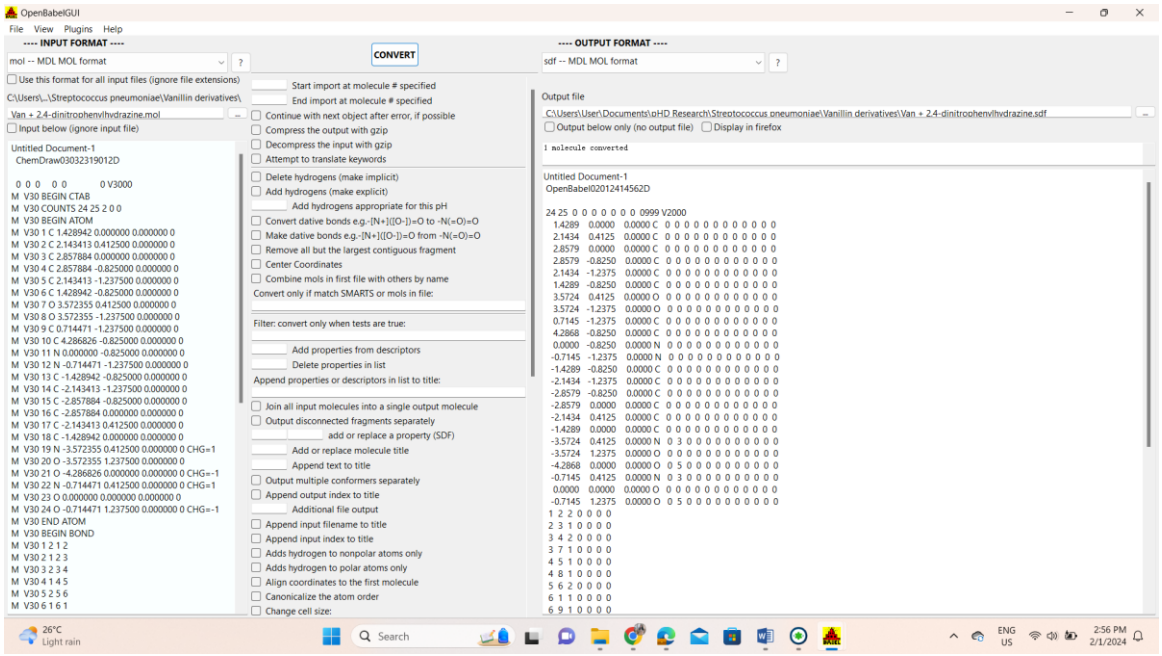


Figure 3.12: Conversion of MDL-mol files of Schiff base vanillin derivatives to MDL-sdf files by using Open Babel GUI 2.3.1

The MDL-sdf file of the first Schiff base vanillin derivative, which is vanillin + salicyl hydrazide, was inserted into the structure-based perspective, followed by the copying of the ligand and pharmacophore models into the alignment perspective. In the alignment perspective, the vanillin derivative and the oseltamivir carboxylate ligand was subjected to alignment based on common pharmacophore features with the pharmacophore model of the oseltamivir carboxylate ligand. Figure 3.13 shows the outcome of successful alignment between the vanillin derivative and ligand, such that the orange spots were the common feature shared between two structures.

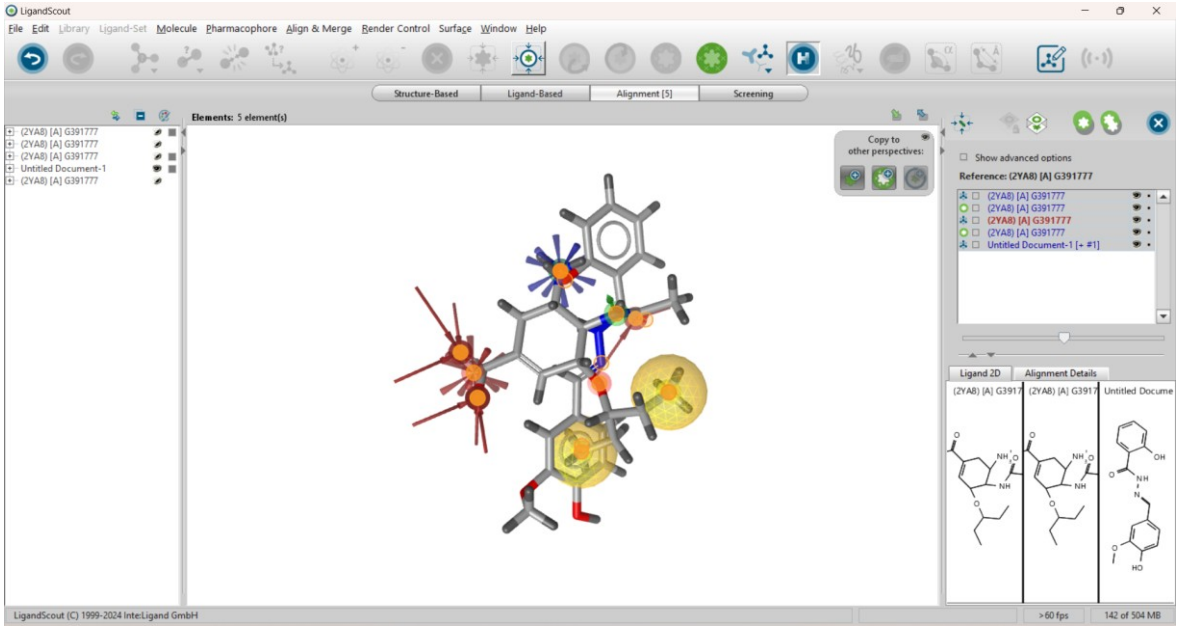


Figure 3.13: Successful alignment between oseltamivir carboxylate ligand and vanillin derivative

Based on the common features shared between the two structures, a shared pharmacophore model was generated, and the pharmacophores were merged, followed by interpolation of overlapping features as depicted in Figure 3.14.

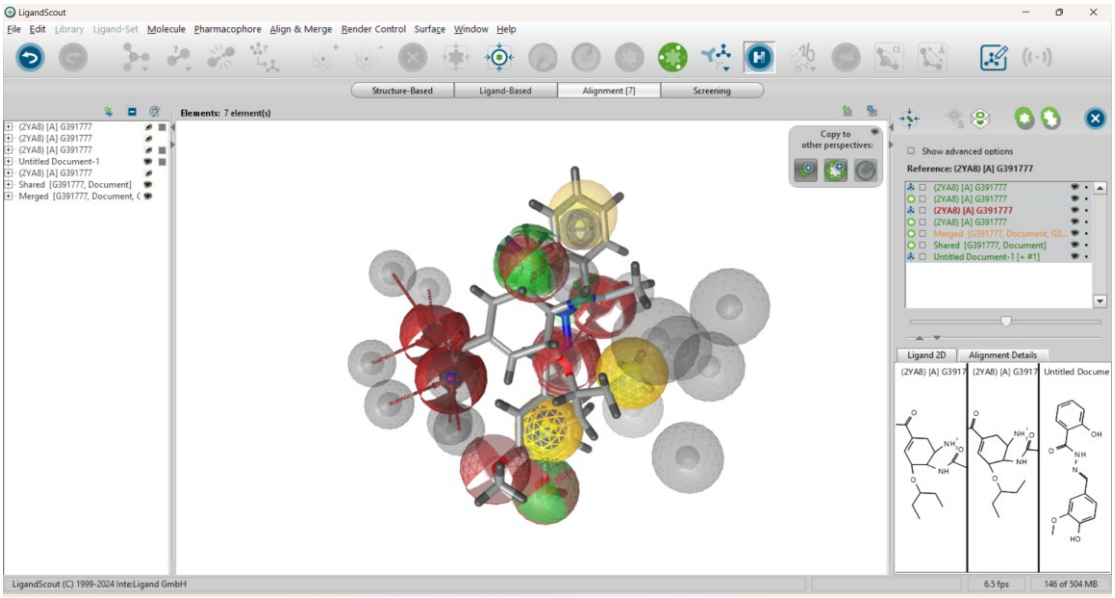


Figure 3.14: Shared feature pharmacophore, merged pharmacophores and interpolated overlapping features

The ligands and pharmacophore models were then injected back into the active site of the crystal structure of protein in the structure-based perspective. From here, the vanillin derivative showed its interaction with the active site of the protein based on the common pharmacophore features with the oseltamivir carboxylate ligand. Figure 3.15 shows the interactions depicted by the vanillin derivative in the active site of 2YA8 in alignment and comparison with oseltamivir carboxylate ligand.

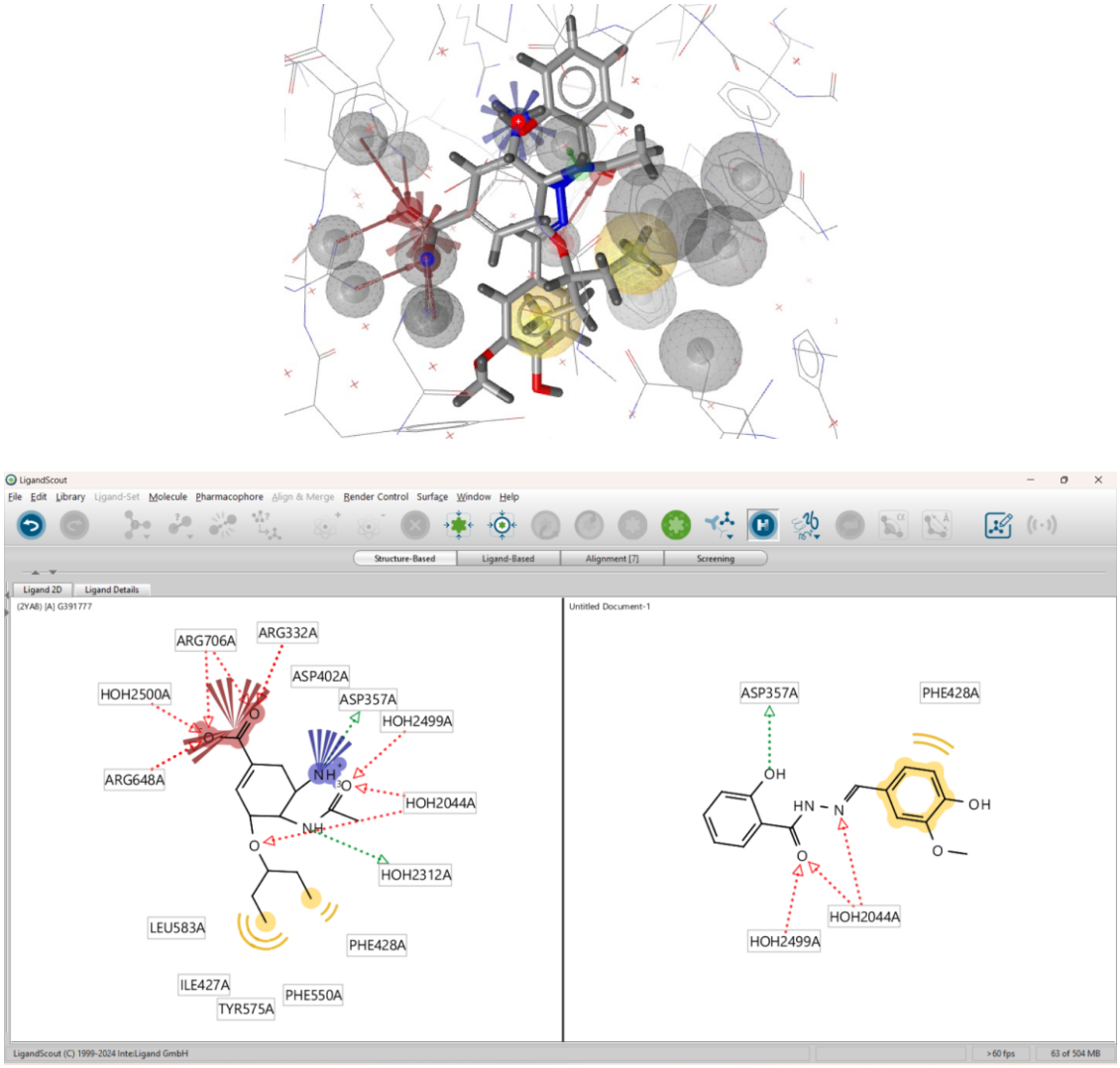


Figure 3.15: Interactions depicted by the vanillin derivative in the active site of 2YA8 in in comparison with oseltamivir carboxylate ligand

3.2.2.2 Docking of Schiff Base Vanillin Derivatives in the Active Site of 2YA8

All the Schiff base vanillin derivatives were later subjected to docking into the active site of 2YA8 to determine their binding affinities by using AutoDock 4.2 and PyMOL. The molecular docking method was done based on method proposed by Trott and Olson (2010). To carry out molecular docking, it is most important to prepare the protein and ligand structures in PDBQT file format. Thus, Protein Data Bank (PDB) file of 2YA8 was first downloaded and imported into AutoDock 4.2 as shown in Figure 3.16.

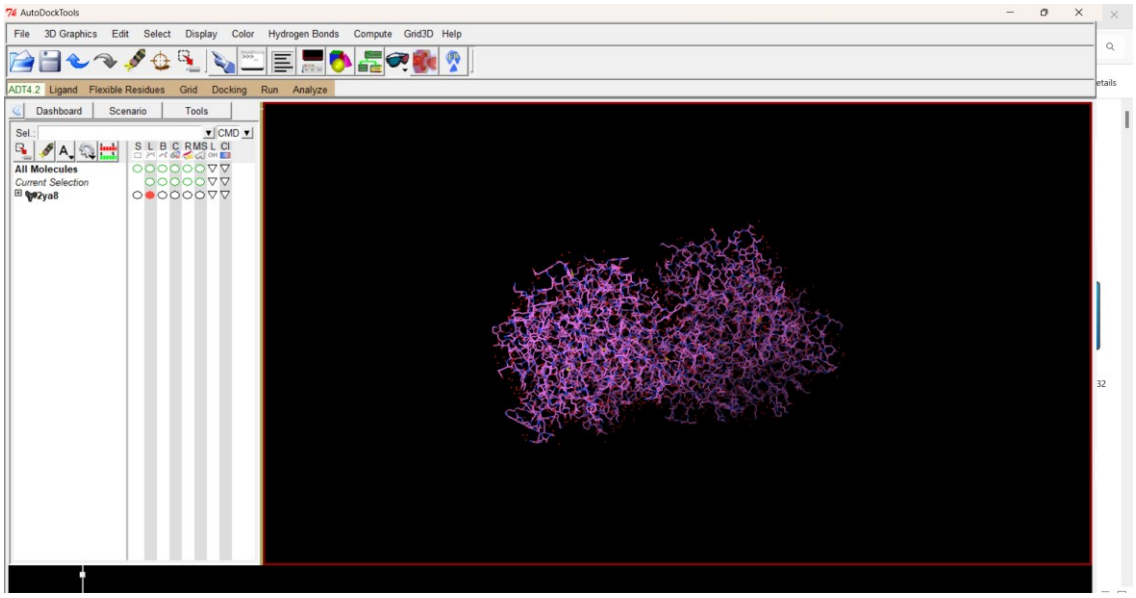


Figure 3.16: Import of 2YA8 in AutoDock 4.2

Water molecules were deleted because the water molecules may decrease the affinity of interaction between ligand and protein molecule. Hydrogens were added to stabilise chemical bonds. Kollman charges were added to increase accuracy as docking algorithms require atoms to be charged (Trott and Olson, 2010). Consequently, the protein macromolecule was selected and save in PDBQT file format.

The Schiff base vanillin derivative in the MDL-sdf file format was imported into PyMOL and exported as PDB file format as shown in Figure 3.17. The PDB file of the Schiff

base vanillin derivative was later imported into AutoDock 4.2 as shown in Figure 3.18. The Schiff base vanillin derivative was selected as ligand, and saved as PDBQT file format.

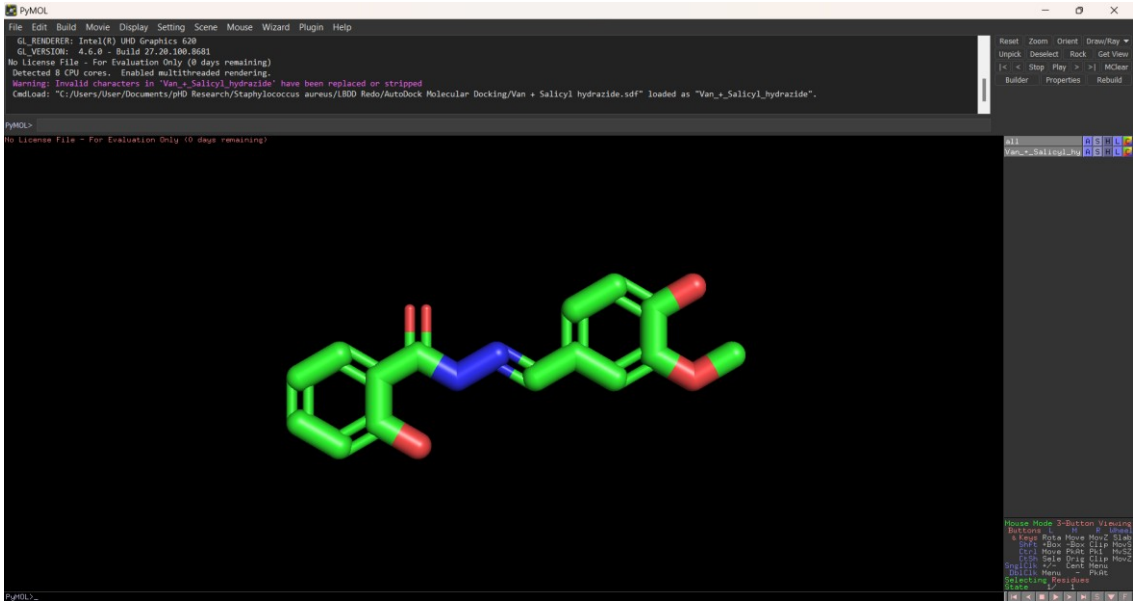


Figure 3.17: Import of MDF-sdf file of vanillin + salicyl hydrazide in PyMOL to be converted to PDB file format

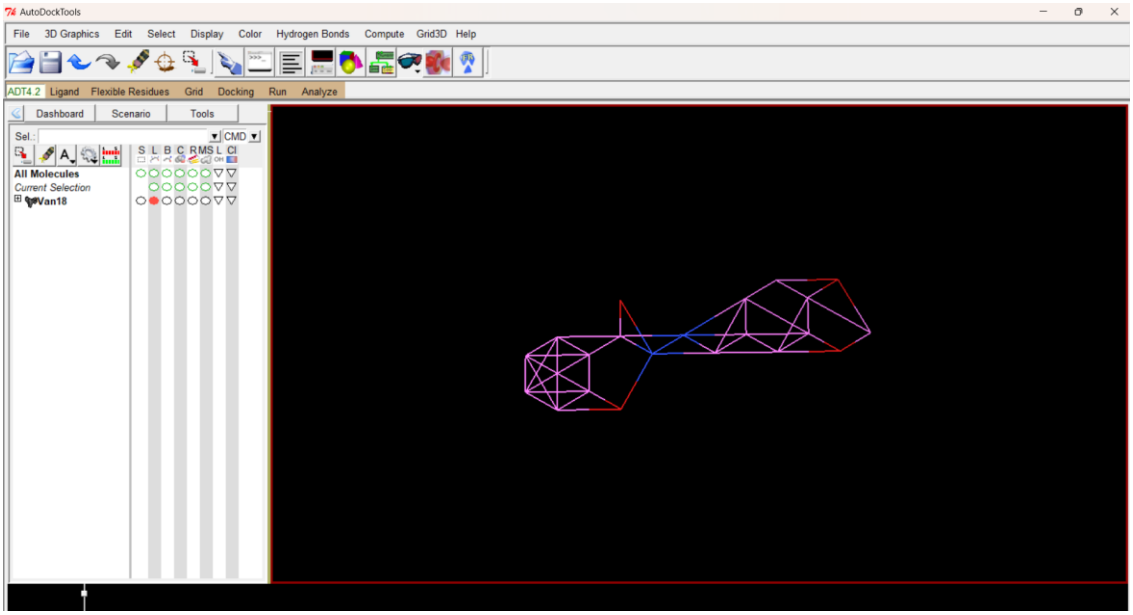


Figure 3.18: Import of PDB file of vanillin + salicyl hydrazide in AutoDock 4.2 to be converted to PDBQT file format

Upon reaching this stage, the PDBQT files of both protein and ligand, which were 2YA8 and Schiff base vanillin derivative respectively, were available for molecular docking.

The PDB file of 2YA8 was imported into AutoDock 4.2 together with the Schiff base vanillin derivative previously, and the protein macromolecule was selected once again, and saved as PDBQT file format to overwrite the previous PDBQT file. The illustration was as depicted in Figure 3.19.

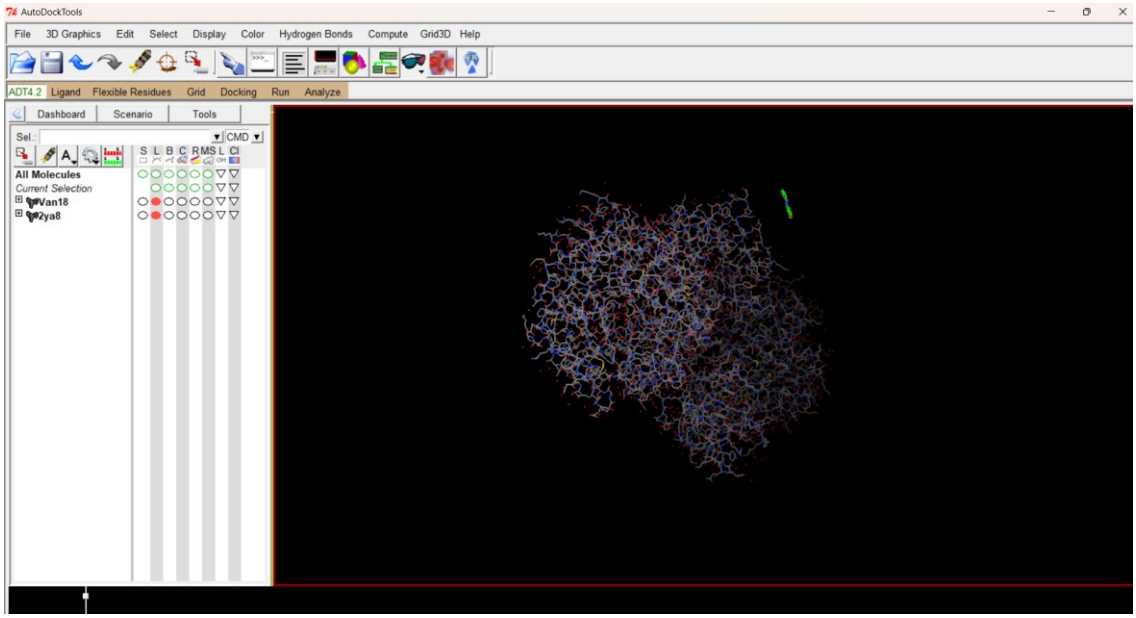


Figure 3.19: PDB file format of 2YA8 and vanillin + salicyl hydrazude in AutoDock 4.2

From here, the grid box was selected to obtain information about the region of binding site of 2YA8 by the Schiff base vanillin derivative as shown in Figure 3.20.

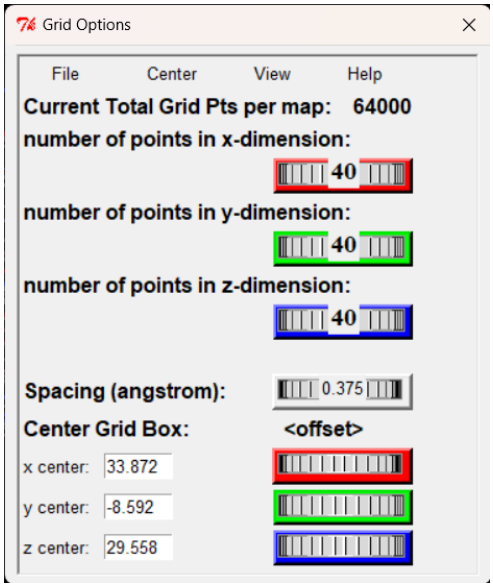


Figure 3.20: Grid box of 2YA8

By using the information, a configuration text was prepared in text document (txt) file. Figure 3.21 described the information required in the configuration text.

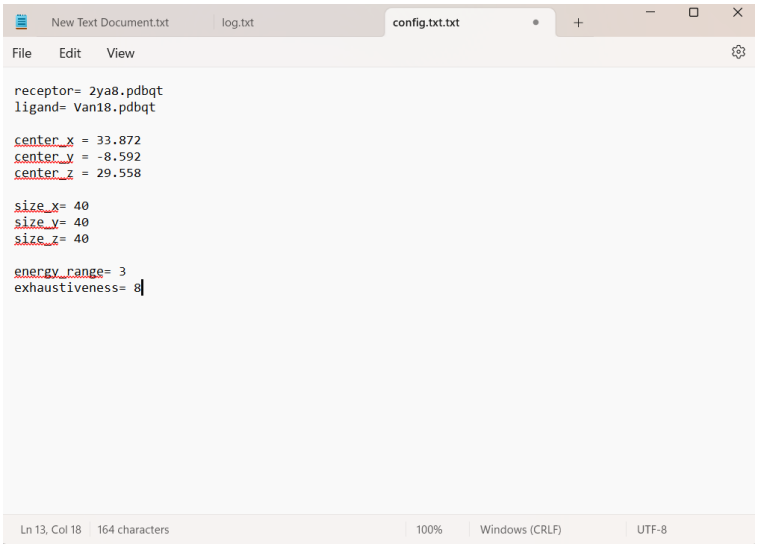


Figure 3.21: Information in configuration text

Accordingly, a command prompt was now prepared to run the molecular docking. By keying in the proper commands, including names of receptors and ligands, configuration text, as well as the log and output file as illustrated in Figure 3.22, molecular docking was

initiated and the binding affinity values were obtained and evaluated, together with the lower boundary and upper boundary of root mean square deviation (RMSD).

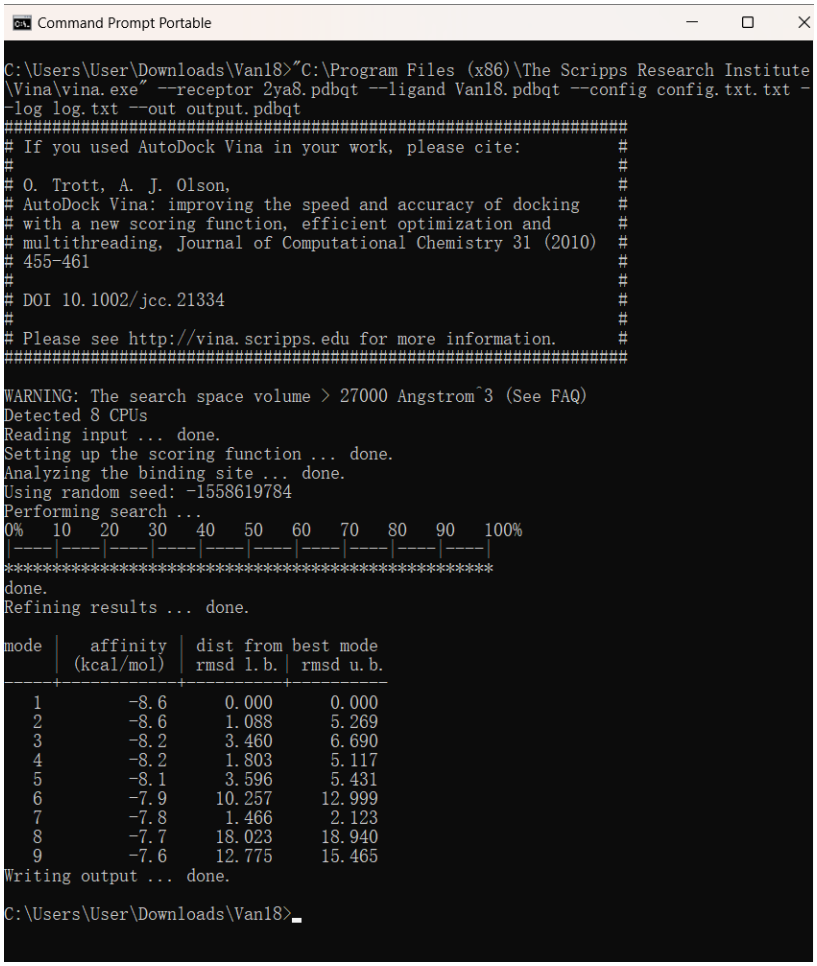


Figure 3.22: Command prompt that successfully show binding affinity value of vanillin + salicyl hydrazide in the active site of 2YA8

In conclusion, for Schiff base vanillin derivatives that were able to show good pharmacophore fit values and matching pharmacophore features in ligand-based pharmacophore modelling, good alignment and matching features with the oseltamivir carboxylate ligand in 2YA8, as well as good binding affinity values upon molecular docking in the active site of 2YA8, the were subjected to synthesis to be further evaluated.

3.3 Computational Evaluations of Schiff Base Vanillin Derivatives against *S. aureus* FtsZ Protein

3.3.1 Ligand-based Pharmacophore Modelling

3.3.1.1 Generation and Validation of Pharmacophore Model

Similar to generation and validation of pharmacophore model in 3.2, a list of chemical compounds that were reported for their inhibitory activity against FtsZ protein of *S. aureus* in previous literature were selected as training sets to generate pharmacophore model. The 2D structures were drawn using ChemDraw Ultra 12.0 and downloaded in the MDL-mol file format. The MDL-mol files of the training sets were imported in the ligand-based perspective of LigandScout 4.4.9. From literature study, the training sets selected were 4 novel compounds which include TXA707, TXA6101 (Fujita et al., 2017), TXH9179 (Bryan et al., 2023) and PC190723 (Matsui et al., 2012). The chemical structures are as illustrated in Table 3.4.

Table 3.4: Training sets to generate pharmacophore model

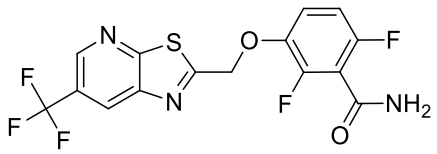
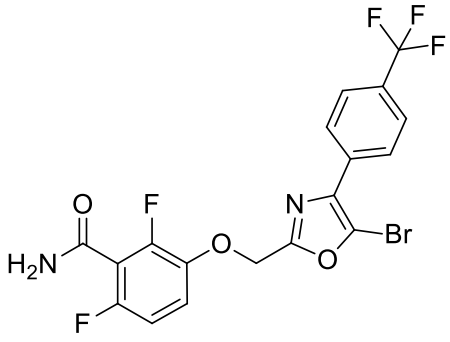
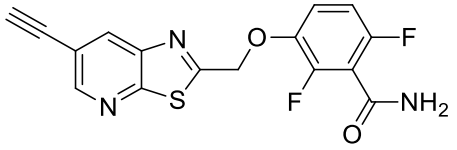
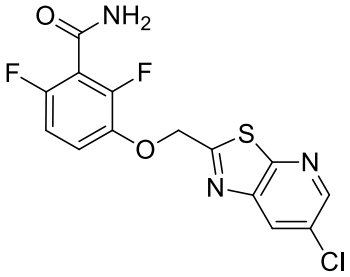
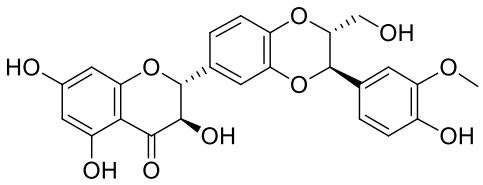
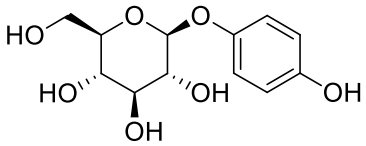
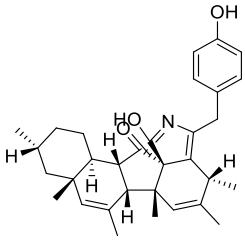
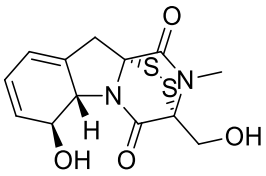
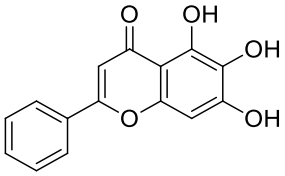
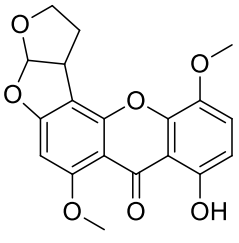
Name of training sets	Chemical structures
TXA707	
TXA6101	

Table 3.4 continued

TXH9179	
PC190723	

Consistently, the generated pharmacophore model was validated by a list of test sets to validate its reliability to evaluate potential inhibitory activity of Schiff base vanillin derivatives against *S. aureus* FtsZ. A list of chemical compounds from natural product discovered and reported for inhibiting FtsZ of *S. aureus* were selected as test sets to validate the reliability of the model. The MDL-mol files of the 2D structures of test sets were prepared in the same manner, such that the structures were drawn and downloaded in MDL-mol file format using ChemDraw Ultra 12.0, and subsequently imported as test sets together with the training sets in the ligand perspective of LigandScout 4.4.9. The list of test sets selected from literature review were silibinin (Basak et al., 2024), arbutin (Migas and Krauze-Baranowska, 2015), diaporthalasin (Khamthong et al., 2014), gliotoxin (Downes et al., 2023), baicalein (Chen et al., 2016) and 5-methoxydihydrosterigmatocystin (Zhao et al., 2022), with their chemical structure depicted in Table 3.5.

Table 3.5: Test sets to validate the generated pharmacophore model

Name of test sets	Chemical structures
Silibinin	
Arbutin	
Diaporthalasin	
Gliotoxin	
Baicalein	
5-methoxydihydrosterigmatocystin	

When all the MDL-mol files of training sets and test sets were imported into the ligand-based perspective of LigandScout 4.4.9, identically, their MMFF94 energies were minimized, conformations of the ligand sets were generated, the ligand sets were clustered. Ligand-based pharmacophore modelling was initiated based on pharmacophore fit scoring function, and the pharmacophore model was generated based on merged pharmacophore feature. In the same way, the training sets should show high pharmacophore fit values and matching features. The model generated was said to be validated for its reliability for evaluation of potential inhibitory activity against FtsZ of *S. aureus* if test sets were able to depict matching features and pharmacophore fit values greater than half of the values shown by training sets. In a similar manner, the RMSD values of the test sets in the pharmacophore model, as well as the cosine similarities in the model were evaluated to affirm the reliability of the generated model. The general workflow is as described from Figure 3.3 to Figure 3.7.

3.3.1.2 Analysis of Schiff Base Vanillin Derivatives as Potential Inhibitors of Generated Pharmacophore Model

The same list of Schiff base vanillin derivatives in Table 3.3 were selected to be evaluated as potential inhibitors of FtsZ of *S. aureus*. Upon the import of training sets, the MDL-mol files of the 21 Schiff base vanillin derivatives were imported as test sets in the ligand-based perspective of LigandScout 4.4.9. Once again, in the same manner, MMFF94 energies were minimized, conformations of the ligand sets were generated, the ligand sets were clustered. By running ligand-based pharmacophore modelling, Schiff base vanillin derivatives that were able to show good pharmacophore fit values and matching features with the pharmacophore model were selected and subjected to structure-based molecular docking for further evaluation and analysis.

3.3.2 Structure-Based Molecular Docking

3.3.2.1 Analysis and Alignment Evaluation of Schiff Base Vanillin Derivatives with PC190723 Novel Inhibitor against FtsZ of *S. aureus*

The Protein Data Bank structure of *S. aureus* FtsZ with a novel inhibitor, PC190723, encoded as 3VOB was first retrieved and imported into the structure-based perspective of LigandScout 4.4.9 as portrayed in Figure 3.23.

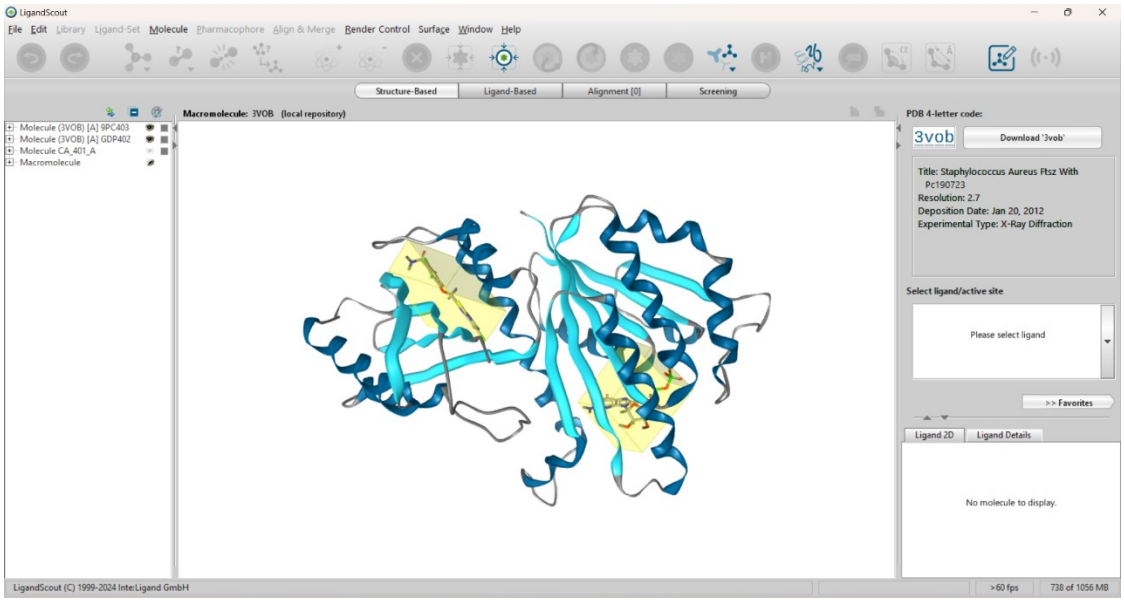


Figure 3.23: *S. aureus* with PC190723 (3VOB)

The PC190723 inhibitor was selected, and pharmacophore model was generated as shown in Figure 3.24. Similar to Figure 3.11, both pharmacophore model and ligand were copied into the alignment perspective as shown in Figure 3.25.

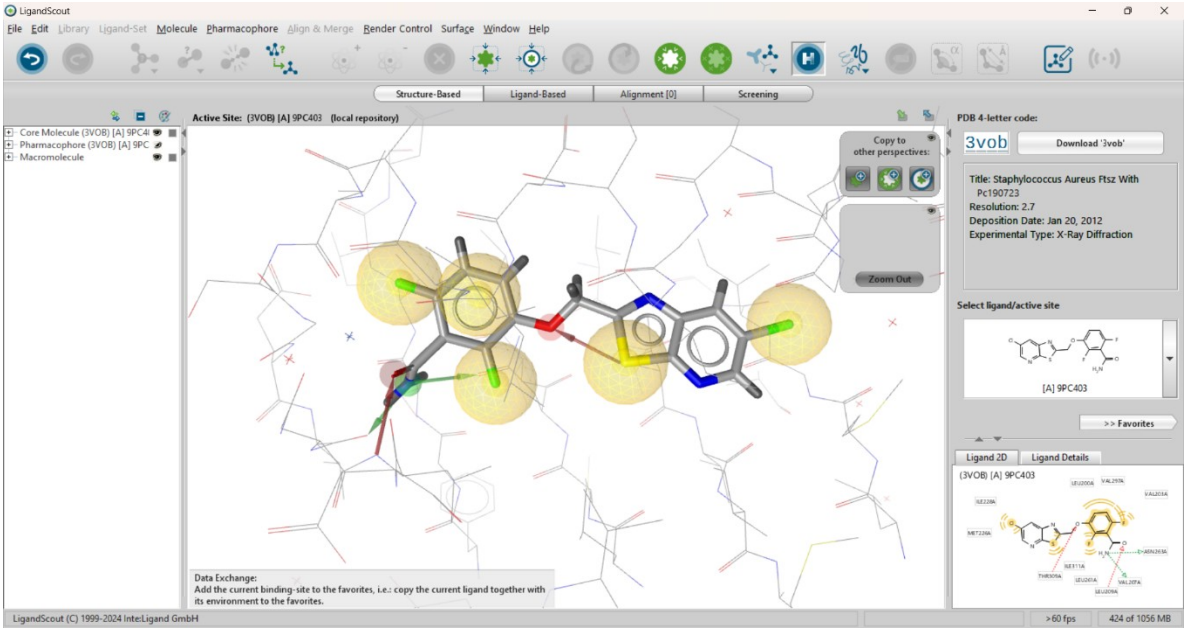


Figure 3.24: Pharmacophore model of the ligand, PC190723

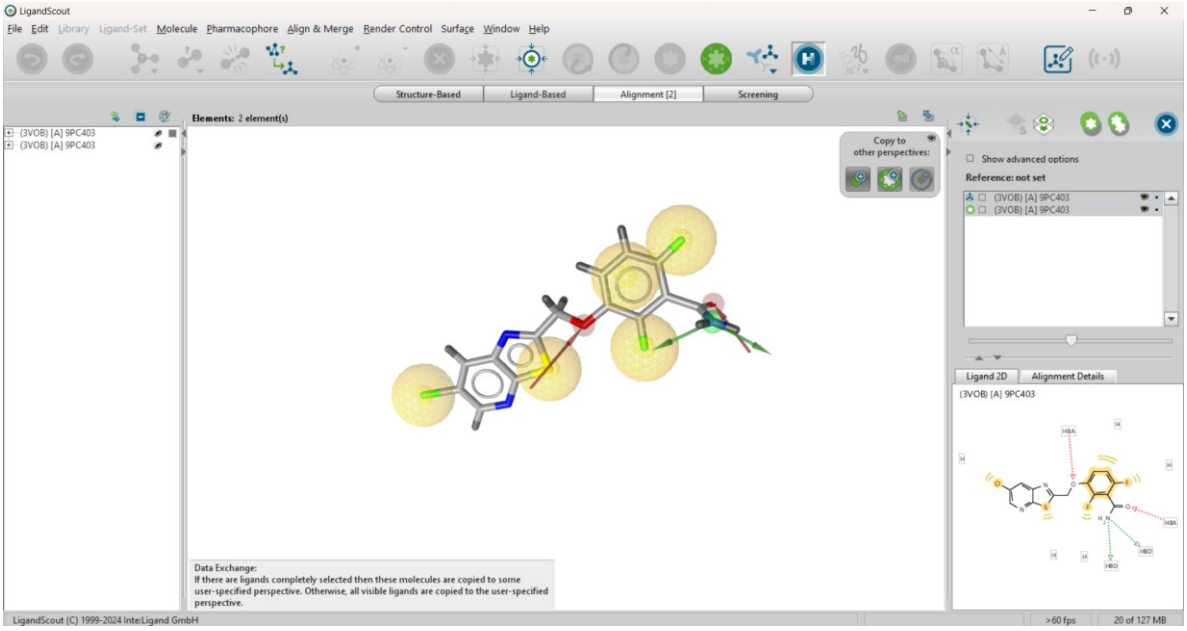


Figure 3.25: PC190723 ligand and pharmacophore model copied to the alignment perspective

The MDL-sdf files of Schiff base vanillin derivatives, beginning from the first Schiff base vanillin derivative, which is vanillin + salicyl hydrazide, was imported in the structure-based perspective. The ligand and pharmacophore models were copied to the alignment perspective together with PC190723 ligand and pharmacophore mode. The vanillin

derivative was subjected to alignment with the PC190723 inhibitor by matching pharmacophore feature with the model based on common pharmacophore feature. Upon successful alignment, a shared pharmacophore model was generated, and the pharmacophores were merged, followed by interpolation of overlapping features, similar to illustrations shown in Figure 3.13 and Figure 3.14. The ligands and pharmacophore models were then injected back to the active site of protein in structure-based perspective, whereby the interaction of vanillin derivative with the active site of 3VOB as well as common pharmacophore feature shown by the vanillin derivative was evaluated, similar to Figure 3.15.

3.3.2.2 Docking of Schiff Base Vanillin Derivatives in the Active Site of 3VOB

Molecular docking of Schiff base vanillin derivatives in the active site of 3VOB were performed in similar method as elaborated in 3.2.2.2, except that the protein structure was changed to 3VOB instead of 2YA8. The PDB file of 3VOB in AutoDock 4.2 is as shown in Figure 3.26.

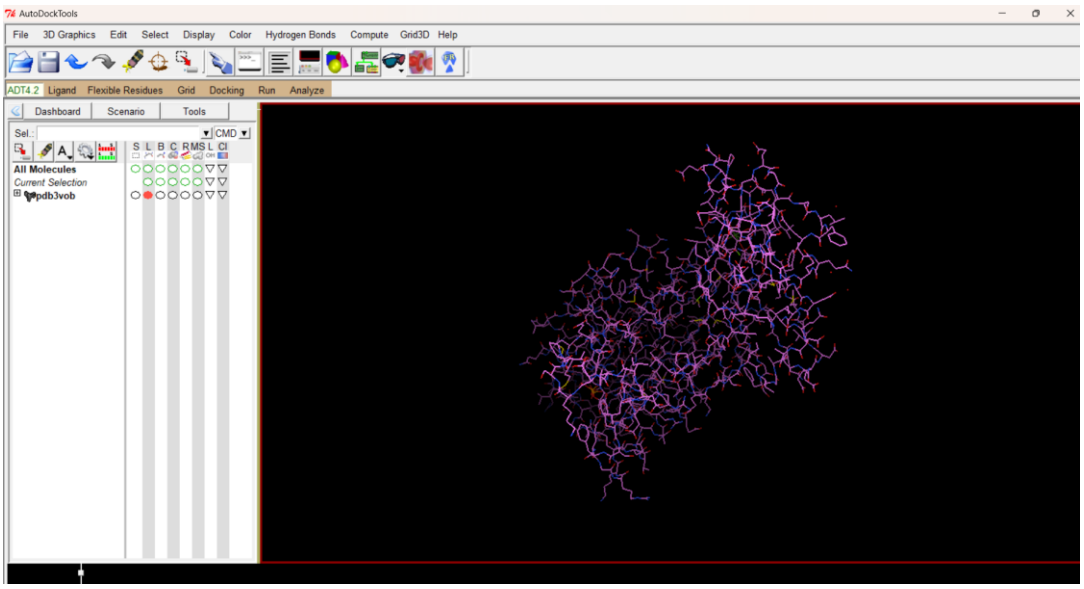


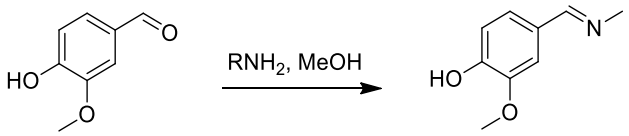
Figure 3.26: Import of 3VOB in AutoDock 4.2

By preparing the PDBQT files of ligand and protein, which were the Schiff base vanillin derivative and 3VOB, followed by preparation of configuration text and running of command prompt, the binding affinity values of Schiff base vanillin derivatives in the active site of 3VOB together with the upper and lower boundary of RMSD were obtained and evaluated.

In conclusion, Schiff base vanillin derivatives that successfully showed potential dual inhibitory activity in ligand-based pharmacophore modelling, structure-based pharmacophore modelling and molecular docking against neuraminidase of *S. pneumoniae* and FtsZ of *S. aureus* were selected and subjected to synthesis for further evaluation.

3.4 Synthesis of Schiff Base Vanillin Derivatives

The syntheses of vanillin derivatives were done based on Schiff base synthesis reaction between primary amines and vanillin purchased from Sigma-Aldrich. Schiff base vanillin derivatives were synthesized based on a mole ratio of vanillin to primary amine of 1:1 ratio. A 0.01 mol of vanillin in methanol was first mixed with various 0.01 mol of methanolic amine solution. The mixture was heated at 65˚C for 2-3 hours with continuous stirring, and allowed to cool at room temperature for 30 minutes until precipitate is observed. Thin layer chromatography (TLC) is performed to continuously monitor the synthesis process to ensure the reaction is complete by using a solvent system of chloroform to methanol of 4:1. The precipitate formed was filtered and washed with methanol solution. The Schiff base vanillin derivative product obtained was dried in oven for 5 minutes (Asaruddin, 2016). The list of Schiff base vanillin derivatives to be synthesized was as listed in Table 3.3. The general synthesis route of Schiff base vanillin derivatives is as shown in Figure 3.27.



.

Figure 3.27: Synthetic scheme of Schiff base vanillin derivatives

3.5 Characterization of Schiff Base Vanillin Derivatives

3.5.1 Thin Layer Chromatography (TLC)

TLC was performed during the synthesis process of Schiff base vanillin derivatives to ensure all vanillin had completely reacted with the primary amine solution, thus to ensure the purity of the product obtained. On a piece of 6cm × 2cm TLC plate (stationary phase), the baseline was marked 1cm from the bottom, and the solvent front was marked 0.5cm from the top of the plate. Two solutions were prepared, which were vanillin and the synthesized compound, each dissolved in ethyl acetate solvent. The two solutions were spotted separately onto the baseline of the TLC plate. The TLC plate was later transferred carefully into the developing chamber (mobile phase) in a beaker, whereby the baseline was ensured to be above the organic solvent. The top of the beaker was covered to avoid evaporation of the organic solvent. When the solvent reaches the solvent front, the TLC plate was taken out and allowed to dry. The TLC plate was later observed under the short and long wavelengths of ultraviolet light, 254 nm and 364 nm respectively, and all spots observed were circled by using a lead pencil. If the synthesized compound depicts two spots along the TLC plate, this indicates the presence of vanillin, and therefore reaction that hasn't complete. If it shows only a distinct spot different from the vanillin spot, this indicates all vanillin has successfully reacted with the primary amine, and thus complete reaction. The general illustration of TLC is as shown in Figure 3.28.

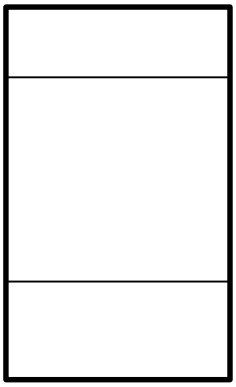


Figure 3.28: General illustration of thin layer chromatography (TLC)

3.5.2 Fourier Transform-Infrared Spectroscopy

In FT-IR, the Perkin Elmer Spectrum GX Fourier Transform-Infrared Spectroscopy (FT-IR) was used to obtain FT-IR spectra results, wavelength ranging from 4000 cm^{-1} to 525 cm^{-1} using attenuated total reflectance (ATR) mode. About 8 mg of sample was placed on the mirror of the spectrometer, and subjected for a total number of 32 scannings. The infrared absorption result was obtained based on the functional groups of the compound.

3.5.3 Nuclear Magnetic Resonance Spectroscopy

The spectroscopies of ^{1}H-NMR of all samples were recorded by using Varian 500 MHz spectrometer to identify the content, purity and the molecular structure of the compound. The common solvent used is deuterated dimethyl sulfoxide (DMSO), and the number of scannings is 32. Signals obtained from the method were recorded in terms of chemical shifts (δ) in ppm from the internal standard, such that tetramethylsilane, TMS was used as the internal standard. The signals were presented as multiplicities, which are singlet, doublet, triplet, quartet, quintet etc.

3.6 Antibacterial Assay

The materials required in antibacterial assay include Mueller-Hinton broth (MHB) purchased from OXOID brand, Mueller-Hinton agar (MHA) purchased from Merck company, *S. aureus* ATCC 25923 bacteria strain and synthesized Schiff base vanillin derivatives. MHA solution was prepared by dissolving 38 g of the agar powder into 1 L of distilled water, whereas MHB solution was prepared by dissolving 21 g of the broth powder into 1 L of distilled water. Both solutions were subjected to autoclave for sterilisation. The bacteria strain was cultured in MHB medium and subjected to incubation at 37°C for 24 hours. The prepared cultured bacteria were used with concentration of concentration of 1.5×10^8 CFU/mL as inoculums in antibacterial assay by agar disk-diffusion method. The methods employed were based on protocols proposed by CLSI (CLSI, 2020).

In agar diffusion method, approximately 15 – 20 mL of MHA solution was poured into sterile Petri dishes and allowed to be solidified. Pure cultures of the bacteria were sub-cultured on MHA, and swabbed by using a sterile cotton swab to create bacterial lawn. All tested compounds were prepared in 1.0×10^3 μg/mL. The agar medium was later punched with wells of 6 mm by using a sterile straw and impregnated with 75 μL of the tested compounds, with cephalothin as positive control and 1% dimethyl sulfoxide (DMSO) solvent as negative control. Upon incubation of the plate at 37°C for 24 hours, the diameter of inhibition zone was measured with a calliper to the nearest 1 mm. All assays were performed in triplicates to obtain the most accurate and optimum results.

An overall research workflow adopted in this research study is as shown in Figure 3.29.

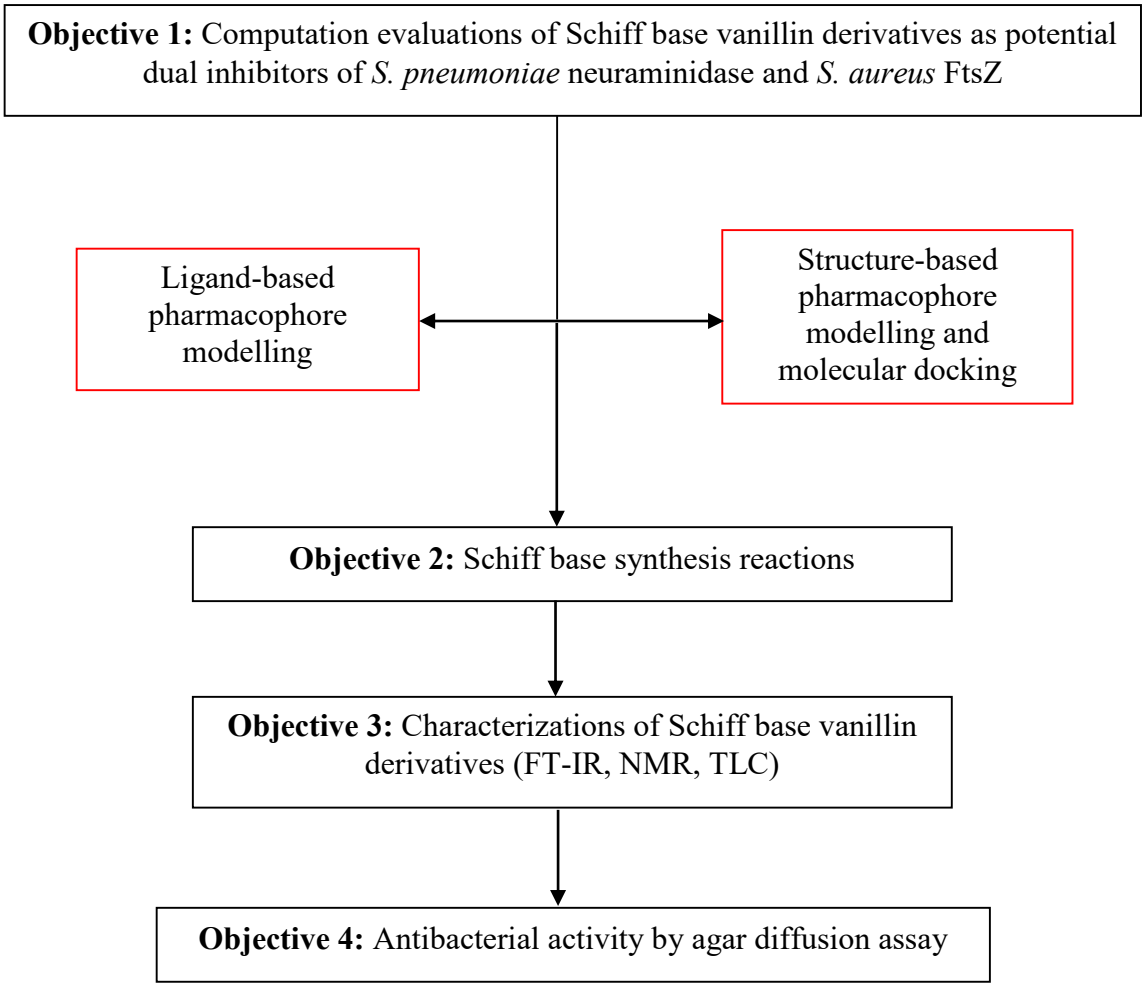


Figure 3.29: Overall research workflow

CHAPTER 4

RESULTS AND DISCUSSION

4.1 CADD Results of Schiff Base Vanillin Derivatives Targeting Neuraminidase of *S. pneumoniae*

4.1.1 Ligand-based Approach

The results in ligand-based approach, which is ligand-based pharmacophore modelling were divided into 2 parts: generation and validation of pharmacophore model, as well as analysis of Schiff base vanillin derivatives as potential inhibitors of the generated pharmacophore model.

4.1.1.1 Generation and Validation of Pharmacophore Model

The 3D chemical structures of the training sets that were drawn by using ChemDraw Ultra 12.0, downloaded in the MDL-mol files and were imported into the ligand perspective of LigandScout 4.4.9. Table 4.1 shows the 3D chemical structures of the training sets in the ligand perspective.

Table 4.1: 3D chemical structures of training sets

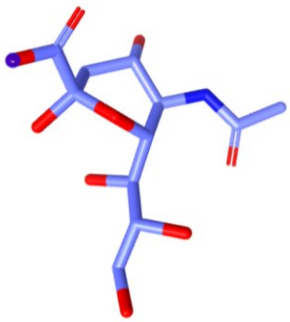
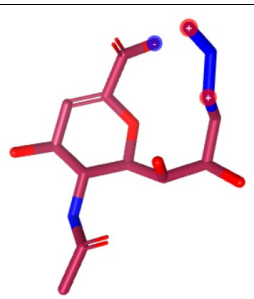
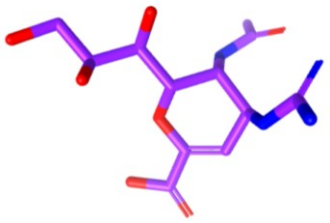
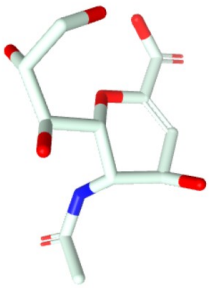
Name of training sets	3D chemical structures
NANA (N-acetyl-alpha-neuraminic acid)	

Table 4.1 continued

9N3Neu5Ac2en (5-acetamido-2,6-anhydro-3,5,9-trideoxy-9-triazan-1-yl-D-glycero-D-galacto-non-2-enonic acid)	
Artocarpin	
Zanamivir	
DANA (2-deoxy-2,3-dehydro-N-acetyl-neuraminic acid)	

Similarly, the 3D chemical structures of test sets drawn by ChemDraw Ultra 12.0 were also imported into the ligand perspective of LigandScout 4.4.9. Table 4.2 shows the 3D chemical structures of test sets to be used to validate the reliability of the generated pharmacophore model.

Table 4.2: 3D chemical structures of test sets for validation of pharmacophore model

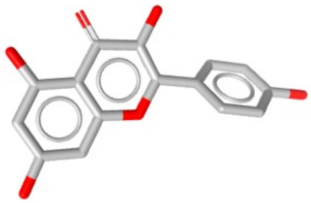
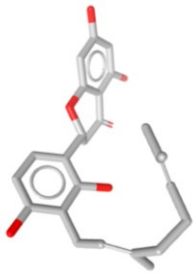
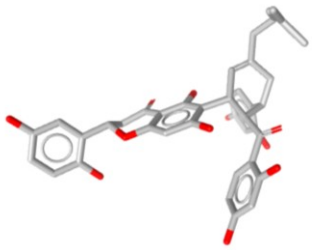
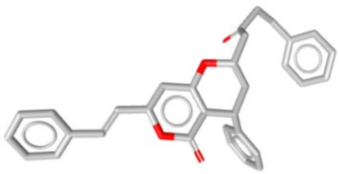
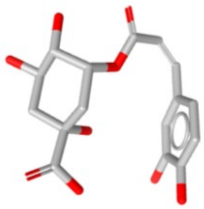
Name of test sets	Chemical structures
Kaempferol	
Sanggenol A	
Sanggenon G	
Katsumadain A	
Chlorogenic acid	

Figure 4.1 shows the generated pharmacophore model by the training sets, which was composed of 10 common pharmacophore features: 5 hydrogen bond donors (HBD) labelled in green and 5 hydrogen bond acceptors labelled in red.

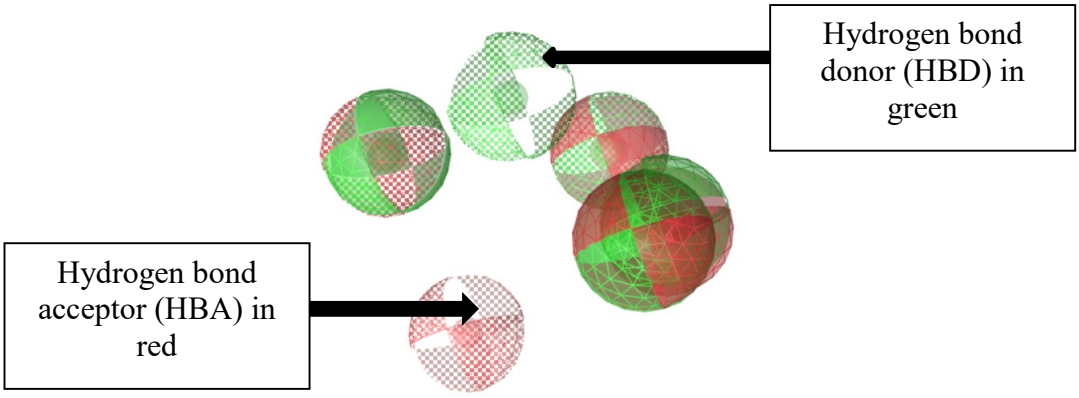


Figure 4.1: Generated pharmacophore model by training sets

The training sets successfully generated a pharmacophore model with high pharmacophore fit values ranging from 74.09 to 98.79 and a great deal of matching features. On top of that, the test sets also successfully depict good fit values ranging from 46.79 to 90.43 in the generated model, such that the fit values test sets, except of katsumadain A, were approximately more than 90% of the fit values shown by training sets. Out of 10 matching features shown by the model, the test sets successfully aligned with 4 to 9 features. showing good matching alignments with the generated model. Thus, the generated model was said to be validated for its reliability as evaluator of Schiff base vanillin derivatives as potential inhibitors of *S. pneumoniae* neuraminidase. Table 4.3 shows the pharmacophore fit values and matching features of training sets and test sets in the generated pharmacophore model.

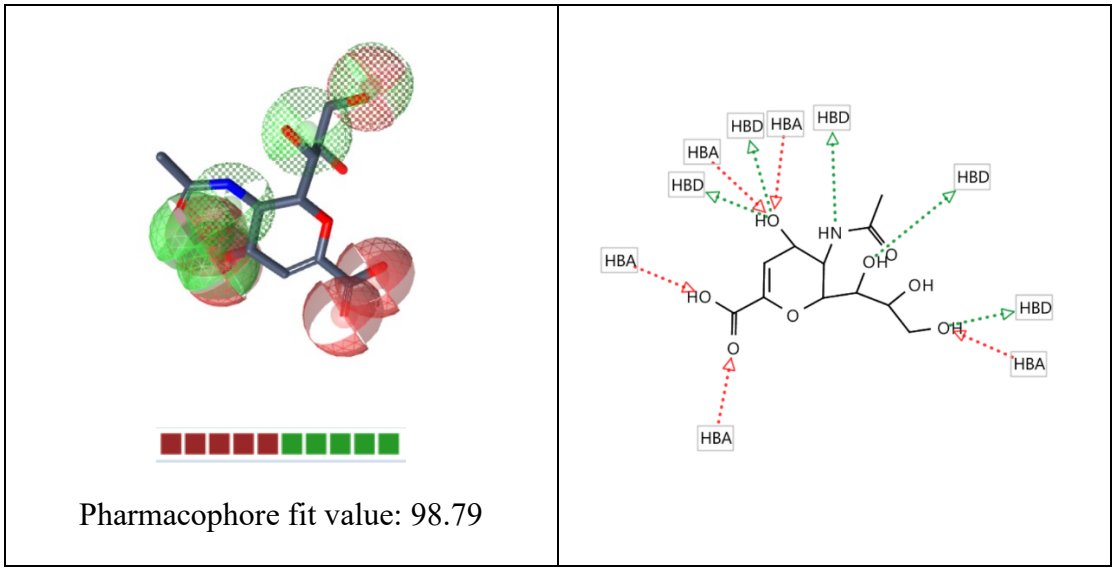
Table 4.3: Pharmacophore fit values and matching features of training sets and test sets in the generated pharmacophore model

Name of chemical compounds	Type of compound	Matching pharmacophore features	Pharmacophore fit values
DANA	Training set		98.79

Table 4.3 continued

NANA	Training set		98.59
Zanamivir	Training set		98.27
9N3Neu5Ac2en	Training set		90.28
Artocarpin	Training set		74.09
Chlorogenic acid	Test set		90.43
Sanggenon G	Test set		82.65
Sanggenol A	Test set		82.28
Kaempferol	Test set		72.02
Katsumadain A	Test set		46.79

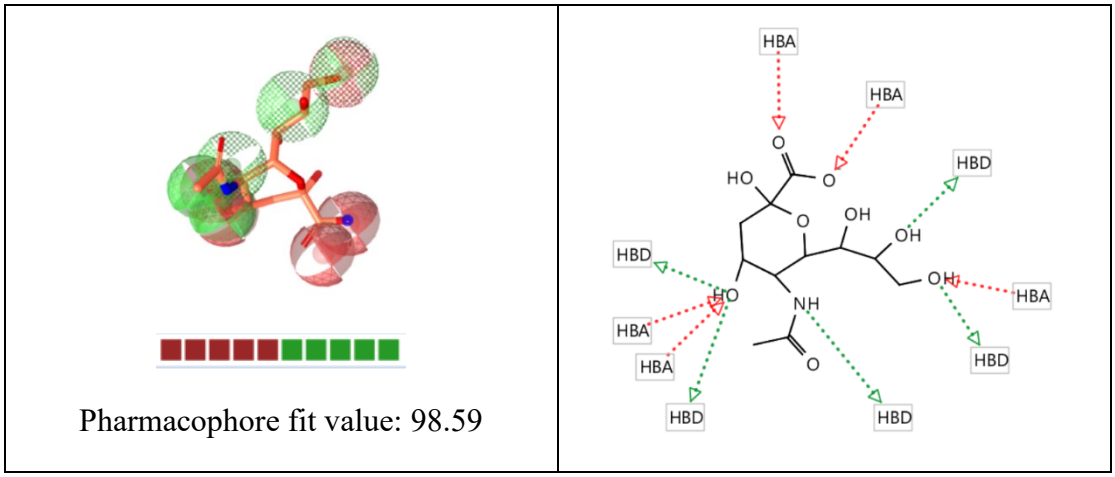
The interactions between training sets and pharmacophore model were illustrated and explained in Figure 4.2 to Figure 4.6. 2-deoxy-2,3-dehydro-N-acetyl-neuraminic acid (DANA) belongs to a type of neuraminic acid or sialic acid which is composed of 9 carbon atoms to form the amino sugar backbone (Blanco and Blanco, 2017). DANA has been reported to be marketed as approved drug compound against both bacterial and viral neuraminidases (Mahal et al., 2021). Most of the pharmacophore features were depicted at the hydroxyl (OH) groups, carbonyl (C=O) group and nitrogen atom (N), with the high pharmacophore fit value of 98.79 and matching feature as shown in Figure 4.2.



Pharmacophore fit value: 98.79

Figure 4.2: Interaction, pharmacophore fit value and matching features of DANA and pharmacophore model

N-acetyl-alpha-neuraminic acid (NANA) is another type of neuraminic acid which depicts similar chemical structure as DANA, therefore showing similar pharmacophore fit value in the generated pharmacophore model. With slight modifications of chemical structure and conformation, the pharmacophore features were also focused on the OH group, C=O group and nitrogen atom, as depicted in Figure 4.3 with fit value of 98.59 and matching features. NANA was reported to portray significant inhibitory activity against neuraminidase of *S. pneumoniae*, thus deposited as ligand in complex with the crystal structure of *S. pneumoniae* neuraminidase, encoded as 3H72 (Hsiao et al., 2009).



Pharmacophore fit value: 98.59

Figure 4.3: Interaction, pharmacophore fit value and matching features of NANA and pharmacophore model

Zanamivir is also another clinically approved drug compound against both viral and bacterial neuraminidases similar to DANA (Blanco and Blanco, 2017). Being a guanido-neuraminic acid which possess similar chemical structures as DANA and NANA, the pharmacophore fit value is also as high as DANA and NANA, with pharmacophore features surrounding OH, C=O and nitrogen atom as well. On top of that, for being a guanidine compound, pharmacophore features are also shown at the amino (NH_2) group, which enhances its pharmacophore fitting result of 98.27 in the pharmacophore model as shown in Figure 4.4.

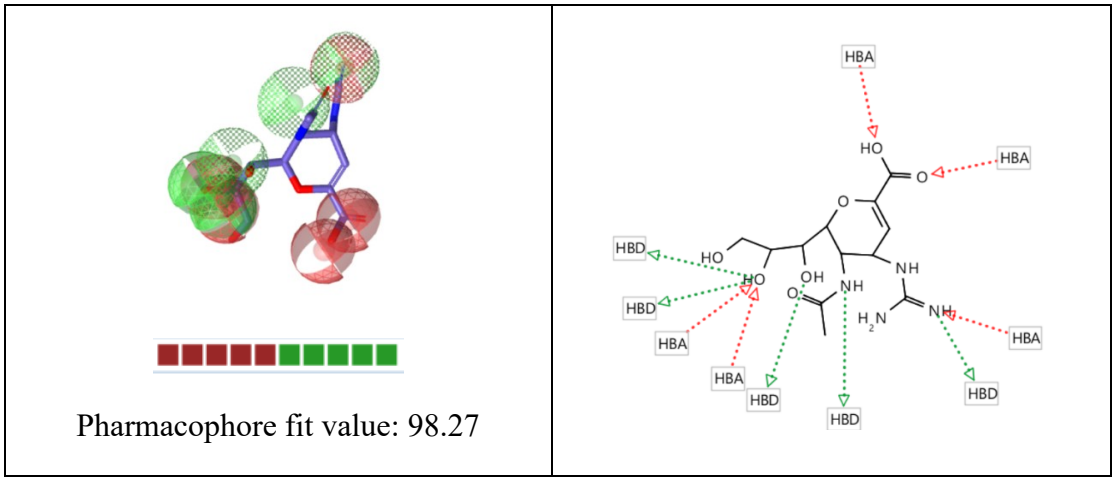
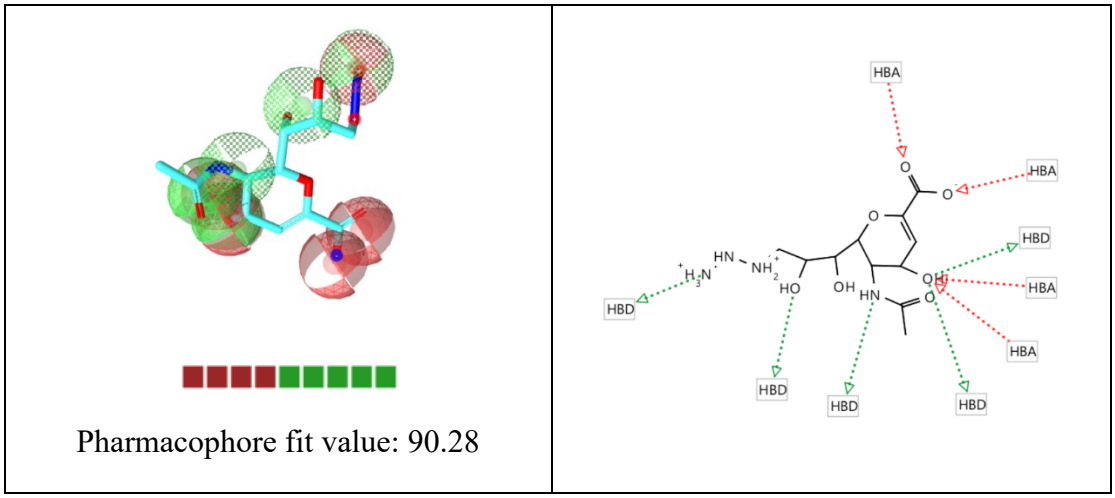


Figure 4.4: Interaction, pharmacophore fit value and matching features of zanamivir and pharmacophore model

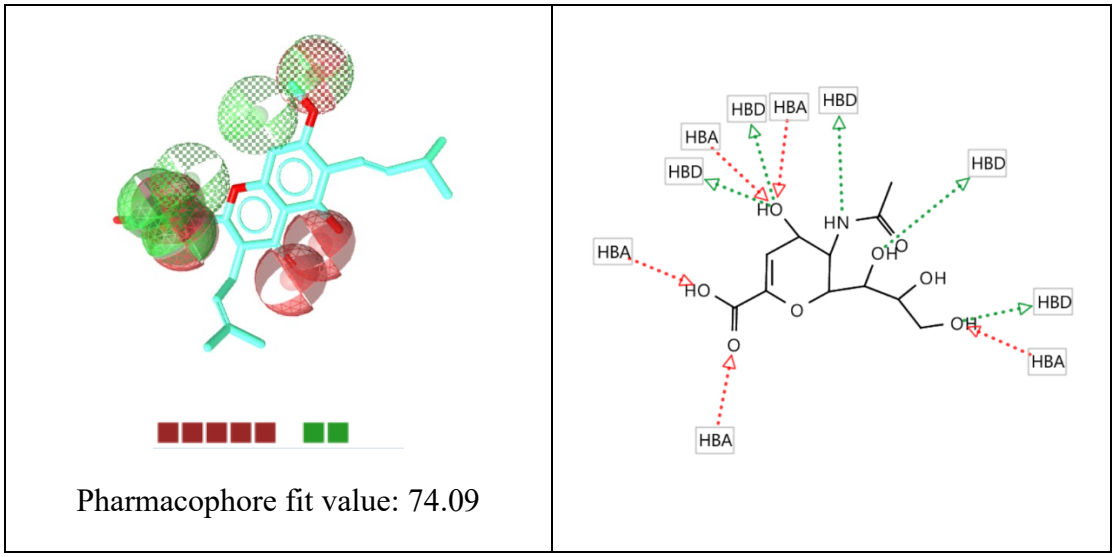
5-acetamido-2,6-anhydro-3,5,9-trideoxy-9-triazan-1-yl-D-glycero-D-galacto-non-2-enonic acid (9N3Neu5Ac2en) is an entry ligand in complex with the PDB structure of crystal structure of *S. pneumoniae* neuraminidase, encoded as 5KKY (Slack and Zhao, 2017). Similarly, as illustrated in Figure 4.5, pharmacophore features were shown by OH, C=O and nitrogen atom due to structural similarity with the previous training sets, but additionally the ammoniumyl ion, NH_3^+.



Pharmacophore fit value: 90.28

Figure 4.5: Interaction, pharmacophore fit value and matching features of 9N3Neu5Ac2en and pharmacophore model

Artocarpin is an isoprenyl flavonoid compound with wide range of biological activity, including anti-neuraminidase activity of *S. pneumoniae* reported by Walther et al. (2017). For having diverse chemical structure as the neuraminic acid analogues, and at the same time reported as strong bacterial neuraminidase inhibitor with strong evidence, it is selected as the training set. Surprisingly, it is still able to show a high pharmacophore fit value of 74.09 to the pharmacophore model despite of its different chemical structure as shown in Figure 4.6, particularly the OH, C=O and the ether (C-O-C) group contributing to the generation of the pharmacophore features of the model. As a result, the generated pharmacophore model possessed stronger reliability due to greater structural diversity of training sets.



Pharmacophore fit value: 74.09

Figure 4.6: Interaction, pharmacophore fit value and matching features of artocarpin and pharmacophore model

A pharmacophore model was said to be validated for its reliability and capability to be tested for potential neuraminidase inhibitors if the test sets successfully depict pharmacophore fit values and matching features approximately more than half or even greater than then training sets. Based on the results obtained, the generated pharmacophore model was successfully validated by the test sets. Figure 4.7 to 4.11 described and explained the matching interactions, matching features and pharmacophore fit values of test sets in the generated pharmacophore model. The pharmacophore fit values and matching features of test sets in the pharmacophore model greatly depends on their functional groups and conformations. During the ligand-based pharmacophore model validation process, a few number of conformations of test sets were generated, whereby the conformations with the best fit value and lowest energy were selected to be evaluated.

Chlorogenic acid was reported for its high inhibitory activity against neuraminidase of both influenza virus and *S. pneumoniae* by molecular simulation (Guan et al., 2020). Being a phenolic acid with alternative name of 5-caffeoylquinic acid formed from caffeic acid and quinic acid, it possessed slight structural similarity to neuraminic acid analogue

(Arauz, Ramos-Tovar and Muriel, 2017). Simultaneously, the chemical structure is composed of great number of OH and C=O groups, thus being able to show high pharmacophore fit value and matching features, which is even greater than two of the training sets as shown in Figure 4.7. This provides strong and significant support to validate the reliability of the model.

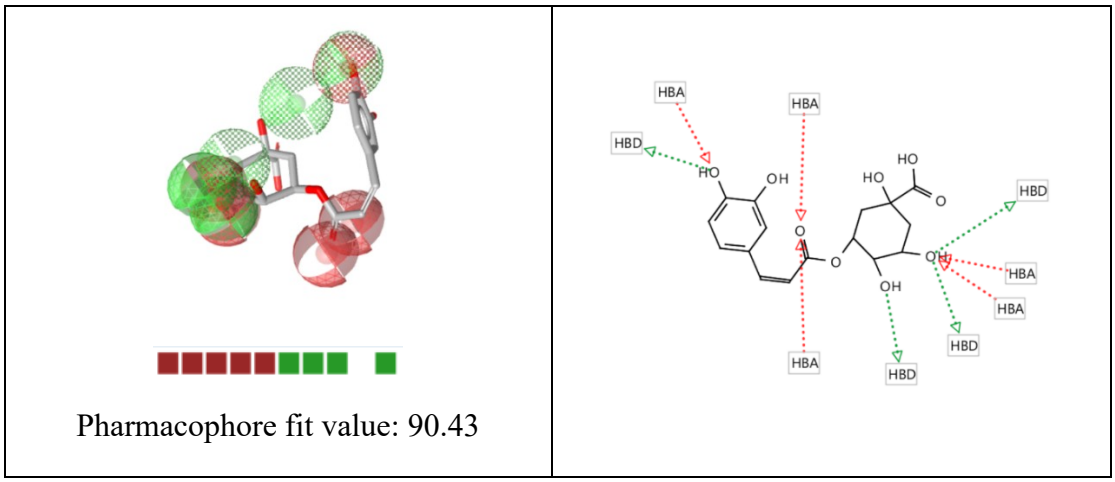


Figure 4.7: Interaction, pharmacophore fit value and matching features of chlorogenic acid and pharmacophore model

Sanggenon G is a flavonoid compound similar to artocarpin training set, particularly a prenylated flavonoid compound extracted from the root bark of mulberry, and was discovered for its inhibitory activity against both influenza and pneumococcal neuraminidase (Grienke et al., 2016). For depicting a significant number of OH and C=O groups, as well as showing suitable conformation in the pharmacophore model, sanggenon G also show good pharmacophore fit value and matching features as shown in Figure 4.8.

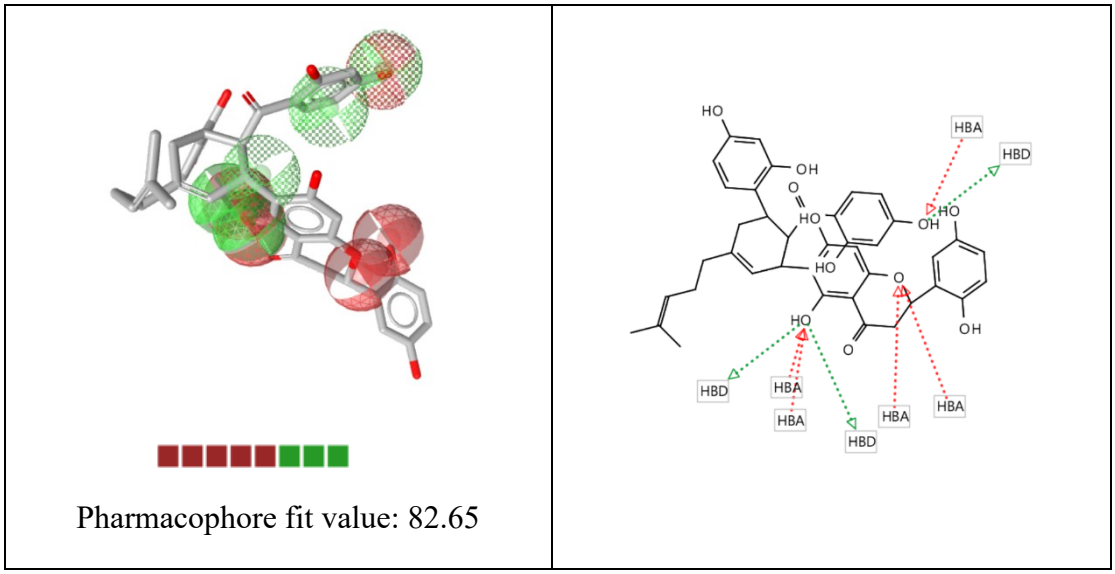
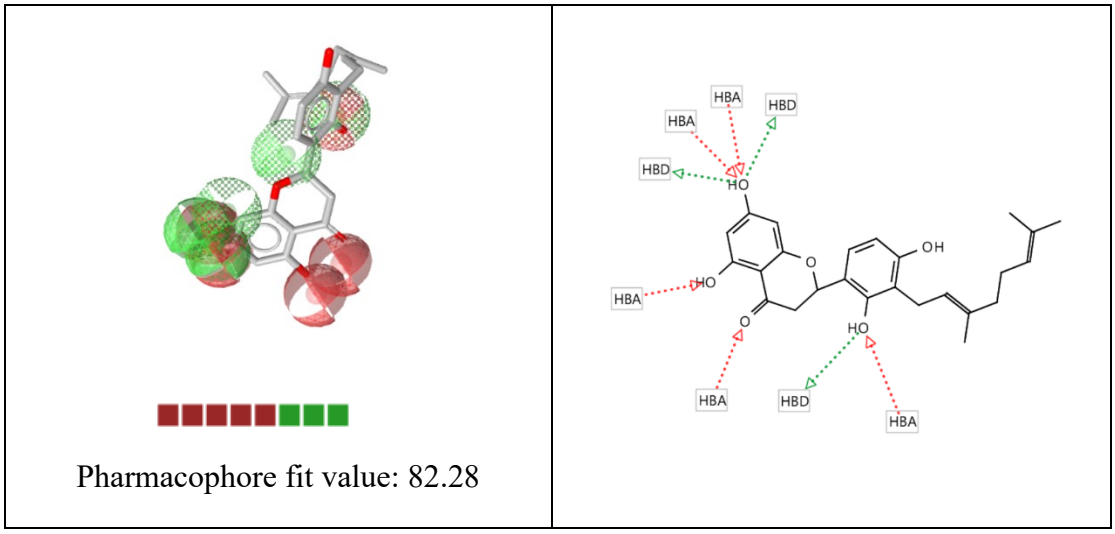


Figure 4.8: Interaction, pharmacophore fit value and matching features of sanggenon G and pharmacophore model

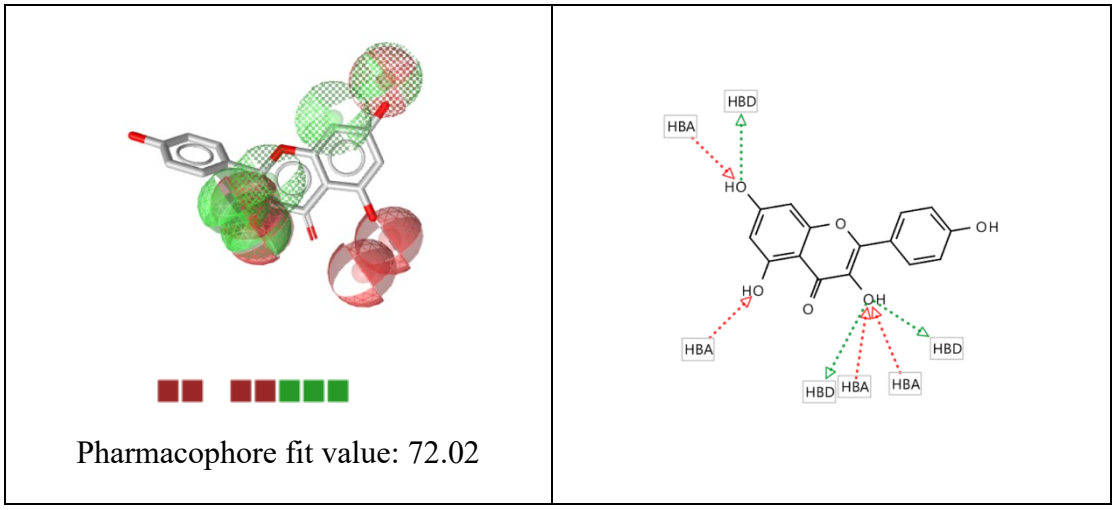
Similar to sanggenon G, sanggenol A is also a flavonoid compound extracted from mulberry root bark and reported for its anti-neuraminidase activity in experimental comparison with the clinically approved oseltamivir inhibitor (Grienke et al., 2016). For possessing strong potential as inhibitors of pneumococcal neuraminidase, the ability of both sanggenol A and sanggenon G to show good fit value in the generated pharmacophore model further strengthen the validation of the dependability of the pharmacophore model. Despite the fact that the molecular size is smaller than sanggenon G, it still depicted similar pharmacophore fit value and same matching interaction as sanggenon G as shown in Figure 4.9, indicating the significance of the backbone of flavonoid compound to evaluate potential inhibitory activity of bacterial neuraminidase.



Pharmacophore fit value: 82.28

Figure 4.9: Interaction, pharmacophore fit value and matching features of sanggenol A and pharmacophore model

Kaempferol is another flavonoid compound derived from many plants which also showed considerable high pharmacophore fit value and 7 out of 10 matching features. It is composed of the flavonoid backbone with mostly OH substituents, thus most of the interactions were shown at the OH groups as illustrated in Figure 4.10. The compound was discovered for its inhibitory mechanism against *S. pneumoniae* (Xu et al., 2023).

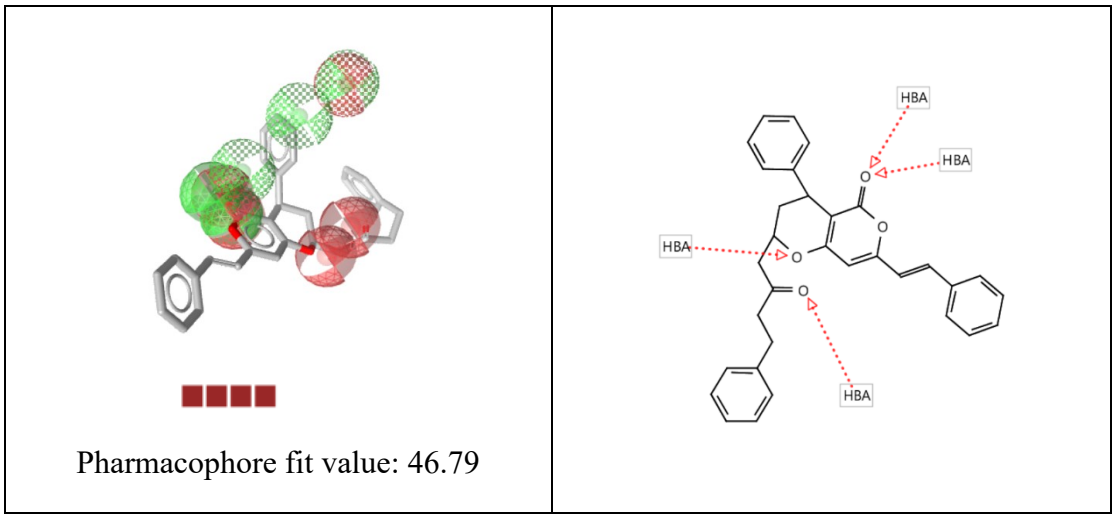


Pharmacophore fit value: 72.02

Figure 4.10: Interaction, pharmacophore fit value and matching features of kaempferol and pharmacophore model

Katsumadain A is a diarylheptanoid compound with completely diverse chemical structure in comparison to all training sets and test sets, which was reported to depict

inhibition against both viral and bacterial neuraminidases through molecular studies (Walther et al., 2014). Despite the low pharmacophore fit value and matching interactions shown, it was still able to show at least 50% of the pharmacophore fit value, with interactions shown at the C=O and C-O-C group based on Figure 4.11.

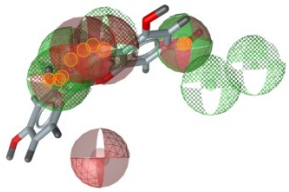
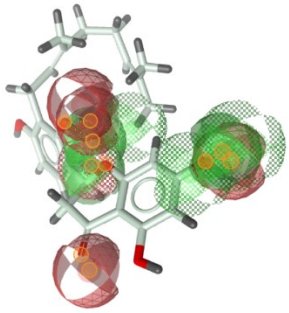
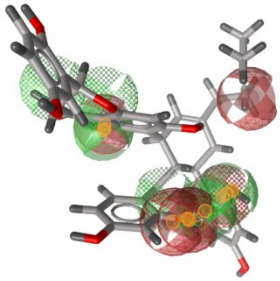
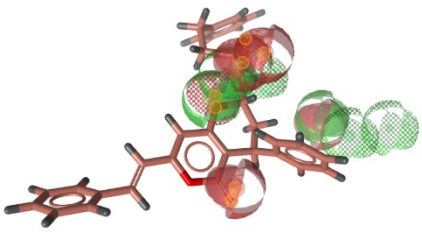
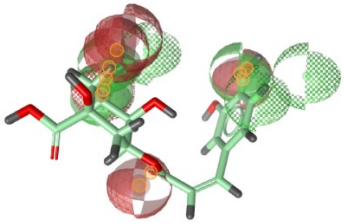


Pharmacophore fit value: 46.79

Figure 4.11: Interaction, pharmacophore fit value and matching features of katsumadain A and pharmacophore model

Based on the RMSD values of the test sets in the pharmacophore model, all test sets were able to show RMSD values less than 1.5 Å. This suggested good agreement between the test sets and the binding poses of the pharmacophore model, thus further supported the reliability of the generated pharmacophore model. The RMSD-based evaluation of test sets alignment to the pharmacophore model was shown in Table 4.4.

Table 4.4: RMSD-based evaluation of test sets alignment to the pharmacophore model

Test sets	Alignment of test sets with pharmacophore model	RMSD values
Kaempferol		0.835
Sanggenol A		1.219
Sanggenon G		0.546
Katsumadain A		1.052
Chlorogenic acid		0.932

Lastly, the calculation of cosine similarities with pharmacophore vector of [5, 5, 0, 0, 0] due to 5 HBA and 5 HBD in the model showed that all 5 test sets were able to show cosine similarity values in between 0 and 1, showing strong similarity with the pharmacophore model. Table 4.5 showed the cosine similarities of test sets and the pharmacophore model.

Table 4.5: Cosine similarities of test sets and the pharmacophore model

Test sets	Vector of test sets	Cosine similarity
Kaempferol	[1, 6, 2, 0, 0]	0.77
Sanggenol A	[2, 3, 2, 1, 0]	0.83
Sanggenon G	[1, 2, 3, 1, 0]	0.55
Katsumadain A	[1, 4, 2, 1, 0]	0.75
Chlorogenic acid	[2, 5, 1, 0, 0]	0.90

As a result, the pharmacophore model was considered validated for its reliability as test sets were able to show good pharmacophore fit values and matching features in the pharmacophore model. In ligand-based pharmacophore modelling. The pharmacophore model was ready to be subjected for analysis and evaluation of the potential inhibitory activity against bacterial neuraminidase of Schiff base vanillin derivatives.

4.1.1.2 Analysis of Schiff Base Vanillin Derivatives Against the Pharmacophore Model

A total of 21 Schiff base vanillin derivatives as depicted in Table 3.3 previously successfully showed 6 to 8 matching features out of 10 pharmacophore features, with pharmacophore fit values ranging from 64.25 to 81.50, thus exhibiting more than 50% of the

pharmacophore fit values of training sets. Table 4.6 shows the 3D chemical structures of the Schiff base vanillin derivatives drawn by using ChemDraw Ultra 12.0, downloaded in the MDL-mol files and imported as test sets in the generated pharmacophore model.

Table 4.6: 3D chemical structures of Schiff base vanillin derivatives

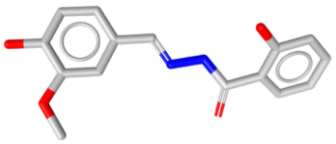
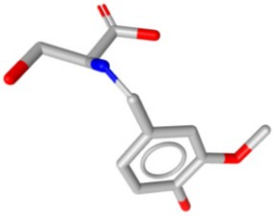
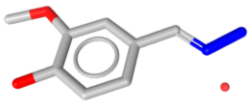
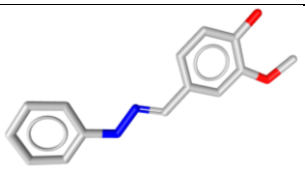
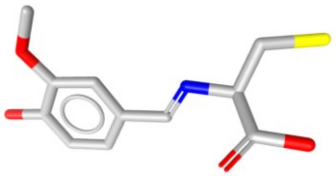
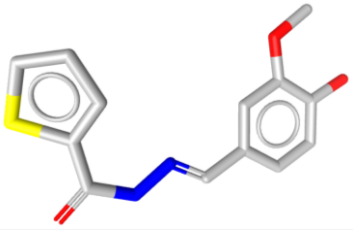
Primary amines	Schiff base vanillin derivatives	Chemical structures
Salicyl hydrazide	**(1)**	
Serine	**(2)**	
Hydrazide hydrate	**(3)**	
Phenylhydrazine	**(4)**	
Cysteine	**(5)**	
2-thiophene carboxylic acid hydrazide	**(6)**	

Table 4.6 continued

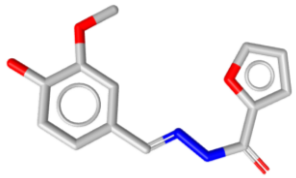
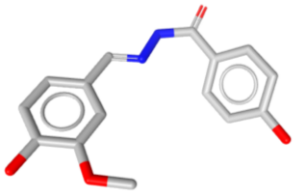
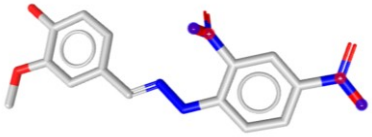
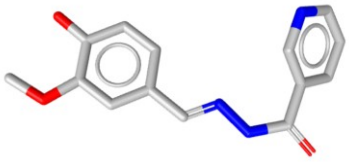
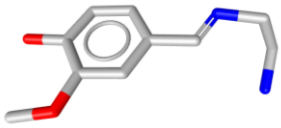
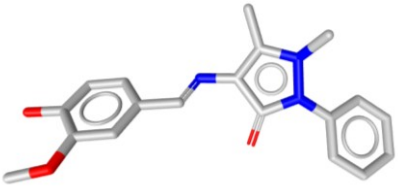
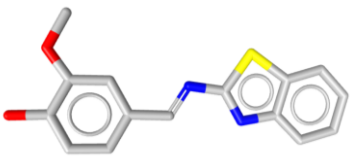
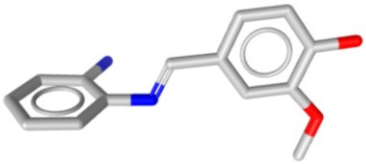
2-furoic acid hydrazide	**(7)**	
4-hydroxybenzhydrazide	**(8)**	
2,4-dinitrophenylhydrazine	**(9)**	
Nicotinic hydrazide	**(10)**	
Ethylenediamine	**(11)**	
4-aminoantipyrine	**(12)**	
2-aminobenzothiazole	**(13)**	
O-phenyldiamine	**(14)**	

Table 4.6 continued

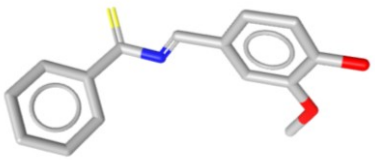
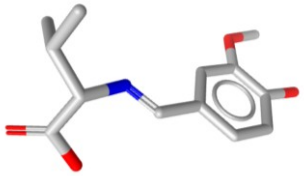
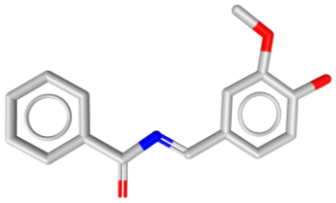
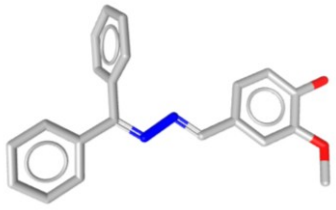
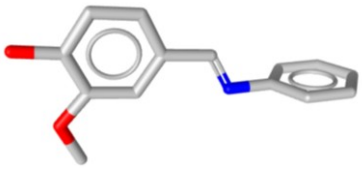
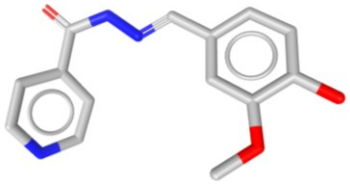
Thiobenzamide	**(15)**	
L-valine	**(16)**	
Sulfamic acid	**(17)**	
Benzamide	**(18)**	
Benzophenone hydrazone	**(19)**	
Aniline	**(20)**	
Isonicotinic acid hydrazide	**(21)**	

Table 4.7 summarises the pharmacophore fit values and matching features shown by the Schiff base vanillin derivatives in the generated pharmacophore model.

Table 4.7: Pharmacophore fit values and matching features of Schiff base vanillin derivatives in the generated pharmacophore model

Schiff base vanillin derivatives (Vanillin + …)	Matching pharmacophore features	Pharmacophore fit values
(1) Salicyl hydrazide		81.50
(2) Serine		81.31
(3) Hydrazide hydrate		74.49
(4) Phenylhydrazine		74.42
(5) Cysteine		74.35
(6) 2-thiophene carboxylic acid hydrazide		74.20
(7) 2-furoic acid hydrazide		74.16
(8) 4-hydroxybenzhydrazide		74.12
(9) 2,4-dinitrophenylhydrazine		73.99
(10) Nicotinic hydrazide		73.29
(11) Ethylenediamine		65.81
(12) 4-aminoantipyrine		64.68
(13) 2-aminobenzothiazole		64.61
(14) O-phenyldiamine		64.61
(15) Thiobenzamide		64.58
(16) L-valine		64.56
(17) Sulfamic acid		64.56
(18) Benzamide		64.56

Table 4.7 continued

(19) Benzophenone hydrazone		64.55
(20) Aniline		64.54
(21) Isonicotinic acid hydrazide		64.25

The pharmacophore fit values and matching features of the Schiff base vanillin derivatives depend on the functional groups, conformations of the chemical structures, and the primary amine structures. Evaluation of the Schiff base vanillin derivatives was done in such a way that high pharmacophore matching values are considered to possess similar bioactivity, which is potential inhibitory activity against neuraminidase of *S. pneumoniae*. For all Schiff base vanillin derivatives, interactions were shown on the OH and C-O-C groups of the vanillin part, indicating the significance of vanillin structure in fitting the model well. This results complement with the literature study of the wide range of biological activities of vanillin, including potential antibacterial activity (Olatunde et al., 2022). Schiff base vanillin derivatives were synthesized by Schiff base synthesis reaction between vanillin and primary amines through formation of C=N imine linkage. It was found out that most of the interactions were shown at the C=N linkage, mostly HBA at the nitrogen atom due to presence of lone pair of electrons being able to accept hydrogen. For the primary amine structures, the functional groups in the structure should be potential HBA and HBD such as OH group, nitrogen atom, sulphur atom etc. to fit in the HBA and HBD features of the model, as well as possessing suitable conformation. ‘

As a whole, the matching features and fit values of the Schiff base vanillin derivatives in the generated pharmacophore model were as shown from Figure 4.12 to 4.32. Based on Figure 4.12, the OH group of the salicyl hydrazide was shown to fit in 2 HBA and 2 HBD

of the model, whereas the nitrogen atom fitted 1 HBD of the model. Together with 1 HBA and 1 HBD shown on the OH group of vanillin, as well as HBA on the nitrogen atom of C=N bond, compound (1) shows pharmacophore fit value even higher than a few training sets, with 8 out of 10 matching features. As a result, compound (1) showed potential antibacterial activity against neuraminidase of *S. pneumoniae*, which has to be further analyzed in structure-based approach.

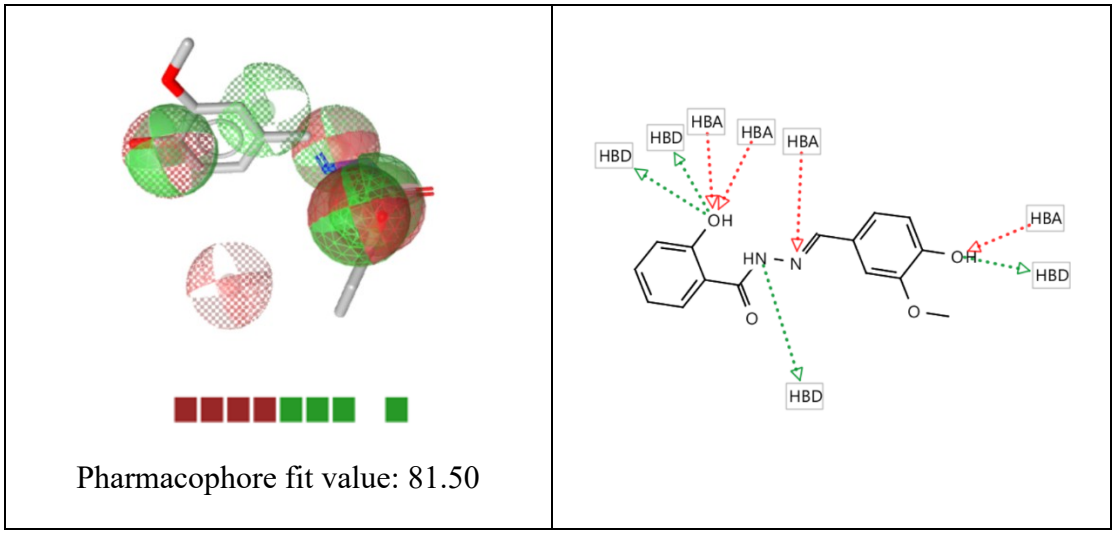


Figure 4.12: Interaction, pharmacophore fit value and matching features of compound (1) and pharmacophore model

Out of all pharmacophore interactions, 2 HBA and 2 HBD were reported to be fitted by OH group of serine. In addition to 1 HBA and 1 HBD depicted on the OH group of vanillin, HBA on the C-O-C group of vanillin, as well as HBA on nitrogen atom of C=N bond, compound (2) also successfully show good pharmacophore fit value of 81.31, also greater than the fit values of a few training sets as shown in Figure 4.13.

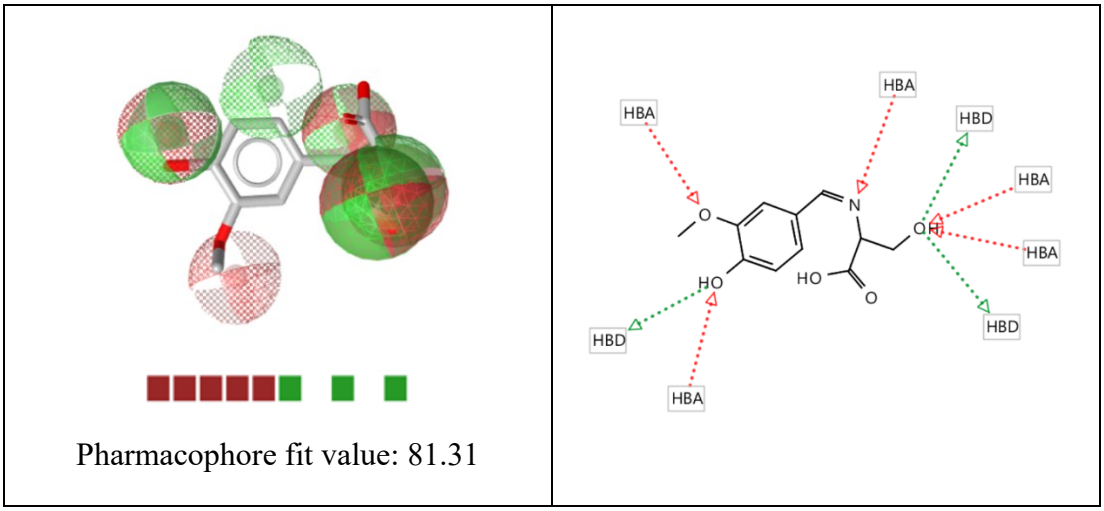


Figure 4.13: Interaction, pharmacophore fit value and matching features of compound (2) and pharmacophore model

By referring to Figure 4.14, the water molecule of hydrazide hydrate shows matching interactions towards 2 HBA and 2 HBD. Additionally, 1 HBA and 1 HBD was shown on OH of vanillin, as well as another HBA on nitrogen atom of C=N bond. By fitting in 7 out of 10 matching features of the pharmacophore model, compound (3) exhibited appreciable fit value of 74.49.

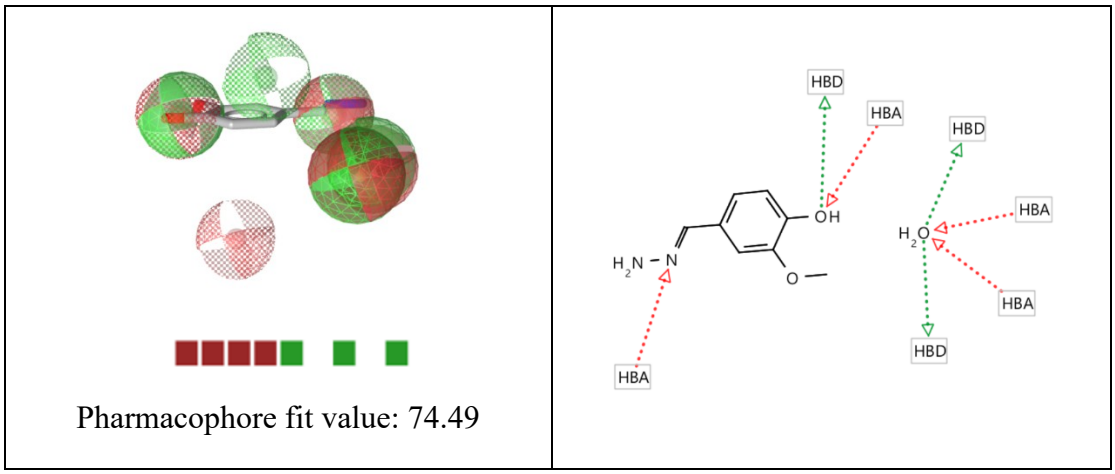


Figure 4.14: Interaction, pharmacophore fit value and matching features of compound (3) and pharmacophore model

As for compound (4), 1 HBD was shown in the nitrogen atom of the phenylhydrazine. Most of the HBA and HBD interactions were shown on the OH group, as

well as 1 HBA on the C-O-C group of vanillin structure. Similar to the previous compounds, HBA was depicted on the nitrogen atom of C=N bond. In a nutshell, compound (4) shows considerably satisfying pharmacophore fit value of 74.42 illustrated in Figure 4.15, being potential neuraminidase inhibitor of *S. pneumoniae*, thus to be further analysed in the structure-based approach.

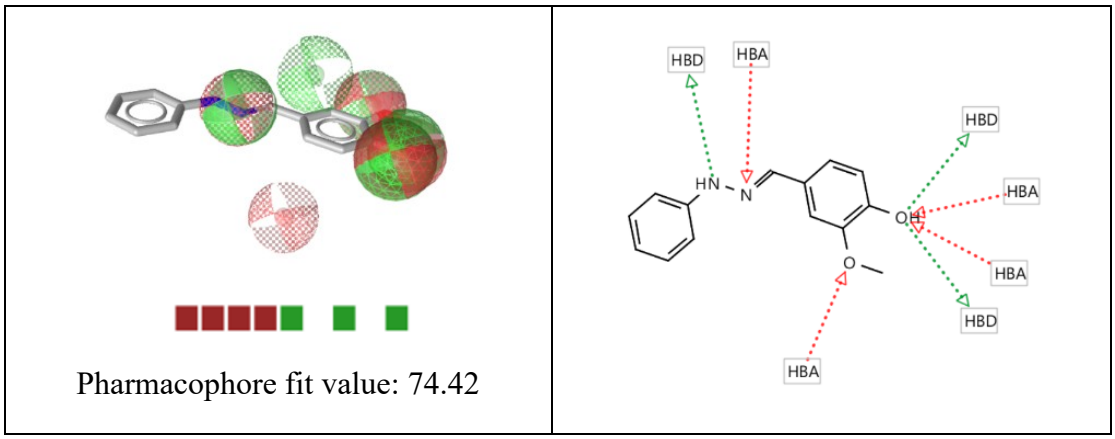
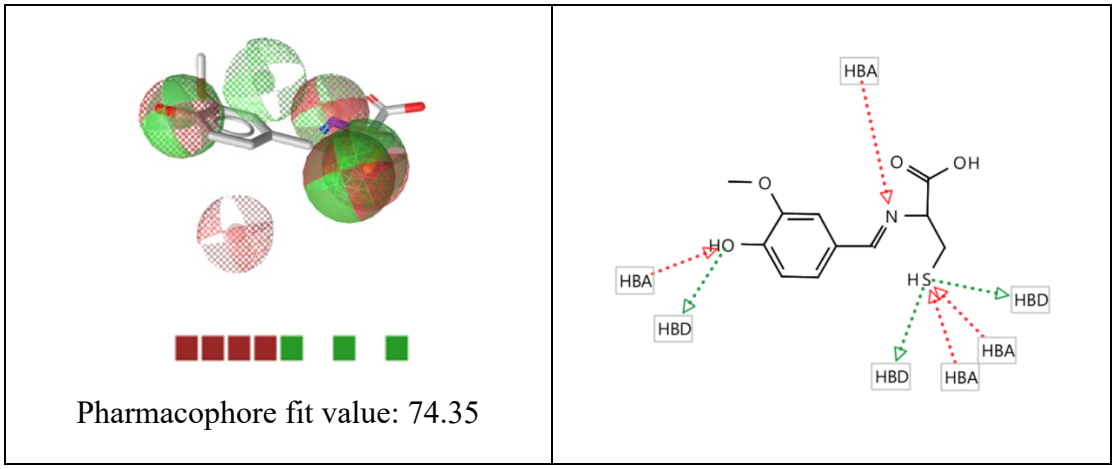


Figure 4.15: Interaction, pharmacophore fit value and matching features of compound (4) and pharmacophore model

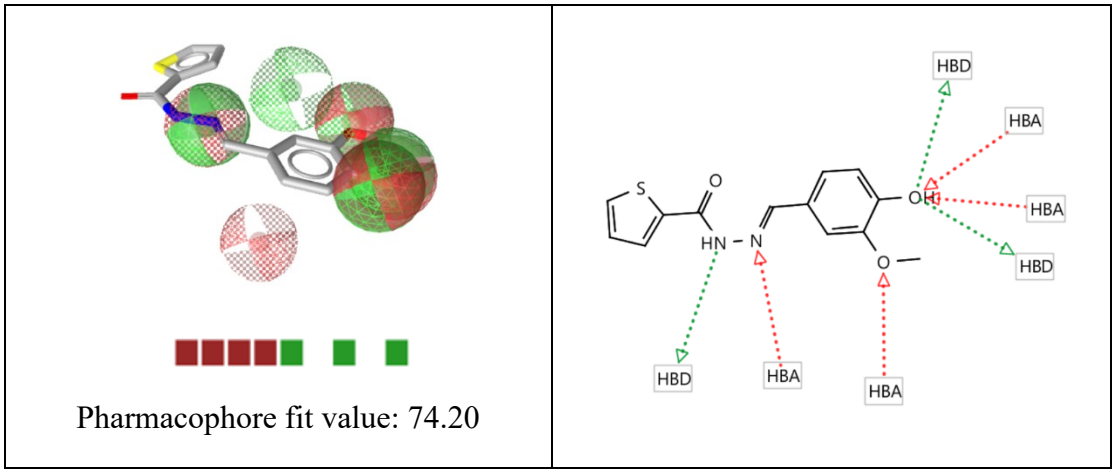
Being an amino acid with a thiol side chain, Schiff base vanillin derivative of cysteine is able to depict 7 out of 10 pharmacophore features with 74.35 fit value as shown in Figure 4.16. The main reason is due to presence of thiol group which serves as very good HBA and HBD similar to OH. Together with 1 HBA and 1 HBD fitted by OH of vanillin, and HBA fitted by nitrogen atom of C=N bond, compound (5) possessed promising potential to show inhibitory activity against *S. pneumoniae* neuraminidase.



Pharmacophore fit value: 74.35

Figure 4.16: Interaction, pharmacophore fit value and matching features of compound (5) and pharmacophore model

Based on Figure 4.17, 1 HBD was depicted on the nitrogen atom of 2-thiophene carboxylic acid hydrazide. Furthermore, most of the interactions were shown on the OH group of vanillin, which is a total of 2 HBA and 2 HBD. Together with the HBA on C-O-C of vanillin structure and HBA on the nitrogen atom of C=N bond, compound (6) was able to show good fitting value of 74.20 in the model.



Pharmacophore fit value: 74.20

Figure 4.17: Interaction, pharmacophore fit value and matching features of compound (6) and pharmacophore model

Similar to compound (6), Schiff base vanillin derivatives of 2-furoic acid hydrazide matched with 7 out of 10 pharmacophore features, with a fit value of 74.16. This is due to matching features of 1 HBD on the nitrogen atom of 2-furoic acid hydrazide, 2 HBA and 2

HBD on the OH of vanillin structure, HBA on the C-O-C group as well as HBA on the nitrogen atom of C=N bond, as illustrated in Figure 4.18.

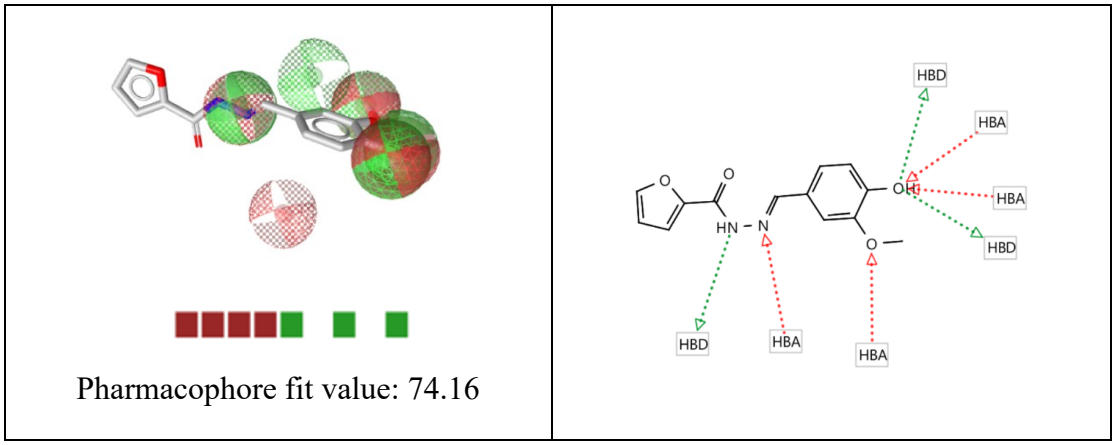


Figure 4.18: Interaction, pharmacophore fit value and matching features of compound (7) and pharmacophore model

For compound (8), most interactions were seen on the amide bond of the primary amine, which is 4-hydroxybenzhydrazide. 2 HBD were shown on the nitrogen atom, and 1 HBA was shown on the C=O of the amide bond, as well as 1 HBA and 1 HBD on the OH of the primary amine. Additionally, 2 HBA were shown on the nitrogen atom of C=N bond. As a result, compound (8) showed a considerably good pharmacophore fit value, which is 74.12 as depicted in Figure 4.19.

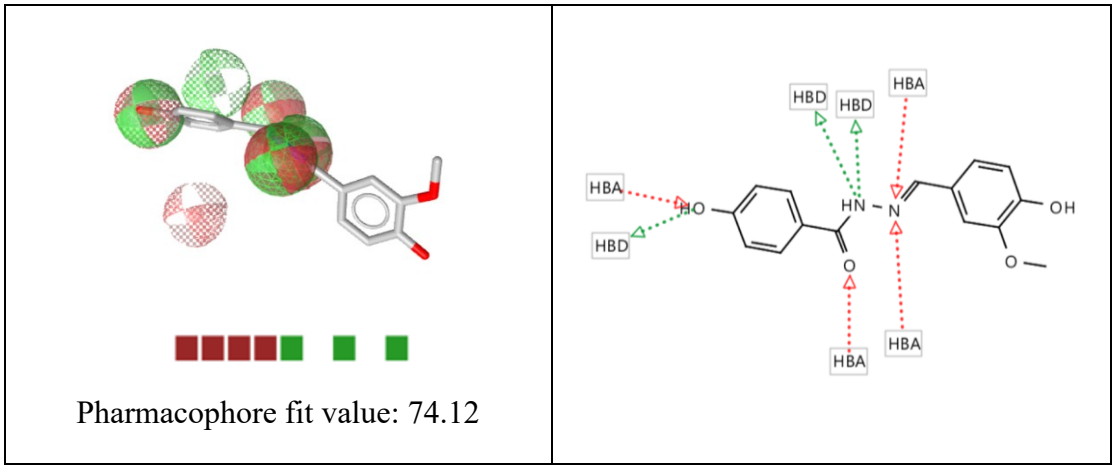


Figure 4.19: Interaction, pharmacophore fit value and matching features of compound (8) and pharmacophore model

As for compound (9), the nitro group (NO_2) and nitrogen atom of 2,4-dinitrophenylhydrazine showed good fitting in HBA and HBD of the pharmacophore model respectively. Similarly, 1 HBA and 1 HBD were depicted on the OH of vanillin structure, and 2 HBA were depicted on the nitrogen atom of C=N bond. As a whole, compound (9) showed a good pharmacophore fit value of 73.99 as illustrated in Figure 4.20.

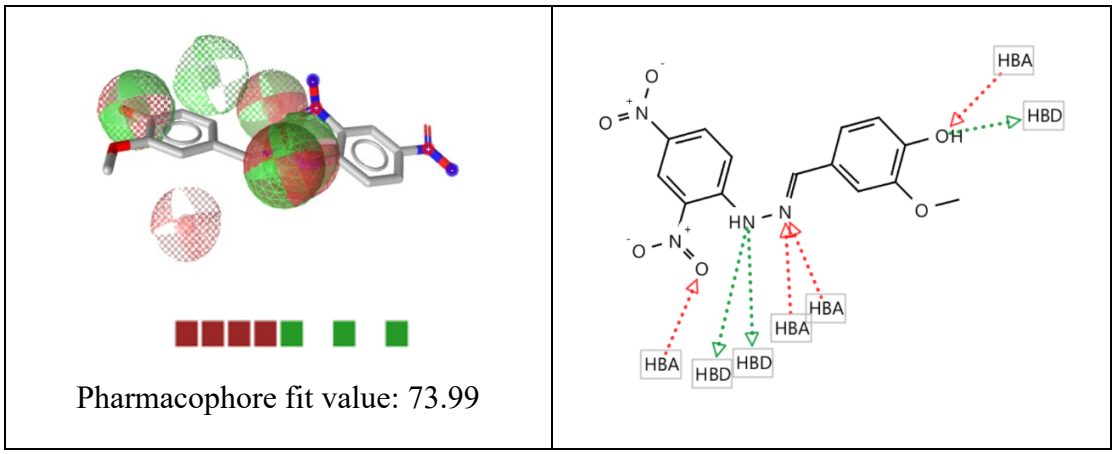
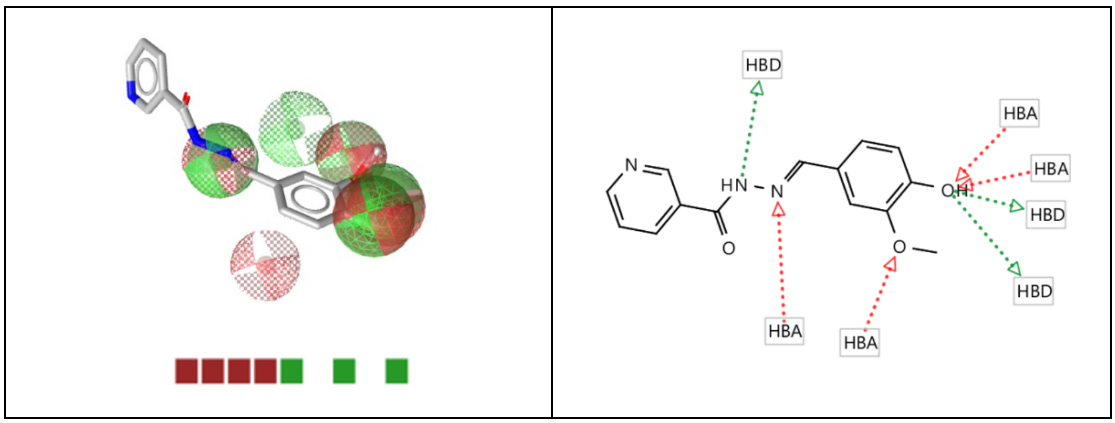


Figure 4.20: Interaction, pharmacophore fit value and matching features of compound (9) and pharmacophore model

Compound (10) was able to show a pharmacophore fit value of 73.29 and 7 out of 10 matching features in the generated pharmacophore model based on Figure 4.21. Based on the illustration, 1 HBD was shown on the nitrogen atom of nicotinic hydrazide. Moreover, 2 HBA and 2 HBD were fitted on the OH of vanillin structure, and 1 HBA was shown on the C-O-C of vanillin structure.1 HBA was also shown on the nitrogen atom of C=N bond.



Pharmacophore fit value: 73.29	

Figure 4.21: Interaction, pharmacophore fit value and matching features of compound (10) and pharmacophore model

Based on Figure 4.22, compound (11) showed 6 out of 10 matching features in the generated pharmacophore model, which include 1 HBD on the amino group of ethylenediamine, 2 HBA and 2 HBD on the OH of vanillin part, and 1 HBA on the C-O-C of the vanillin part as well. Thus, the compound portrayed a pharmacophore fit value of 65.81.

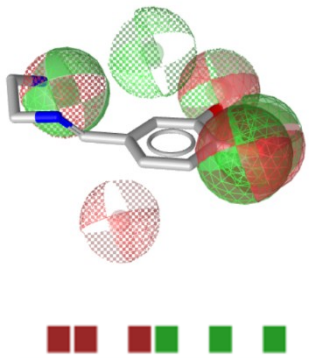
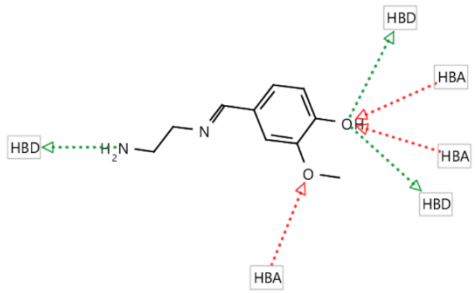
 Pharmacophore fit value: 65.81	

Figure 4.22: Interaction, pharmacophore fit value and matching features of compound (11) and pharmacophore model

Beginning from compound (12) to (20), interactions were only depicted on the OH of vanillin structure, C-O-C of the vanillin structure, and nitrogen atom of the C=N bond. 2 HBA and 2 HBD were shown on the OH of vanillin, 1 HBA was shown on the C-O-C of vanillin, and 1 HBA was shown on the nitrogen of C=N bond. Therefore, the pharmacophore fit values of compound (12) to (20) were very near to each other. Matching interactions were not depicted on the primary amines part, which can be due to the lack of suitable functional groups to fit in the model, or the lack of proper molecular orientations to show the best fit value with the lowest possible energy. Despite that, compound (12) to (20) were still able to

show good pharmacophore fit values more than 50% of the fit values of the training sets. Based on Figure 4.23, compound (12) derived from 4-aminoantipyrine showed a fit value of 64.68.

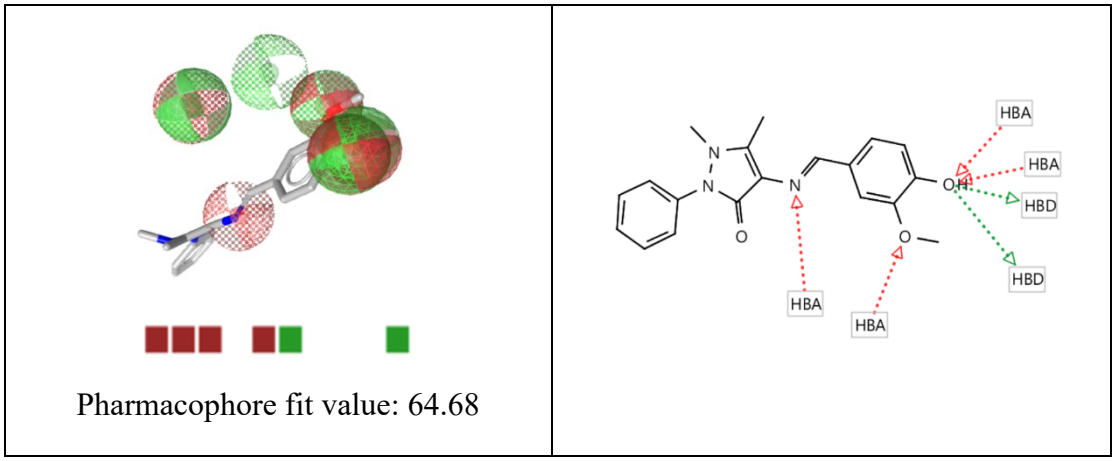


Figure 4.23: Interaction, pharmacophore fit value and matching features of compound (12) and pharmacophore model

For compound (13) derived from 2-aminobenzothiazole, a pharmacophore fit value of 64.61 was depicted as shown in Figure 4.24.

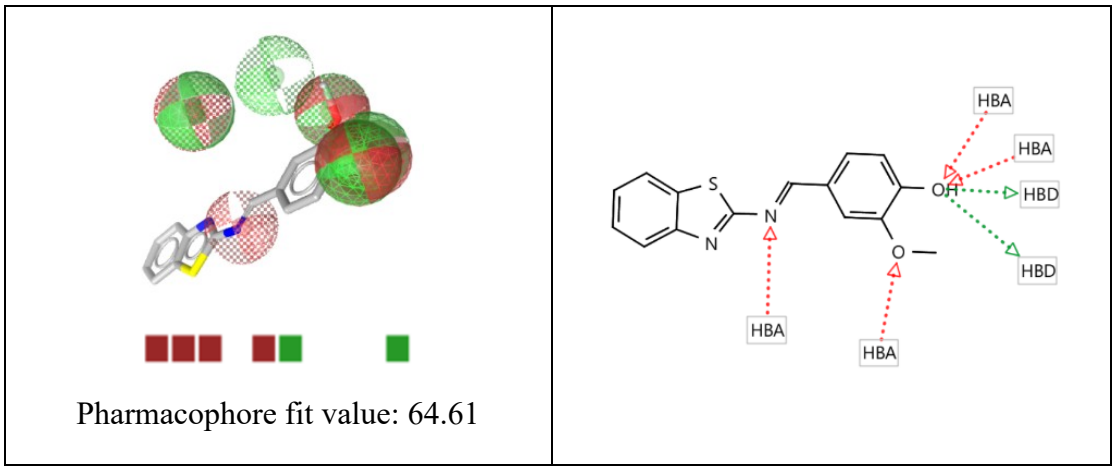
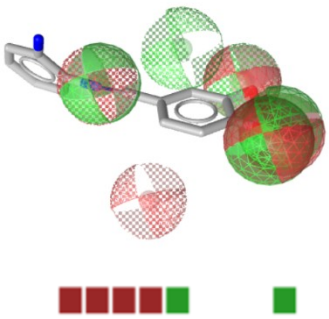


Figure 4.24: Interaction, pharmacophore fit value and matching features of compound (13) and pharmacophore model

The Schiff base vanillin derivative of O-phenyldiamine, which is compound (14) was able to show the same pharmacophore fit value as compound (13) in the generated model, which was 64.61 as well as shown in Figure 4.25.



Pharmacophore fit value: 64.61

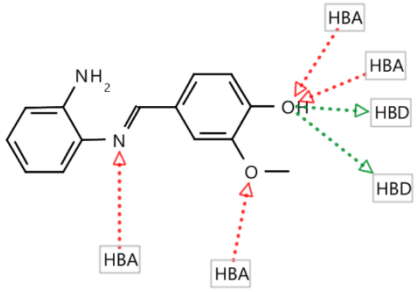
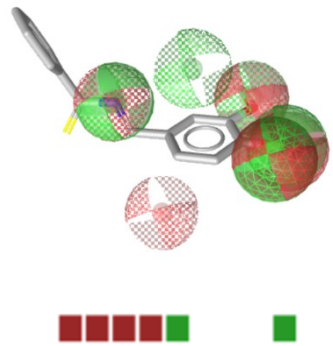


Figure 4.25: Interaction, pharmacophore fit value and matching features of compound (14) and pharmacophore model

Compound (15) derived from thiobenzamide showed a pharmacophore fit value of 64.58 in the model, showing similar matching features as the previous compounds as depicted in Figure 4.26.



Pharmacophore fit value: 64.58

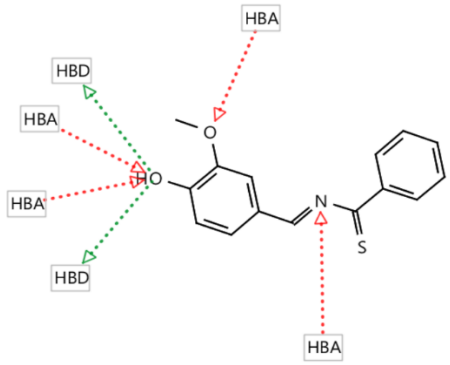
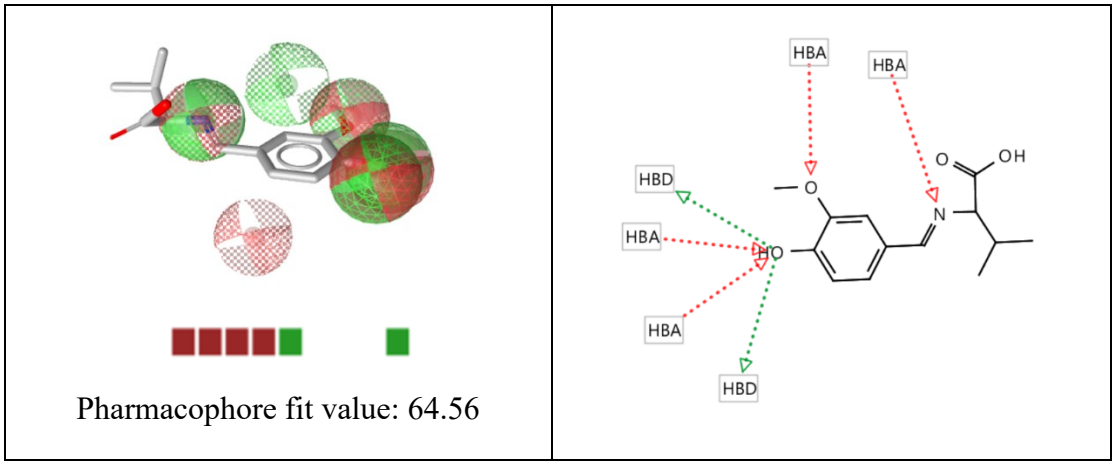


Figure 4.26: Interaction, pharmacophore fit value and matching features of compound (15) and pharmacophore model

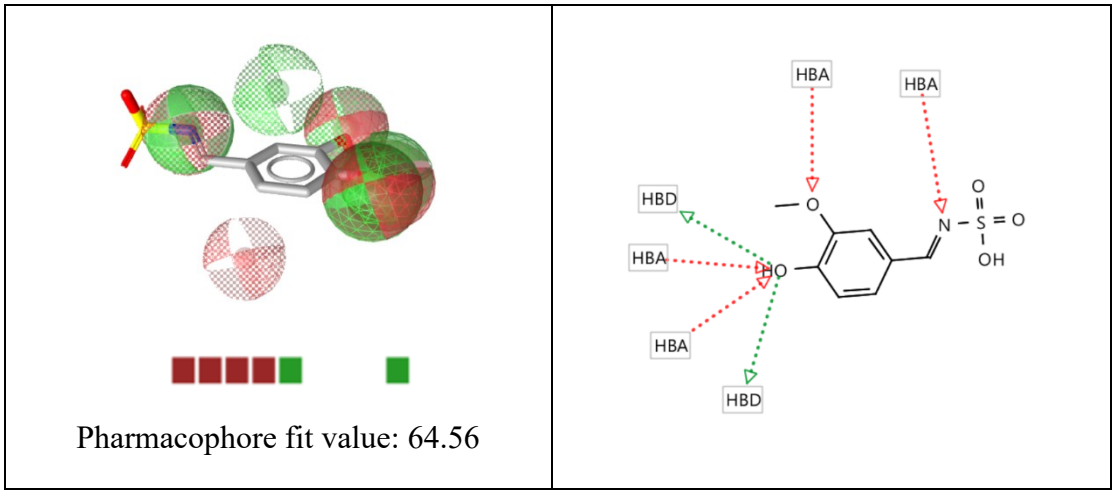
Schiff base vanillin derivative of L-valine, giving compound (16), exhibited a pharmacophore fit value of 64.56 as illustrated in Figure 4.27.



Pharmacophore fit value: 64.56

Figure 4.27: Interaction, pharmacophore fit value and matching features of compound (16) and pharmacophore model

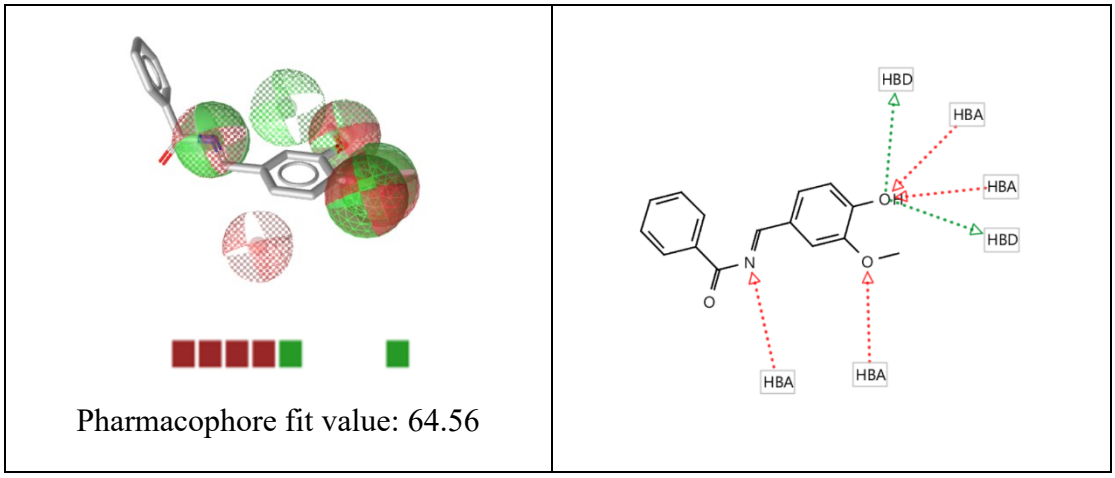
Compound (17) was able to fit in the model as well with the same pharmacophore fit value as compound (16), which was 64.56 as shown in Figure 4.28. Despite interactions were not found on the sulfamic acid, compound (17) was still able to show considerably high pharmacophore fit value and matching features.



Pharmacophore fit value: 64.56

Figure 4.28: Interaction, pharmacophore fit value and matching features of compound (17) and pharmacophore model

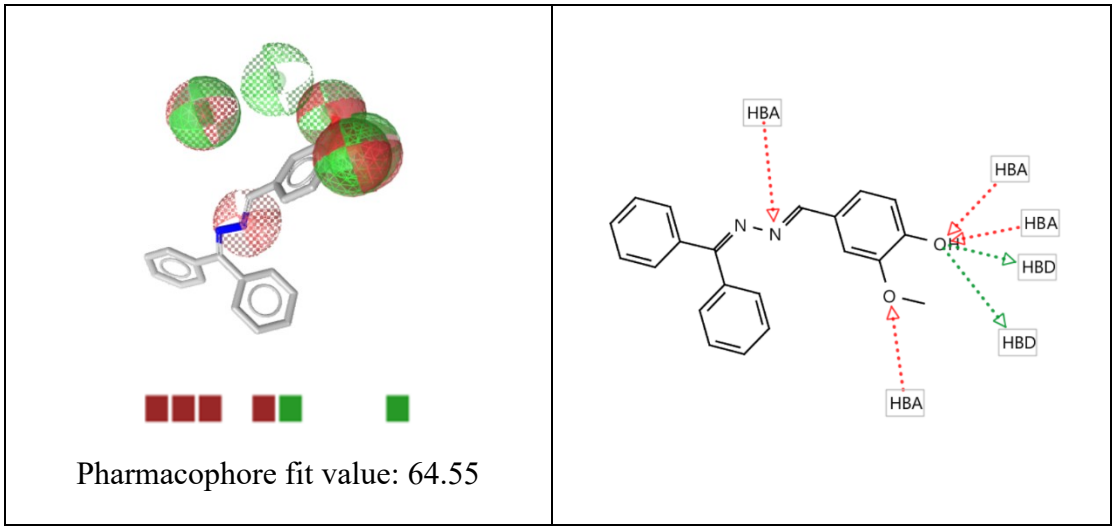
Compound (18), which was a Schiff base vanillin derivative derived from benzamide, also showed the same pharmacophore fit value as compound (16) and (17), which was 64.56 as delivered in Figure 4.29.



Pharmacophore fit value: 64.56

Figure 4.29: Interaction, pharmacophore fit value and matching features of compound (18) and pharmacophore model

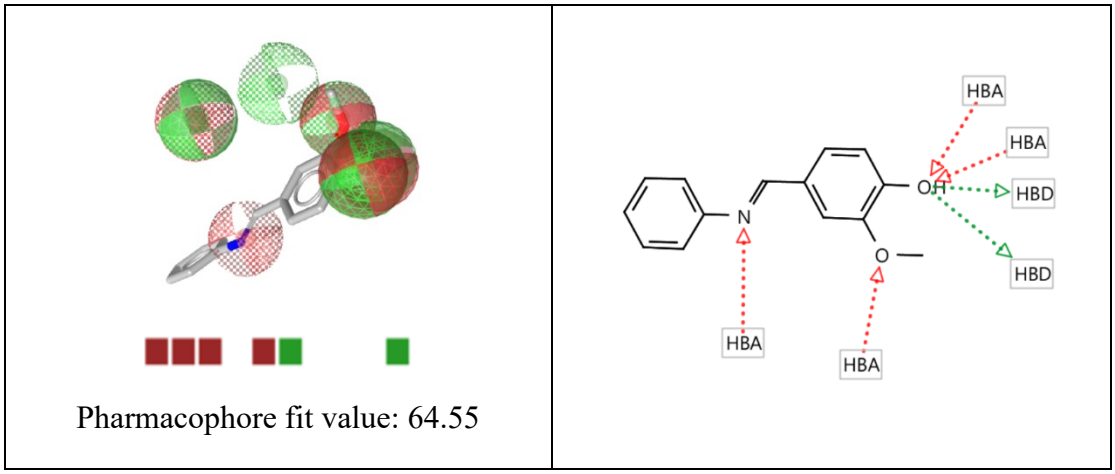
Similarly, based on Figure 4.28, a pharmacophore fit value of 64.55 and 6 out of 10 matching features were shown by compound (19), a Schiff base vanillin derivative synthesised from benzophenone hydrazone.



Pharmacophore fit value: 64.55

Figure 4.30: Interaction, pharmacophore fit value and matching features of compound (19) and pharmacophore model

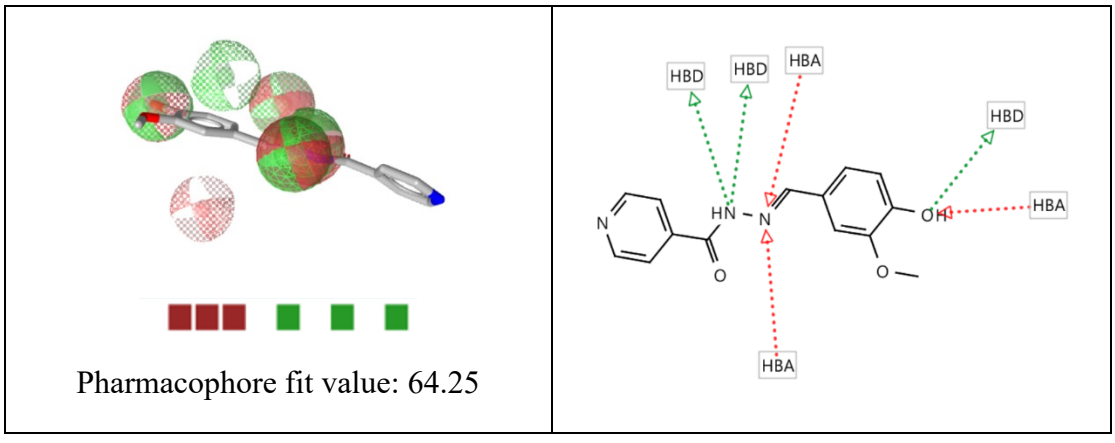
Moreover, compound (20) derived from aniline also portrayed similar pharmacophore fit value, which was 64.55, as well as 6 matching features in the model as depicted in Figure 4.31.



Pharmacophore fit value: 64.55

Figure 4.31: Interaction, pharmacophore fit value and matching features of compound (20) and pharmacophore model

Last but not least, compound (21) was able to fit in the model with the lowest pharmacophore fit value, which was 64.25 as well as 6 matching pharmacophore features as illustrated in Figure 4.32. Despite showing the lowest fit value, some of the matching pharmacophore features were shown on the primary amine part, which was isonicotinic acid hydrazide, specifically 2 HBD on the amide bond. Additionally, 1 HBA and 1 HBD were found on the OH of vanillin, and 2 HBA were shown on the nitrogen atom of C=N.



Pharmacophore fit value: 64.25

Figure 4.32: Interaction, pharmacophore fit value and matching features of compound (21) and pharmacophore model

In conclusion to the results obtained from the ligand-based approach, all 21 Schiff base vanillin derivatives were able to fit in the pharmacophore model and depicted satisfying

pharmacophore fit values and matching pharmacophore features. Most essentially, pharmacophore features were depicted in the OH group and C-O-C group of vanillin structure, as well as nitrogen atom of C=N bond of all 21 Schiff base vanillin derivatives, thus proving the promising potential of vanillin structure and Schiff base imine bond as neuraminidase inhibitors of *S. pneumoniae*. Schiff base vanillin derivatives had been previously reported for their excellent inhibitory activity against other bacterial strains including *S. aureus* and *E. coli* due to the presence of C=N bond and vanillin chemical structure (Hissam et al., 2024). This may explain the great potential of Schiff base vanillin derivatives as *S. pneumoniae* neuraminidase, thus showing good results in ligand-based approach and to be further evaluated in the structure-based approach.

4.1.2 Structure-Based Approach

As mentioned earlier, all 21 Schiff base vanillin derivatives were subjected to structure-based approach for further evaluation upon satisfactory results in ligand-based pharmacophore modelling. Evaluations in structure-based approach were divided into two parts, which were structure-based pharmacophore modelling and structure-based molecular docking.

4.1.2.1 Structure-Based Pharmacophore Modelling

Based on the crystal structure of *S. pneumoniae* neuraminidase A, NanA (TIGR4) in complex with oseltamivir carboxylate, encoded as 2YA8 in PDB, the pharmacophore model of the oseltamivir carboxylate ligand in the active site of 2YA8 was generated. The model was composed of 19 pharmacophore features towards their respective active sites, which were 8 HBA towards HOH2499, HOH2044, HOH2500, ARG648, ARG706 and ARG332, 2 HBD towards HOH2312 and ASP357, 1 positive ionisable area (PI) towards ASP402, 3

negative ionisable area (NI) towards ARG648, ARG706 and ARG332, as well as 5 hydrophobic interactions (HI) towards PHE428, LEU583, PHE550, TYR575 and ILE427 as depicted in Figure 4.33. Evaluations were done based on the alignment of MDL-sdf files of Schiff base vanillin derivatives with the oseltamivir carboxylate ligand, as well as the pharmacophore fitting of Schiff base vanillin derivatives in the pharmacophore model of the ligand, in addition to their interactions towards the active sites of 2YA8, thus analysing their potential inhibitory activity against neuraminidase of *S. pneumoniae*.

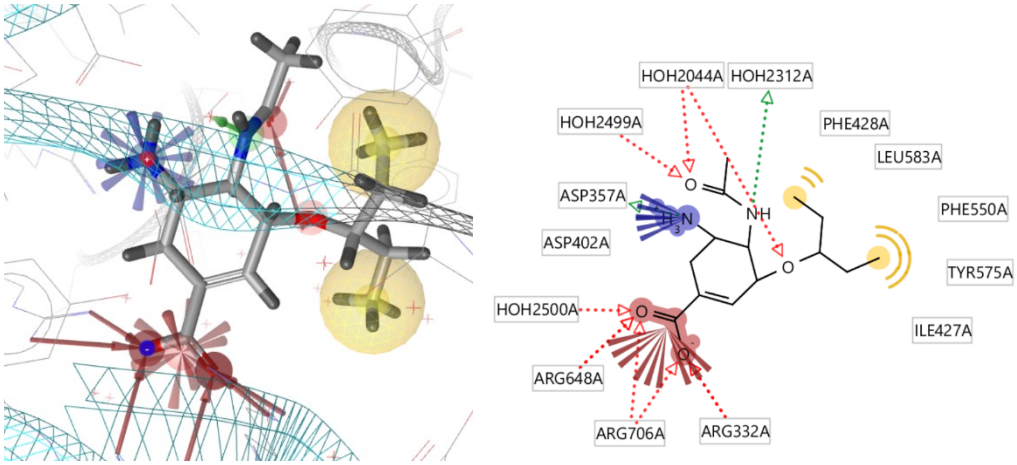
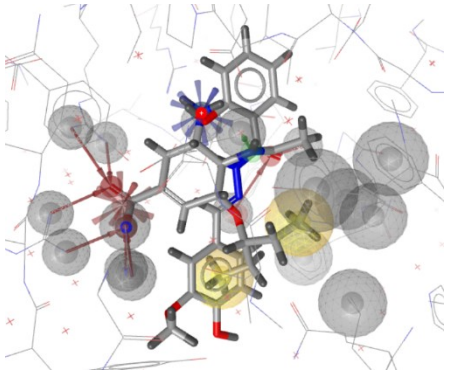


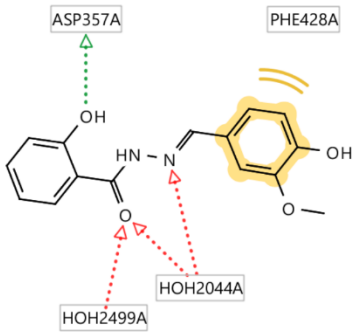
Figure 4.33: Pharmacophore model of oseltamivir carboxylate ligand in 2YA8

Based on the results obtained, 20 out of 21 MDL-sdf files of Schiff base vanillin derivatives were able show good alignment with the oseltamivir carboxylate ligand, thus depicted good pharmacophore interactions towards the important binding sites of 2YA8 as well as promising potential against the neuraminidase structure. The alignment and interactions of Schiff base vanillin derivatives with the oseltamivir carboxylate ligand and the pharmacophore model in the protein pocket of 2YA8 were elaborated and illustrated from Figure 4.34 to Figure 4.53. Beginning from compound (1), most of the alignments and matching interactions were shown on the primary amine part of the structure, which was salicyl hydrazide. These include 1 HBD towards ASP357 by OH group, as well as 2 HBA

towards HOH2499 and HOH2044 depicted by the carbonyl, C=O group of salicyl hydrazide. Interactions were also aligned by the benzene ring of vanillin structure, which aligned to HI towards PHE428, as well as 1 HBA towards HOH2044 shown by nitrogen atom of the C=N bond. The alignment and matching interactions shown by compound (1) were delivered in Figure 4.34.



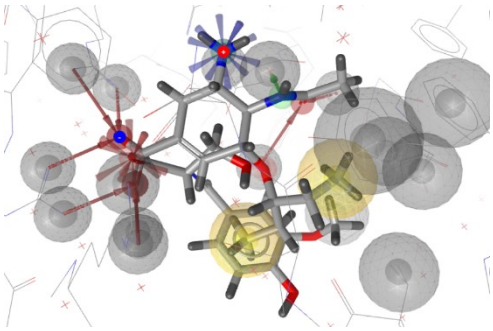
Alignment of compound (1) to the oseltamivir carboxylate ligand



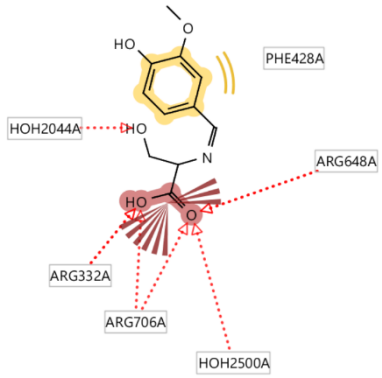
Matching interactions of compound (1) with the pharmacophore model

Figure 4.34: Alignment of compound (1) with oseltamivir carboxylate ligand and the matching interactions with the pharmacophore model

Based on Figure 4.35, compound (2) showed good alignment with oseltamivir carboxylate ligand, such that 4 HBA towards ARG332, ARG706, ARG648 and HOH2500, as well as 3 NI towards ARG332, ARG706, ARG648 were depicted by the carboxyl group of serine. Another HBA was also shown by OH of serine towards HOH2044. On top of that, HI was also depicted by the benzene ring of vanillin structure towards PHE428.



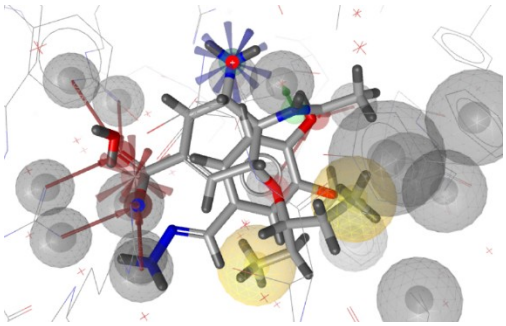
Alignment of compound (2) to the oseltamivir carboxylate ligand



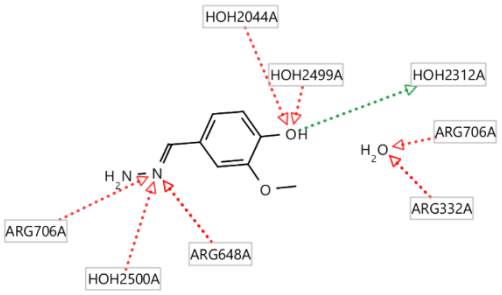
Matching interactions of compound (2) with the pharmacophore model

Figure 4.35: Alignment of compound (2) with oseltamivir carboxylate ligand and the matching interactions with the pharmacophore model

Upon alignment of compound (3) towards oseltamivir carboxylate ligand, 7 HBA were depicted towards HOH2044 and HOH2499 by OH of vanillin structure, ARG706, HOH2500 and ARG648 by nitrogen atom of C=N bond, as well as ARG706 and ARG332 by the water molecule. The OH of vanillin also showed HBD towards HOH2312, hence showing considerable pharmacophore fit in the model as shown in Figure 4.36.



Alignment of compound (3) to the oseltamivir carboxylate ligand

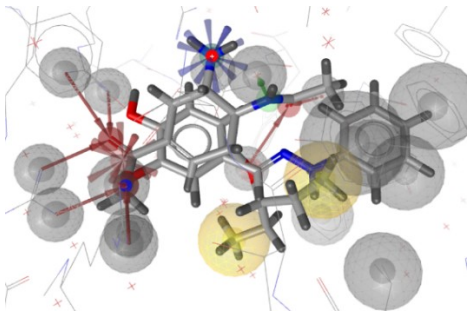


Matching interactions of compound (3) with the pharmacophore model

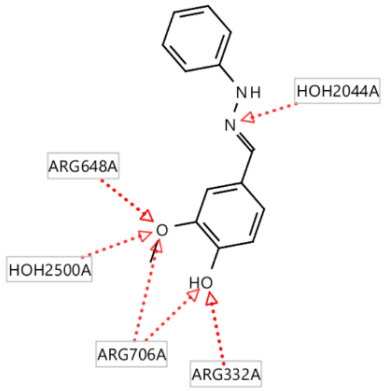
Figure 4.36: Alignment of compound (3) with oseltamivir carboxylate ligand and the matching interactions with the pharmacophore model

Compound (4) depicted a total of 6 matching interactions, which were all HBA as shown in Figure 4.37. OH of vanillin showed 2 HBA towards ARG706 and ARG332,

whereas C-O-C showed 3 HBA towards ARG648, HOH2500 and ARG706. Another HBA was depicted on nitrogen atom of C=N bond towards HOH2044.



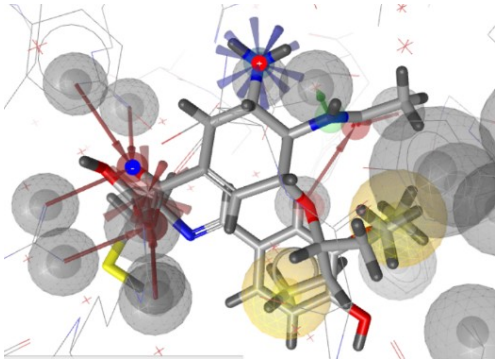
Alignment of compound (4) to the oseltamivir carboxylate ligand



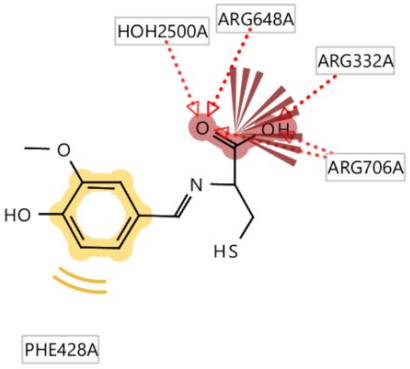
Matching interactions of compound (4) with the pharmacophore model

Figure 4.37: Alignment of compound (4) with oseltamivir carboxylate ligand and the matching interactions with the pharmacophore model

For compound (5), the cysteine primary amine structure depicted and aligned with quite a number of interactions particularly at the carboxyl group, including 5 HBA towards HOH2500, ARG648, ARG332 and ARG706, as well as 3 NI towards ARG648, ARG332 and ARG706. Similarly, HI was shown by the benzene ring of vanillin structure towards PHE428. As a result, compound (5) was able to show good alignment with the oseltamivir carboxylate ligand as well as depicting good pharmacophore fit in the model as illustrated in Figure 4.38.



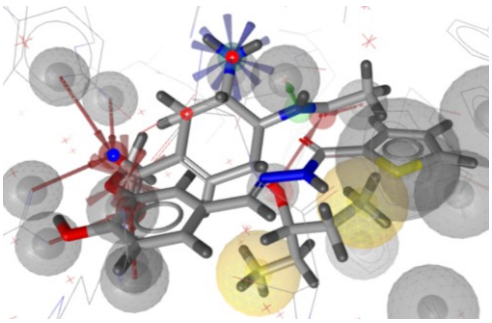
Alignment of compound (5) to the oseltamivir carboxylate ligand



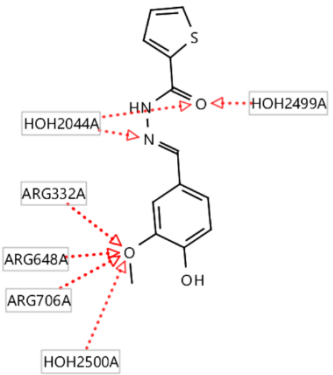
Matching interactions of compound (5) with the pharmacophore model

Figure 4.38: Alignment of compound (5) with oseltamivir carboxylate ligand and the matching interactions with the pharmacophore model

Compound (6) also successfully showed good alignment with the ligand and pharmacophore model. Most of the interactions were aligned by the C-O-C of vanillin, including 4 HBA towards ARG332, ARG648, ARG706 and HOH2500. The nitrogen atom of C=N bond also depicted 1 HBA towards HOH2044, and additionally, 2 HBA were shown by carbonyl group of 2-thiophene carboxylic acid hydrazide towards HOH2044 and HOH2499. Thus, a total of 7 HBA matching interactions were elaborated in Figure 4.39.



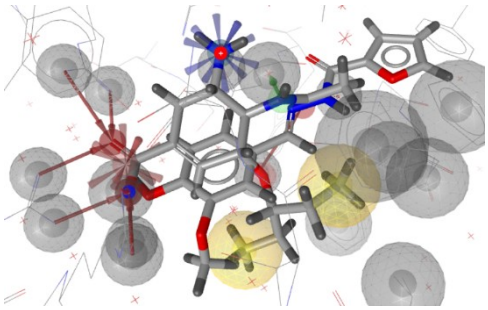
Alignment of compound (6) to the oseltamivir carboxylate ligand



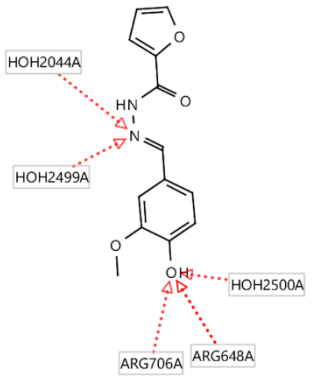
Matching interactions of compound (6) with the pharmacophore model

Figure 4.39: Alignment of compound (6) with oseltamivir carboxylate ligand and the matching interactions with the pharmacophore model

Based on Figure 4.40, compound (7) was also able to illustrate alignment with the ligand, while depicting matching pharmacophore interactions in the pharmacophore model. A total of 5 HBA were matched by compound (7), such that 2 HBA were shown by nitrogen atom of the C=N bond towards HOH2044 and HOH2499, whereas 3 HBA were shown by OH of vanillin part towards HOH2500, ARG706 and ARG648.



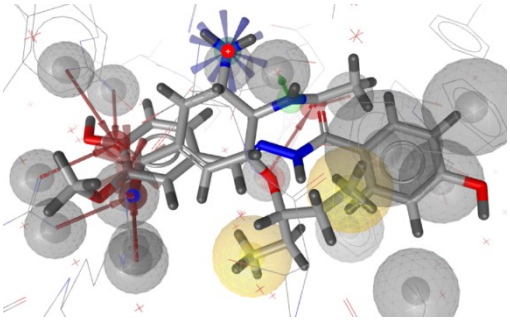
Alignment of compound (7) to the oseltamivir carboxylate ligand



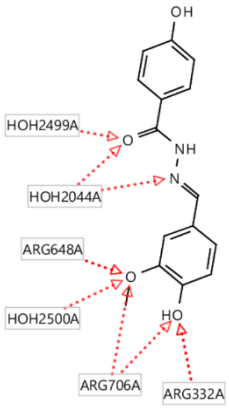
Matching interactions of compound (7) with the pharmacophore model

Figure 4.40: Alignment of compound (7) with oseltamivir carboxylate ligand and the matching interactions with the pharmacophore model

Similarly, compound (8), which is the Schiff base vanillin derivative of 4-hydroxybenzhydrazide also showed considerable alignment with oseltamivir carboxylate ligand and depicted only HBA interactions in the pharmacophore model. According to Figure 4.41, 2 HBA towards ARG706 and ARG332 were shown by OH of vanillin, 3 HBA towards ARG648, ARG706 and HOH2500 were pictured by C-O-C of vanillin, 1 HBA towards HOH2044 was shown by nitrogen atom of C=N bond, and 2 HBA towards HOH2044 and HOH2499 were depicted by the carbonyl group of amide bond of 4-hydroxybenzhydrazide.



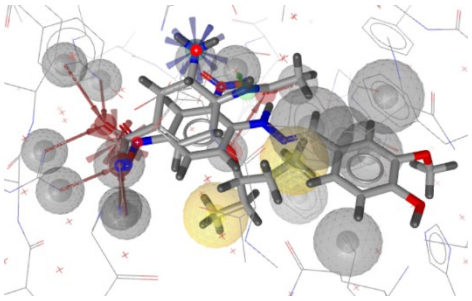
Alignment of compound (8) to the oseltamivir carboxylate ligand



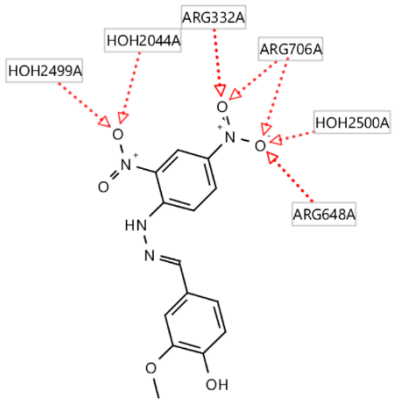
Matching interactions of compound (8) with the pharmacophore model

Figure 4.41: Alignment of compound (8) with oseltamivir carboxylate ligand and the matching interactions with the pharmacophore model

For compound (9), all matching interactions were aligned by nitro groups of 2,4-dinitrophenylhydrazine, which were a total of 7 HBA towards HOH2499, HOH2044, ARG332, ARG706, HOH2500 and ARG648. The alignment of compound (9) to oseltamivir carboxylate ligand and the illustration of matching interactions were as portrayed in Figure 4.42.



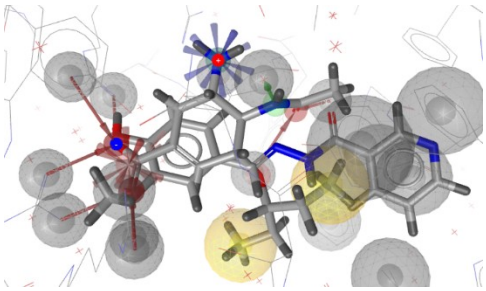
Alignment of compound (9) to the oseltamivir carboxylate ligand



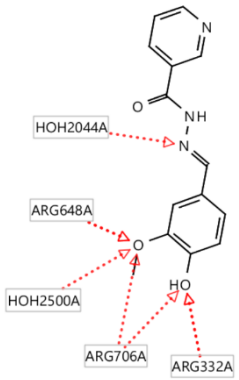
Matching interactions of compound (9) with the pharmacophore model

Figure 4.42: Alignment of compound (9) with oseltamivir carboxylate ligand and the matching interactions with the pharmacophore model

Compound (10) was also able to depict satisfactory alignment with the ligand, thus showing a total of 6 HBA matching interactions with the pharmacophore model. Similarly, OH of vanillin structure was able to match with 2 HBA towards ARG706 and ARG332, C-O-C of vanillin structure was able to match with 3 HBA towards ARG648, HOH2500 and ARG706. Another HBA towards HOH2044 was also shown and aligned by nitrogen atom of C=N bond, as pictured in Figure 4.43.



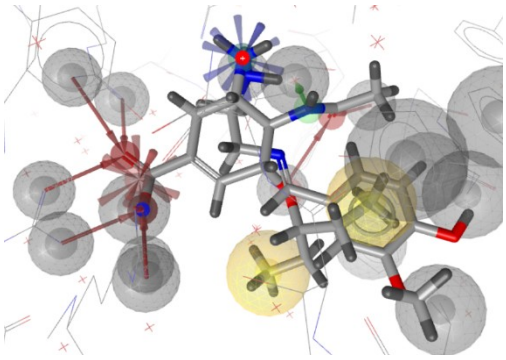
Alignment of compound (10) to the oseltamivir carboxylate ligand



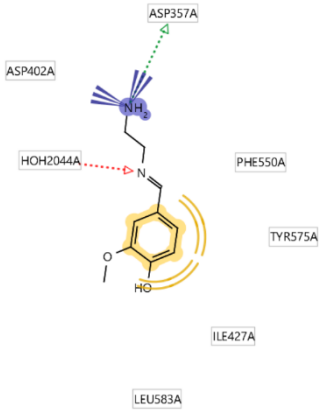
Matching interactions of compound (10) with the pharmacophore model

Figure 4.43: Alignment of compound (10) with oseltamivir carboxylate ligand and the matching interactions with the pharmacophore model

The Schiff base vanillin derivative of ethylenediamine, which is compound (11) showed only 1 HBA towards HOH2044 by the nitrogen atom of C=N bond. On top of that, the benzene ring was shown to align and match with 4 HI interactions of the pharmacophore model towards PHE550, TYR575, ILE427 and LEU583. Particularly, the amino, NH_2 of ethylenediamine depicted quite a number of matching interactions, including 1 HBA towards ASP357 and 2 PI towards ASP357 and ASP402. All alignments and interactions were illustrated in Figure 4.44.



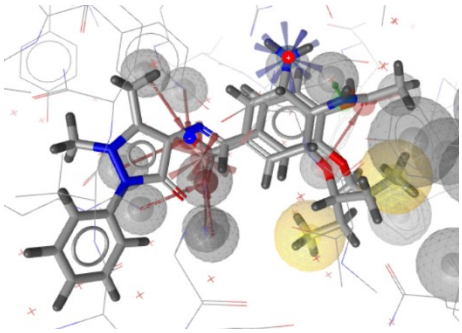
Alignment of compound (11) to the oseltamivir carboxylate ligand



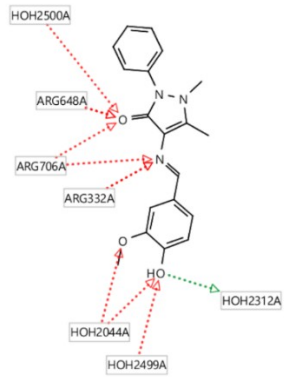
Matching interactions of compound (11) with the pharmacophore model

Figure 4.44: Alignment of compound (11) with oseltamivir carboxylate ligand and the matching interactions with the pharmacophore model

Furthermore, compound (12) was also able to show good alignment with the oseltamivir carboxylate ligand as well as depicting good pharmacophore fit in the generated model. 8 HBA were depicted by the chemical structure of compound (12), such that OH of vanillin aligned with 2 HBA towards HOH2044 and HOH2499, and C-O-C of vanillin aligned with 1 HBA towards HOH2044. Nitrogen atom of C=N bond showed alignment with 2 HBA towards ARG706 and ARG332, whereas carbonyl group of 4-aminoantipyrine depicted 3 HBA alignment towards HOH2500, ARG648 and ARG706. Additionally, 1 HBD was shown by OH of vanillin towards HOH2312. All alignments and matching interactions were illustrated in Figure 4.45.



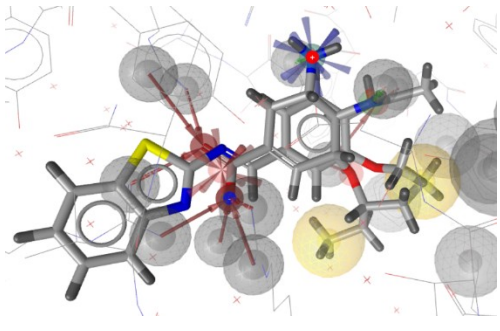
Alignment of compound (12) to the oseltamivir carboxylate ligand



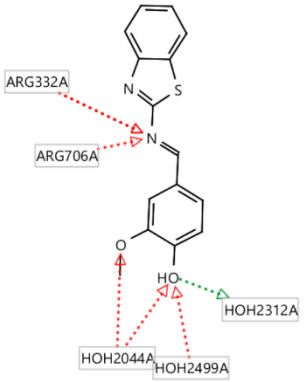
Matching interactions of compound (12) with the pharmacophore model

Figure 4.45: Alignment of compound (12) with oseltamivir carboxylate ligand and the matching interactions with the pharmacophore model

As for compound (13), which was the Schiff base vanillin derivative of 2-aminobenzothiazole, matching interactions were pictured by OH and C-O-C group of vanillin structure, as well as nitrogen atom of C=N bond as pictured in Figure 4.46. Specifically, 2 HBA were depicted by OH of vanillin towards HOH2044 and HOH2499, as well as 1 HBD towards HOH2312. C-O-C of vanillin showed alignment with 1 HBA towards HOH2044, as well as nitrogen atom of C=N bond showed alignment with 2 HBA towards ARG332 and ARG706.



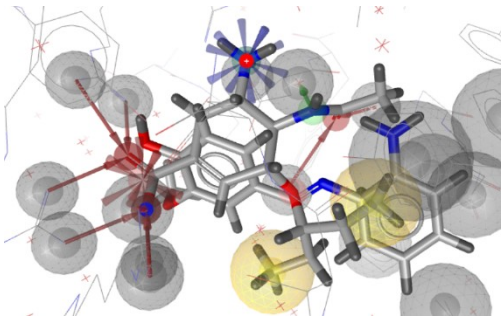
Alignment of compound (13) to the oseltamivir carboxylate ligand



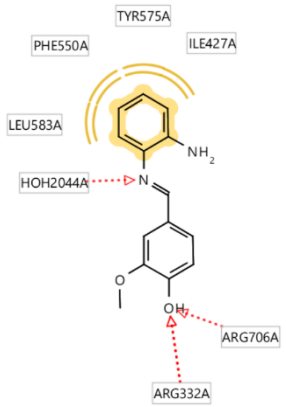
Matching interactions of compound (13) with the pharmacophore model

Figure 4.46: Alignment of compound (13) with oseltamivir carboxylate ligand and the matching interactions with the pharmacophore model

Most of the matching alignments and interactions were pictured by the benzene ring of O-phenyldiamine of compound (14), including 4 HI towards LEU583, PHE550, TYR575 and ILE427. 3 HBA were also aligned by compound (14), which were 2 HBA by OH of vanillin towards ARG332 and ARG706, as well as 1 HBA by nitrogen atom of C=N bond towards HOH2044 as shown in Figure 4.47.



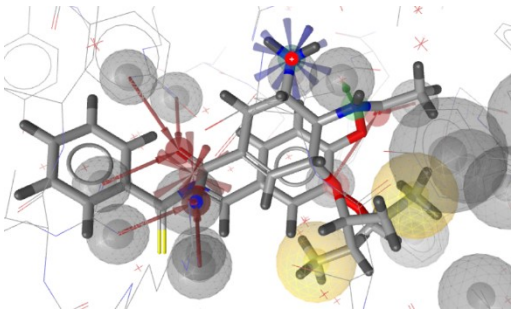
Alignment of compound (14) to the oseltamivir carboxylate ligand



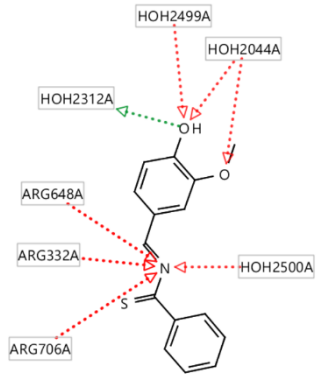
Matching interactions of compound (14) with the pharmacophore model

Figure 4.47: Alignment of compound (14) with oseltamivir carboxylate ligand and the matching interactions with the pharmacophore model

Moreover, the oseltamivir carboxylate ligand was also able to align with compound (15), Schiff base vanillin derivative of thiobenzamide. It was clearly depicted in Figure 4.48 that the matching interactions were HBA and HBD only. Beginning from the vanillin structure, 2 HBA towards HOH2499 and HOH2044, and 1 HBD towards HOH2312 were shown by OH of vanillin, as well as 1 HBA towards HOH2044 by C-O-C of vanillin. The remaining 4 HBA towards ARG706, ARG332, ARG648 and HOH2500 were depicted by nitrogen atom of C=N bond.



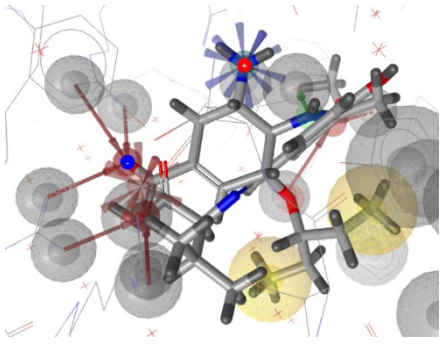
Alignment of compound (15) to the oseltamivir carboxylate ligand



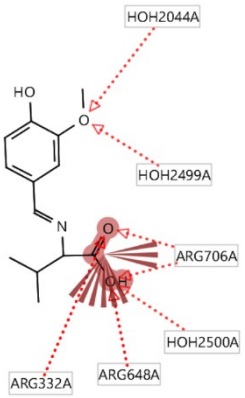
Matching interactions of compound (15) with the pharmacophore model

Figure 4.48: Alignment of compound (15) with oseltamivir carboxylate ligand and the matching interactions with the pharmacophore model

Based on Figure 4.49, compound (16) portrayed a total of 6 HBA and 3 NI upon alignment with the ligand. C-O-C of vanillin aligned with 2 HBA towards HOH2044 and HOH2499, whereas the carboxyl group of L-Valine was able to show good alignment with the rest of the interactions, particularly 5 HBA towards ARG706, ARG332, ARG648 and HOH2500, as well as 3 NI towards ARG706, ARG332 and ARG648.



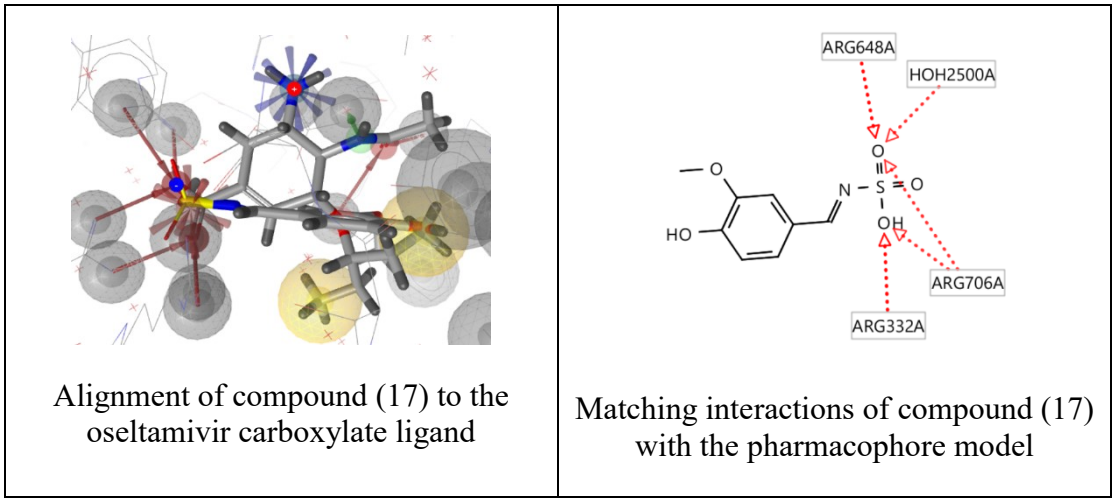
Alignment of compound (16) to the oseltamivir carboxylate ligand



Matching interactions of compound (16) with the pharmacophore model

Figure 4.49: Alignment of compound (16) with oseltamivir carboxylate ligand and the matching interactions with the pharmacophore model

Compound (17), which was the Schiff base vanillin derivative of sulfamic acid, showed a total of 5 HBA in alignment and fitting with the oseltamivir carboxylate ligand as well as the pharmacophore model. All 5 HBA were shown by the sulfo group, SO_3H of sulfamic acid, specifically 3 HBA at the S=O of sulfo group towards ARG648, ARG706 and HOH2500, as well as 2 HBA at the OH of sulfo group towards ARG332 and ARG706, as depicted in Figure 4.50.

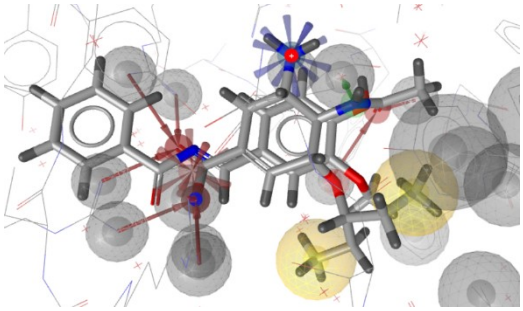


Alignment of compound (17) to the oseltamivir carboxylate ligand

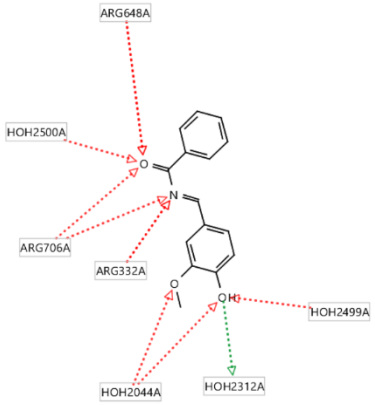
Matching interactions of compound (17) with the pharmacophore model

Figure 4.50: Alignment of compound (17) with oseltamivir carboxylate ligand and the matching interactions with the pharmacophore model

For compound (18), a total of 9 matching interactions, which were 8 HBA and 1 HBD, were shown upon alignment with the ligand and pharmacophore model. According to Figure 4.51, the carbonyl group of benzamide aligned well with 3 HBA towards ARG648, ARG706 and HOH2500, together with 2 HBA towards ARG706 and ARG332 by nitrogen atom of C=N bond. In addition to the interactions, C-O-C of vanillin also aligned with 1 HBA towards HOH2044, OH of vanillin aligned with 2 HBA against HOH2044 and HOH2499, as well as 1 HBD against HOH2312.



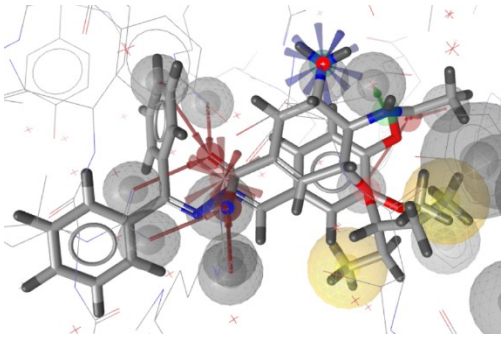
Alignment of compound (18) to the oseltamivir carboxylate ligand



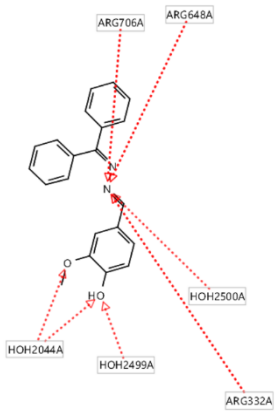
Matching interactions of compound (18) with the pharmacophore model

Figure 4.51: Alignment of compound (18) with oseltamivir carboxylate ligand and the matching interactions with the pharmacophore model

Similar to a few previous compounds, compound (19) was able to show alignment with the ligand and pharmacophore model, particularly at the OH and C-O-C of vanillin, as well as nitrogen atom of C=N bond. 1 HBA was shown by C-O-C of vanillin towards HOH2044, 2 HBA were shown by OH of vanillin towards HOH2044 and HOH2499, whereas 4 HBA were depicted by nitrogen atom of C=N bond towards ARG706, ARG648, ARG332 and HOH2500. The matching interactions were clearly pictured in Figure 4.52.



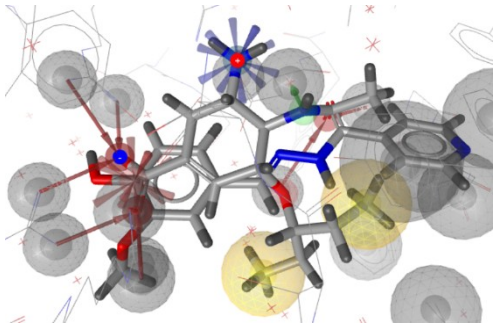
Alignment of compound (19) to the oseltamivir carboxylate ligand



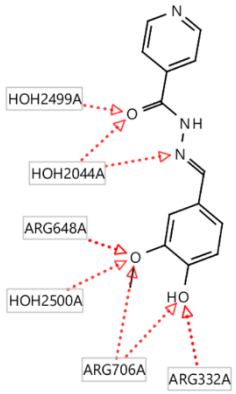
Matching interactions of compound (19) with the pharmacophore model

Figure 4.52: Alignment of compound (19) with oseltamivir carboxylate ligand and the matching interactions with the pharmacophore model

Last but not least, compound (21) was also able to picture satisfactory alignment with the oseltamivir carboxylate ligand and showed good pharmacophore fit in the generated model as shown in Figure 4.53. A total of 8 HBA were illustrated, such that 2 HBA towards ARG332 and ARG706 were shown by OH of vanillin, and 3 HBA towards ARG706, ARG648 and HOH2500 were shown by C-O-C of vanillin. On top of that, 1 HBA was shown by nitrogen atom of C=N bond towards HOH2044, as well as 2 HBA towards HOH2499 and HOH2044 by carbonyl of isonicotinic acid hydrazide.



Alignment of compound (21) to the oseltamivir carboxylate ligand



Matching interactions of compound (21) with the pharmacophore model

Figure 4.53: Alignment of compound (21) with oseltamivir carboxylate ligand and the matching interactions with the pharmacophore model

Out of all Schiff base vanillin derivatives, compound (20) failed to show alignment with the pharmacophore model of oseltamivir carboxylate ligand due to the lack of functional groups which may show alignment with the pharmacophore features of the model as shown in Figure 4.54. The other possible reason might also be the lack of suitable conformation to show the best fitting result in the pharmacophore model.

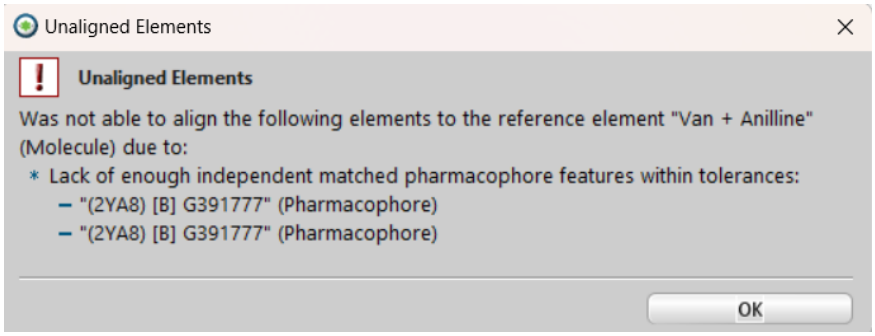


Figure 4.54: Failure of compound (20) to align with oseltamivir carboxylate ligand and the pharmacophore model

Neuraminidase A of *S. pneumoniae* is composed of two domains: one lectin and one catalytic domain (Sharapova, Švedas and Suplatov, 2021). In the active site of 2YA8, the catalytic domain is the part of binding site which depicts interactions with a substrate or chemical compound that binds to it, thus resulting in an enzymatic reaction. Out of all active site residues present in the pocket, the key active site residues are essential and attractive targets of inhibitor compounds. The key active site residues of the catalytic domain of 2YA8 are ARG332, ASP357, GLU632, ARG648, ARG706, and TYR737, which were colored in cyan as shown in Figure 4.55.

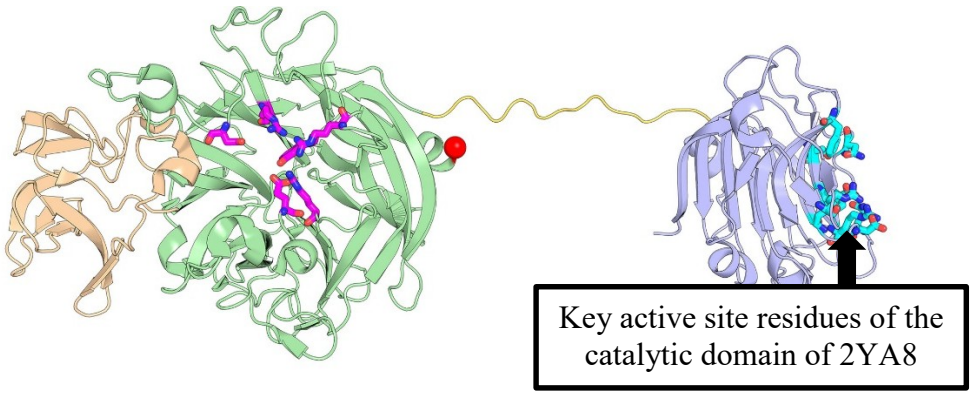


Figure 4.55: Key active site residues of catalytic domain of 2YA8

Based on the Schiff base vanillin derivatives results, most of the vanillin derivatives showed matching interactions towards 3 of the key active site residues, which were ARG332, ARG648 and ARG706. A total of 15 vanillin derivatives which depicted matching

interactions toward ARG332, ARG648 and ARG706 were 15 out of 21 Schiff base vanillin derivatives, which were compounds (2), (3), (4), (5), (6), (8), (9), (10), (12), (15), (16), (17), (18), (19) and (21). Additionally, compound (7) showed matching interactions towards ARG648 and ARG706 only, whereas compound (13) and (14) pictured matching interactions towards ARG332 and ARG706. On top of that, another 2 vanillin derivatives which were compound (1) and (11) depicted interaction towards only one key active site residue, which was ASP357. In explanation with theory, the 15 Schiff base vanillin derivatives were said to possess similar biological activity as oseltamivir carboxylate ligand in 2YA8, which were potential inhibitors of bacterial neuraminidase. As a result, the 15 Schiff base vanillin derivatives possessed high and promising potential to show enzymatic activity towards the catalytic domain of 2YA8 for being able to show interaction towards the key active site residues, thus being potential neuraminidase inhibitors of *S. pneumoniae*. Therefore, the derivatives were subjected to molecular docking to analyze and evaluate their binding affinity in the active site of 2YA8.

4.1.2.2 Structure-Based Molecular Docking

Aforementioned in literature review, binding affinity of the Schiff base vanillin derivative is measured in equilibrium dissociation constant (K_D), whereby the smaller the value of KD, the stronger the binding affinity of the ligand in the binding site of protein structure (Yartsev, 2017). Theoretically, a satisfactory binding affinity value should be less than –6.00 kcal/mol to be considered as active molecules, and binding affinity values more than –6.00 kcal/mol were considered inactive (Shityakov and Förster, 2014). Upon molecular docking of the 15 Schiff base vanillin derivatives into the active site of 2YA8, all the Schiff base vanillin derivatives successfully depicted binding affinity values less than –6.00 kcal/mol which were calculated in triplicates. Based on the results in Table 4.8, the

range of binding affinity values shown were from –6.10 kcal/mol to –7.60 kcal/mol, as a result showing strong binding interaction towards the binding site of 2YA8. The results were considered consistent, with great probability due to the presence of similar functional groups in the chemical structures, in which all Schiff base vanillin derivatives are composed of OH group, benzene ring and C-O-C group in the vanillin chemical structure, as well as imine linkage of Schiff bases. On top of that, suitable and favorable conformations and lowest conformational energies are the other possible reasons resulted in good binding affinity values of Schiff base vanillin derivatives.

Table 4.8: Binding affinity values of Schiff base vanillin derivatives in the active site of 2YA8

Schiff base vanillin derivatives (Vanillin + …)	Binding affinity values (kcal/mol)
(2) Serine	-6.50 ± 0.11
(3) Hydrazide hydrate	-7.00 ± 0.05
(4) Phenylhydrazine	-6.40 ± 0.24
(5) Cysteine	-7.60 ± 0.27
(6) 2-thiophene carboxylic acid hydrazide	-6.00 ± 0.17
(8) 4-hydroxybenzhydrazide	-6.60 ± 0.32
(9) 2,4-dinitrophenylhydrazine	-6.60 ± 0.26
(10) Nicotinic hydrazide	-6.20 ± 0.02
(12) 4-aminoantipyrine	-6.20 ± 0.07
(15) Thiobenzamide	-7.50 ± 0.14
(16) L-valine	-6.50 ± 0.16
(17) Sulfamic acid	-6.70 ± 0.23
(18) Benzamide	-7.20 ± 0.09

Table 4.8 continued

(19) Benzophenone hydrazone	-7.10 ± 0.28
(21) Isonicotinic acid hydrazide	-6.50 ± 0.34

4.1.2.3 Summary of Schiff Base Vanillin Derivatives as Neuraminidase Inhibitors of *S. pneumoniae*

As a summary, 15 out of 21 Schiff base vanillin derivatives were concluded as potential neuraminidase inhibitors of *S. pneumoniae* by performing ligand-based pharmacophore modelling, structure-based pharmacophore modelling and molecular docking. Except for compound (20) which failed to depict outstanding result in structure-based approach, and compounds (1), (7), (11), (13) and (14) showing only 1 to 2 interactions to the key active site residues, the remaining 15 Schiff base vanillin derivatives were promising drug candidates to depict inhibitory activity against bacterial neuraminidase.

Based on the ligand-based approach results, out of the 10 pharmacophore features of the generated pharmacophore model, all 21 Schiff base vanillin derivatives were able to show 6 to 8 out of 10 matching pharmacophore features. Moreover, the pharmacophore fit values depicted range from 64.25 to 81.50, which were greater than 50% of the pharmacophore fit values of the training sets ranging from 74.09 to 98.79. In complementary with the theory of pharmacophore modeling, the Schiff base vanillin derivatives were concluded to possess similar biological activity to the training sets which generated the pharmacophore model, which were potential neuraminidase inhibitors of *S. pneumoniae*.

Upon subjection to structure-based pharmacophore modelling, 15 out of 21 Schiff base vanillin derivatives were able to depict successful alignment with the oseltamivir

carboxylate ligand in the active site of 2YA8 protein structure, particularly depicting interactions to the key active site residues. Other than compound (20), the other Schiff base vanillin derivatives successfully aligned with the ligand, as well as showed ideal pharmacophore fit in the pharmacophore model of oseltamivir carboxylate ligand. Out of 19 pharmacophore features of the ligand, the vanillin derivatives were able to match with 5 to 10 pharmacophore features. Most importantly, among the depicted pharmacophore features, the derivatives successfully aligned with the key active site residues of the catalytic domain of 2YA8, which were remarkably essential for the neuraminidase activity. The key active site residues that were being aligned were specifically ARG332, ARG648, ARG706 and ASP357. Thus, the results further affirmed the reassurance of the Schiff base vanillin derivatives as potential bacterial neuraminidase inhibitors, with similar biological activity as oseltamivir carboxylate ligand. Out of all, 15 Schiff base vanillin derivatives depict at least half of the features, which were matching interactions with 4 out of 6 important key active site residues, including compounds (2), (3), (4), (5), (6), (8), (9), (10), (12), (15), (16), (17), (18), (19) and (21). As a result, these derivatives were considered to possess greater potential as inhibitors of bacterial neuraminidase, thus given priority to be subjected to synthesis later. Due to the lack of functional groups and suitable conformations to align with oseltamivir carboxylate ligand and fit in the pharmacophore model, compound (20) was unable to show ideal result in structure-based pharmacophore model, hence excluded to be further evaluated.

By subjecting the 15 Schiff base vanillin derivatives to molecular docking into the binding site of 2YA8, all of them were able to show binding affinity values lower than –6.00 kcal/mol, thus depicting active and strong binding interaction towards the protein pocket of 2YA8. As a whole, results from structure-based molecular docking greatly strengthened the capability of 15 Schiff base vanillin derivatives as *S. pneumoniae* neuraminidase inhibitors.

4.2 CADD Results of Schiff Base Vanillin Derivatives Targeting FtsZ of *S. aureus*

4.2.1 Ligand-Based Approach

Similar to the ligand-based approach of Schiff base vanillin derivatives targeting neuraminidase of *S. pneumoniae*, the results in ligand-based approach of Schiff base vanillin derivatives targeting FtsZ of *S. aureus* were also divided into 2 parts: generation and validation of pharmacophore model, consequently analysis of Schiff base vanillin derivatives as potential inhibitors of the generated pharmacophore model.

4.2.1.1 Generation and Validation of Pharmacophore Model

The 3D chemical structures of training sets to generate the pharmacophore model were drawn by using ChemDraw Ultra 12.0. Subsequently, the MDL-mol files of training sets were downloaded and imported in the ligand perspective of LigandScout 4.49, with the chemical structures as shown in Table 4.9.

Table 4.9: 3D chemical structures of training sets

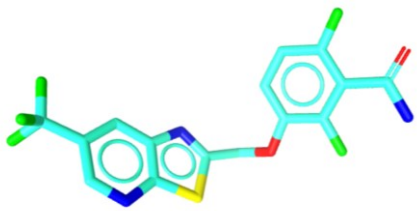
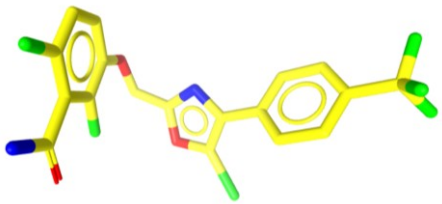
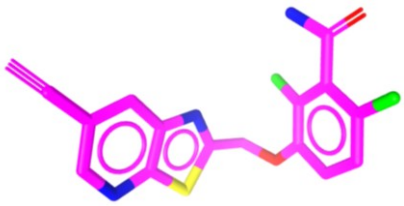
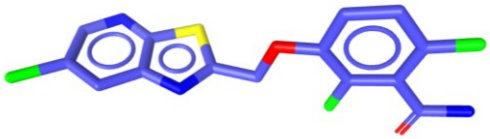
Name of training sets	3D chemical structures
TXA707	
TXA6101	

Table 4.9 continued

TXH9179	
PC190723	

The MDL-mol files of 3D chemical structures of test sets which were drawn by using ChemDraw Ultra 12.0 were subsequently imported as test sets in the ligand perspective of LigandScout 4.4.9 to validate the reliability of pharmacophore model. The 3D chemical structures of test sets were as depicted in Table 4.10.

Table 4.10: 3D chemical structures of test sets for validation of pharmacophore model

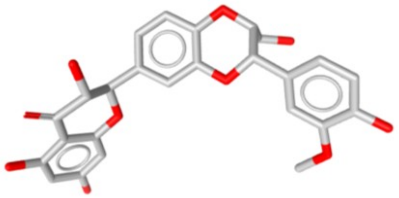
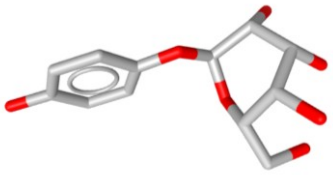
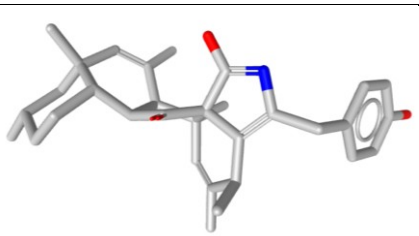
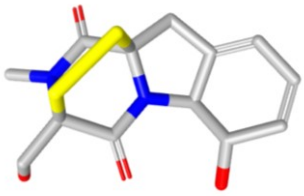
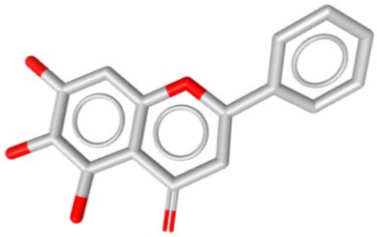
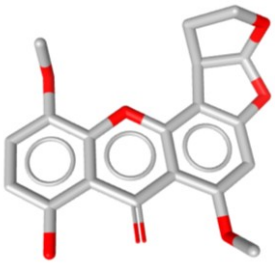
Name of test sets	Chemical structures
Silibinin	
Arbutin	

Table 4.10 continued

Diaporthalasin	
Gliotoxin	
Baicalein	
5-methoxydihydrosterigmatocystin	

A pharmacophore model composed of 16 pharmacophore features was generated by the training sets in Table 4.7 as portrayed in Figure 4.56. The pharmacophore features of the model were 7 hydrogen bond acceptors (HBA), 1 hydrogen bond donor (HBD), 5 hydrophobic interactions (HI), 3 aromatic rings (AR).

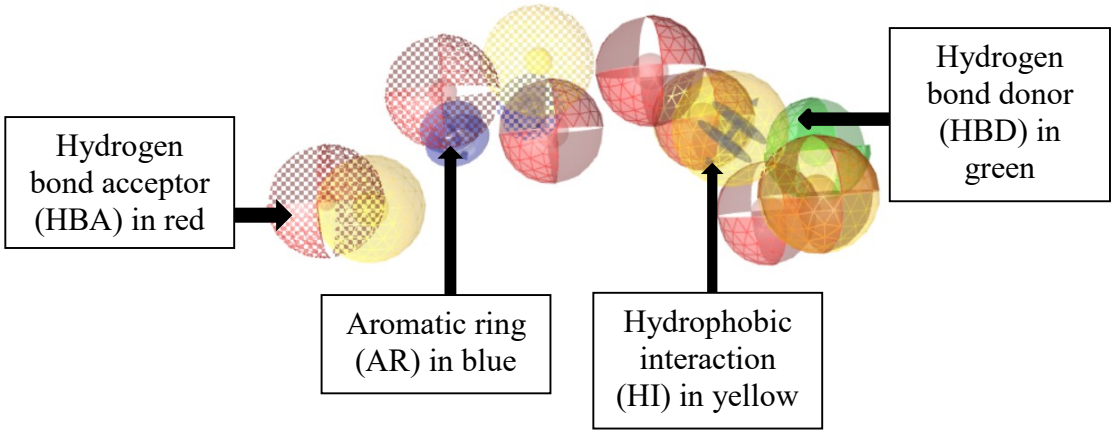


Figure 4.56: Generated pharmacophore model by training sets

The training sets were able to show good alignment and generate a pharmacophore model with considerably high pharmacophore fit values and matching features, ranging from 131.85 to 156.06. On top of that, the test sets were also able to depict excellent pharmacophore fit value ranging from 63.15 to 80.66, simultaneously showed 6 to 8 out of 16 matching pharmacophore features upon alignment in the generated pharmacophore model. For depicting at least 50% of the pharmacophore fit values of training sets, as well as showing about half of the matching features, the pharmacophore model was said to be verified for its dependability to evaluate the inhibitory activity of Schiff base vanillin derivatives targeting FtsZ of *S. aureus*. As a whole, the pharmacophore fit values and matching features of training sets and test sets in the pharmacophore model were delivered in Table 4.11.

Table 4.11: Pharmacophore fit values and matching features of training sets and test sets in the generated pharmacophore model

Name of chemical compounds	Type of compound	Matching pharmacophore features	Pharmacophore fit values
TXA707	Training set		156.06

Table 4.11 continued

TXH9179	Training set		151.28
PC190723	Training set		151.24
TXA6101	Training set		131.85
Silibinin	Test set		80.66
Arbutin	Test set		78.30
Diaporthalasin	Test set		68.46
Gliotoxin	Test set		66.27
Baicalein	Test set		66.20
5-methoxydihydrostegmatocystin	Test set		63.15

Figure 4.57 to Figure 4.60 elaborated the detailed interactions between training sets and the generated pharmacophore model. Based on Figure 4.57, TXA707, or full IUPAC name 2,6-bis(fluoranyl)-3-[[6-(trifluoromethyl)-[1,3]thiazolo[5,4-b]pyridin-2-yl]methoxy]benzamide was responsible for the greatest number of pharmacophore features in the generated pharmacophore model. The compound was generally a benzamide-based FtsZ inhibitor, such that the HBD was depicted by the amide group, and 1 HBA was shown by the carbonyl group of the benzamide structure. The benzene ring of benzamide structure also depicted AR interaction of the pharmacophore model. On top of that, the 2 fluorine atoms of the benzamide ring formed alignment with 2 HBA feature of the model, and together with the benzene ring, a total of 3 HI interactions were also aligned in the pharmacophore model. Towards the right side of TXA707, a thiazolo[5,4-b]pyridine structure also depicted a great number of pharmacophore features, such that the thiazole ring

and pyridine ring aligned with 2 AR interactions each. Moreover, the sulphur atom of thiazole ring showed HI interaction, and the 2 nitrogen atoms of both thiazole and pyridine ring depicted 2 HBA of the pharmacophore model. Additionally, the trifluoromethyl group was responsible for the alignment of 1 HBA and 1 HI. Last but not least, the ether bond C-O-C showed alignment with 1 HBA of the pharmacophore model. As a whole, TXA707 was able to show the best pharmacophore fit value of 156.06 and matching features in the generated model, as illustrated in Figure 4.57.

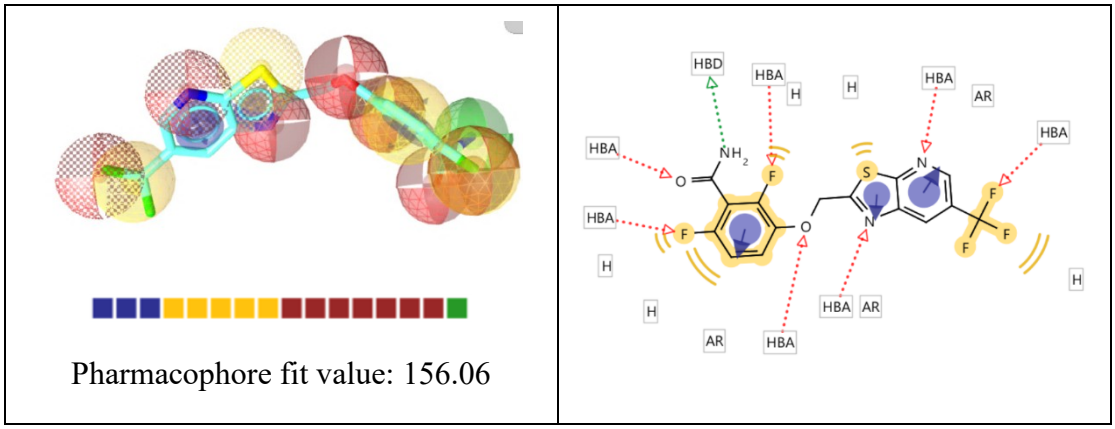


Figure 4.57: Interaction, pharmacophore fit value and matching features of TXA707 and pharmacophore model

TXH9179, or 3-[(6-ethynyl-[1,3]thiazolo[5,4-b]pyridin-2-yl)methoxy]-2,6-bis(fluoranyl)benzamide, is another new benzamide-based FtsZ inhibitor derived from chemical modulation of TXA707. It was reported to exhibit 4 times greater potential against particularly methicillin-sensitive *S. aureus* (MSSA) and MRSA in comparison to TXA707 (Bryan et al., 2023). As a result, all the interactions aligned by TXH9179 were the same as TXA707, except that the trifluoromethyl group was replaced by an ethynyl group which aligned with only 1 HI interaction. As a result, 1 HBA was not aligned from the pharmacophore model, resulting pharmacophore fit value of 151.28 as depicted in Figure 4.58.

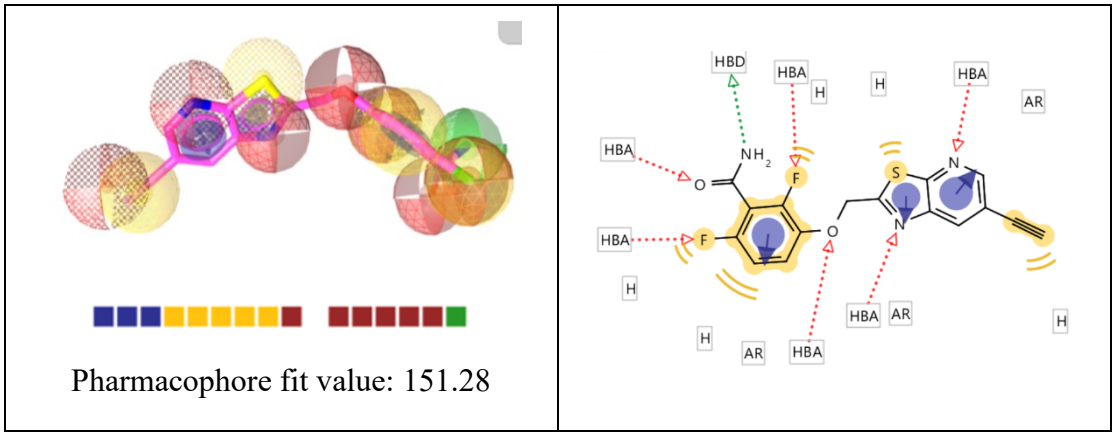


Figure 4.58: Interaction, pharmacophore fit value and matching features of TXH9179 and pharmacophore model

PC190723, also known for its IUPAC name as 3-[(6-chloro[1,3]thiazolo[5,4-b]pyridin-2-yl)methoxy]-2,6-difluorobenzamide, is another benzamide-based FtsZ inhibitor, which serves as the derivative of TXA707, such that the trifluoromethyl group was originally a chlorine atom. As a whole, all the matching interactions were the same as TXA707 except that the chlorine atom was responsible for the alignment towards 1 HI interaction of the pharmacophore model. For exhibiting exactly the same number and types of matching pharmacophore features as TXH9179, PC190723 depicted a pharmacophore fit value of 151.24 as shown in Figure 4.59.

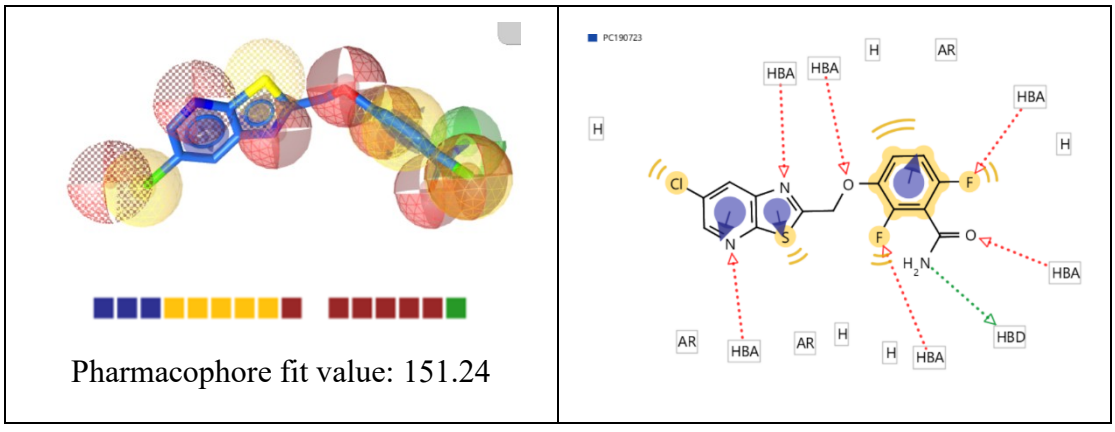


Figure 4.59: Interaction, pharmacophore fit value and matching features of PC190723 and pharmacophore model

As for the last training set, TXA6101, or 3-[[5-bromanyl-4-[4-(trifluoromethyl)phenyl]-1,3-oxazol-2-yl]methoxy]-2,6-bis(fluoranyl)benzamide, showed structure similarity as TXA707, but reported to possess greater structural flexibility, as well as inhibitory activity particularly against mutant FtsZ (Fujita et al., 2017). The structural modulation is that the thiazolo[5,4-b]pyridine was replaced by an oxazole ring with bromine atom and a phenyl ring, based on Figure 4.60, the nitrogen atom of the oxazole ring aligned with the HBA of pharmacophore model, whereas the phenyl ring showed AR interaction of the pharmacophore model. With the other matching interactions being remained the same, TXA6101 showed slightly lowered pharmacophore fit value of 131.85 and fitting in 13 matching pharmacophore features.

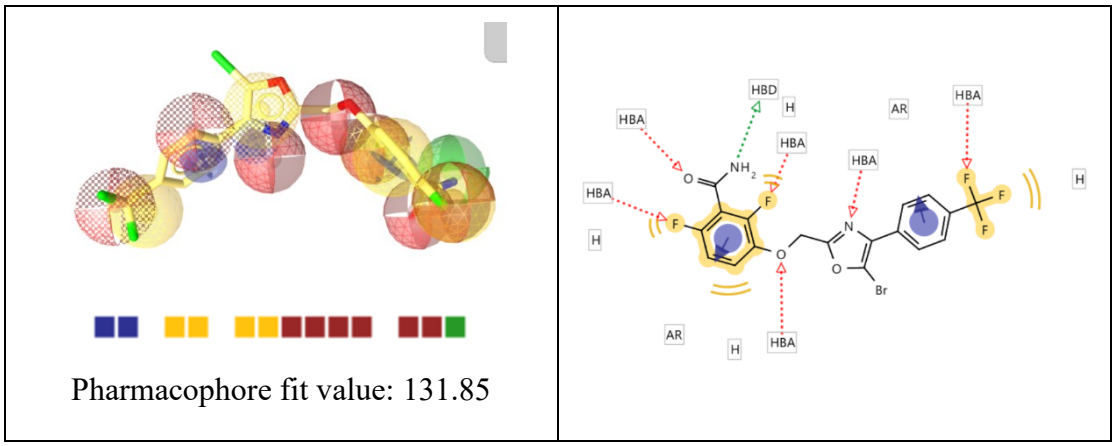


Figure 4.60: Interaction, pharmacophore fit value and matching features of TXA6101 and pharmacophore model

As elaborated earlier, a pharmacophore model was confirmed for its reliability as evaluation model of Schiff base vanillin derivatives as FtsZ inhibitors of *S. aureus* upon analysis by test sets. The test sets should be able to show pharmacophore fit values and matching pharmacophore features more than half of the training sets in order to confirm the dependability of the pharmacophore model. Since the test sets were able to show pharmacophore fit values and matching pharmacophore features more than 50% of the

training sets, the pharmacophore model was said to possess similar bioactivity of the test sets, which is inhibitory activity against FtsZ, thus validated the reliability.

The pharmacophore fit values and matching features of test sets in the pharmacophore model were elaborated and depicted from Figure 4.61 to Figure 4.66. Based on Figure 4.61, silibinin depicted the highest pharmacophore fit values and matching features out of all test sets by showing good alignment with 8 out of 16 matching features, as well as pharmacophore fit value of 80.66. Being a polyphenol flavonoid compound from *Silybum marianum*, it was reported to show inhibitory activity against the growth of *S. aureus* by inhibiting FtsZ activity (Basak et al., 2024). The HBA interactions were mostly shown at the C-O-C groups, whereas the benzene rings were able to depict both HI and AR interactions. On top of that, the OH group were able to align with HBA and HBD.

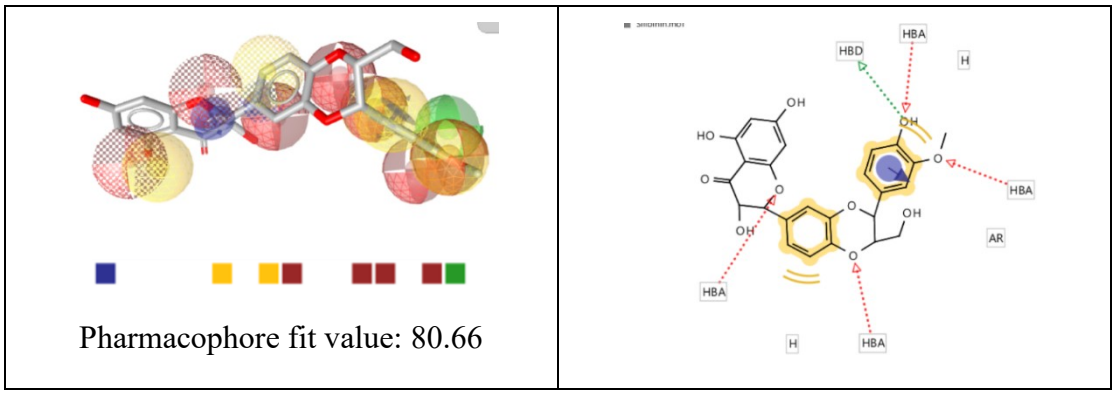


Figure 4.61: Interaction, pharmacophore fit value and matching features of silibinin and pharmacophore model

The next test set, arbutin, is a glycosylated hydroquinone compound reported for its antibacterial activity against *S. aureus* (Migas and Krauze-Baranowska, 2015). For possessing great number of OH groups, most of the HBA and HBD were able to show excellent alignment with the OH groups. 1 of the HBA was found to align with the C-O-C group, whereas the benzene ring was responsible for the alignment towards both HI and AR

feature of the pharmacophore model. As a whole, the compound depicted also 8 out of 16 matching features, with pharmacophore fit value of 78.30 as shown in Figure 4.62.

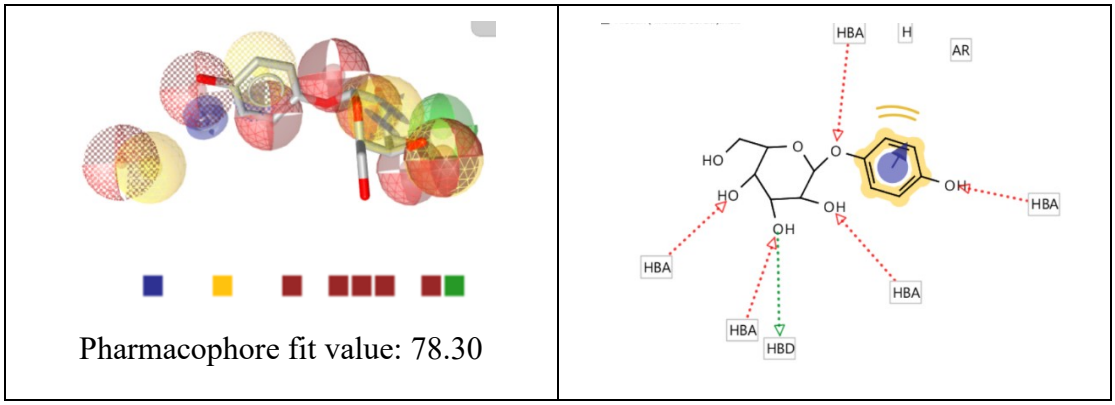


Figure 4.62: Interaction, pharmacophore fit value and matching features of arbutin and pharmacophore model

Diaporthalasin is a type of pentacyclic cytochalasin derivative which was discovered for its antibacterial activity towards both *S. aureus* and MRSA (Khamthong et al., 2014). The test set was able to portray a pharmacophore fit value of 68.46 in the pharmacophore model, as well as showing 7 out of 16 matching features. These include HBA alignment by OH, nitrogen atom of the pentacyclic structure, as well as C=O group. Additionally, 2 HI interactions were also shown by the carbon atoms of both cyclohexene structures. the benzene ring of the phenol structure was also able to depict both AR and HI as illustrated in Figure 4.63.

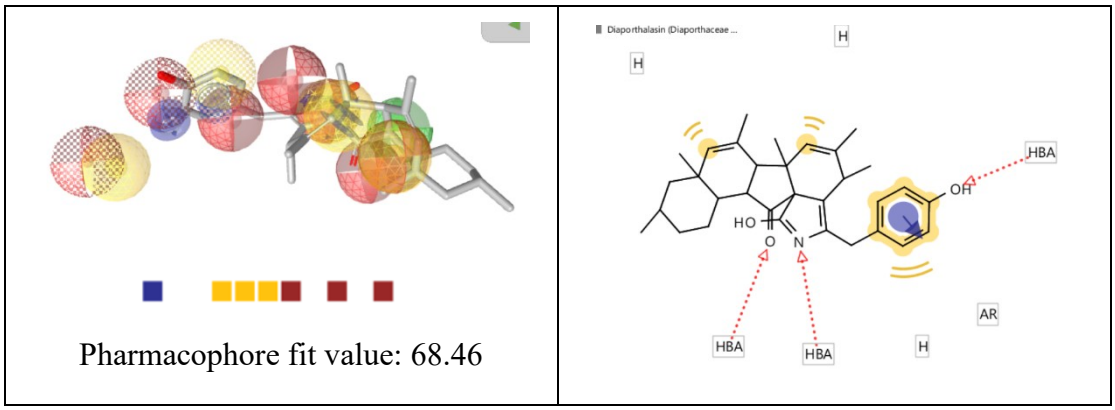
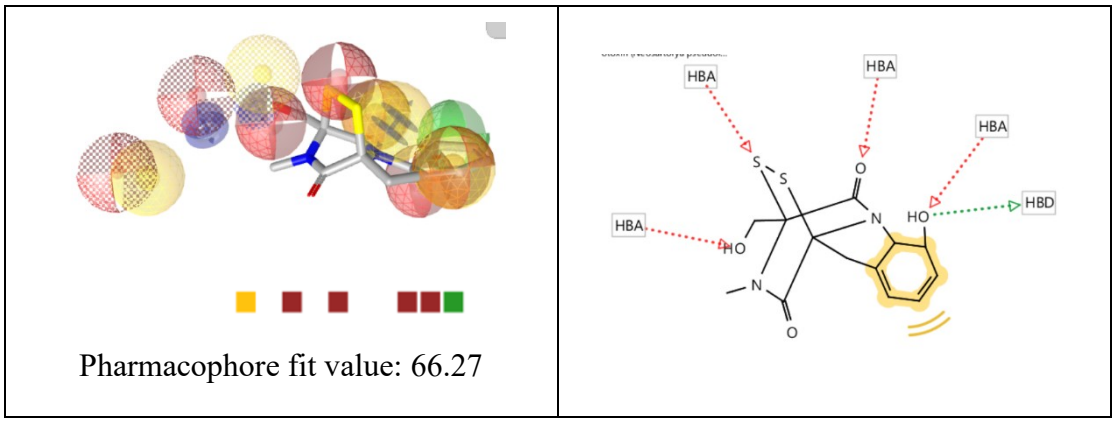


Figure 4.63: Interaction, pharmacophore fit value and matching features of diaporthalasin and pharmacophore model

Gliotoxin is a epidithiodioxopiperazine metabolite produced by fungus such as *Aspergillus fumigatus* reported to show inhibitory activity against MRSA and vancomycin-intermediate *S. aureus* (VISA) (Esteban et al., 2021). According to Figure 4.64, 4 HBA were aligned by functional groups including OH, C=O and sulphur atom of disulphide bridge. OH also depicted the HBD feature, and HI interaction was also shown by the cyclic structure of the test set. Therefore, 6 out of 16 features were matched, resulting in a pharmacophore fit value of 66.27.



Pharmacophore fit value: 66.27

Figure 4.64: Interaction, pharmacophore fit value and matching features of gliotoxin and pharmacophore model

Based on Figure 4.65, baicalein test set was also able to picture 6 out of 16 matching pharmacophore features and 66.20 pharmacophore fit value in the generated pharmacophore model. Being another flavonoid compound extracted from Chinese herb known as *Scutellaria baicalensis*, it was reported to show antibacterial activity against *S. aureus* particularly the biofilm formation (Chen et al., 2016). All HBA and HBD interactions were aligned by the great number of OH groups of the compound. In addition to that, AR and HI was also shown by the carbon atom of benzene ring of the flavonoid compound. The matching pharmacophore features and fit value were pictured in Figure 4.65.

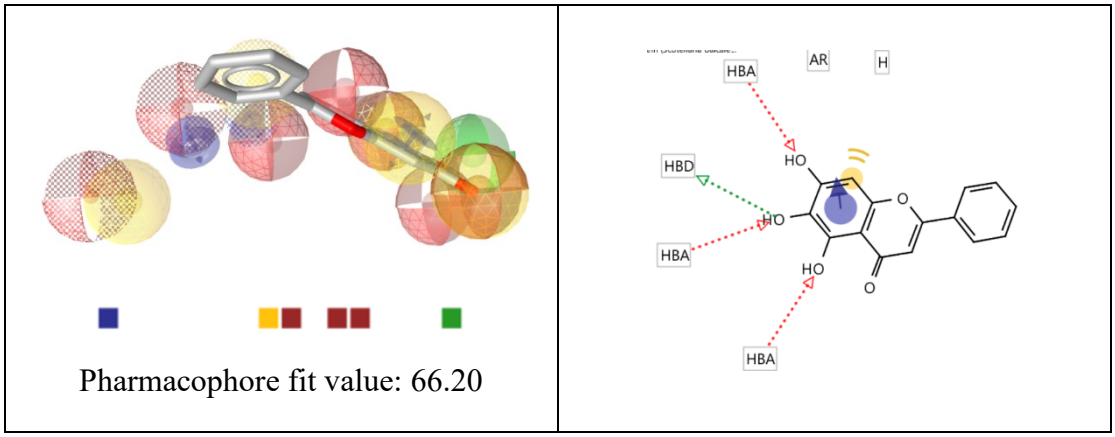


Figure 4.65: Interaction, pharmacophore fit value and matching features of baicalein and pharmacophore model

Lastly, 5-methoxydihydrosterigmatocystin extracted from *Aspergillus versicolor MF359* was reported for depicting antibacterial activity to a list of bacteria, including *S. aureus* and MRSA (Song et al., 2014). A total of 7 out of 16 matching features were shown by the test set, such that the 4 HBA were aligned by OH, C=O and C-O-C of the pentacyclic structures, whereas 1 AR and 2 HI were depicted by cyclic structures. As a result, the test set were able to depict good alignment in the pharmacophore model with fit value of 63.15 as illustrated in Figure 4.66.

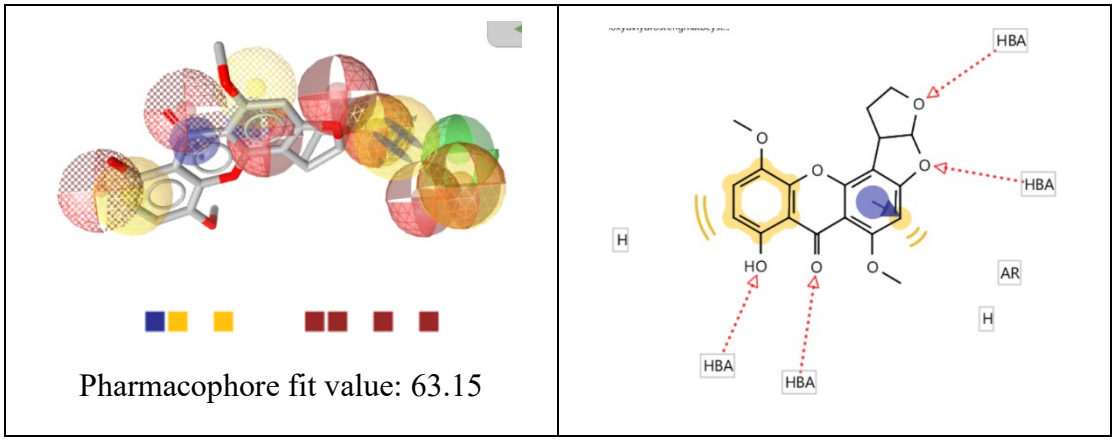


Figure 4.66: Interaction, pharmacophore fit value and matching features of 5-methoxydihydrosterigmatocystin and pharmacophore model

All test sets were able to show RMSD values less than 1.5 Å. For this reason, the test sets were said to show good agreement with the pharmacophore features of the generated

model, thus provided further fundamental support to the reliability of the pharmacophore model. Table 4.12 shows the summary of all RMSD values of test sets in the pharmacophore model, which were all less than 1.5 Å.

Table 4.12: RMSD-based evaluation of test sets alignment to the pharmacophore model

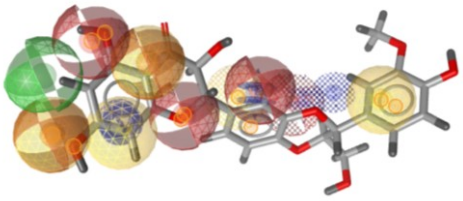
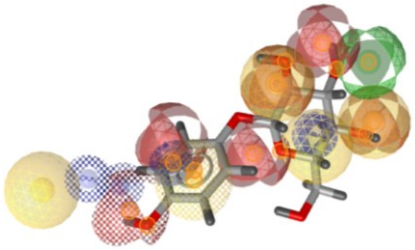
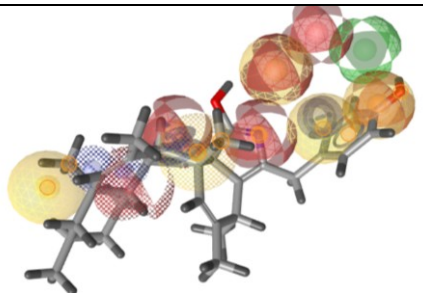
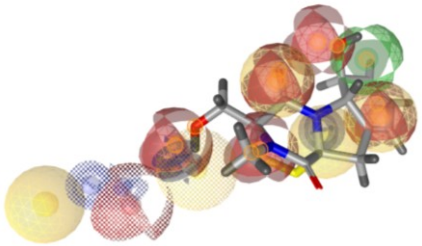
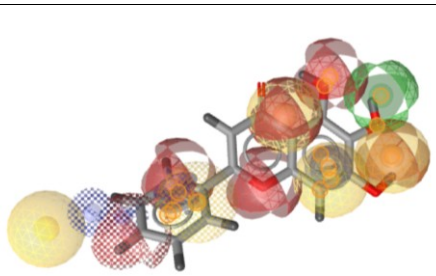
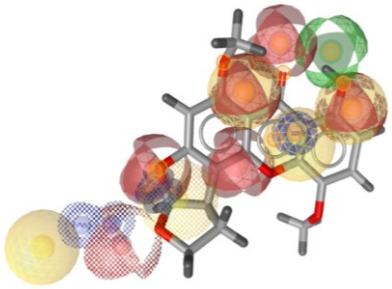
Test sets	Alignment of test sets with pharmacophore model	RMSD values
Silibinin		1.093
Arbutin		1.087
Diaporthalasin		1.178
Gliotoxin		1.029

Table 4.12 continued

Baicalein		0.982
5-methoxydihydrosterigmatocystin		1.181

The calculation of cosine similarities was based on pharmacophore vector of [7, 1, 3, 5, 0] due to 7 HBA, 1 HBD, 3 AR and 5 HI in the model. Based on the results, all the 6 test sets successfully showed cosine similarity values in between 0 and 1, which depicted strong similarity with the pharmacophore features of the model. This result further validated the reliability of the pharmacophore model. Table 4.13 showed the cosine similarities of test sets and the pharmacophore model.

Table 4.13: Cosine similarities of test sets and the pharmacophore model

Test sets	Vector of test sets	Cosine similarity
Silibinin	[10, 5, 3, 2, 0]	0.89
Arbutin	[7, 4, 1, 1, 0]	0.81
Diaporthalasin	[6, 2, 4, 2, 0]	0.99

Table 4.13 continued

Gliotoxin	[4, 2, 3, 2, 0]	0.97
Baicalein	[6, 3, 2, 2, 0]	0.91
5-methoxydihydrosterigmatocystin	[5, 1, 4, 3, 0]	0.99

In conclusion, the pharmacophore model was said to be affirmed and reliable to evaluate potential FtsZ inhibitory activity of Schiff base vanillin derivatives.

4.2.1.2 Analysis of Schiff Base Vanillin Derivatives Against the Pharmacophore Model

The same list of Schiff base vanillin derivatives as listed in Table 4.4 were selected as test sets to be evaluated towards the generated pharmacophore model. In this analysis, the pharmacophore model generated by the training sets depicted an extra HBA as compared to the pharmacophore model generated in the validation stage, thus depicting a total of 17 pharmacophore features. As a whole, all the 21 Schiff base vanillin derivatives successfully portrayed 6 to 10 matching pharmacophore features out of 17 pharmacophore features of the model. Additionally, the Schiff base vanillin derivatives also showed pharmacophore fit values ranging from 66.45 to 104.06. As compared to the pharmacophore fit values of training sets which were from 146.87 to 161.91, except for compounds (2), (3) (4) and (11), the other 17 Schiff base vanillin derivatives were able to depict a minimum of 50% of the pharmacophore fit values of training sets. Table 4.14 elaborated the pharmacophore fit values and matching pharmacophore features of all Schiff base vanillin derivatives in the generated pharmacophore model.

Table 4.14: Pharmacophore fit values and matching features of Schiff base vanillin derivatives in the generated pharmacophore model

Schiff base vanillin derivatives (Vanillin + …)	Matching pharmacophore features	Pharmacophore fit values
(13) 2-aminobenzothiazole		104.06
(12) 4-aminoantipyrine		103.43
(1) Salicyl hydrazide		93.17
(9) 2,4-dinitrophenylhydrazine		92.98
(19) Benzophenone hydrazone		86.09
(6) 2-thiophene carboxylic acid hydrazide		86.01
(5) Cysteine		85.99
(8) 4-hydroxybenzhydrazide		85.94
(7) 2-furoic acid hydrazide		85.88
(17) Sulfamic acid		85.68
(21) Isonicotinic acid hydrazide		85.60
(20) Aniline		83.82
(10) Nicotinic hydrazide		83.82
(14) O-phenyldiamine		83.80
(18) Benzamide		83.64
(15) Thiobenzamide		83.51
(16) L-valine		83.51
(2) Serine		76.15
(4) Phenylhydrazine		75.91
(11) Ethylenediamine		75.84

Table 4.14 continued

(3) Hydrazide hydrate		66.45

Similarly, evaluations were done based on the functional groups possessed by Schiff base vanillin derivatives and their structural conformations, such that Schiff base vanillin derivatives with high pharmacophore fit values and matching pharmacophore features are said to show similar inhibitory activity with the training sets against *S. aureus* FtsZ. First and foremost, all Schiff base vanillin derivatives depicted interactions at the vanillin structure, particularly at the benzene ring, OH and C-O-C bond, proving the importance and potential of vanillin structure in the study. Based on literature review, vanillin possessed wide range of biological activities, including particularly antibacterial activity (Olatunde et al., 2022). This further supported the obtained results. Moreover, all Schiff base vanillin derivatives also portrayed interactions at the nitrogen atom of imine linkage, which bonded vanillin and primary amine structure. This results proved the significance of Schiff base structures as potential *S. aureus* FtsZ inhibitors. For primary amine structures, interactions were vastly shown by OH, benzene ring, C=O group etc. which were elaborated together with the matching pharmacophore features and pharmacophore fit values from Figure 4.67 to 4.87.

Beginning from Figure 4.67, compounds (13) showed the highest pharmacophore fit value of 104.06 and 10 matching features in the pharmacophore model. The benzene ring of vanillin was able to align with HI and AR interactions of the model, the OH group showed interactions towards 1 HBA and 1 HBD, whereas the C-O-C showed interaction towards 1 HBA. Additionally, 1 HBA was interacted by the nitrogen atom of C=N bond. On top of that, interactions were also greatly aligned by the 2-aminobenzothiazole, HI and AR were

pictured by the thiazole ring, as well as 1 HBA towards the nitrogen atom of the thiazole ring, and 1 AR was shown by the benzene ring. By depicting a great number of matching pharmacophore features and high fit value, compound (13) was considered to possess great potential as *S. aureus* FtsZ inhibitor.

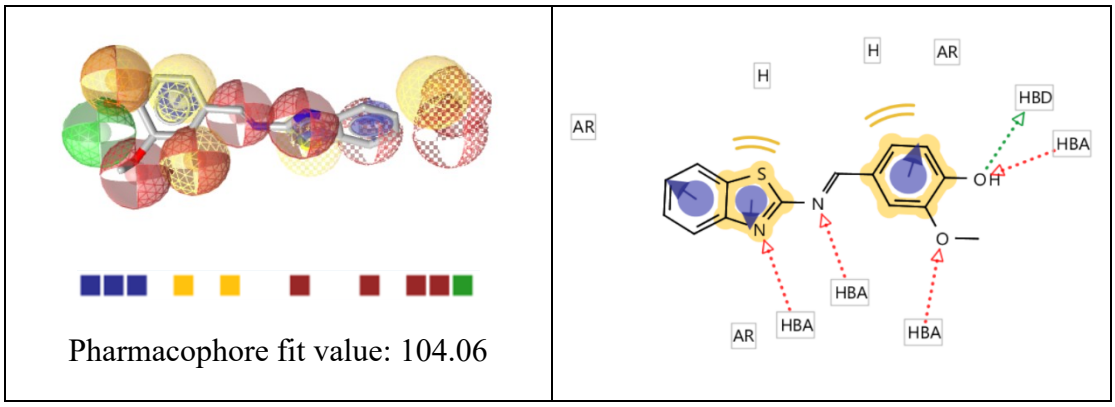


Figure 4.67: Interaction, pharmacophore fit value and matching features of compound (13) and pharmacophore model

For Schiff base vanillin derivative of 4-aminoantipyrine, which is compound (12), similar interactions were portrayed by the vanillin structure and nitrogen atom of C=N bond as compound (13), which include HI and AR interactions matched by benzene ring, 1 HBA and 1 HBD matched by OH group, and 1 HBA matched by C-O-C of vanillin structure. Also, 1 HBA was also aligned by nitrogen atom of C=N bond. 4-aminoantipyrine was able to depict great number of pharmacophore features as well, including 2 HI interactions on benzene ring and methyl group of the antipyrine structure, 1 AR interaction on the antipyrine structure, and 1 HBA towards C=O group. Thus, compound (12) was able to show fit value as high as 103.43, and 10 matching features as well as elaborated in Figure 4.68.

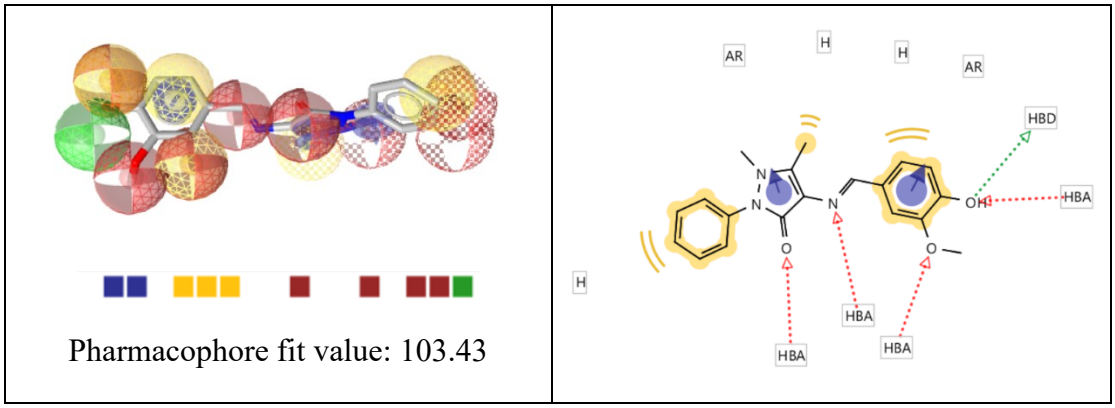


Figure 4.68: Interaction, pharmacophore fit value and matching features of compound (12) and pharmacophore model

Compound (1) was able to show 9 matching pharmacophore features and pharmacophore fit value of 93.17 in the pharmacophore model, hence being the third most potential *S. aureus* FtsZ inhibitor. Interactions depicted by benzene ring, OH and C-O-C of vanillin structure, as well as nitrogen atom of imine bond were exactly the same as compound (12) and (13). As for the primary amine structure, 2 HBA were shown by the OH and C=O group, and 1 AR was shown by the benzene ring of salicyl hydrazide. Thus, the matching features and pharmacophore fit values of compound (1) towards the pharmacophore model were depicted in Figure 4.69.

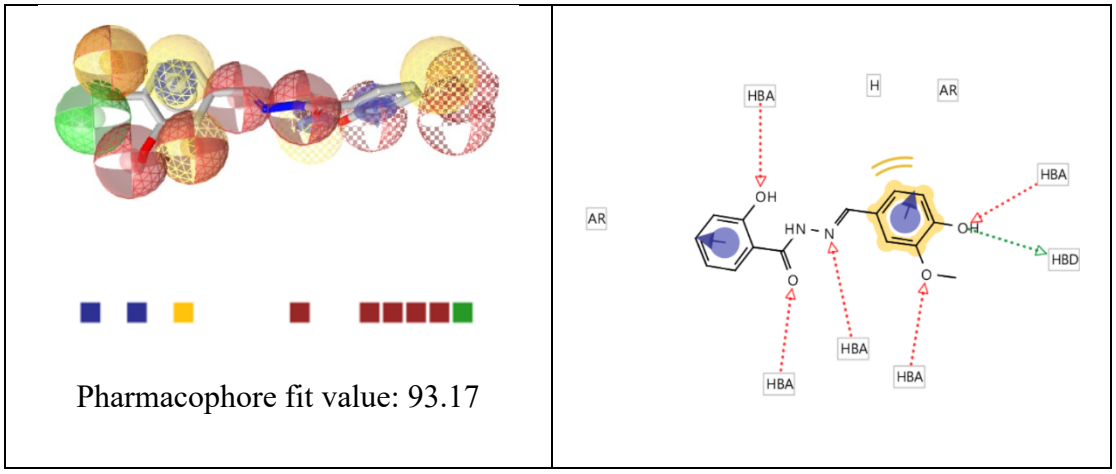


Figure 4.69: Interaction, pharmacophore fit value and matching features of compound (1) and pharmacophore model

Based on Figure 4.70, compound (9) was able to portray 9 matching features as well with fit value of 92.98. Similarly, benzene ring of vanillin structure depicted 1 AR and 1 HI, OH group showed 1 HBA and 1 HBD, and C-O-C of vanillin structure showed 2 HBA. On top of that, 1 HBA was shown on the nitrogen atom of C=N bond. For 2,4-dinitrophenylhydrazine, 1 HBA was depicted by the nitro group, whereas 1 HI was depicted by C atom of benzene ring. Thus, compound (9) was also considered to show potential inhibitory activity against FtsZ of *S. aureus*.

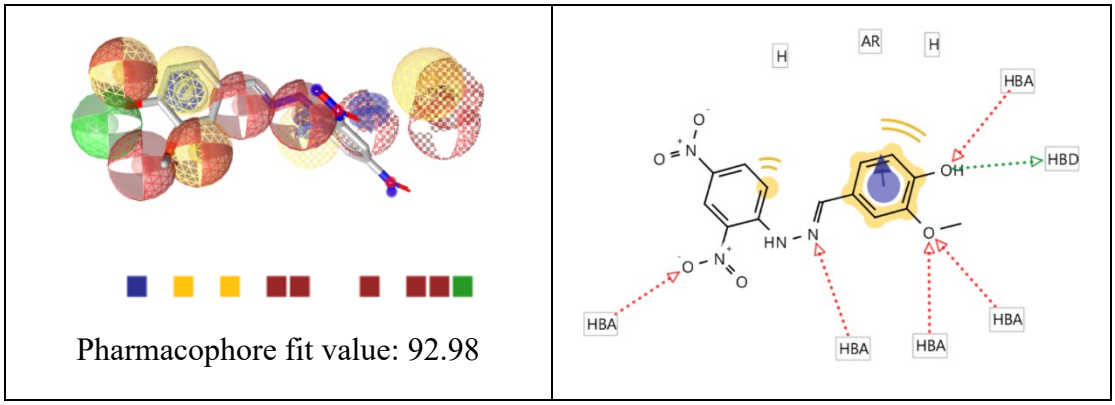


Figure 4.70: Interaction, pharmacophore fit value and matching features of compound (9) and pharmacophore model

For compound (19), the benzene ring, OH and C-O-C of vanillin structure, as well as nitrogen atom of C=N bond aligned with exactly the same interactions as compound (1), (12) and (13), elaborating the great significance as FtsZ inhibitor. Additionally, 1 HBA and 1 AR were shown by the nitrogen atom and benzene ring of benzophenone hydrazone respectively. As a whole, compound (19) depicted a pharmacophore fit value of 86.09, showed 8 matching features in the generated model as shown in Figure 4.71.

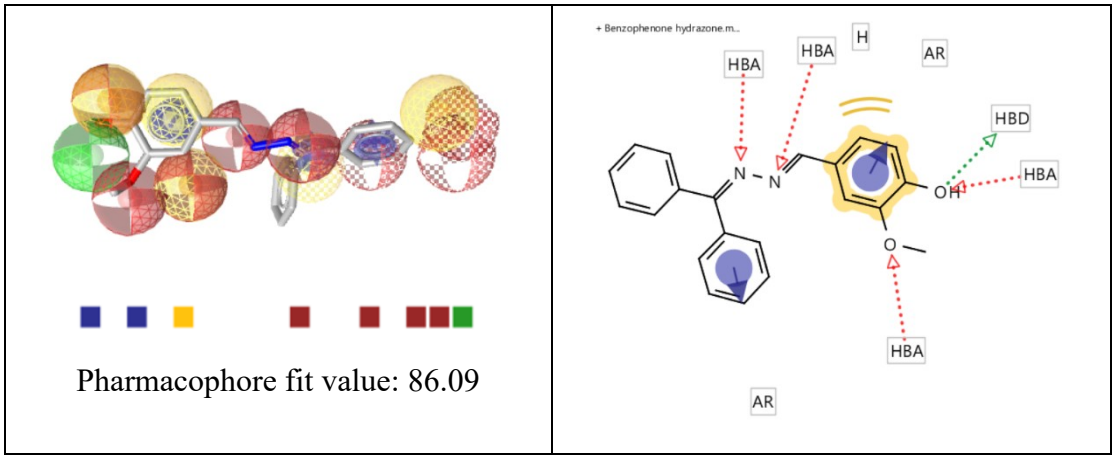


Figure 4.71: Interaction, pharmacophore fit value and matching features of compound (19) and pharmacophore model

Schiff base vanillin derivative of 2-thiophene carboxylic acid hydrazide, which is compound (6) was able to fit in the pharmacophore model with fit value of 86.01 and aligned with 8 matching pharmacophore features. Matching features were considered very similar to compound (19) as shown in Figure 4.71. 1 AR was shown on the thiophene ring, and 1 HBA was shown on the C=O of the primary amine structure. Other than that, benzene ring, OH and C-O-C group of vanillin structure, and nitrogen atom of C=N bond showed the same matching features as compounds (1), (12), (13) and (19). All matching features and fit value of compound (6) in the pharmacophore model were pictured in Figure 4.72.

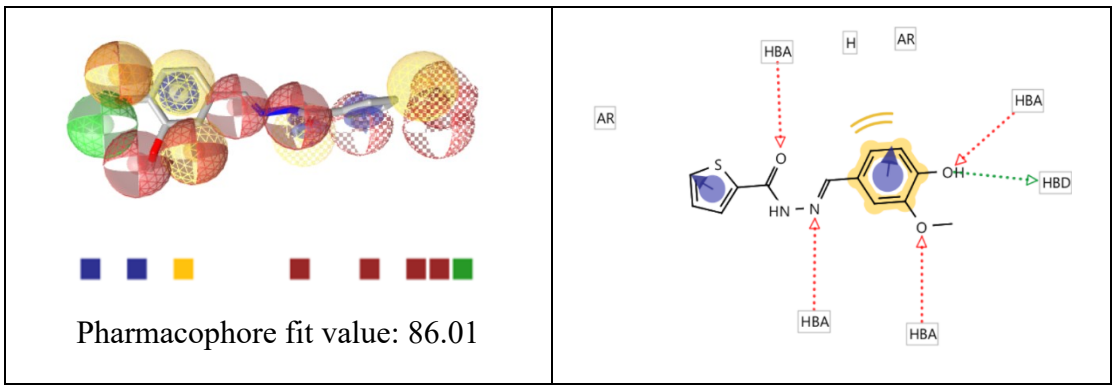


Figure 4.72: Interaction, pharmacophore fit value and matching features of compound (6) and pharmacophore model

Compound (5) fitted in the pharmacophore model with fit value of 85.99 and matched with 8 pharmacophore features as illustrated in Figure 4.73. The OH of carboxyl group of cysteine aligned with 1 HBA of the model. Additionally, the benzene ring of vanillin structure matched with 1 AR and 1 HI, OH of vanillin structure matched with 1 HBA and 1 HBD, whereas the C-O-C matched with 2 HBA, exactly the same as compound (9). 1 HBA was also depicted by the nitrogen atom of C=N bond.

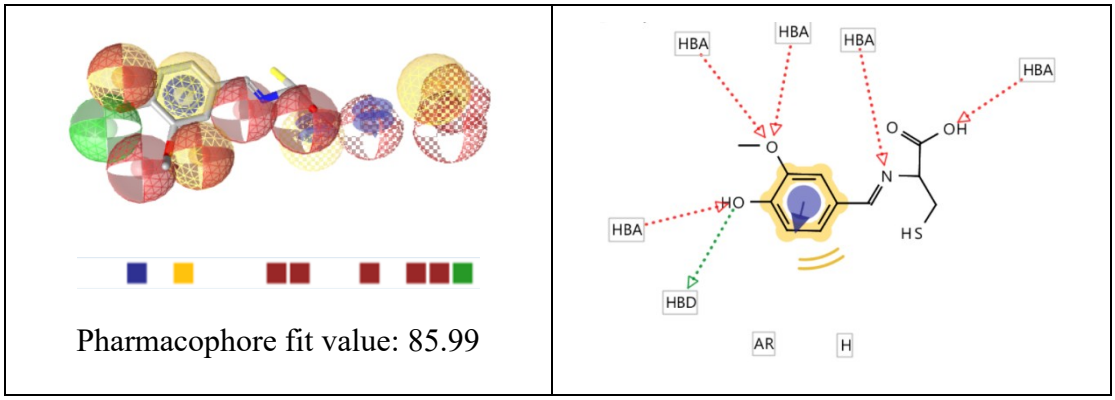


Figure 4.73: Interaction, pharmacophore fit value and matching features of compound (5) and pharmacophore model

For compound (8), 9 matching features in alignment with the pharmacophore model were shown. Despite more matching features than compound (6) and (19), compound (8) showed slightly lower pharmacophore fit value, which was 85.94. Aforementioned, this is most probably due to the structural conformation, such than compound (8) might not fit as well as compound (6) and (19). According to Figure 4.74, matching features depicted by the vanillin structure and imine bond were the same as compound (1), (6), (12), (13) and (19). As for the matching features shown by the primary amine, which was 4-hydroxybenzhydrazide, 1 AR was depicted on the benzene ring, and 2 HBA were depicted by the OH group.

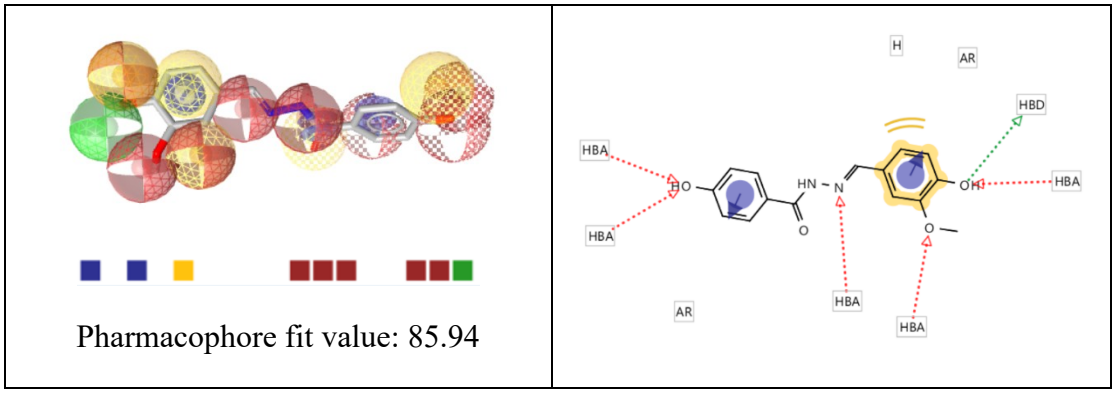


Figure 4.74: Interaction, pharmacophore fit value and matching features of compound (8) and pharmacophore model

Moreover, compound (7), which is the Schiff base vanillin derivative of 2-furoic acid hydrazide, once again depicted similar matching features at the vanillin structure and imine linkage as compound (1), (6), (8), (12), (13) and (19). Furthermore, 1 AR was shown on the furan ring, whereas 1 HBA was shown on the C=O group. As a result, compound (7) successfully depicted pharmacophore fit value of 85.88, and 8 matching pharmacophore features as illustrated in Figure 4.75.

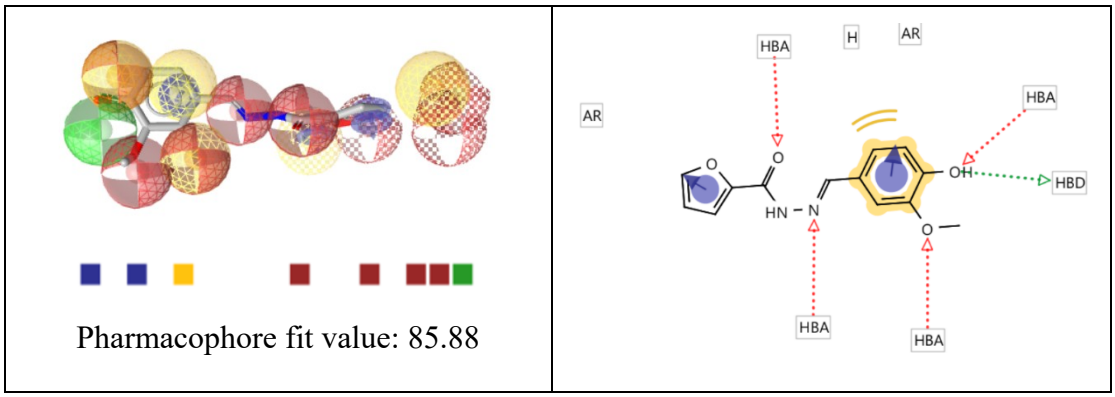


Figure 4.75: Interaction, pharmacophore fit value and matching features of compound (7) and pharmacophore model

Schiff base vanillin derivative of sulfamic acid, which is compound (17), was also able to show good fitting value of 85.68 and 8 matching pharmacophore features in the pharmacophore model as elaborated in Figure 4.76. Based on the results obtained, matching

features shown on the vanillin structure and imine bond were the same as compound (5) and (9). Additionally, 1 HBA was depicted by the OH of sulfamic acid.

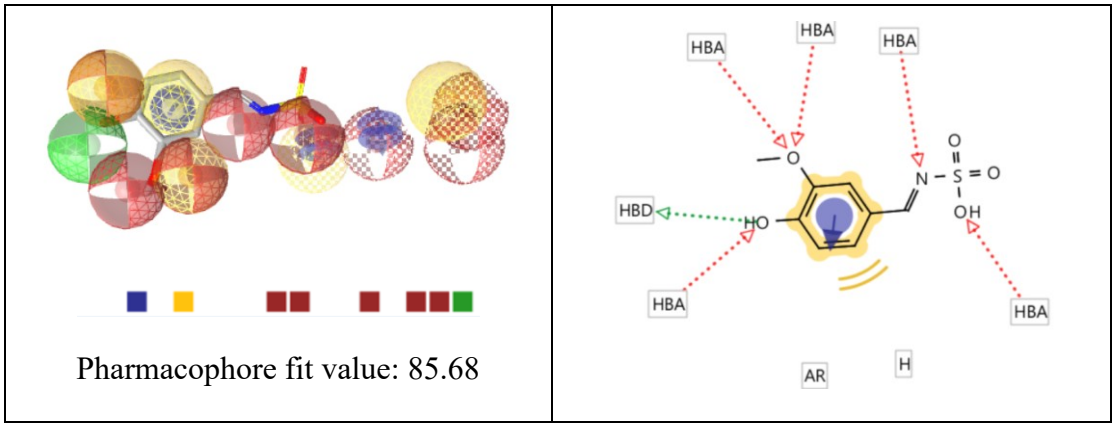


Figure 4.76: Interaction, pharmacophore fit value and matching features of compound (17) and pharmacophore model

For compound (21), a pharmacophore fit value of 85.60 and 8 matching pharmacophore features were illustrated in alignment with the pharmacophore model. Similarly, 1 HI and 1 AR were depicted by benzene ring of vanillin, 2 HBA were depicted by C-O-C group, 1 HBA and 1 HBD were depicted by the OH group of vanillin structure, and additionally, 1 HBA was shown by nitrogen atom of C=N bond. As for the primary amine, the benzene ring of isonicotinic acid hydrazide was observed to show 1 AR interaction. All matching features and fit value were as shown in Figure 4.77.

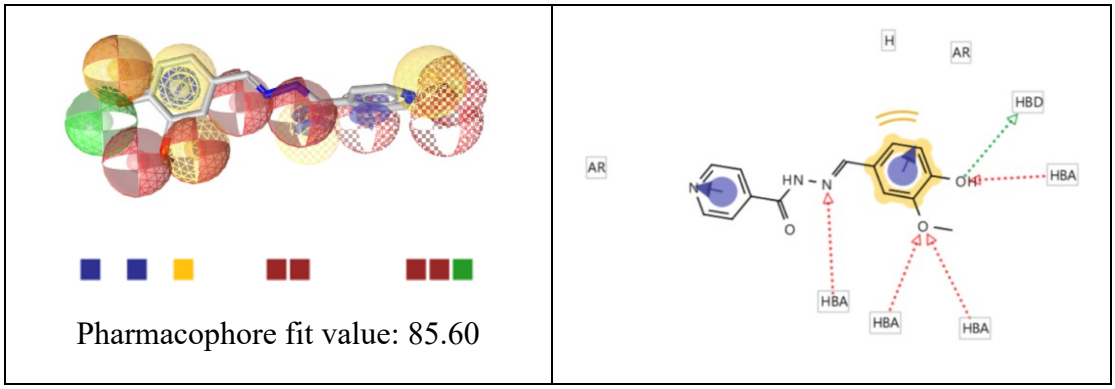


Figure 4.77: Interaction, pharmacophore fit value and matching features of compound (21) and pharmacophore model

Furthermore, Schiff base vanillin derivative of aniline, which makes compound (20), was also able to show good fitting and matching features in the pharmacophore model. Two benzene rings from aniline and vanillin structure showed matching interactions with 1 AR and 1 HI each. On top of that, the OH of vanillin structure pictured 1 HBA and 1 HBD of the model similar to compound (1), (6), (7), (8), (12), (13) and (19). 2 HBA were shown by nitrogen atom of C=N bond and C-O-C respectively. In a nutshell, compound (20) fitted in the pharmacophore model with value of 83.82 as illustrated in Figure 4.78.

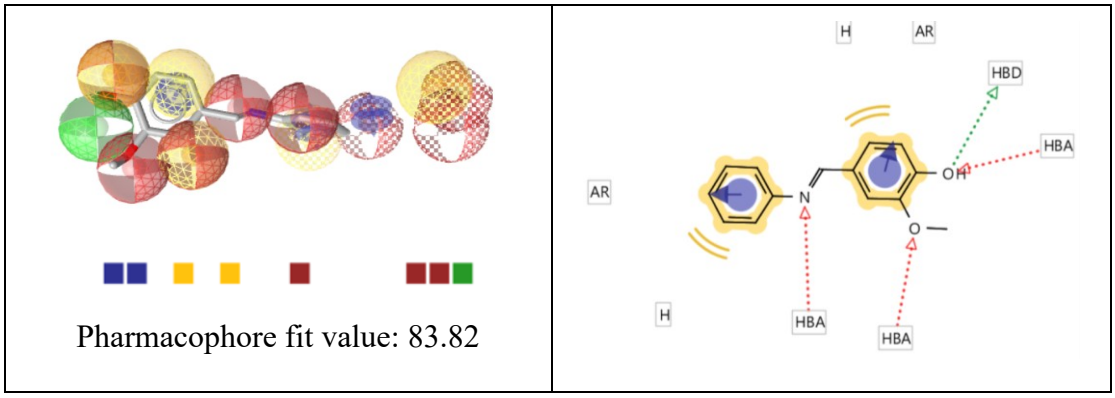


Figure 4.78: Interaction, pharmacophore fit value and matching features of compound (20) and pharmacophore model

Compound (10), Schiff base vanillin derivative of nicotinic hydrazide, showed structural similarity as compound (21). The difference between compound (10) and (21) is the position of nitrogen atom on the pyridine ring. As a result, the pharmacophore fit value and matching features were considered similar, except that for compound (10), only 1 HBA was shown on the C-O-C of vanillin structure, and 1 HBA was also shown on the nitrogen atom on the pyridine ring. With other features depicted the same as compound (21), compound (10) illustrated a pharmacophore fit value of 83.82 and 8 matching features as well as elaborated in Figure 4.79.

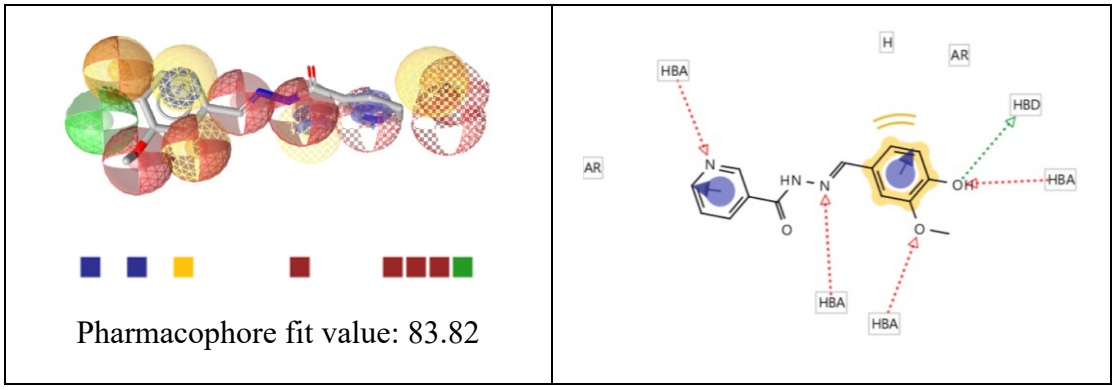


Figure 4.79: Interaction, pharmacophore fit value and matching features of compound (10) and pharmacophore model

For compound (14), matching features at the vanillin structure and imine linkage were the same as (1), (6), (7), (8), (10), (12), (13), (19) and (20). Additionally, the benzene ring of O-phenylenediamine showed 1 AR and 1 HI matching features. For these matching features depicted, a pharmacophore fit value of 83.80 and 8 matching features were successfully delivered, as shown in Figure 4.80.

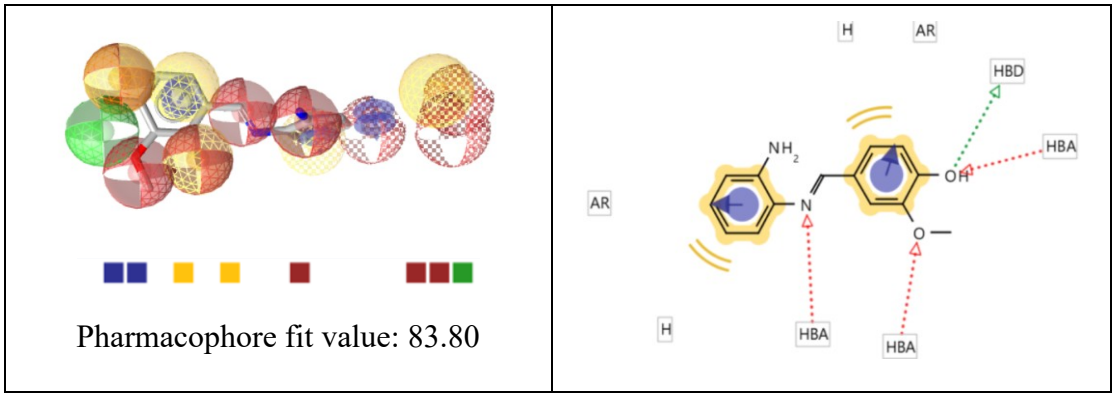


Figure 4.80: Interaction, pharmacophore fit value and matching features of compound (14) and pharmacophore model

Based on Figure 4.81, benzamide of compound (18) was able to show matching features, particularly 1 HI by the benzene ring, and 1 HBA at the C=O group. With matching features at the vanillin and imine bond the same as (1), (6), (7), (8), (10), (12), (13), (14), (19) and (20), compound (18) showed 83.64 pharmacophore fit value and 8 matching features as well.

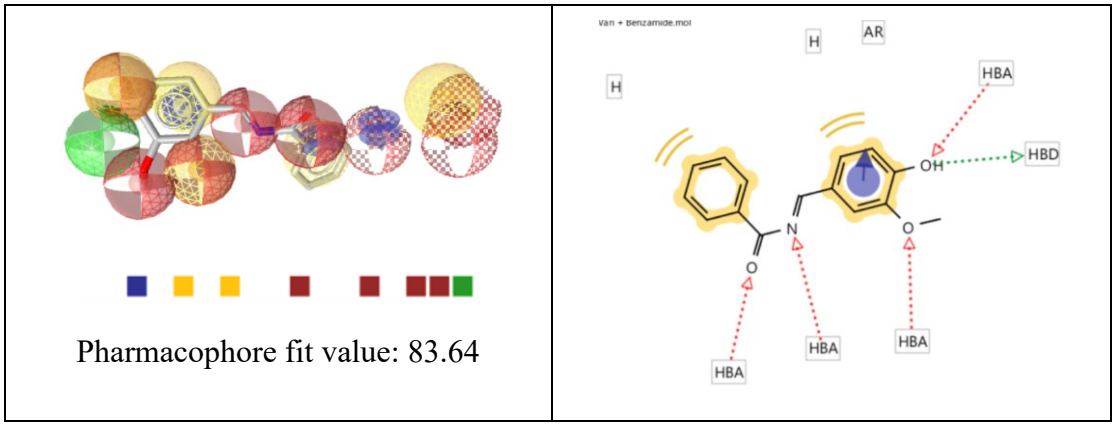


Figure 4.81: Interaction, pharmacophore fit value and matching features of compound (18) and pharmacophore model

Matching features shown by compound (15) were considered very similar to compound (18). The difference between benzamide and thiobenzamide is that C=O is replaced with C=S instead. Despite the difference, the matching features were still the same, which were 1 HI shown by benzene ring and 1 HBA shown by C=S. With the same matching features depicted at the vanillin and imine linkage, a pharmacophore fit value of 83.51 and the exact same 8 matching features were shown by compound (15) in the pharmacophore model, as illustrated in Figure 4.82.

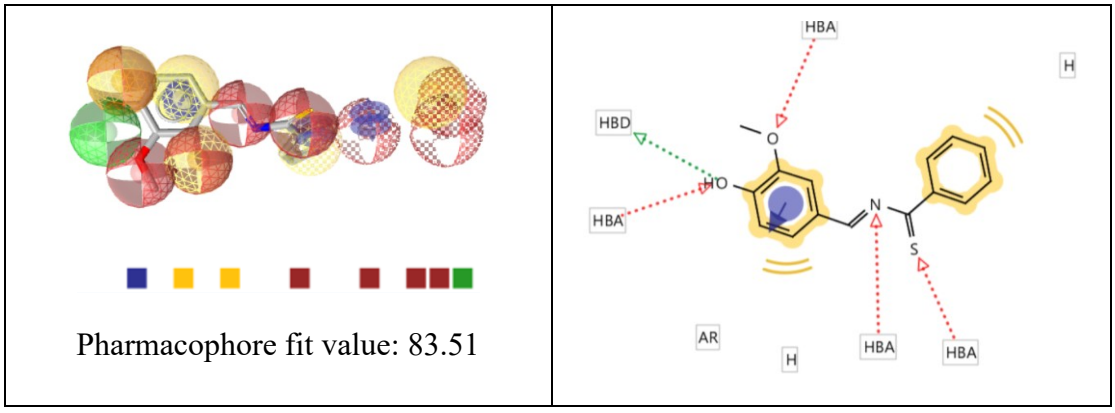


Figure 4.82: Interaction, pharmacophore fit value and matching features of compound (15) and pharmacophore model

Moving on to compound (16), the Schiff base vanillin derivative of L-valine portrayed a pharmacophore fit value of 83.51 and 8 features as well in alignment with the

pharmacophore model as shown in Figure 4.83. Similarly, based on the vanillin structure of compound (16), 1 HI and 1 AR were shown by benzene ring, 1 HBA and 1 HBD were shown by the OH group, and 2 HBA were shown by the C-O-C group. The nitrogen atom of C=N bond also aligned with 1 HBA of the pharmacophore model. Furthermore, the isopropyl structure of L-valine aligned with 1 HI of the pharmacophore model.

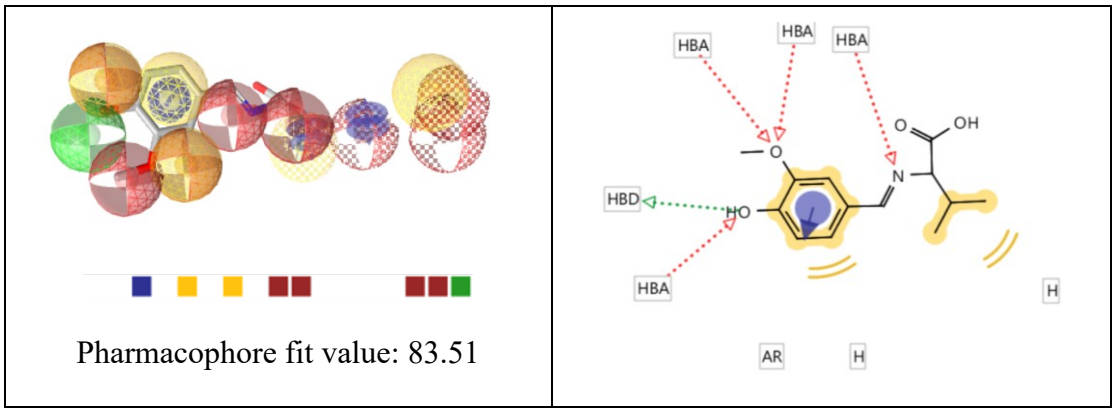


Figure 4.83: Interaction, pharmacophore fit value and matching features of compound (16) and pharmacophore model

The last four compounds showed slightly lower pharmacophore fit values and matching features, thus considered to possess lower potential as FtsZ inhibitors of *S. aureus*. Based on Figure 4.84, compound (2) showed a fit value of 76.15 and 7 matching features. Matching features at the benzene ring, OH and C-O-C of vanillin part, as well as nitrogen atom of C=N bond were the same as compounds (1), (6), (7), (8), (10), (12), (13), (14), (15), (18), (19) and (20). 1 HBA was also depicted by the OH of serine compound.

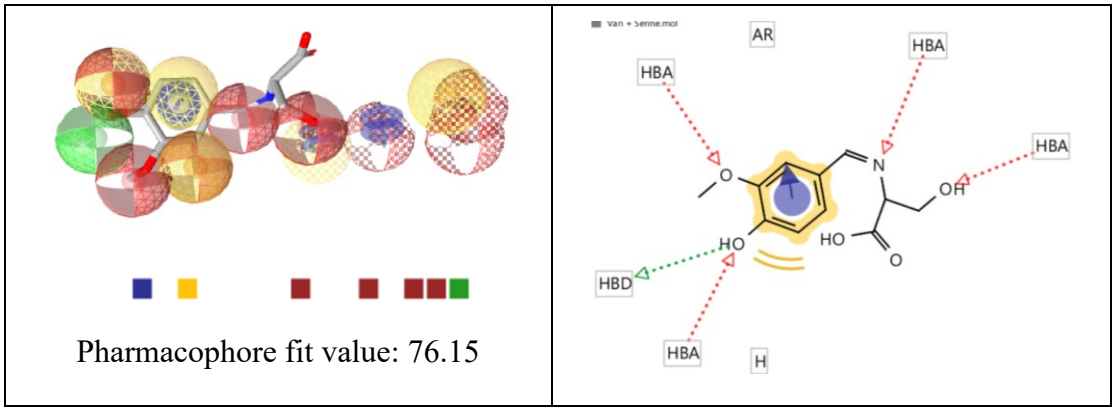


Figure 4.84: Interaction, pharmacophore fit value and matching features of compound (2) and pharmacophore model

As for compound (4), the benzene ring of phenylhydrazine aligned with 1 AR feature of the model. With the matching features at the vanillin and imine bond the same as (1), (2), (6), (7), (8), (10), (12), (13), (14), (15), (18), (19) and (20), a total of 7 features were matched, and with 75.91 fit value as shown in Figure 4.85.

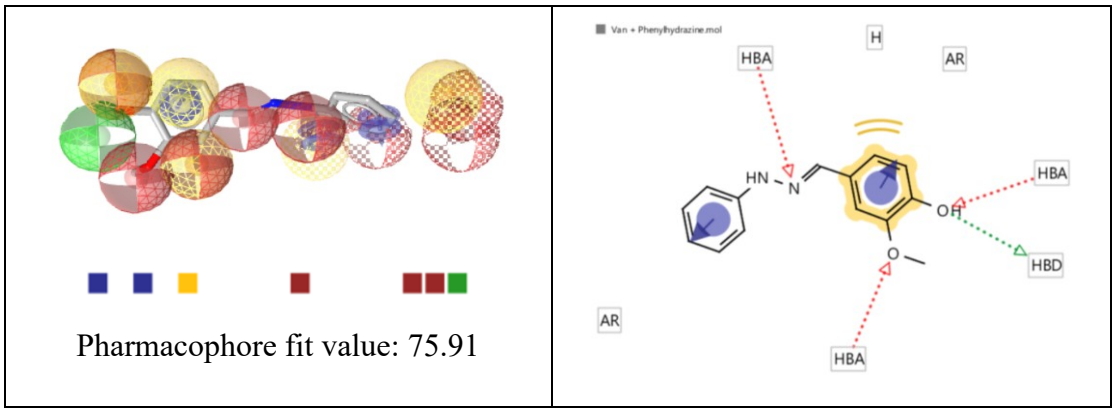


Figure 4.85: Interaction, pharmacophore fit value and matching features of compound (4) and pharmacophore model

Based on Figure 4.86, compound (11) showed a fit value of 75.84 and 7 matching features in the pharmacophore model. Similarly, 1 HBA was shown on the nitrogen atom of imine bond, 1 HI and 1 AR were shown on the benzene ring of vanillin structure, 1 HBA and 1 HBD were shown on the OH, and 2 HBA were shown on the C-O-C of vanillin structure. Despite that, no matching features were shown on the ethylenediamine structure, thus potential to possess antibacterial activity against *S. aureus* FtsZ was slightly low.

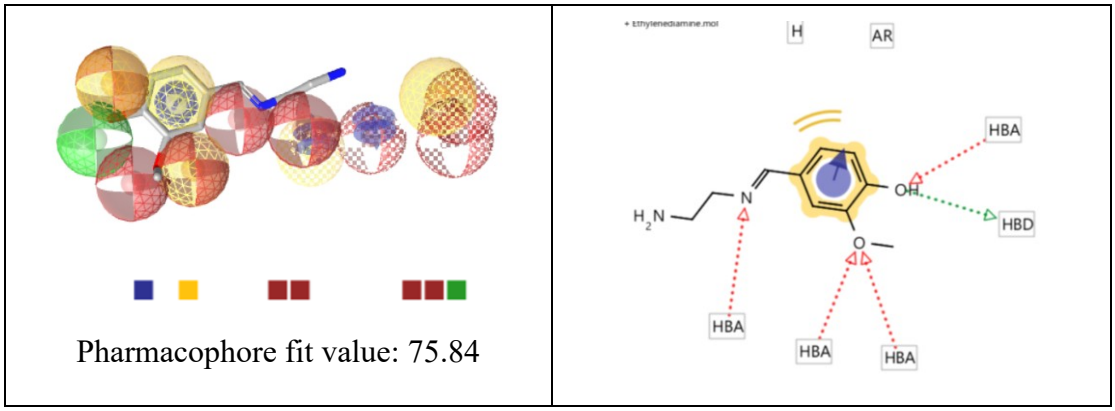


Figure 4.86: Interaction, pharmacophore fit value and matching features of compound (11) and pharmacophore model

Last but not least, compound (3) showed the lowest pharmacophore fit value of 66.45 and with only 6 matching features as shown in Figure 4.87. Benzene ring of vanillin structure showed 1 HI and 1 AR features, and C-O-C showed only 1 HBA. The OH of vanillin structure only aligned with 1 HBA, being the only Schiff base vanillin derivative that do not align with any HBD. On top of that, 2 HBA were shown by the nitrogen atom of imine bond and water molecule respectively.

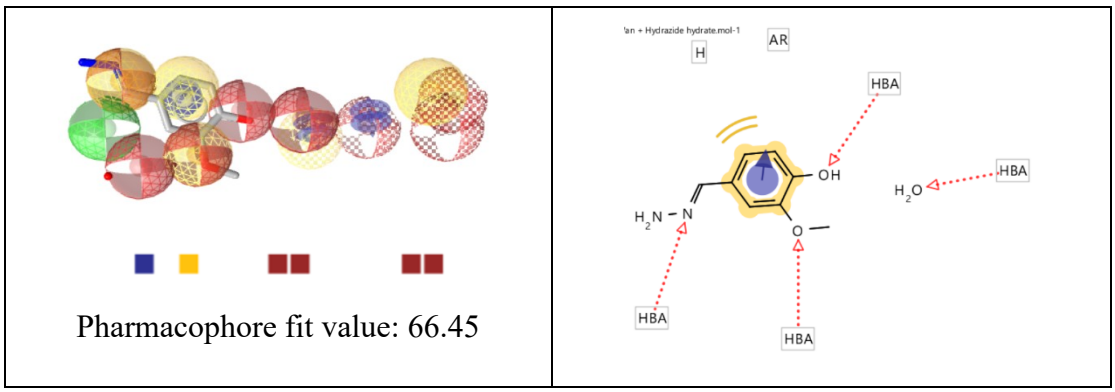


Figure 4.87: Interaction, pharmacophore fit value and matching features of compound (3) and pharmacophore model

Despite the fact that compound (2), (3), (4) and (11) showed slightly lower pharmacophore fit values and matching features, the remaining 17 Schiff base vanillin derivatives were still considered able to fit in the pharmacophore model and depict considerably good pharmacophore fit values and matching features. Aforementioned, Schiff

base vanillin derivatives depict good inhibitory activity against a series of bacterial strains, including *S. aureus*, particularly at the imine linkage and vanillin structure (Hissam et al., 2024). The literature review supported the obtained results, such that matching features were discovered at the vanillin structures and imine bond of all Schiff base vanillin derivatives. Thus, all Schiff base vanillin derivatives were proceeded for evaluations in the structure-based approach to confirm their potential inhibitory activity against *S. aureus* FtsZ.

4.2.2 Structure-Based Approach

Similarly, structure-based approach evaluations were separated into two parts: structure-based pharmacophore modelling and structure-based molecular docking through similar methods but different crystal structure of protein.

4.2.2.1 Structure-Based Pharmacophore Modelling

The structure-based pharmacophore modelling was done by first retrieving *S. aureus* FtsZ in complex with the inhibitor ligand, known as PC190723, from PDB which is encoded as 3VOB. Upon generation of pharmacophore model of PC190723 ligand, the pharmacophore model was composed of a total of 19 pharmacophore features as well as shown in Figure 4.88.

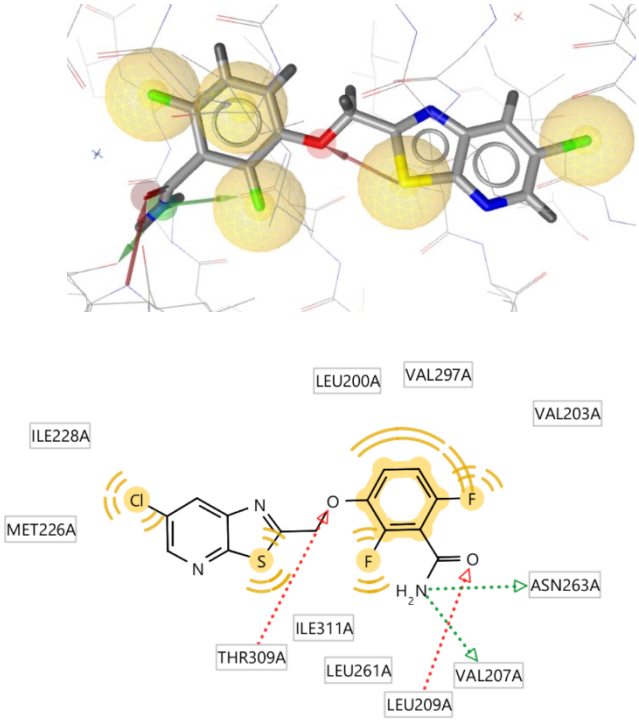
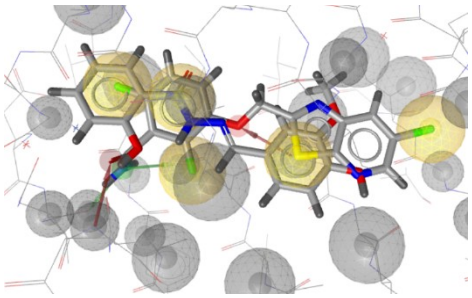


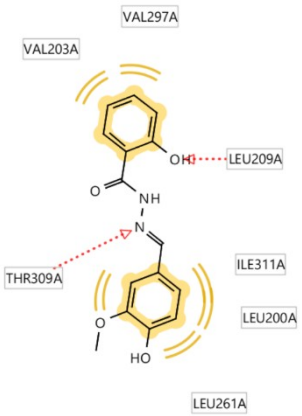
Figure 4.88: Pharmacophore model of PC190723 ligand in 3VOB

As depicted in Figure 4.88, the pharmacophore model was greatly composed of HI features, such that there were a total of 15 HI towards MET226, ILE228, LEU200, VAL297, VAL203, THR309, ILE311 and LEU261. Additionally, 2 HBA towards THR309 and LEU209, as well as 2 HBD towards VAL207 and ASN263 were also depicted by the pharmacophore model of PC190723. 20 out of 21 Schiff base vanillin derivatives were able to show alignment to the ligand and pharmacophore model of PC190723, thus showing matching interactions towards the active sites of 3VOB. Their alignment and matching interactions towards the active sites of 3VOB were illustrated and elaborated from Figure 4.89 to Figure 4.108. Most of the Schiff base vanillin derivatives showed alignment with the pharmacophore model of PC190723 ligand as well as matching interactions particularly at the vanillin structure and imine bond. This indicated the significance of Schiff base vanillin derivative structures as potential inhibitors of *S. aureus* FtsZ.

Figure 4.89 showed the alignment and interactions portrayed by compound (1) towards the active site of 3VOB. 8 out of 19 pharmacophore features of the model were being aligned and matched by compound (1). Beginning from the vanillin structure, the benzene ring depicted a total of 4 HI towards ILE311, LEU200, LEU261 and THR309. Additionally, nitrogen atom of the C=N bond showed HBA alignment with THR309. On top of that, the benzene ring of salicyl hydrazide depicted 2 HI towards VAL203 and VAL297, and the OH depicted HBA towards LEU209, thus showing considerably good alignment.



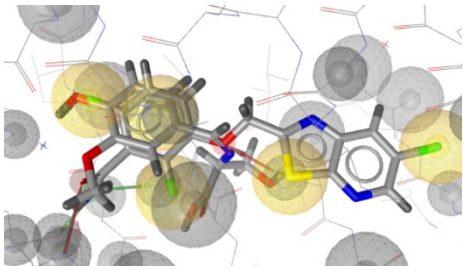
Alignment of compound (1) to the PC190723 ligand



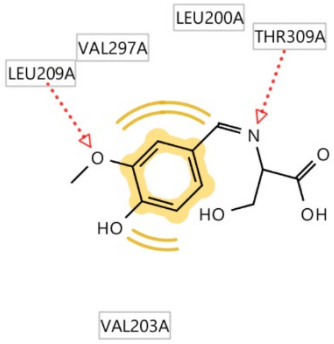
Matching interactions of compound (1) with the pharmacophore model

Figure 4.89: Alignment of compound (1) with PC190723 ligand and the matching interactions with the pharmacophore model

For compound (2), matching interactions were discovered at the vanillin structure and imine linkage of the Schiff base vanillin derivative of serine. The benzene ring matched with 3 HI towards VAL297, LEU200 and VAL203, the C-O-C showed HBA towards LEU209, whereas the nitrogen atom of C=N bond showed HBA as well towards THR309. The alignment and matching interactions of compound (2) to the ligand and pharmacophore model were shown in Figure 4.90.



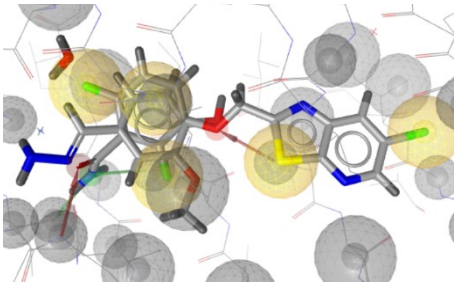
Alignment of compound (2) to the PC190723 ligand



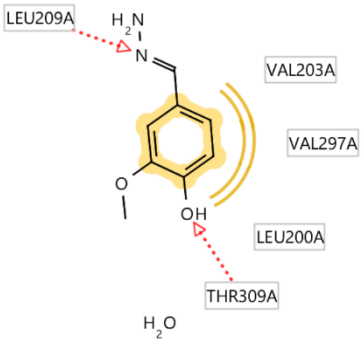
Matching interactions of compound (2) with the pharmacophore model

Figure 4.90: Alignment of compound (2) with PC190723 ligand and the matching interactions with the pharmacophore model

In exactly the same way as compound (2), for compound (3), (4) and (5), the benzene ring also showed matching interactions with 3 HI towards VAL297, LEU200 and VAL203. Additionally, OH of vanillin part depicted HBA towards THR309, and nitrogen atom of C=N showed matching interactions with LEU209. Therefore, compound (3) was also able to show good alignment to PC190723 ligand and satisfied matching interactions with the pharmacophore model, pictured and illustrated in Figure 4.91.



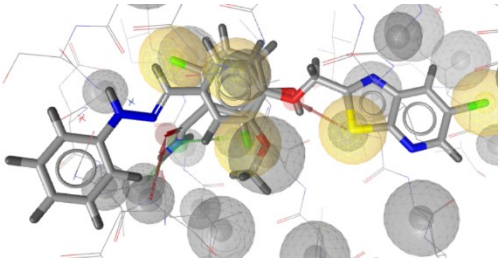
Alignment of compound (3) to the PC190723 ligand



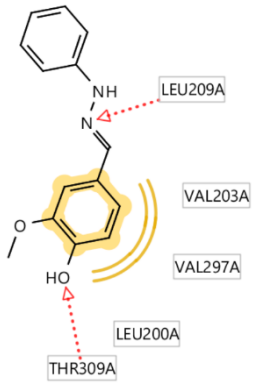
Matching interactions of compound (3) with the pharmacophore model

Figure 4.91: Alignment of compound (3) with PC190723 ligand and the matching interactions with the pharmacophore model

Compound (4) showed alignment with the PC190723 ligand and good pharmacophore fit in the model, with matching features same as compound (3) as elaborated earlier. Figure 4.91 showed the alignment and matching interactions of compound (4) with the ligand and pharmacophore model of PC190723 in 3VOB.



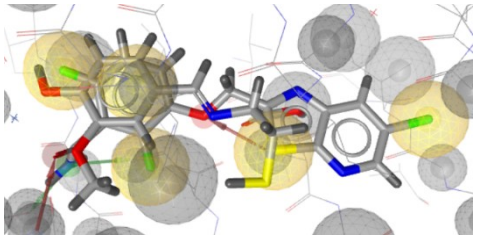
Alignment of compound (4) to the PC190723 ligand



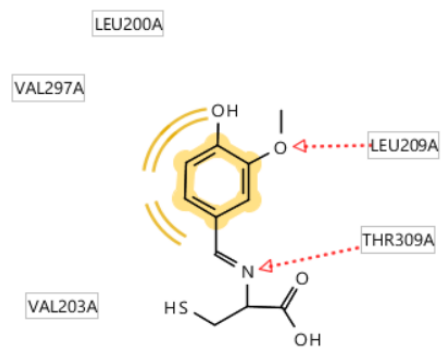
Matching interactions of compound (4) with the pharmacophore model

Figure 4.92: Alignment of compound (4) with PC190723 ligand and the matching interactions with the pharmacophore model

Compound (5), which is Schiff base vanillin derivative of cysteine, also showed similar alignment and matching interactions as compound (2), (3) and (4), except that the HBA towards LEU209 was aligned to C-O-C of the vanillin as depicted in Figure 4.93.



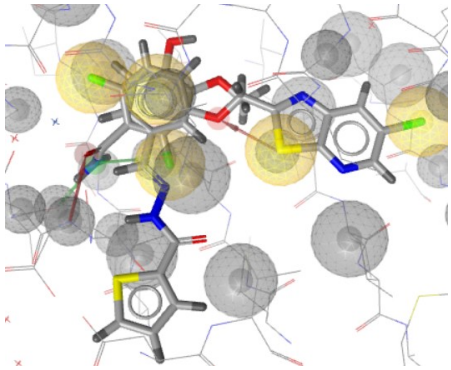
Alignment of compound (5) to the PC190723 ligand



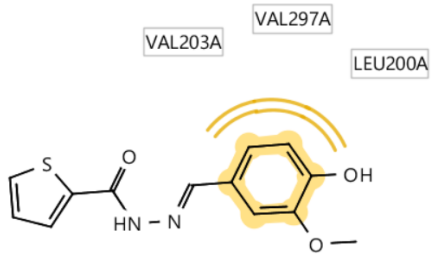
Matching interactions of compound (5) with the pharmacophore model

Figure 4.93: Alignment of compound (5) with PC190723 ligand and the matching interactions with the pharmacophore model

For compound (6), the alignment and matching interactions with PC190723 ligand and pharmacophore model was not as good as the other compounds. Only 3 interactions were being aligned and matched, which were 3 HI towards VAL297, LEU200 and VAL203 by the benzene ring of vanillin structure, as shown in Figure 4.94. Despite that, the compound still showed alignment to the ligand, thus was still subjected to structure-based molecular docking for further evaluation.



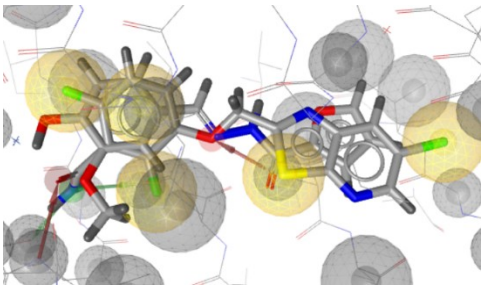
Alignment of compound (6) to the PC190723 ligand



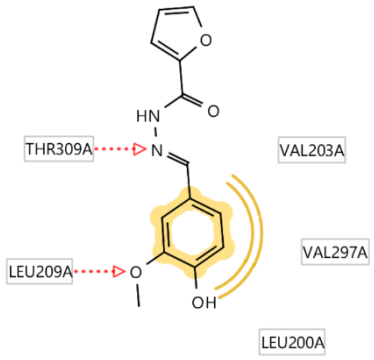
Matching interactions of compound (6) with the pharmacophore model

Figure 4.94: Alignment of compound (6) with PC190723 ligand and the matching interactions with the pharmacophore model

Furthermore, Schiff base vanillin derivative of 2-furoic acid hydrazide also depicted similar matching interactions and alignment as the previous compounds (2), (3), (4) and (5). 3 HI were depicted by the benzene ring of vanillin structure towards VAL297, LEU200 and VAL203, 2 HBA were depicted each by nitrogen atom of C=N bond towards THR309, and C-O-C of vanillin structure towards LEU209. All matching interactions and alignment were shown in Figure 4.95.



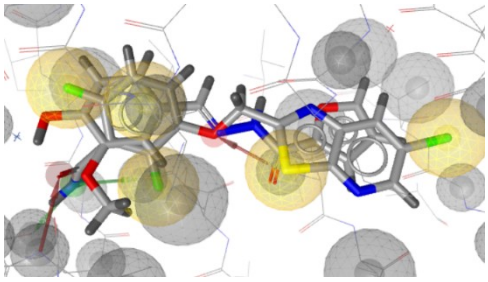
Alignment of compound (7) to the PC190723 ligand



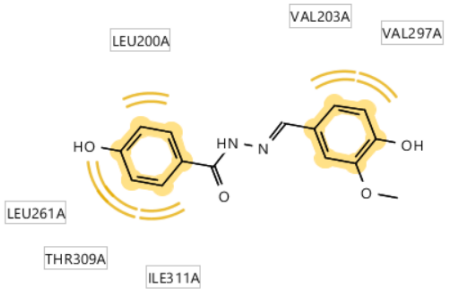
Matching interactions of compound (7) with the pharmacophore model

Figure 4.95: Alignment of compound (7) with PC190723 ligand and the matching interactions with the pharmacophore model

Compound (8) showed considerably good alignment with PC190723 ligand, and with good pharmacophore fit in the model illustrated in Figure 4.96. The benzene ring of vanillin structure showed 2 HI towards VAL203 and VAL297, whereas the benzene ting of 4-hydroxybenzhydrazide showed 4 HI towards LEU200, LEU261, THR309 amd ILE311.



Alignment of compound (8) to the PC190723 ligand

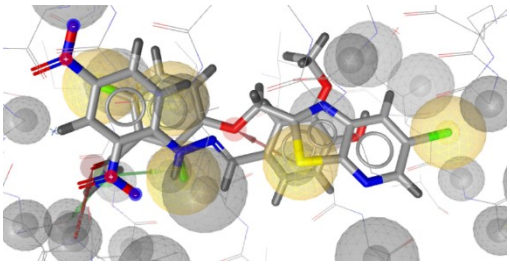


Matching interactions of compound (8) with the pharmacophore model

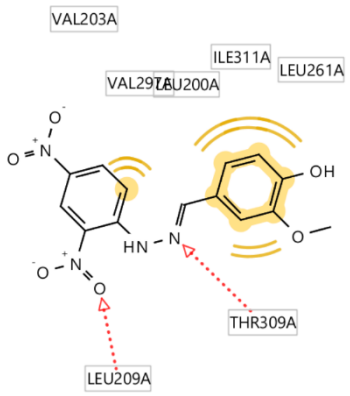
Figure 4.96: Alignment of compound (8) with PC190723 ligand and the matching interactions with the pharmacophore model

Moreover, compound (9) was also able to show good alignment with PC190723 ligand and satisfactory pharmacophore fit in the pharmacophore model. The benzene ring of vanillin structure depicted a total of 4 HI towards LEU200, ILE311, LEU261 and THR309,

whereas the carbon atom of benzene ring of 2,4-dinitrophenylhydrazine depicted also 2 HI towards VAL297 and VAL203. On top of that, the nitrogen atom of C=N bond showed 1 HBA towards THR309, and the nitro group also showed 1 HBA towards LEU209. By depicting a total of 7 matching pharmacophore interactions towards active site of 3VOB, the alignment and fit were considered satisfactory as shown in Figure 4.97.



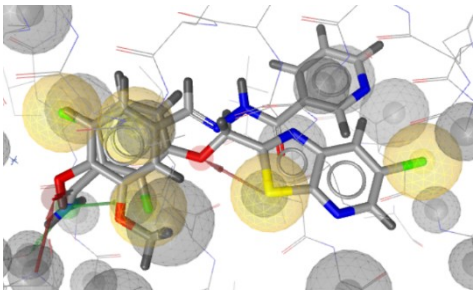
Alignment of compound (9) to the PC190723 ligand



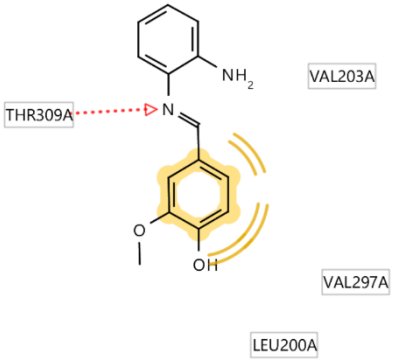
Matching interactions of compound (9) with the pharmacophore model

Figure 4.97: Alignment of compound (9) with PC190723 ligand and the matching interactions with the pharmacophore model

As for compound (10) and (11), once again similarly, the Schiff base vanillin derivatives were only able to depict matching interactions similar to compound (2), (3), (4), (5) and (7). These include 3 HI towards VAL297, VAL203 and LEU200 by the benzene ring of vanillin structure. The nitrogen atom of C=N bond showed 1 HBA towards THR309. The alignment and matching interactions of compound (10) to the ligand and its pharmacophore model were shown in Figure 4.98.



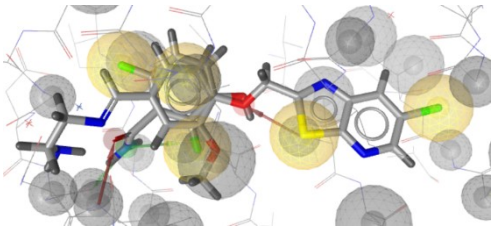
Alignment of compound (10) to the PC190723 ligand



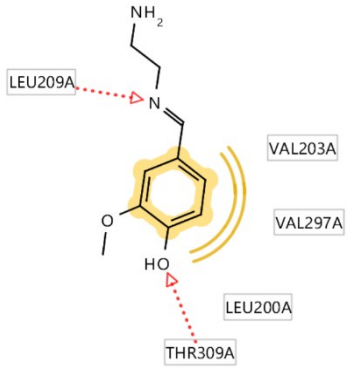
Matching interactions of compound (10) with the pharmacophore model

Figure 4.98: Alignment of compound (10) with PC190723 ligand and the matching interactions with the pharmacophore model

Aforementioned, compound (11) showed the similar matching interactions as compound (10), except that 2 HBA towards THR309 and LEU209 by OH bond of vanillin and nitrogen atom of C=N bond respectively, with the alignment and matching interactions towards the PC190723 in 3VOB as illustrated in Figure 4.99.



Alignment of compound (11) to the PC190723 ligand

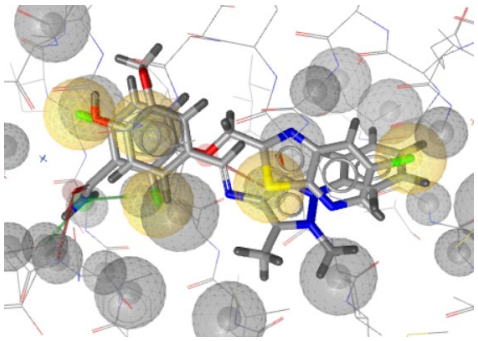


Matching interactions of compound (11) with the pharmacophore model

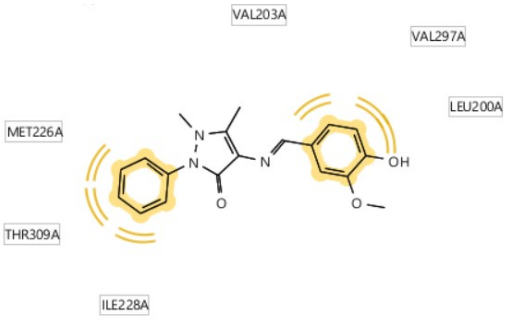
Figure 4.99: Alignment of compound (11) with PC190723 ligand and the matching interactions with the pharmacophore model

Compound (12) was able to show more matching interactions with the pharmacophore model of PC190723 in the active site of 3VOB. Based on Figure 4.100, a

total of 6 HI were depicted, which include 3 HI towards VAL203, VAL297, LEU200 by benzene ring of vanillin structure, and 3 HI towards MET226, THR309 and ILE228 by benzene ring of 4-aminoantipyrine. As a result, the alignment of compound (12) towards PC190723 ligand was considerably good.



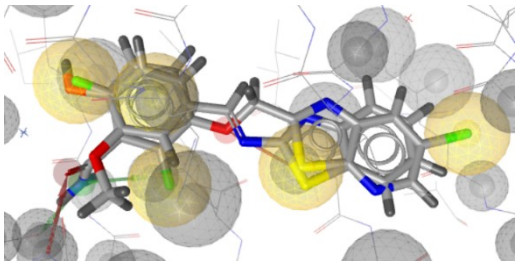
Alignment of compound (12) to the PC190723 ligand



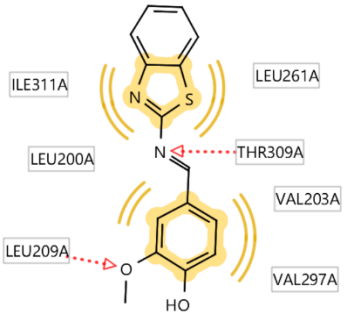
Matching interactions of compound (12) with the pharmacophore model

Figure 4.100: Alignment of compound (12) with PC190723 ligand and the matching interactions with the pharmacophore model

On top of that, compound (13), which is the Schiff base vanillin derivative of 2-aminobenzothiazole, also showed quite a fine alignment to PC190723, as well as good matching interactions to the active site of 3VOB. Figure 4.101 showed that 3 HI were pictured by the benzene ring of vanillin structure towards VAL297, VAL203, LEU200, whereas 4 HI were shown by the thiazole group towards ILE311, LEU261, LEU200 and THR309. Additionally, 2 HBA were portrayed towards THR309 and LEU209 by nitrogen atom of C=N bond and C-O-C of vanillin part respectively.



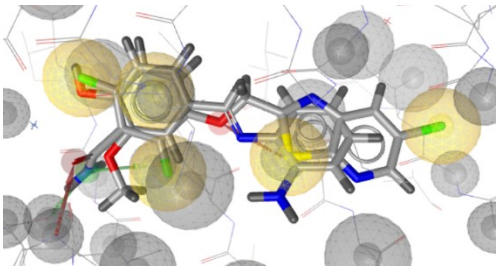
Alignment of compound (13) to the PC190723 ligand



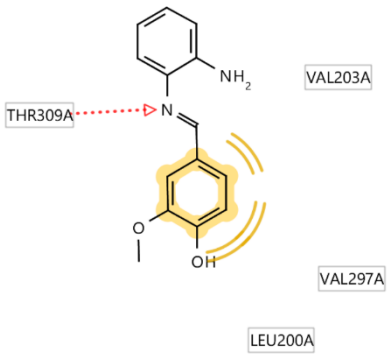
Matching interactions of compound (13) with the pharmacophore model

Figure 4.101: Alignment of compound (13) with PC190723 ligand and the matching interactions with the pharmacophore model

For compound (14), the matching interactions were slightly less than the previous compounds, including 3 HI towards VAL203, VAL297 and LEU200 by benzene ring of vanillin part, as well as 1 HBA towards THR309 by nitrogen atom of C=N bond. The alignment of compound (14) to the PC190723 ligand, as well as the matching interactions in the active site of 3VOB were delivered in Figure 4.102.



Alignment of compound (14) to the PC190723 ligand

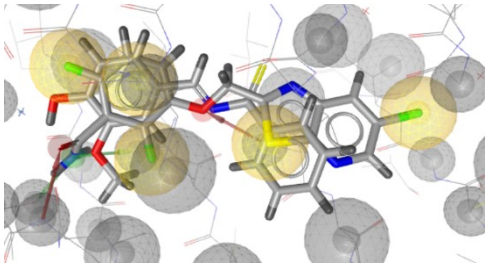


Matching interactions of compound (14) with the pharmacophore model

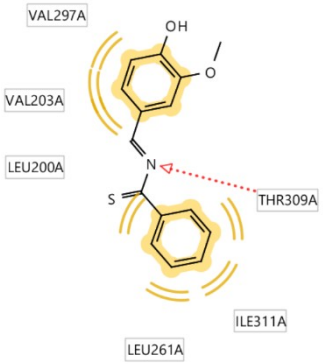
Figure 4.102: Alignment of compound (14) with PC190723 ligand and the matching interactions with the pharmacophore model

Schiff base vanillin derivative of thiobenzamide, which is compound (15), was able to depict a great number of matching interactions in the active site of 3VOB as well.

According to Figure 4.103, similarly, the benzene ring of vanillin structure was able to show 3 HI towards VAL203, VAL297 and LEU200, whereas the benzene ring of thiobenzamide also showed 4 HI towards LEU26, ILE311. THR309 and LEU200. On top of that, 1 HBA was depicted by nitrogen atom of C=N bond towards THR309.



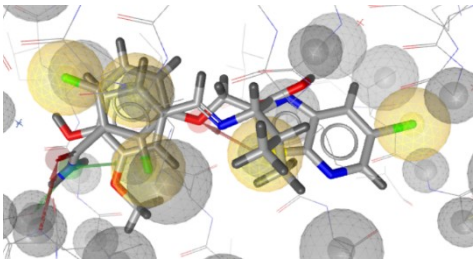
Alignment of compound (15) to the PC190723 ligand



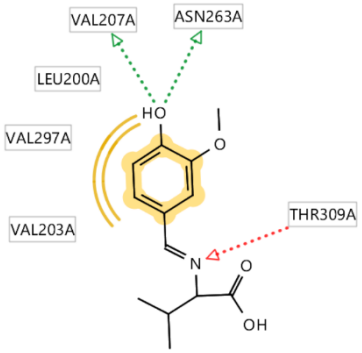
Matching interactions of compound (15) with the pharmacophore model

Figure 4.103: Alignment of compound (15) with PC190723 ligand and the matching interactions with the pharmacophore model

For compound (16), 3 HI were also depicted by the benzene ring of vanillin structure towards VAL203, VAL297 and LEU200. The OH of vanillin structure showed HBD alignment with two active sites of 3VOB, which include VAL207 and ASN263. Additionally, 1 HBA was also aligned by the nitrogen atom of C=N bond towards THR309. As a result, compound (16) showed quite a satisfactory alignment and matching interactions with the PC190723 ligand and the pharmacophore model respectively as illustrated in Figure 4.104.



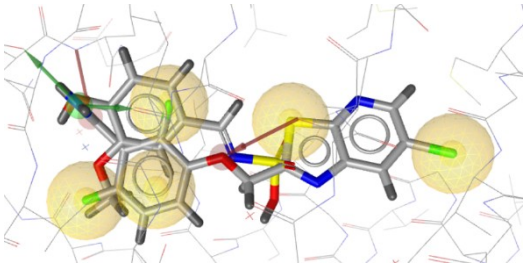
Alignment of compound (16) to the PC190723 ligand



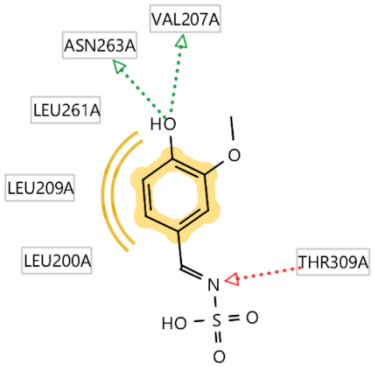
Matching interactions of compound (16) with the pharmacophore model

Figure 4.104: Alignment of compound (16) with PC190723 ligand and the matching interactions with the pharmacophore model

Compound (17), which is the Schiff base vanillin derivative of sulfamic acid, was also able to show quite a number of matching interactions with the pharmacophore model of PC190723 similar to compound (16), thus a good alignment with the ligand. Based on Figure 4.105, the benzene ring of vanillin structure of compound (17) portrayed 3 HI towards LEU200, LEU209 and LEU261, whereas the OH of vanillin structure pictures 2 HBD towards ASN263 and VAL207. Additionally, the nitrogen of C=N bond depicted a HBA towards THR309.



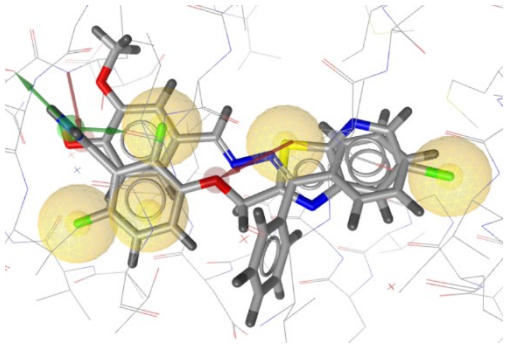
Alignment of compound (17) to the PC190723 ligand



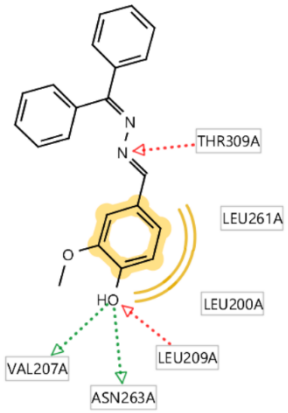
Matching interactions of compound (17) with the pharmacophore model

Figure 4.105: Alignment of compound (17) with PC190723 ligand and the matching interactions with the pharmacophore model

Compound (19), which is the Schiff base vanillin derivative of benzophenone hydrazine, depicted alignment towards PC190723 ligand as well. Matching interactions include 3 HI towards LEU261, LEU200 and LEU209 by benzene of vanillin, 2 HBD towards VAL207 and ASN263 by OH of vanillin, and 1 HBA towards THR309 by nitrogen of C=N bond as shown in Figure 4.106.



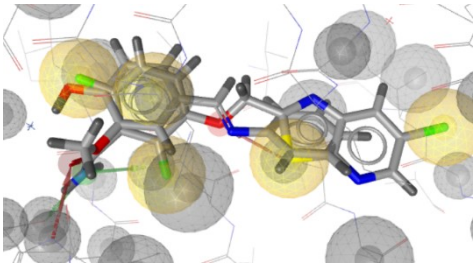
Alignment of compound (19) to the PC190723 ligand



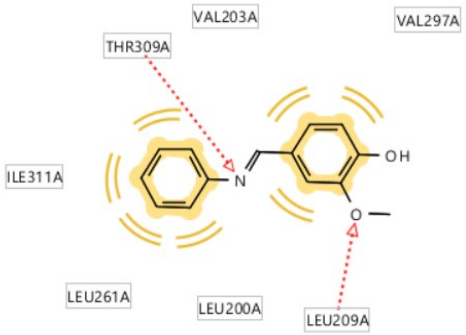
Matching interactions of compound (19) with the pharmacophore model

Figure 4.106: Alignment of compound (19) with PC190723 ligand and the matching interactions with the pharmacophore model

Figure 4.107 showed the alignment and matching interactions of compound (20) towards the ligand and its pharmacophore model in the active site of 3VOB. The figure clearly illustrated that a total of 7 HI were aligned by compound (20), which were 3 HI towards VAL203, VAL297 and LEU200 by benzene ring of vanillin part, and 4 HI towards THR309, ILE311, LEU261 and LEU200 by benzene ring of aniline structure. On top of that, 2 HBA were also depicted by nitrogen of C=N and C-O-C of vanillin structure towards THR309 and LEU209 respectively.



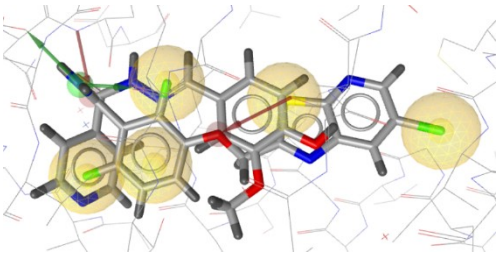
Alignment of compound (20) to the PC190723 ligand



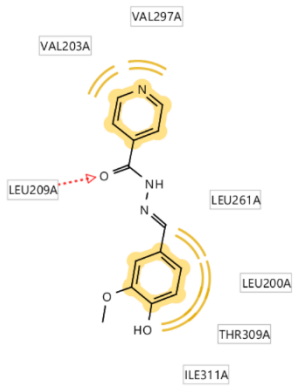
Matching interactions of compound (20) with the pharmacophore model

Figure 4.107: Alignment of compound (20) with PC190723 ligand and the matching interactions with the pharmacophore model

Lastly, Schiff base of isonicotinic acid hydrazide, which made compound (21), also showed excellent alignment with the PC190723 ligand. The matching interactions with the pharmacophore model of the ligand were 4 HI by benzene ring of vanillin towards LEU261, LEU200, THR309 and ILE311, 2 HI by the pyridine structure of isonicotinic acid hydrazide towards VAL203 and VAL297, as well as 1 HBA towards LEU209 by C=O of isonicotinic acid hydrazide. All matching interactions and alignments were as shown in Figure 4.108.



Alignment of compound (21) to the PC190723 ligand



Matching interactions of compound (21) with the pharmacophore model

Figure 4.108: Alignment of compound (21) with PC190723 ligand and the matching interactions with the pharmacophore model

Out of all Schiff base vanillin derivatives, compound (18) failed to show alignment with the PC190723 ligand, thus failed to match with the pharmacophore features of the ligand due to molecule interaction with the exclusion volume sphere as shown in Figure 4.109. Lack of suitable conformations and functional groups to show alignment with the pharmacophore model may also resulted in the failure of compound (18) to depict matching interactions with the pharmacophore model of PC190723.

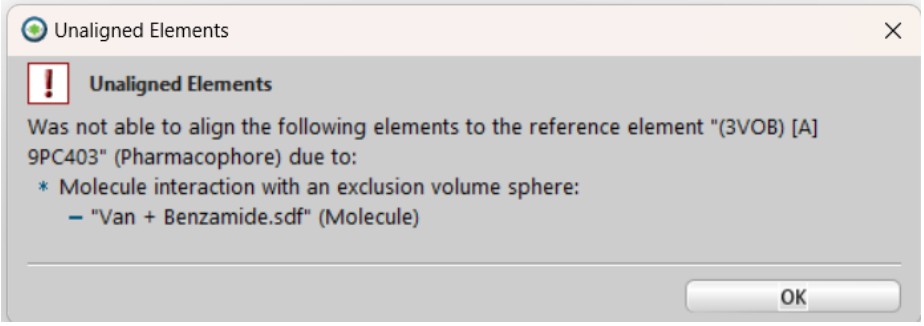


Figure 4.109: Failure of compound (18) to align with oseltamivir carboxylate ligand and the pharmacophore model

The two distinct binding pockets of FtsZ were the nucleotide-binding domain (NBD), or also known as the GTP binding site, as well as the inter-domain cleft binding site (IDC) (Pradhan et al., 2021). Located between N-terminal and C-terminal domains, the IDC served as an attractive target domain for the discovery of inhibitors. Out of great number of classes of compounds, benzamides-based inhibitors of diverse chemical structures are reported to depict potential inhibitory activity towards IDC, which include PC190723 (Casiraghi et al., 2020). Similarly, the IDC of *S. aureus* is composed of key active site residues important to be inhibited, such that out of all key active site residues, the residues that were depicted by the pharmacophore model of PC190723 in 3VOB were VAL297, VAL203, THR309, LEU200, LEU209 and ASN263 (Pradhan et al., 2021).

The 20 Schiff base vanillin derivatives were able to show 3 to 6 matching interactions with the 6 key active site residues, thus showing great potential as FtsZ inhibitors of *S. aureus*. The only compound that successfully aligned with all 6 key active site residues was compound (16), Schiff base vanillin derivative of L-valine. Most of the compounds were able to show 5 matching interactions with the key active site residues, which were compounds (1), (2), (3), (4), (5), (7), (10), (11), (13), (17), (19), (20) and (21), which is considered as excellent alignment and potential FtsZ inhibitors as well. Additionally, compounds (8), (9), (12), (14) and (15) successfully aligned with 4 matching interactions. On top of that, compound (6) only depicted with 3 matching interactions with the key active site residues, which were VAL203, VAL297 and LEU200, thus possessed lower potential inhibitory activity against *S. aureus* FtsZ. Thus, the 19 Schiff base vanillin derivatives, except compound (6), were theoretically explained as potential inhibitors of *S. aureus* FtsZ, as to have similar biological activity as the PC190723 ligand in 3VOB. Consequently, the derivatives were proceeded to structure-based molecular docking for further evaluation of their binding affinity in the binding site of 3VOB.

4.2.2.2 Structure-Based Molecular Docking

As mentioned earlier, a considerable binding affinity value which possess strong binding interaction towards binding pocket should be less than –6.00 kcal/mol to indicate cluster active (Shityakov and Förster, 2014). Based on Table 4.15, all 19 Schiff base vanillin derivatives, calculated in triplicates, were able to show binding affinity values less than –6 kcal/mol, ranging from -6.10 to -10.40 kcal/mol, thus indicating strong binding interaction towards the binding pocket of 3VOB. Suitable chemical conformations with the lowest conformational energies, as well as favorable functional groups may be the possible factors which resulted the binding affinity values range.

Table 4.15: Binding affinity values of Schiff base vanillin derivatives in the active site of 3VOB

Schiff base vanillin derivatives (Vanillin + …)	Binding affinity values (kcal/mol)
(1) Salicyl hydrazide	-9.90 ± 0.12
(2) Serine	-7.80 ± 0.35
(3) Hydrazide hydrate	-6.10 ± 0.24
(4) Phenylhydrazine	-8.20 ± 0.22
(5) Cysteine	-7.60 ± 0.08
(7) 2-furoic acid hydrazide	-8.70 ± 0.19
(8) 4-hydroxybenzhydrazide	-9.60 ± 0.29
(9) 2,4-dinitrophenylhydrazine	-9.50 ± 0.11
(10) Nicotinic hydrazide	-8.80 ± 0.23
(11) Ethylenediamine	-6.60 ± 0.16
(12) 4-aminoantipyrine	-10.40 ± 0.07
(13) 2-aminobenzothiazole	-9.60 ± 0.18
(14) O-phenyldiamine	-9.00 ± 0.15
(15) Thiobenzamide	-8.50 ± 0.16
(16) L-valine	-8.20 ± 0.20
(17) Sulfamic acid	-7.10 ± 0.21
(19) Benzophenone hydrazone	-9.80 ± 0.33
(20) Aniline	-8.50 ± 0.03
(21) Isonicotinic acid hydrazide	-8.80 ± 0.07

4.2.2.3 Summary of Schiff Base Vanillin Derivatives as FtsZ Inhibitors of *S. aureus*

In conclusion, 15 out of 21 Schiff base vanillin derivatives were discovered to possess potential inhibitory activity towards FtsZ of *S. aureus* based on ligand-based and structure-based approach. Out of all Schiff base vanillin derivatives, compound (18) was unable to show good result in structure-based pharmacophore modelling and molecular docking.

Based on results from ligand-based approach, all 21 Schiff base vanillin derivatives showed 6 to 10 matching pharmacophore features out of a total of 17 pharmacophore features from the generated pharmacophore model, with pharmacophore fit values ranging from 66.45 to 104.06. The pharmacophore fit values, except for compounds (2), (3), (4) and (11), were greater than 50% of the pharmacophore fit values of training sets, ranging from 146.87 to 161.97. Hence, based on theory, the remaining 17 Schiff base vanillin derivatives were considered to possess similar biological activity as the generated pharmacophore model, which is inhibitory activity against FtsZ of *S. aureus*.

In structure-based pharmacophore modelling, 19 out of 21 Schiff base vanillin derivatives were able to show alignment with the PC190723 ligand in 3VOB active site, as well as matching interactions in the active site, showing great potential as FtsZ inhibitors of *S. aureus*. Out of 19 pharmacophore features of PC190723 ligand, the 20 Schiff base vanillin derivatives showed 3 to 9 matching features in alignment with the ligand. Out of the 6 key active site residues, including VAL297, VAL203, THR309, LEU200, LEU209 and ASN263, the 19 Schiff base vanillin derivatives were able to depict matching interactions with 4 to 6 of the residues, with compound (6) only depicting 3 interactions to the key active site residues. This result provided further support for the results in ligand-based approach,

affirming the potential inhibitory activity of the 19 Schiff base vanillin derivatives against FtsZ of *S. aureus*. However, compound (18) failed to show alignment with the PC190723 ligand due to molecule interaction with the exclusion volume sphere, and possibly lack of suitable functional groups and conformation which can align with the pharmacophore model of PC190723. As a result, compound (18) was not proceeded to molecular docking. 19 Schiff base vanillin derivatives that showed more than half of the matching features, which were 4 to 6 matching features out of a total of 6 features and prioritized to be subjected to synthesis include compounds (1), (2), (3), (4), (5), (7), (8), (9), (10), (11), (12), (13), (14), (15), (16), (17), (19), (20) and (21).

Upon molecular docking of the Schiff base vanillin derivatives in the active site of 3VOB, the binding affinity values were all less than –6.00 kcal/mol. This showed that they depict active and strong binding interaction with the active site of 3VOB, thus giving further fundamental support to the results obtained from ligand and structure-based approach.

4.3 Conclusion of Schiff Base Vanillin Derivatives as Potential Inhibitors of Neuraminidase of *S. pneumoniae* and FtsZ of *S. aureus*

In combination of the ligand-based and structure-based results of Schiff base vanillin derivatives as both neuraminidase inhibitors of *S. pneumoniae* and FtsZ inhibitors of *S. aureus*, all results were as shown in Table 4.16, such that compounds shaded in blue indicated satisfactory results, and compounds shaded in pink indicated unsatisfied results. In ligand-based approach, Schiff base vanillin derivatives that showed pharmacophore fit value and matching features 50% and above of the training sets were considered satisfactory. In structure-based approach, Schiff base vanillin derivatives that showed great number of matching interactions with more than half towards the key active site residues were considered satisfactory.

Table 4.16: Conclusion of Schiff base vanillin derivatives as neuraminidase inhibitors of *S. pneumoniae* and FtsZ inhibitors of *S. aureus*

Neuraminidase inhibitors of *S. pneumoniae*		**FtsZ inhibitors of *S. aureus***	
Schiff base vanillin derivatives			
Ligand-based approach	Structure-based approach	Ligand-based approach	Structure-based approach
(1)	**(1)**	**(1)**	**(1)**
(2)	**(2)**	**(2)**	**(2)**
(3)	**(3)**	**(3)**	**(3)**
(4)	**(4)**	**(4)**	**(4)**
(5)	**(5)**	**(5)**	**(5)**
(6)	**(6)**	**(6)**	**(6)**
(7)	**(7)**	**(7)**	**(7)**
(8)	**(8)**	**(8)**	**(8)**
(9)	**(9)**	**(9)**	**(9)**
(10)	**(10)**	**(10)**	**(10)**
(11)	**(11)**	**(11)**	**(11)**
(12)	**(12)**	**(12)**	**(12)**
(13)	**(13)**	**(13)**	**(13)**
(14)	**(14)**	**(14)**	**(14)**
(15)	**(15)**	**(15)**	**(15)**
(16)	**(16)**	**(16)**	**(16)**
(17)	**(17)**	**(17)**	**(17)**
(18)	**(18)**	**(18)**	**(18)**

Table 4.16 continued

(19)	**(19)**	**(19)**	**(19)**
(20)	**(20)**	**(20)**	**(20)**
(21)	**(21)**	**(21)**	**(21)**

As a result, a total of 10 Schiff base vanillin derivatives, which were compounds (5), (8), (9), (10), (12), (15), (16), (17), (19) and (21) were concluded as potential inhibitors of *S. pneumoniae* neuraminidase and *S. aureus* FtsZ *via* computational-aided methods. Based on the chemical structures of these compounds, primary amines of (5), (8), (12) and (16) are electron donating groups (EDG). The EDG are able to increase the electron density of the imine bond and aromatic structure. This promotes strong HBD interaction sites and π–π stacking, as well as being able to show good binding interaction with HI and Ar features in the active site (Shaikh et al., 2024). Primary amines of (9), (10), (15), (17), (19) and (21) are electron withdrawing groups (EWG). Since they reduce electron density around the imine bond, this strengthen their role as HBA which favors ionic interactions in the active site (Shaikh et al., 2024). For having suitable molecular size and stable conformations in the active sites simultaneously, they were able to show promising potential as dual inhibitors of both *S. pneumoniae* neuraminidase and *S. aureus* FtsZ.

For being able to show good fit values, matching pharmacophore features and docking results in computational studies, the Schiff base vanillin derivatives were concluded to be pharmacophore-compliant and geometrically compatible to the binding site of neuraminidase and FtsZ. Despite that, good binding scores are still not sufficient as the solubility, permeability, metabolism and stability in the active site should also be taken into consideration. As a whole, results from computational studies should be combined with the

evaluation of druglikeness to analyse the ADMET properties of the vanillin derivatives. This is because modelling and docking results can only be predictive as they do not reflect the actual binding energy. Supportive evidence from druglikeness properties including good absorption and strong stability should be analysed to enhance the role of the vanillin derivatives as potential dual inhibitors of neuraminidase and FtsZ.

4.4 Lipinski's Rule of 5

Lipinski's Rule of 5, or known as RO5, is a set of rules utilized to evaluate the druglikeness or drugability of chemical compounds with particular biological activity, which is to be orally effective and active and to be absorbed by human body (Roskoski, 2019). RO5 provided description about the molecular properties greatly significant for a drug's pharmacokinetics in humans, which is known as 'ADME': absorption, distribution, metabolism, and excretion. Based on RO5, chemical compounds that were considered orally active with excellent absorption and permeation should have not more than 5 HBD, not more than 10 HBA, molecular weight less than 500 g/mol and calculated octanol-water partition coefficient value (c log P) not more than 5 (Lipinski, 2004). The origin of the name RO5 is because all numbers in the list of rules are of multiples of five.

Based on results from 4.1 and 4.2, the 10 Schiff base vanillin derivatives which showed considerably good results as potential neuraminidase and FtsZ inhibitors fulfilled all rules in RO5, which have less than 5 HBD, less than 10 HBA, molecular weight less than 500 g/mol and c log P less than 5 as depicted in Table 4.17. As a result, the 10 Schiff base vanillin derivatives were shown to exhibit favorable physicochemical properties for oral bioavailability, such as appropriate molecular size, lipophilicity, and hydrogen bonding capacity, which support their potential role as orally active drug candidates. Additionally,

this provided further fundamental support for the potential of the 10 Schiff base vanillin derivatives as neuraminidase and FtsZ inhibitors of *S. pneumoniae* and *S. aureus* respectively.

Table 4.17: Lipinski's Rule of 5 of Schiff base vanillin derivatives

Schiff base vanillin derivatives	c log P	Hydrogen bond donors (HBD)	Hydrogen bond acceptors (HBA)	Molecular weight (g/mol)
(5)	1.583	2	6	255.292
(8)	1.639	3	5	286.287
(9)	2.663	2	7	332.272
(10)	1.328	2	5	271.276
(12)	2.949	1	4	337.379
(15)	3.195	1	4	271.338
(16)	1.929	1	5	251.282
(17)	1.703	1	6	231.226
(19)	4.272	1	4	330.387
(21)	1.328	2	5	271.276

Exhibiting druglikeness reflect the ADMET properties of the Schiff base vanillin derivatives as orally active drugs. In combination with the results obtained from pharmacophore modelling and molecular docking, this suggests that the derivatives not only fullfill key physicochemical criteria for oral absorption, but also strong binding interactions with the target proteins. Their potential as promising lead candidates is strengthened and thus subjected to Schiff base synthesis reactions to be further evaluated.

4.5 Schiff Base Synthesis Reaction

Out of 10 Schiff base vanillin derivatives which showed good results in computational methods as potential neuraminidase and FtsZ inhibitors of *S. pneumoniae* and *S. aureus*, 6 Schiff base vanillin derivatives were successfully synthesized and characterized, which include (8), (9), (12), (15), (17) and (21). Generally, 1.52 g of vanillin, which is 0.01 mol of vanillin, reacted with 0.01 mol of primary amines to synthesize 0.01 mol of Schiff base vanillin derivatives. Upon monitor with TLC, the 6 Schiff base vanillin derivatives depict a single spot on the TLC plate when observed under ultraviolet light of 254 nm and 364 nm, indicating successful synthesis. The general synthetic routes of the 6 Schiff base vanillin derivatives were as illustrated in Table 4.18.

Table 4.18: General synthetic route of Schiff base vanillin derivatives

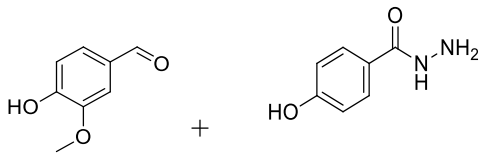
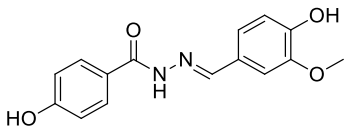
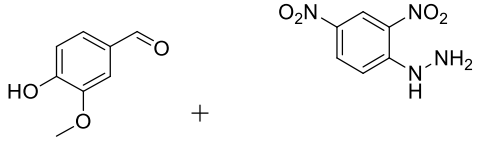
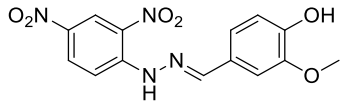
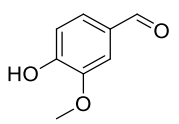
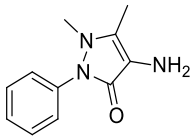
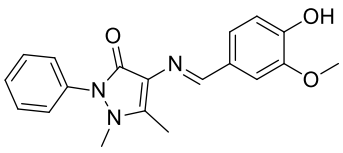
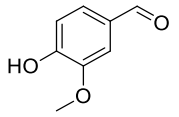
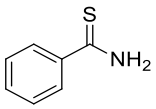
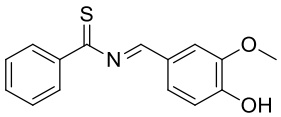
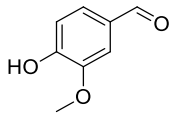
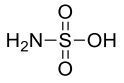
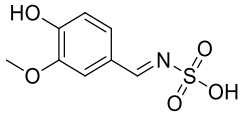
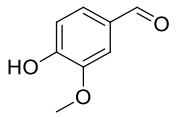
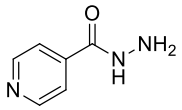
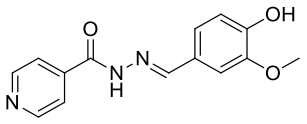
Vanillin + Primary amines	Schiff base vanillin derivatives
 Vanillin + 4-hydroxybenzhydrazide →	 **(8)** 4-hydroxy-N'-(4-hydroxy-3-methoxybenzylidene)benzohydrazide
 Vanillin + 2,4-dinitrophenylhydrazine →	 **(9)** 4-((2-(2,4-dinitrophenyl)hydrazono)methyl)-2-methoxyphenol

Table 4.18 continued

 Vanillin +  4-aminoantipyrine	→	 **(12)** 4-((4-hydroxy-3-methoxybenzylidene)amino)-1,5-dimethyl-2-phenyl-1H-pyrazol-3(2H)-one
 Vanillin +  Thiobenzamide	→	 **(15)** N-(4-hydroxy-3-methoxybenzylidene)benzothioamide
 Vanillin +  Sulfamic acid	→	 **(17)** (E)-(4-hydroxy-3-methoxybenzylidene)sulfamic acid
 Vanillin +  Isonicotinic acid hydrazide	→	 **(21)** N'-(4-hydroxy-3-methoxybenzylidene)isonicotinohydrazide

For the synthesis of compound (8), 1.52 g of vanillin was dissolved in 10 ml of methanol, making 0.01 mol of methanolic vanillin solution. 1.52 g of 4-hydroxybenzhydrazide was also dissolved in 10 ml of methanol, forming 0.01 mol of

methanolic solution of compound (8). The two methanolic solutions were reacted and subjected to heating at 65°C for 2 to 3 hours, with continuous stirring by using a magnetic stirrer, as well as continuous monitoring with TLC. Upon single spot being observed on the TLC plate, the heating was stopped and the solution was left to cool at room temperature until precipitate was formed. The precipitate was filtered, rinsed with methanol solution and dried in oven for about 5 minutes. 2.42 g of yellow crystals of compound (8) were successfully obtained, resulting in percentage yield of 84.62%.

In similar methodology, 1.52 g of 0.01 mol methanolic vanillin solution was reacted with 1.98 g of 0.01 mol of methanolic 2,4-dinitrophenylhydrazine, both dissolved in 10 ml of methanol solution respectively. Red crystals of compound (9) were obtained, which was weighed 2.87 g and percentage yield of 86.45%.

For the synthesis of compound (12), 1.52 g of 0.01 mol methanolic vanillin solution was mixed with 2.03 g of 0.01 mol methanolic 4-aminoantipyrine solution. Orange crystals of compound (12) were also successfully synthesized. The compound was weighed 2.53 g and percentage yield of 75.07%.

In order to synthesize compound (15), 1.52 g of 0.01 mol vanillin dissolved in methanol solution was subjected to reaction with 1.37 g of 0.01 mol of methanolic thiobenzamide solution. 1.78 g of yellow crystals of compound (15) were obtained, thus the percentage yield was 65.68%.

Compound (17) was synthesized by reacting 1.52 g of 0.01 mol methanolic vanillin solution with 0.97 g of 0.01 mol sulfamic acid, which resulted in production of yellow crystals that weighed 1.86 g. As a result, the percentage yield was 80.52%.

Last but not least, 1.52 g of 0.01 mol methanolic vanillin solution was mixed with 1.37 g of 0.01 mol of isonicotinic acid hydrazide. The resulting compound (21) was observed as white crystals, with weight of 2.17g and percentage yield of 80.07%. The 6 Schiff base vanillin derivatives that were successfully synthesized were as depicted in Figure 4.110.

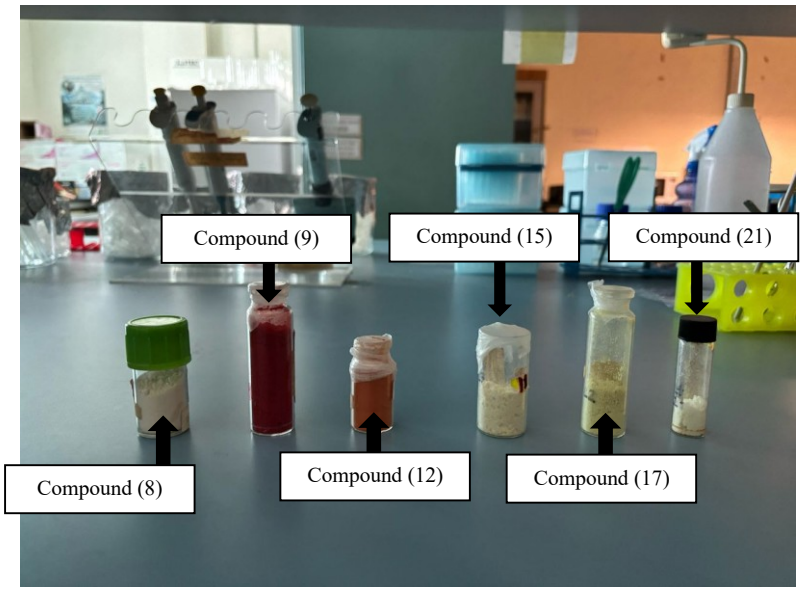


Figure 4.110: Synthesized Schiff base vanillin derivatives

4.6 Characterizations of Synthesized Schiff Base Vanillin Derivatives

4.6.1 Fourier Transform Infrared Spectroscopy

Upon Schiff base synthesis reaction, the synthesized Schiff base vanillin derivatives were subjected to FT-IR with wavelength ranged from 4000 cm^{-1} to 525 cm^{-1} to confirm the chemical functional groups present. Important functional groups of a vanillin compound include OH hydroxyl group, C-O-C ether group, C=O carbonyl group and the benzene ring. According to Figure 4.110, the first and most distinct peak was the stretching of OH group shown at about 3500 cm^{-1}. Consequently, C-H bonds were present in vanillin compound, thus peaks were observed around 2500 cm^{-1} to 3000 cm^{-1}. The two most significant peaks were peaks at about 2700 cm^{-1} and 2800 cm^{-1}, indicated for stretching of C-H at the ether

group and stretching of C-H at the benzene ring respectively. Theoretically, =C-H stretching at alkene should possess higher wavenumber than –C-H stretching at alkane. The C=O bond stretching was shown at peak value of about 1700 cm^{-1}, whereas the peak around 1600 cm^{-1} indicated aryl C=C stretching. On top of that, the stretching of C-O bond of aryl ether group was shown at peak value in between 1100 cm^{-1} and 1200 cm^{-1}. Additionally, the bending of C-H at the ether group was shown at about peak value between 1400 cm^{-1} to 1500 cm^{-1}, and O-H bending was indicated at peak value about 1400 cm^{-1}. The FT-IR spectra of the Schiff base vanillin derivatives were compared to the FT-IR spectrum of the starting material, vanillin, as pictured in Figure 4.111.

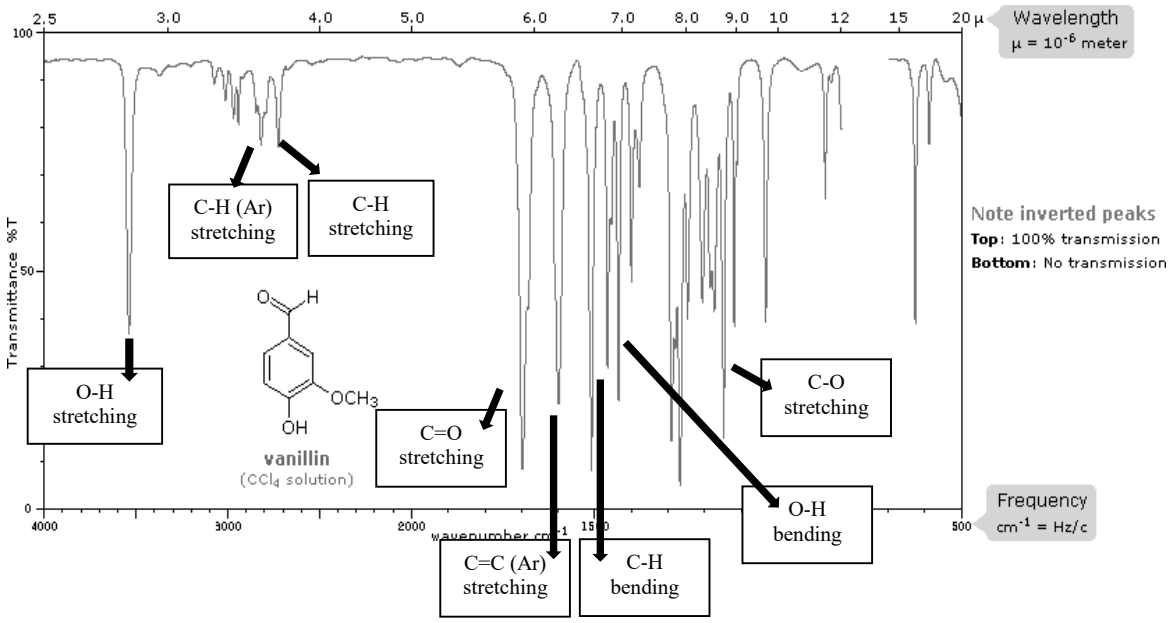


Figure 4.111: FT-IR spectrum of vanillin (Reusch, 2013)

In Schiff base synthesis reactions, imine bond, C=N was formed in combination with primary amine, which resulted in the loss of C=O bond. As a result, peak at around 1700 cm^{-1} should not be observed theoretically, and a peak value slightly less than 1700 cm^{-1}, which is around the range of 1640 cm^{-1} to 1690 cm^{-1} should be observed. The absence of stretching of C=O bond attached to vanillin and presence of stretching of C=N bond indicated

successful synthesis of Schiff base vanillin derivatives. Despite that, peak for C=O from the primary amine should be observed, around 1690 cm^{-1}. On top of that, functional groups of the primary amines in reaction with vanillin compound should also be observed. The FT-IR spectra of Schiff base vanillin derivatives were evaluated and compared to the FT-IR spectra of vanillin compound, as elaborated in Figure 4.111 to 4.116.

Compound (8) is the Schiff base vanillin derivative of 4-hydroxybenzhydrazide. Based on the FT-IR spectrum of compound (8) as illustrated in Figure 4.111, all important functional groups were successfully shown. The most important functional group was C=N bond, as the presence of wavenumber for C=N functional group indicated successful synthesis. As a result, peak value of 1604.31 cm^{-1} indicated the stretching of C=N bond. The first and most distinct peak with a value of 3258.43 cm^{-1} indicate presence of stretching of N-H bond, and the bending of N-H bond was shown at 1587.15 cm^{-1}, present at the 4-hydroxybenzhydrazide. Moreover, the peak at 3053.73 cm^{-1} indicated stretching of O-H bond, whereby the bending of O-H bond was also indicated at the peak around 1300 cm^{-1} to 1400 cm^{-1}. O-H bond was present at both 4-hydroxybenzhydrazide and vanillin structure. The peaks next to O-H stretching were shown for stretching of C-H bond, such that stretching of C-H bond on the benzene ring was indicated by peak around 3000 cm^{-1}, and stretching of C-H bond on the ether group of vanillin was indicated by peak around 2900 cm^{-1}. Additionally, bending of C-H bond of ether group was shown at 1456.49 cm^{-1}. Despite the fact that C=O from vanillin was no longer present, C=O bond was still found at 4-hydroxybenzhydrazide, thus peak value at about 1640.11 cm^{-1} was present to prove the presence of stretching of C=O bond. Theoretically, C=O stretching for vanillin as aldehyde group should be around 1720 cm^{-1} to 1740 cm^{-1}, and C=O stretching for 4-hydroxybenzhydrazide as primary amide should be around the range of 1690 cm^{-1}. For this

reason, peak value at 1640.11 cm^{-1} indicated C=O stretching of 4-hydroxybenzhydrazide instead of C=O stretching of vanillin compound. On top of that, C=C of benzene ring stretched at peak value of 1551.43 cm^{-1}. The stretching C-N bond found on the amide bond of 4-hydroxybenzhydrazide was confirmed for its presence by peak value at 1036.43 cm^{-1}. Lastly, C-O bond on the aryl ether group was discovered for its stretching at peak value of 1066.02 cm^{-1}. As a whole. compound (8) was said to be successfully synthesized.

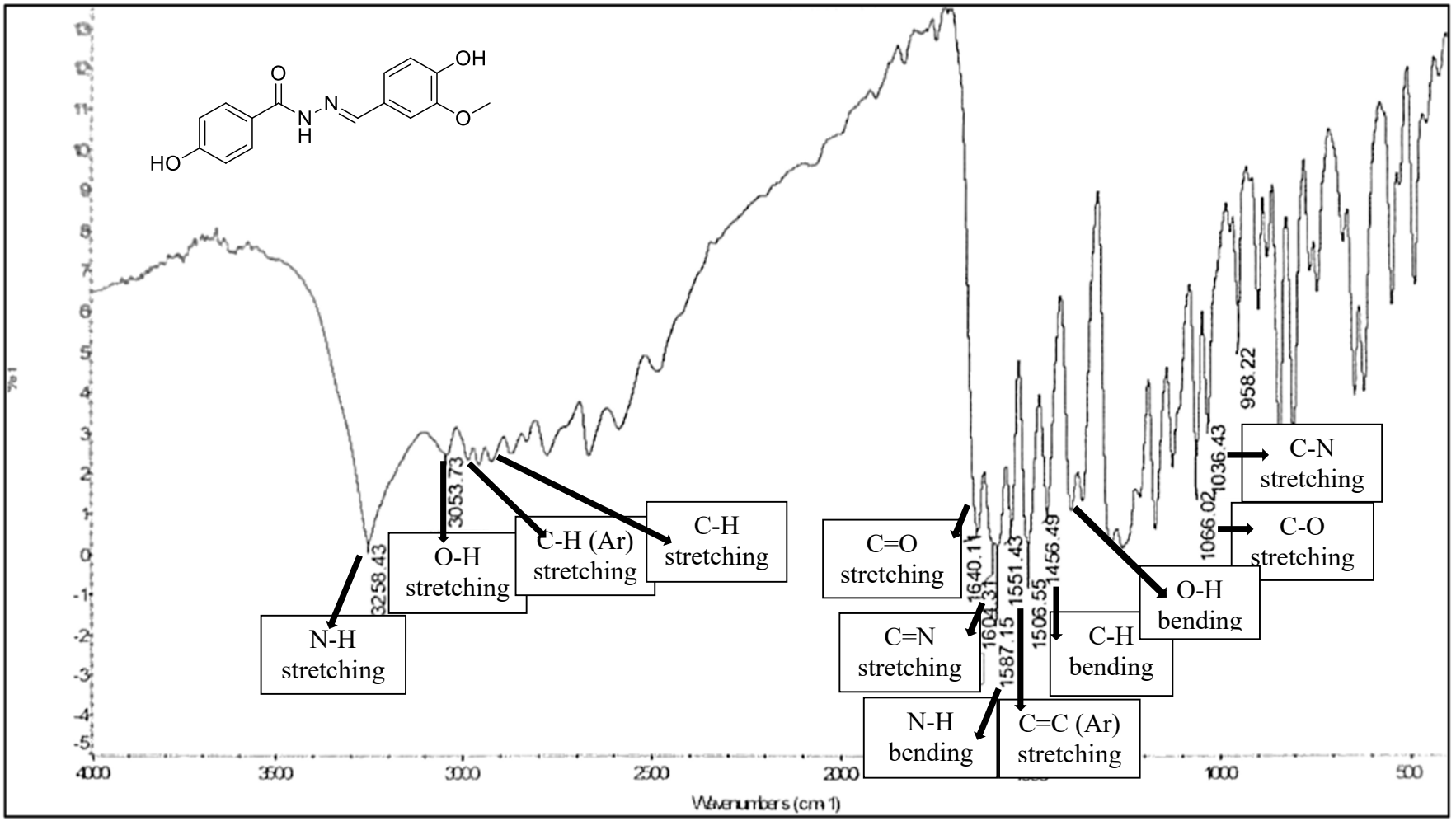


Figure 4.112: FT-IR spectrum of compound (8)

Compound (9) is the Schiff base vanillin derivative synthesized from 2,4-dinitrophenylhydrazine. Based on the FT-IR spectrum in Figure 4.113, the peak value shown at 1605.86 cm^{-1} indicated the presence of stretching of C=N bond. Simultaneously, wavenumber for C=O bond at around 1700 cm^{-1} was not present. This results confirmed the successful synthesis of imine linkage between 2,4-dinitrophenylhydrazine and vanillin compound, thus successful synthesis of compound (9). Peak values of 3363.24 cm^{-1} and 3274.49 cm^{-1} were dedicated for the presence of N-H stretching and O-H stretching respectively. Consequently, the bending of N-H and O-H bonds were shown at peak values of 1588.63 cm^{-1} and 1389.56 cm^{-1} respectively. There are two types of C-H bond in compound (9), which were =C-H bond at the benzene ring and –C-H bond at the methyl group of ether. The stretching behaviours of =C-H bond was depicted by wavenumber 3111.30 cm^{-1}, and –C-H bond was shown at peak value of about 3000 cm^{-1}. Subsequently, peak value of 1463.05 cm^{-1} was dedicated for bending of –C-H bond. On top of that, functional group NO_2 was present in 2,4-dinitrophenylhydrazine, whereby the stretching of N-O bond was shown in the FT-IR spectrum by the peak value of 1511.54 cm^{-1}. Additionally, stretching of C=C bond of benzene ring was indicated by wavenumber of 1541.84 cm^{-1}. Stretching of C-O bond at the ether group of vanillin was discovered at peak value of 1261.03 cm-1, whereas stretching of C-N bond at the 2,4-dinitrophenylhydrazine was confirmed by the presence of peak at 1208.79 cm^{-1}. As a whole, compound (9) was considered successfully synthesized.

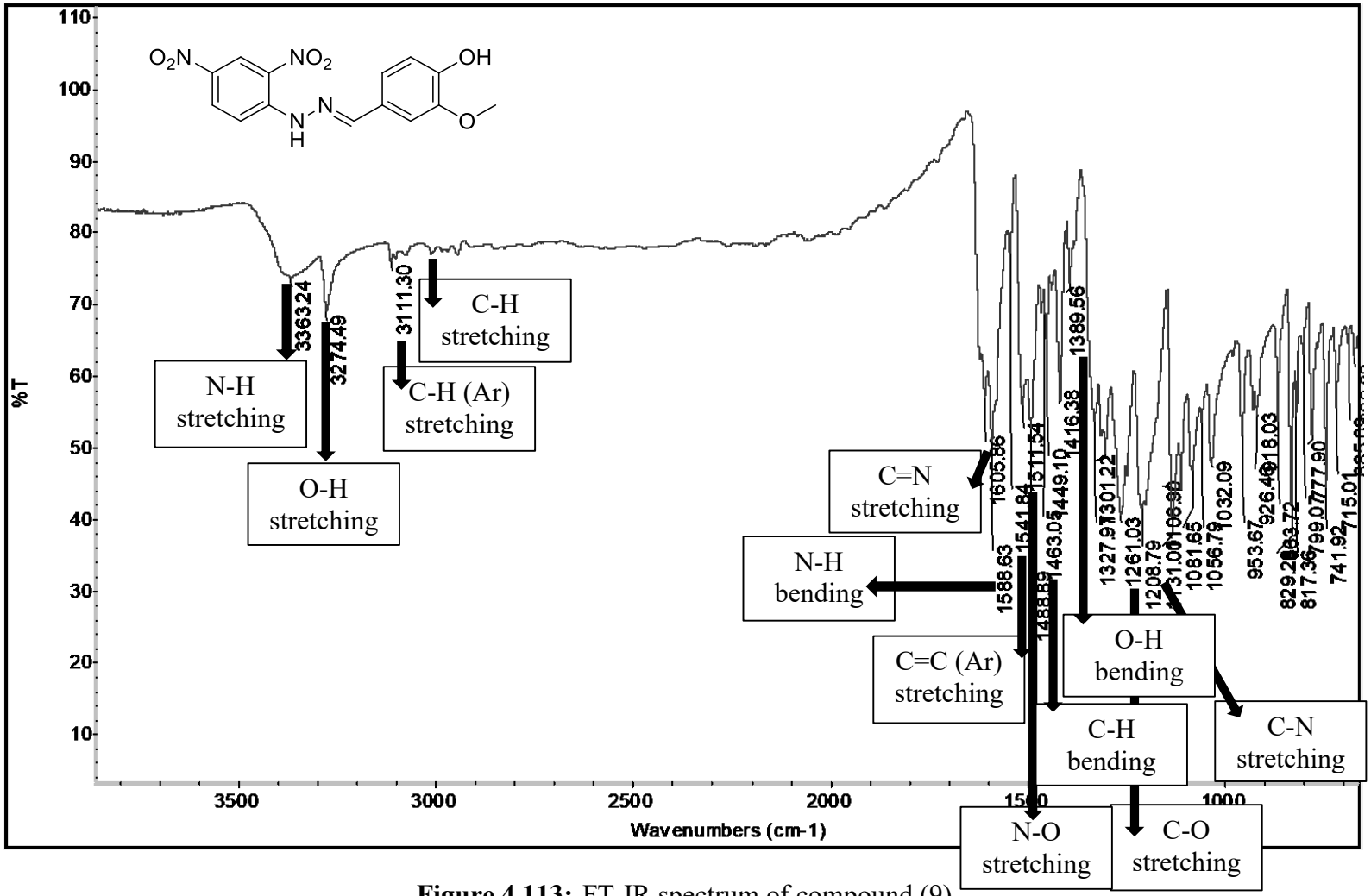


Figure 4.113: FT-IR spectrum of compound (9)

For compound (12), Schiff base vanillin derivative of 4-aminoantiopyrine was considered successful due to presence of stretching of C=N bond at the imine linkage. Peak value at 1580.23 cm^{-1} was dedicated for the formation of imine bond between 4-aminoantiopyrine and vanillin compound. C=O bond of vanillin compound was no longer present due to formation of imine linkage, but peak for stretching of C=O bond was still discovered due to presence of C=O bond at the 4-aminoantiopyrine, which was at 1625.10 cm^{-1}. 3107.40 cm^{-1} peak value was indicated for stretching of O-H bond from vanillin structure, followed by the peak at around 1300 cm^{-1} indicated for bending of O-H bond. Similarly, there are two types of C-H bond, which were =C-H bond from benzene ring and –C-H bond from methyl group of ether as well as methyl group attached to the antipyrine ring. The stretching of =C-H and –C-H bond were shown at wavenumbers about 3000 cm^{-1} and 2900 cm^{-1} respectively. Consequently, bending of –C-H bond of methyl groups was indicated by peak value at 1489.37 cm^{-1}. Furthermore, the stretching of C=C bond of benzene ring was shown by observation of peak at value of 1515.96 cm^{-1}. In similar way, stretching of C-O bond of ether group from vanillin compound was shown at peak value of 1035.80 cm-1, whereas stretching of C-N bond of 4-aminoantiopyrine was observed at peak value of 1128.79 cm-1. Peak value of C-N stretching should be theoretically slightly higher than stretching of C-O as the C-N stretching of aromatic amine, which is 4-aminoantiopyrine, should be higher than stretching of C-N bond of aliphatic amine, as well as stretching of C-O of ether. Therefore, compound (12) was synthesized successfully, with the FT-IR spectrum as illustrated in Figure 4.114.

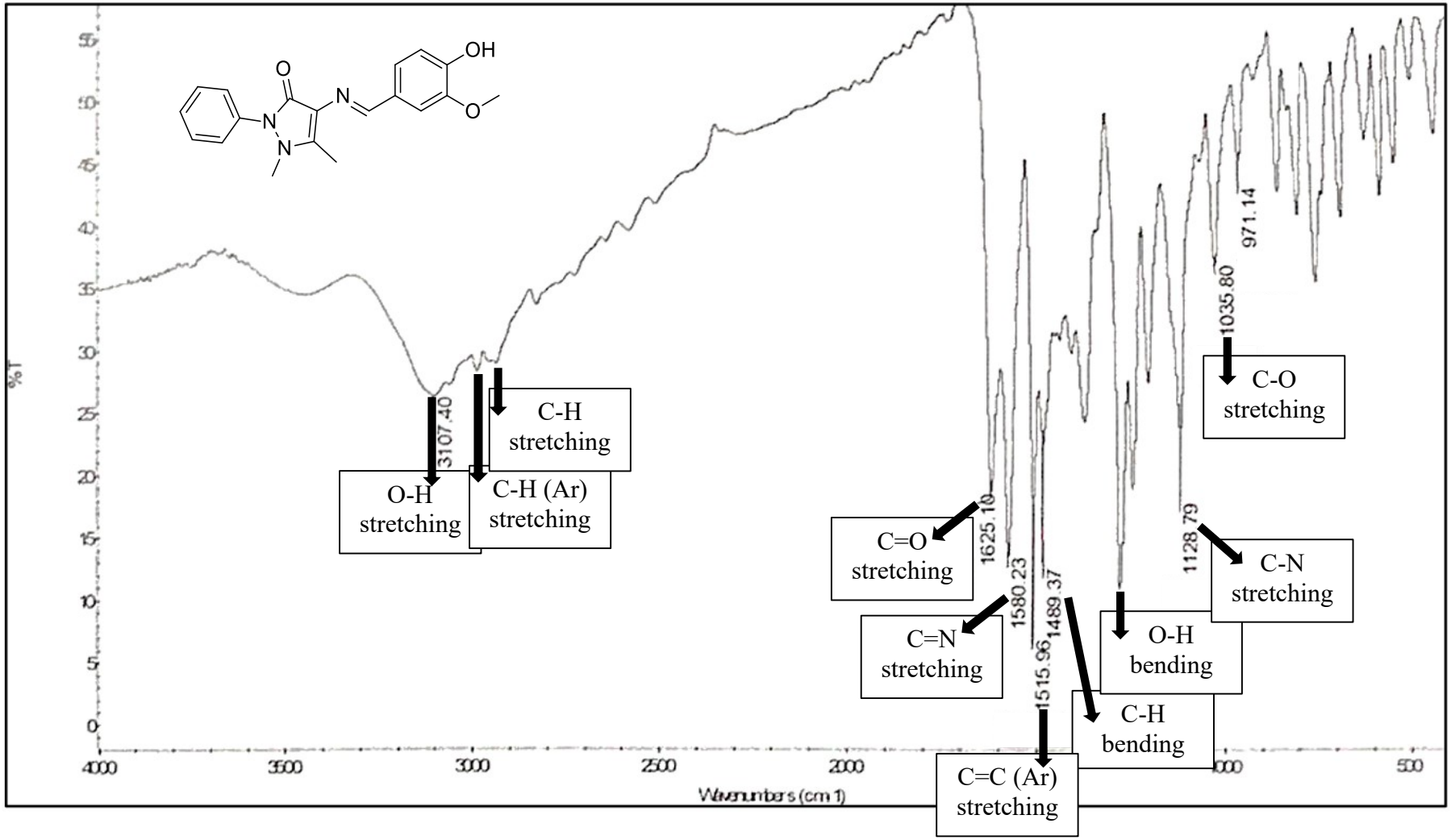


Figure 4.114: FT-IR spectrum of compound (12)

Schiff base vanillin derivative of thiobenzamide, which is compound (15), was also successfully synthesized due to the presence of stretching of C=N bond and absence of stretching of C=O bond. When thiobenzamide reacted with vanillin which formed imine bond in between, stretching of C=N bond was discovered by peak value at 1621.09 cm^{-1}, whereas no peaks were observed at around 1700 cm^{-1}, indicating that C=O bond was no longer present. There were only three distinct peaks at the beginning of the FT-IR spectrum, beginning from the peak value at 3346.93 cm^{-1}, this was dedicated for O-H stretching at the vanillin structure. Simultaneously, the bending of O-H bond was indicated at 1397.24 cm^{-1} peak value. The next two peaks were indicated for the presence of stretching of C-H bond, such that peak value of 3280.66 cm^{-1} was shown by stretching of aromatic C-H bond from benzene rings, and peak value of 3148.50 cm^{-1} was depicted by the stretching of aliphatic C-H bond from methyl group of ether. Additionally, the bending of aliphatic C-H bond was confirmed for the presence at wavenumber of 1448.20 cm^{-1}. Other than that, C=C of benzene ring was also observed for its stretching behavior at peak value of 1593.57 cm^{-1}. The other functional group of vanillin other was ether group, such that the stretching of C-O bond of ether group was identified as peak value of 1279.76 cm^{-1}. Lastly, stretching of C-N bond from thiobenzamide was found at 1132.70 cm^{-1} peak value. For the discovery of all important functional groups, compound (15) was considered successfully synthesized as Schiff base vanillin derivative of thiobenzamide. The FT-IR spectrum of compound (15) was as shown in Figure 4.115.

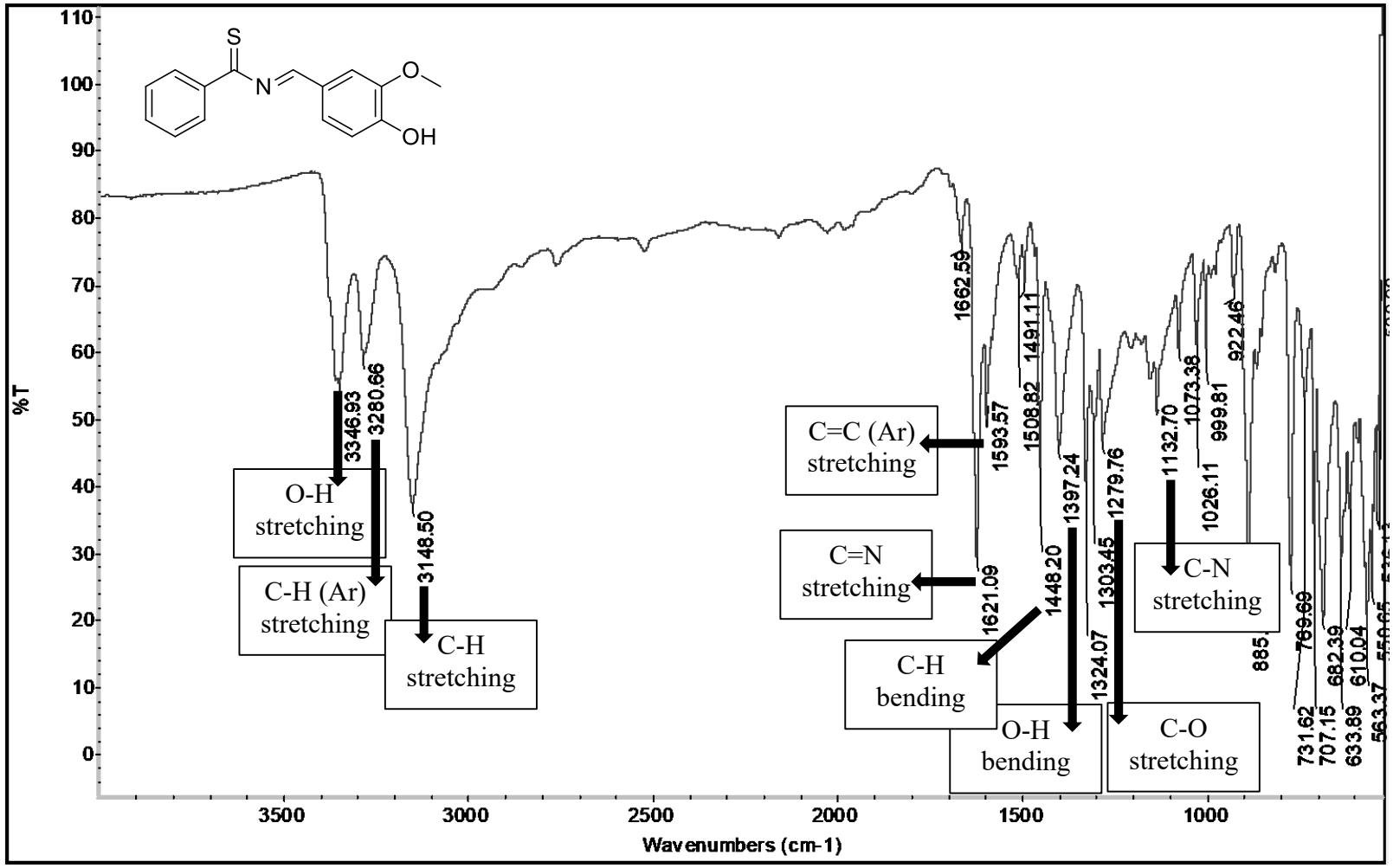


Figure 4.115: FT-IR spectrum of compound (15)

Compound (17) was derived from the Schiff base synthesis reaction between vanillin and sulfamic acid. Based on the FT-IR spectrm of compound (17) as depicted in Figure 4.116, C=N bond stretching was discovered at peak value of 1624.92 cm^{-1}, while peak value for C=O around 1700 cm^{-1} was not present. Thus, imine bond was successfully formed. Furthermore, there were 2 peaks shown for the stretching of O-H bonds. Peak value at around 3600 cm^{-1} was indicated for the stretching of O-H bond from sulfamic acid, whereas peak value of 3490.40 cm^{-1} was indicated for the stretching of phenolic O-H from vanillin structure. Simultaneously, the bending of O-H bonds was found at peak values of 1440.92 cm^{-1} for O-H from sulfamic acid, and 1388.72 cm^{-1} for the phenolic O-H. Similarly, stretching of C-H bond was found as two peaks, which include peak values at around 3200 cm^{-1} and 3074.45 cm^{-1}, dedicated to confirm the presence of stretching of C-H bond from benzene ring and stretching of C-H bond from methyl group of ether respectively. At the same time, the bending of C-H bond of ether group was depicted at peak value of 1471.90 cm^{-1}. Moreover, peak value of 1588.29 cm^{-1} was illustrated for the stretching of C=C bond from the benzene ring. Additionally, another important functional group from sulfamic acid, which is S=O, was discovered for the stretching behavior at peak value of 1267.60 cm^{-1}. Lastly, C-O bond stretching was shown at peak value of 1033.31 cm^{-1}. All the important functional groups were shown by the FT-IR spectrum of compound (17), thus compound (17) was said to be successfully synthesized.

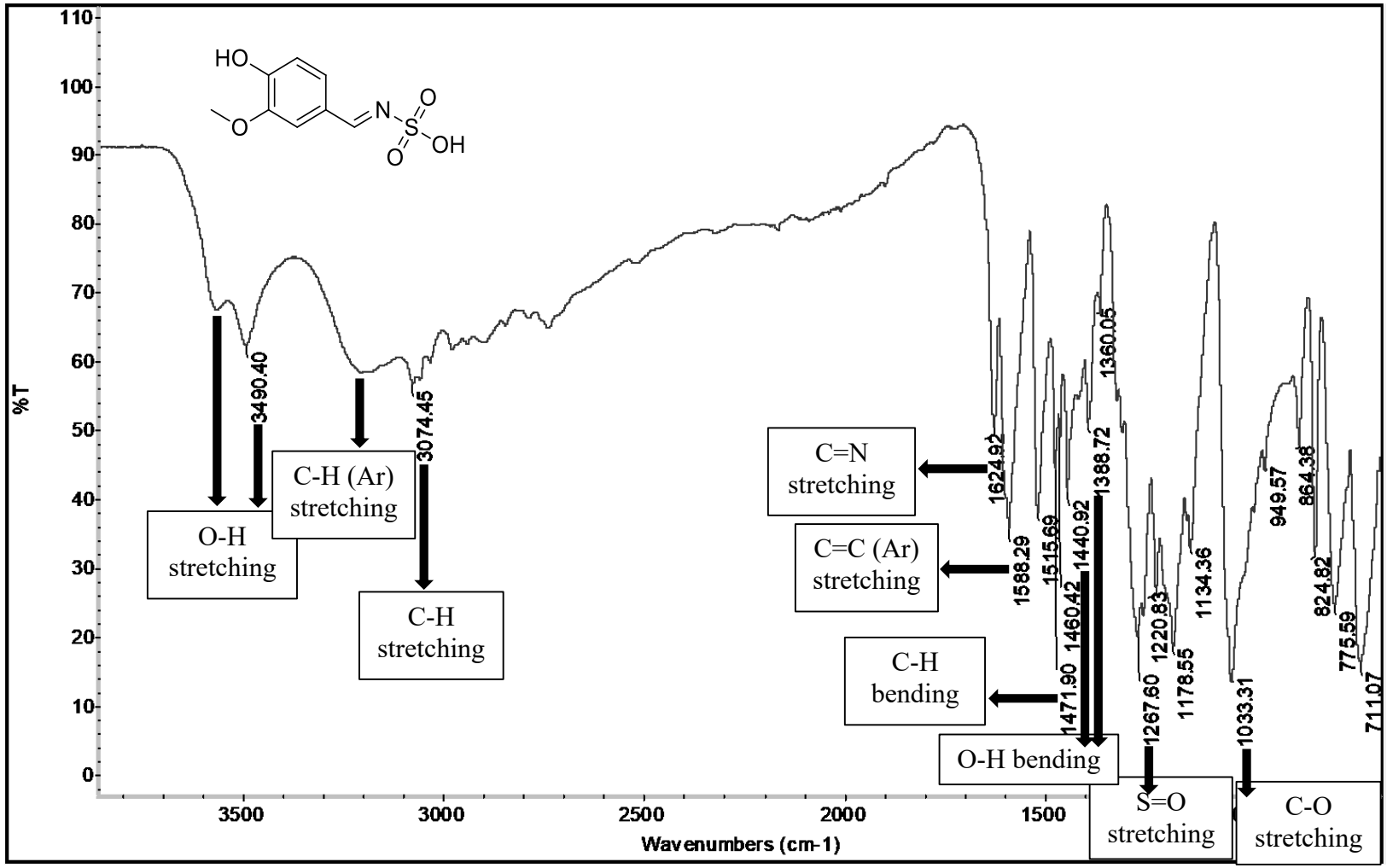


Figure 4.116: FT-IR spectrum of compound (17)

For the Schiff base vanillin derivative of isonicotinic acid hydrazide, which makes compound (21), the presence of stretching of C=N bond was shown by the peak value of 1603.18 cm^{-1}. Similarly, this indicated the successful synthesis of imine linkage between the vanillin and isonicotinic acid hydrazide, hence successful synthesis of compound (21). The C=O bond of vanillin structure was absent, thus peak value around 1700 cm^{-1} was not observed. However, peak value of 1690.99 cm^{-1} was still observed due to the presence of C=O bond from isonicotinic acid hydrazide. Theoretically, C=O bonded to vanillin should possess higher wavenumber value than C=O of primary amide, thus peak value of 1690.99 cm^{-1} was shown for C=O of isonicotinic acid hydrazide instead of C=O of vanillin compound. The first peak of the FT-IR spectrum of compound (21) was depicted for the presence of N-H bond stretching from the amide bond of isonicotinic acid hydrazide, which was 3202.14 cm^{-1}, while the bending of the bond was shown by the peak of 1567.28 cm^{-1}. Moreover, O-H of vanillin structure was depicted by peak value of 3002.44 cm^{-1}, whereas the bending of the O-H bond was shown by peak value of around 1300 cm^{-1}. Similarly, presence of two types of C-H bond, which were aromatic C-H bond of benzene ring, and aliphatic C-H bond from ether group, resulted in presence of peaks around 2900 cm^{-1} and 2800 cm^{-1} respectively. Simultaneously, the bending behavior of C-H bond was present at wavenumber of around 1400 cm^{-1}. Peak value of 1465.13 cm^{-1} was dedicated for the stretching of C=C bond of benzene ring. On top of that, stretching of C-O bond from ether group was shown at peak value of 1105.53 cm^{-1}, whereas stretching of C-N bond from amide bond was shown at peak value of 1074.52 cm^{-1}. Based on the FT-IR spectrum of compound (21) in Figure 4.117, all important functional groups were shown, hence the Schiff base synthesis of compound (21) was considered successful too.

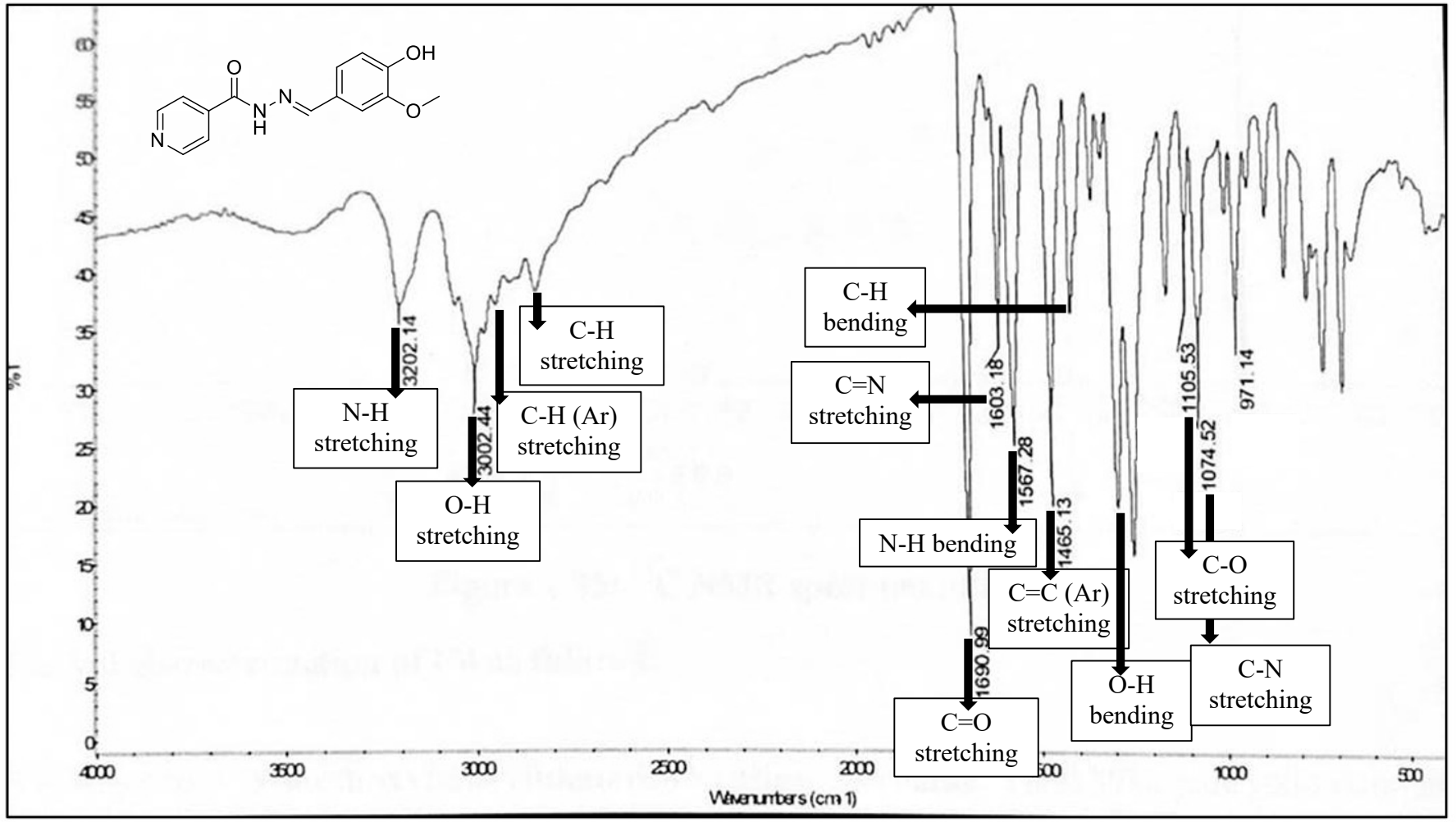


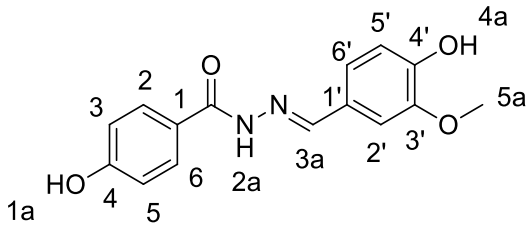
Figure 4.117: FT-IR spectrum of compound (21)

4.6.2 Nuclear Magnetic Resonance Spectroscopy

Proton NMR (^{1}H NMR) spectroscopies were done on the 6 Schiff base vanillin derivatives. Deuterated DMSO (DMSO-d_6) was selected as solvent to dissolve the vanillin derivatives to be subjected to ^{1}H NMR. As a result, for all the spectrums, signal at about δ 2.4 to δ 2.5 indicated the peak value for DMSO-d_6 solvent.

The proton NMR (^{1}H NMR) analysis of compound (8) indicated the presence of 12 protons in the chemical structure, which was done and summarised in Table 4.19.

Table 4.19: ^{1}H NMR of compound (8)



Numbers of protons	^{1}H NMR δ (ppm)	Multiplicity	J values (Hz)
1a	9.475	s	-
2	6.742, 6.725	d	8.59
3	6.819, 6.801, 6.784	t	17.18
5	6.819, 6.801, 6.784	t	17.18
6	6.742, 6.725	d	8.59
2a	11.413	s	-
3a	8.266	s	-
2’	7.027, 7.012	d	7.45
5’	7.767, 7.737	d	8.59

Table 4.19 continued

6’	7.647, 7.643, 7.633, 7.629	dd	1.72, 1.72
4a	10.066	s	-
5a	3.786	s	-

Based on the ^{1}H NMR analysis, signal discovered at δ 11.413 was indicated for the H-2a bonded to the nitrogen atom, which was discovered as the most downfield peak due to deshielding effect by the high electronegativity of nitrogen atoms. 2 singlets were shown at δ 10.066 and δ 9.475, indicated for the H-4a of OH of the vanillin structure and H-1a of OH of the 4-hydroxybenzhydrazide respectively. The reason H-4a showed signal slightly downfield compared to the signal depicted by H-1a was due to the slight deshielding effect of neighbouring C-O-C group next to H-4a. As for H-3a, which is the H atom bonded to the imine linkage, a singlet at δ 8.266 was detected to indicate its presence. Signals shown by the aromatic protons of vanillin structure were mostly downfield compared to the aromatic protons of 4-hydroxybenzhydrazide, due to the effective deshielding effect caused by the OH and C-O-C group. For the aromatic protons of vanillin structure, a doublet signal of δ 7.767 and δ 7.737 (J = 8.59 Hz) was depicted by H-5’ due to the coupling constant with H-6’. Furthermore, the signal shown as doublet of doublets at δ 7.647, δ 7.643, δ 7.633 and δ 7.629 (J = 1.72 Hz, 1.72 Hz) was indicative for the presence of H-6’, which showed coupling constant with the ortho H-5’ and meta H-2’. Similarly, H-2’ also portrayed coupling constant with H-6’, thus resulting in the presence of doublet signal at δ 7.027 and δ 7.012 (J = 7.45 Hz). The J value is lower than the J value for ortho coupling of H-5’ to H-6’ due to meta coupling of H-2’ to H-6’. For the aromatic protons of 4-hydroxybenzhydrazide, H-3 and H-5 should show a doublet signal due to their coupling with H-2 and H-6 respectively.

However, a triplet signal at δ 6.819, δ 6.801 and δ 6.784 (J = 17.18 Hz) was observed. This may be due to the solvent DMSO-d_6 which might engage to hydrogen bonding to the OH at 1a, thus resulting in alteration of the J values which lead to formation of triplet instead of a doublet (Smith, 2006). Another doublet signal at δ 6.742 and δ 6.725 (J = 8.59 Hz) was dedicated for H-2 and H-6 which depicted coupling constant with H-3 and H-5 respectively. Lastly, H-3a of the methoxy group at vanillin structure depicted a singlet signal at δ 3.786. The ^{1}H NMR spectrum was as shown in Figure 4.118. Expansions of several sections of the spectrum were also depicted in Figure 4.119.

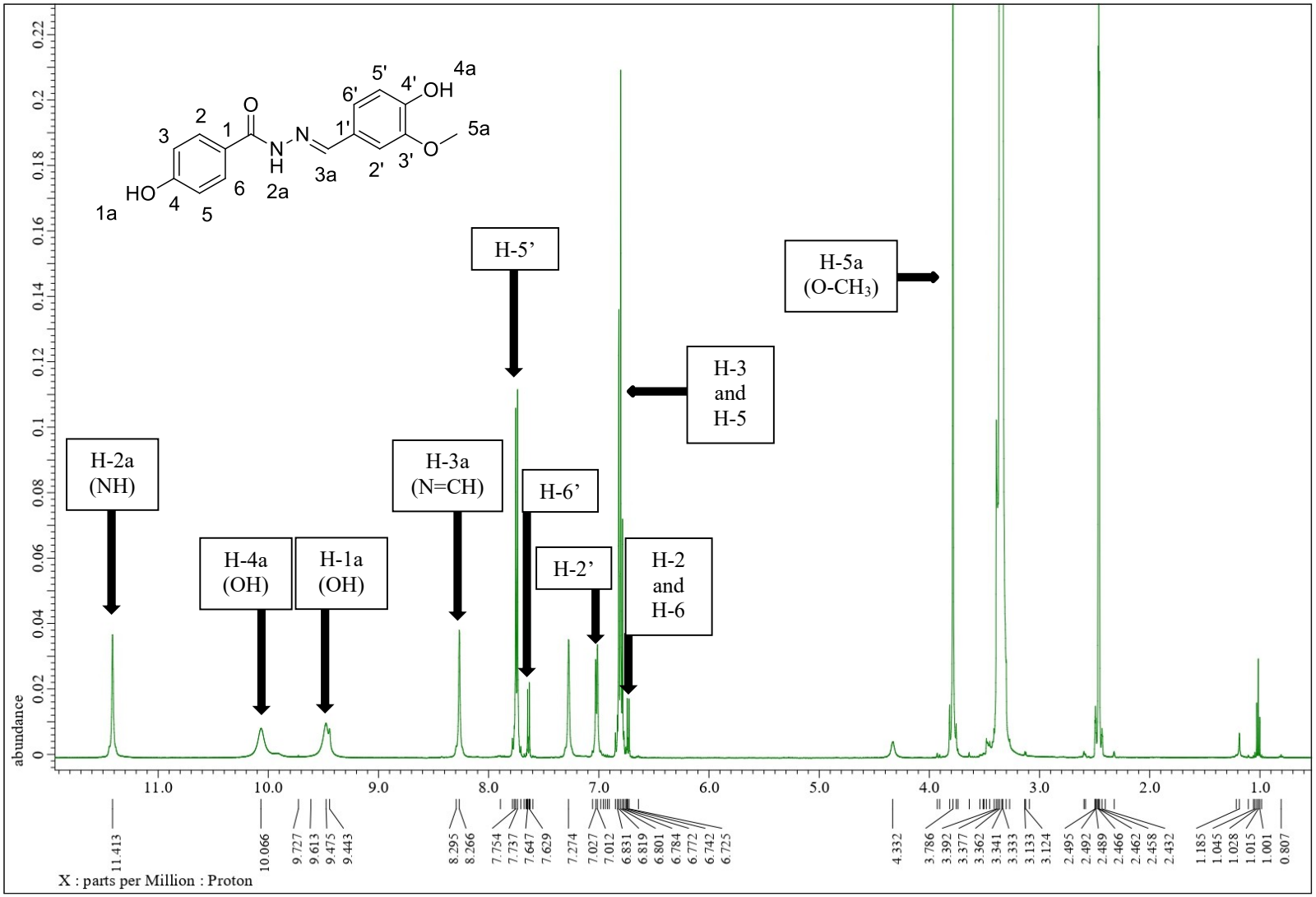


Figure 4.118: ^{1}H NMR of compound (8)

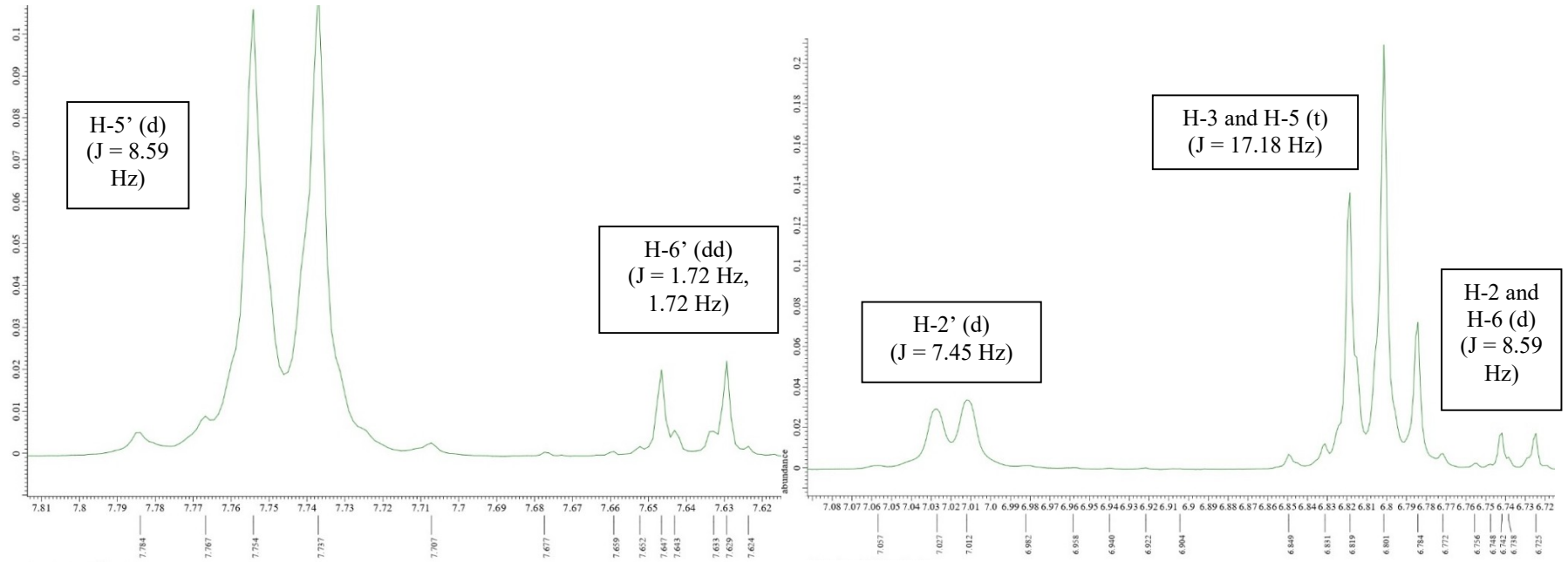
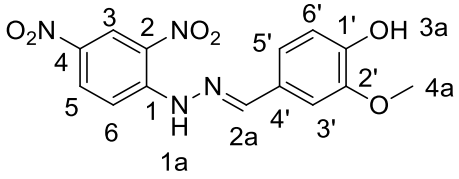


Figure 4.119: Expansion of several sections of ^{1}H NMR of compound (8)

Table 4.20 summarizes the ^{1}H NMR analysis results of compound (9). Based on the results, a total of 10 protons where shown.

Table 4.20: ^{1}H NMR of compound (9)



Numbers of protons	^{1}H NMR δ (ppm)	Multiplicity	J values (Hz)
3	8.824, 8.819	d	2.29
5	8.319, 8.313, 8.299, 8.294	dd	2.86, 2.86
6	8.060, 8.040	d	9.74
1a	11.517	s	-
2a	8.497	s	-
3’	7.352, 7.349	d	1.72
5’	7.147, 7.131	d	8.02
6’	6.838, 6.822	d	8.02
3a	9.693	s	-
4a	3.818	s	-

The ^{1}H NMR spectrum of compound (9) was as shown in Figure 4.120, with expansions of a few sections as shown in Figure 4.121. Based on the spectrum, a singlet signal at δ 11.517 was depicted to indicate the presence of H-1a, which was the H bonded to nitrogen atom. The signal was the most downfield peak due to the strong electronegativity

of nitrogen atoms, thus effectively deshield the proton. Moreover, 2 singlets shown at δ 9.693 and δ 8.497 were indicated for H-3a of OH of vanillin structure and H-2a of the imine bond respectively. For the aromatic protons, most aromatic protons of 2,4-dinitrophenylhydrazine were slightly more downfield than the aromatic protons of vanillin structure due to the presence of NO_2 groups, which were more deshielding substituents compared to OH and methoxy groups. H-3 was able to show coupling constant with the meta H-5, thus depicting a doublet signal at δ 8.824 and δ 8.819 (J = 2.29 Hz). Due to meta coupling, the J value is lower. A doublet of doublets at δ 8.319, δ 8.313, δ 8.299 and δ 8.294 (J = 2.86 Hz, 2.86 Hz) was dedicated for the coupling of H-5 with the ortho H-6 and meta H-3. Furthermore, a doublet formed at δ 8.060 and δ 8.040 (J = 9.74 Hz) indicated the coupling constant of H-6 with ortho H-5, thus resulting in higher J value. For the aromatic protons of vanillin structure, H-3' showed coupling constant with H-5', hence resulting in the formation of a doublet signal at δ 7.352 and δ 7.349 (J = 1.72 Hz), with low J value due to meta positions of H-3' and H-5'. On the other hand, H-6' depicted coupling with H-5' at the ortho position, thus forming a doublet signal with higher J value at δ 6.838 and δ 6.822 (J = 8.02 Hz). Theoretically, H-5' should form coupling with the ortho H-6' and meta H-3' to form a doublet of doublets signal. A broad doublet signal at δ 7.147 and δ 7.131 (J = 8.02 Hz) was observed instead. This may be due to the overlapping of peak due to very similar J values which led to the merging of peaks to produce a broad doublet signal. Lastly, a singlet signal at δ was shown by H-4a of methoxy group.

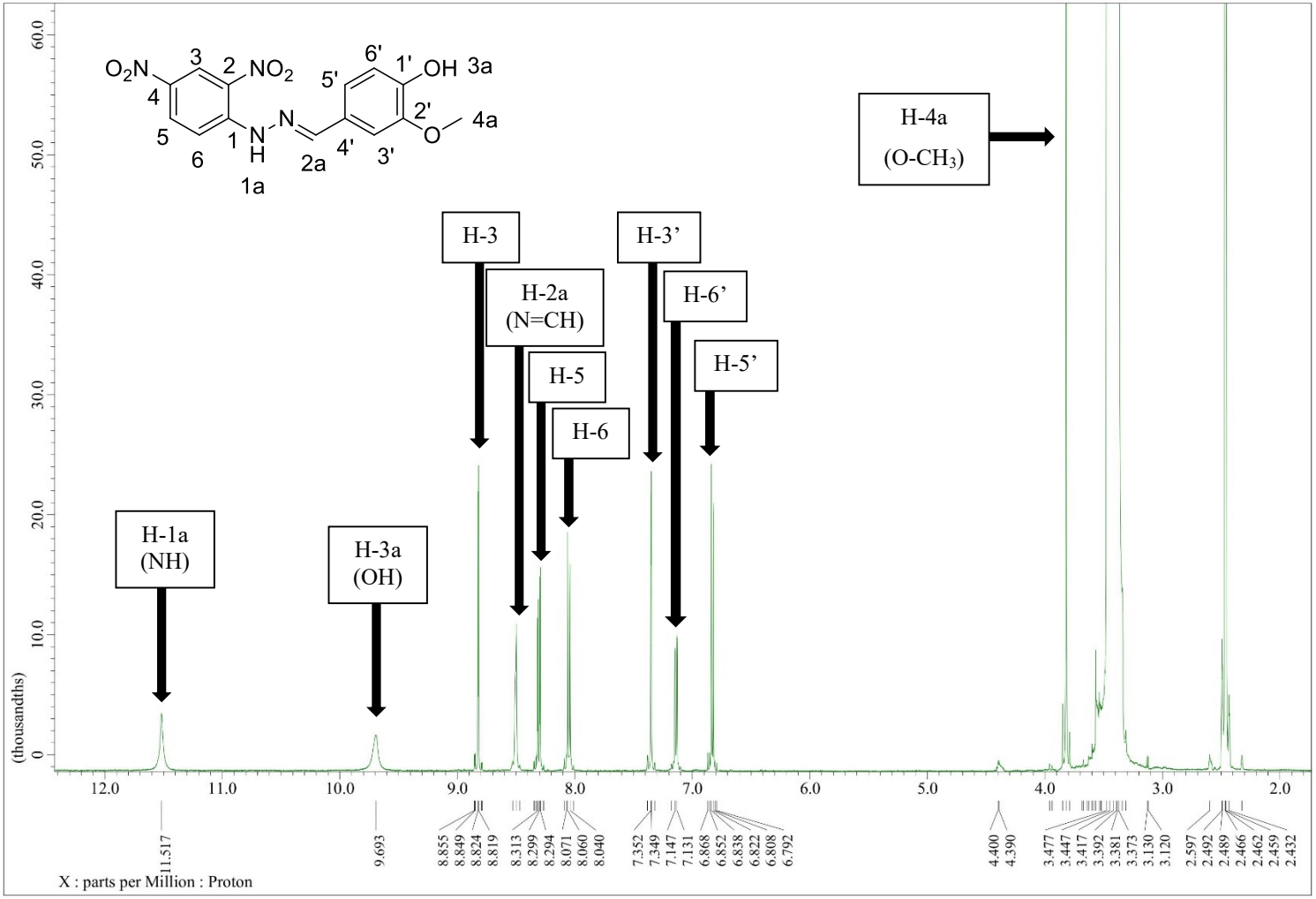


Figure 4.120: ^{1}H NMR of compound (9)

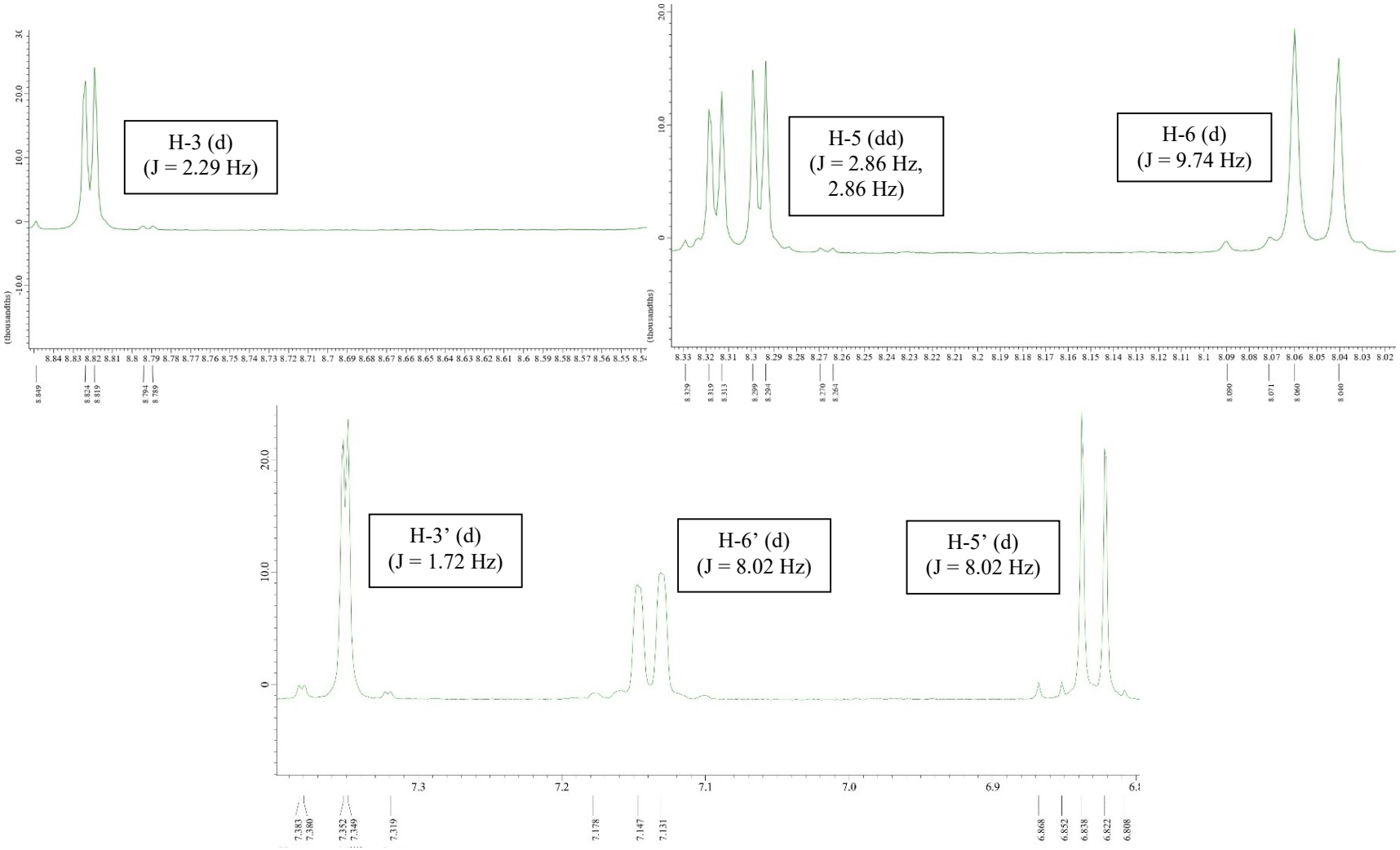
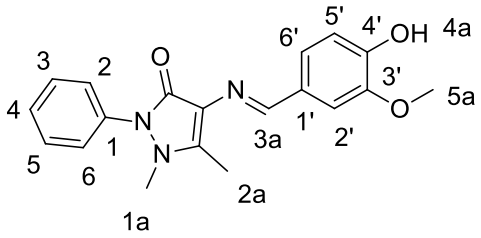


Figure 4.121: Expansion of several sections of ^{1}H NMR of compound (9)

The summary of the ^{1}H NMR analysis results of compound (12) was as tabulated in Table 4.21. A total of 13 protons showed their respective signals in the spectrum.

Table 4.21: ^{1}H NMR of compound (12)



Numbers of protons	^{1}H NMR δ (ppm)	Multiplicity	J values (Hz)
1a	3.094	s	-
2a	2.395	s	-
2	7.343, 7.329, 7.317, 7.302	m	-
3	7.499, 7.483, 7.468	t	15.46
4	7.343, 7.329, 7.317, 7.302	m	-
5	7.499, 7.483, 7.468	t	15.46
6	7.343, 7.329, 7.317, 7.302	m	-
3a	9.414	s	-
2’	7.385, 7.381	d	2.29
5’	6.811, 6.793	d	8.59
6’	7.156, 7.152, 7.139, 7.136	dd	6.87, 7.45
4a	9.747	s	-
5a	3.798	s	-

The most downfield signal recorded was a singlet at δ 9.747, indicated for H-4a of OH group of vanillin structure. The highly electronegative oxygen atom effective deshield the proton, thus resulting in formation of a more downfield signal. Subsequently, another singlet at δ 9.414 was dedicated for H-3a, which was H atom of imine bond of the Schiff base vanillin derivative. A triplet signal was discovered at δ 7.499, δ 7.483 and δ 7.468 (J = 15.46 Hz). This signal was depicted by H-3 and H-5 of the aromatic protons on 4-aminoantipyrine, such that H-3 showed coupling constant with H-2 and H-4 and ortho positions, while H-5 showed coupling constant with H-4 and H-6 at ortho positions, resulting in formation of a triplet signal. Due to ortho coupling, the J value was considerably high. As for H-2 and H-6, the expected signal should be a doublet of doublets, such that H-2 should portray coupling constant with the ortho H-3 and meta H-4, whereas H-6 should portray coupling constant with the ortho H-5 and meta H-4. Additionally, the H-4 should depict a doublet signal due to the equal coupling constant with both H-3 and H-5. However, complex multiplets were observed at δ 7.343, δ 7.329, δ.7.317 and δ 7.302 instead of separate signals. This is most probably due to similar chemical shifts, especially monosubstituted aromatic ring, leading to overlapping peaks which results in formation of complex splitting patterns as depicted in the ^{1}H NMR spectrum. Moreover, H-6’ of the vanillin benzene ring was able to depict coupling constant with H-5’ at ortho position and H-2’ at meta position, thus was responsible for the formation of a doublet of doublets at δ 7.156, δ 7.152, δ 7.139 and δ 7.136 (J = 6.87 Hz, 7.45 Hz). The meta coupling of H-2’ with H-6’ was confirmed by the presence of a doublet signal at δ 7.385 and δ 7.381 (J = 2.29 Hz), whereas the ortho coupling of H-5’ with H-6’ was indicated by a doublet signal at δ 6.811 and δ 6.793 (J = 8.59 Hz). The two doublets are differentiated by the J value, such that the J value of ortho coupling of H-5’ with H-6’ was higher than the J value of meta coupling of H-2’ with H-6’. Based on the

chemical structure of compound (12), there were a total of 3 types of methyl groups which produce 3 different signals in the spectrum. Singlet at δ 3.798 was indicated for the H-5a of methoxy group of vanillin compound, whereas singlets at δ 3094 and δ 2.395 were shown by H-1a and H-2a respectively. H-1a was slightly downfield than H-2a due to the deshielding effect by the nearby electronegative nitrogen atom. As a whole, the ^{1}H NMR spectrum was as pictured in Figure 4.122. Additionally, Figure 4.123 also depict the expansions of several sections of the NMR spectrum.

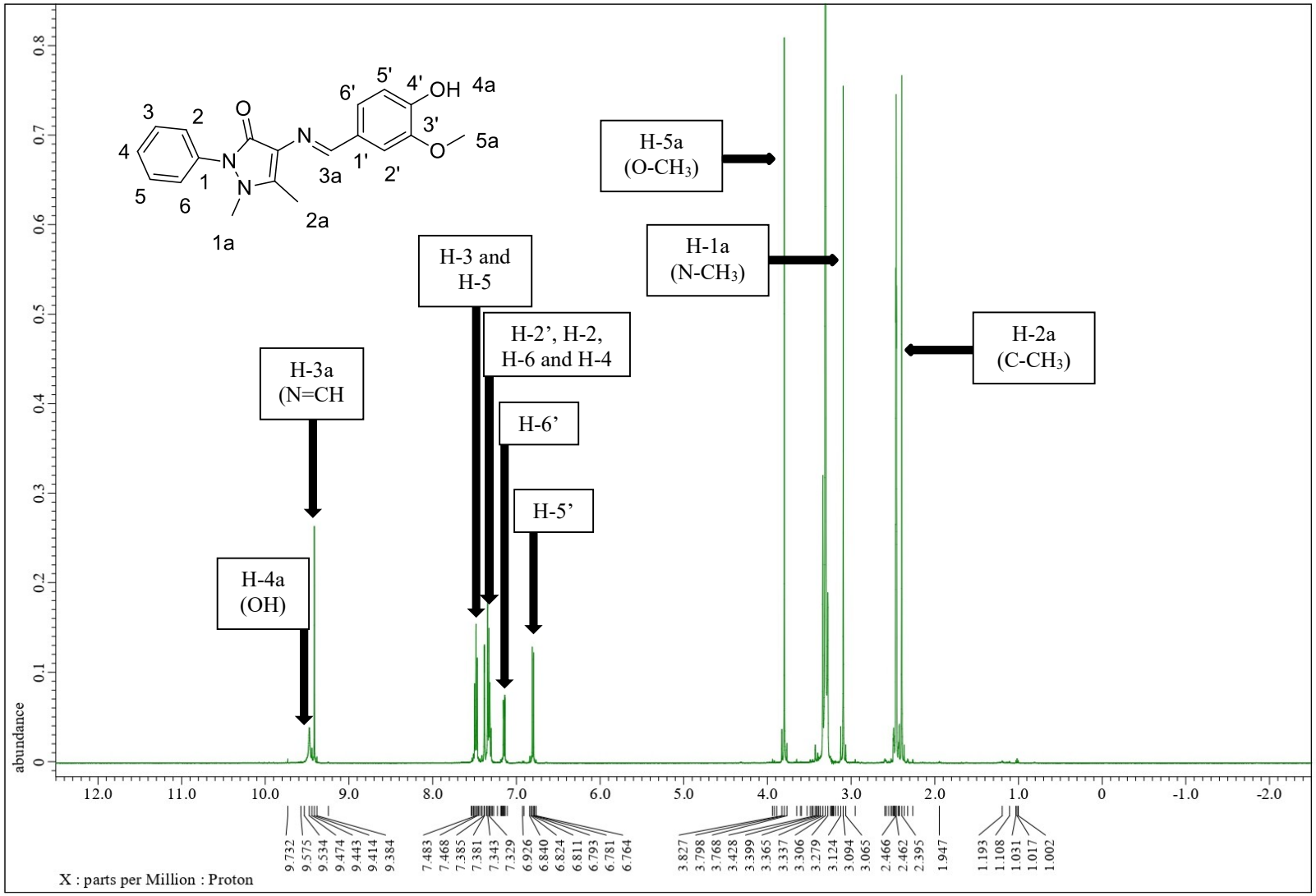


Figure 4.122: ^{1}H NMR of compound (12)

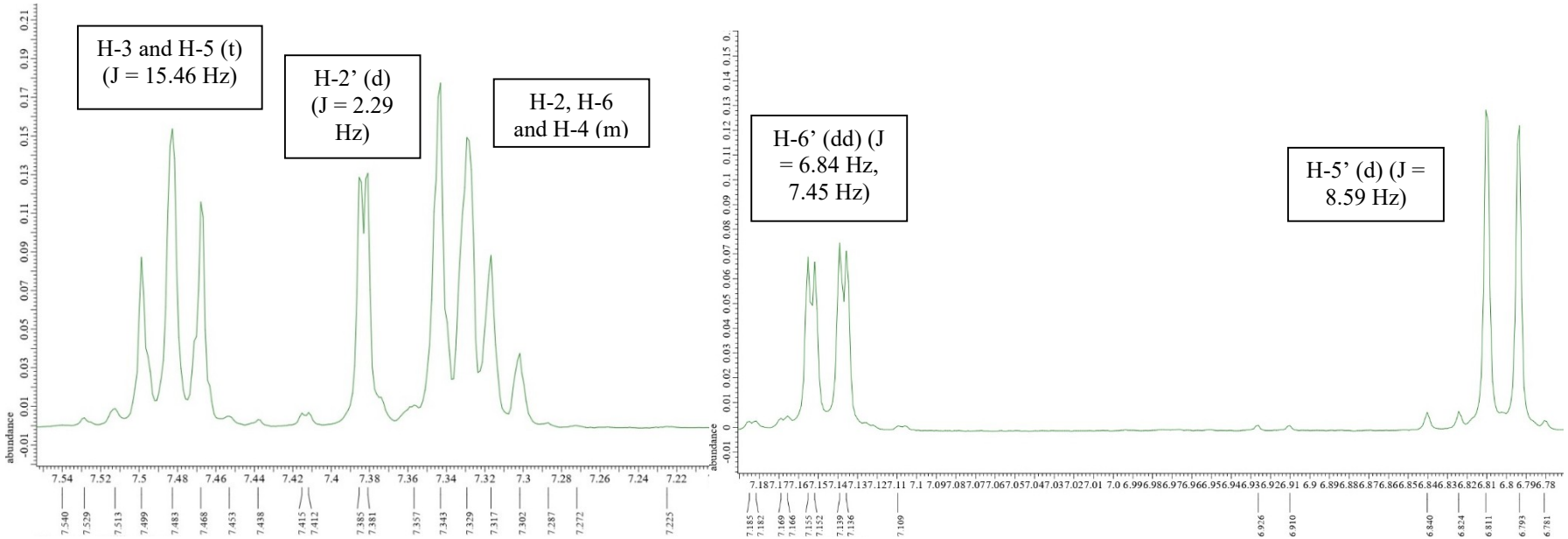
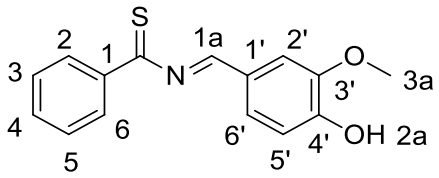


Figure 4.123: Expansion of several sections of ^{1}H NMR of compound (12)

For compound (15), a total of 11 protons were indicated by the ^{1}H NMR spectrum. All results were as tabulated in Table 4.22.

Table 4.22: ^{1}H NMR of compound (15)



Numbers of protons	^{1}H NMR δ (ppm)	Multiplicity	J values (Hz)
1a	9.731	s	-
2	7.391, 7.387, 7.371, 7.355, 7.349, 7.345	m	-
3	7.474, 7.459, 7.444	t	14.89
4	7.391, 7.387, 7.371, 7.355, 7.349, 7.345	m	-
5	7.474, 7.459, 7.444	t	14.89
6	7.391, 7.387, 7.371, 7.355, 7.349, 7.345	m	-
2’	7.391, 7.387, 7.371, 7.355, 7.349, 7.345	m	-
5’	6.926, 6.918	d	8.02
6’	7.847, 7.845, 7.831, 7.829	dd	1.15, 1.15
2a	9.816	s	-
3a	3.799	s	-

Based on the ^{1}H NMR spectrum of compound (15) as illustrated in Figure 4.124, H-2a of the OH group of vanillin structure depicted the most downfield signal, which was a singlet at δ 9.816 due to the deshielding effect of the electronegative oxygen atom. Similarly, another singlet at δ 9.731 was indicated for the chemical shift of H-1a at the imine linkage. H-6' of vanillin structure depicted a doublet of doublets at δ 7.847, δ 7.845, δ 7.831 and δ 7.829 (J = 1.15 Hz) due to the coupling constant with the ortho H-5' and meta H-2'. However, due to the very small J values, the peaks were almost merged and not very obvious as shown in Figure 4.124. The triplet signal at δ 7.474, δ 7.459 and δ 7.444 (J = 14.89 Hz) was shown by H-3 and H-5 of thiobenzamide, such that H-3 was able to depict coupling constant with the ortho H-2 and H-4, whereas H-5 was able to show coupling constant with the ortho H-4 and H-6. Once again, complex multiplets were observed at δ 7.391, δ 7.387, δ 7.371, δ 7.355, δ 7.349 and δ 7.345. Formation of complex multiplets was greatly due to similar chemical shifts, thus resulting in the overlapping of peaks. H-2 and H-6 of the thiobenzamide should theoretically form a doublet of doublets signal due to ortho coupling with H-3 and H-5 respectively, as well as meta coupling with H-4. On top of that, H-4 should picture a doublet signal due to the depiction of coupling constant with ortho H-3 and H-5. Furthermore, H-2' should also show coupling constant with meta H-6', theoretically resulting in the formation of a doublet signal. The overlapping and merging of these signals due to similar chemical shifts was greatly responsible for the formation of the complex multiplet. Moreover, a doublet signal at δ 6.926 and δ 6.918 (J = 8.02 Hz) was observed due to the ortho coupling constant shown by H-5' with H-6'. Last but not least, H-3a of methoxy group from vanillin structure depicted a singlet at δ 3.799. Aside from Figure 4.124, the expansion of the doublets and multiplets were as shown in Figure 4.125.

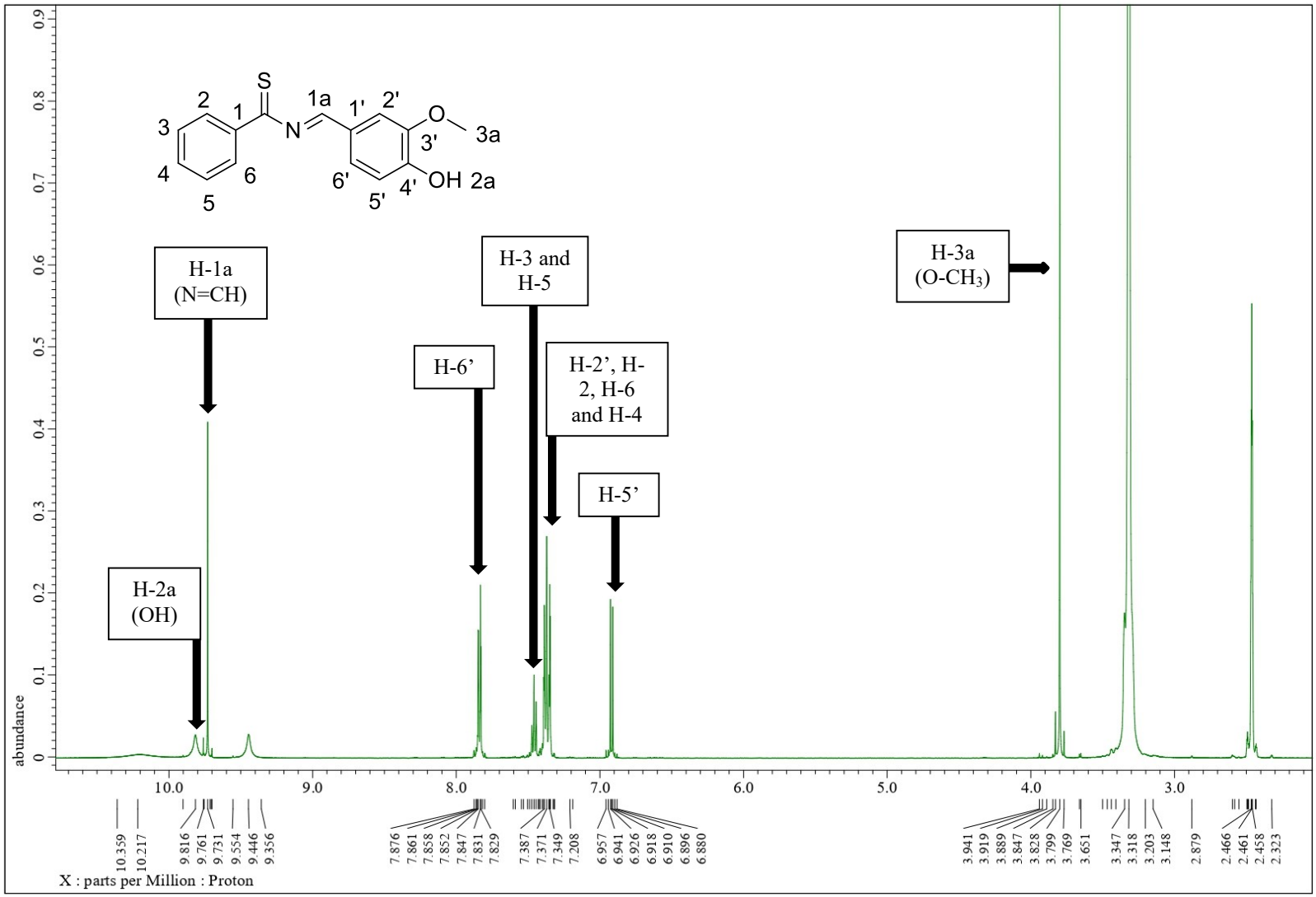


Figure 4.124: ^{1}H NMR of compound (15)

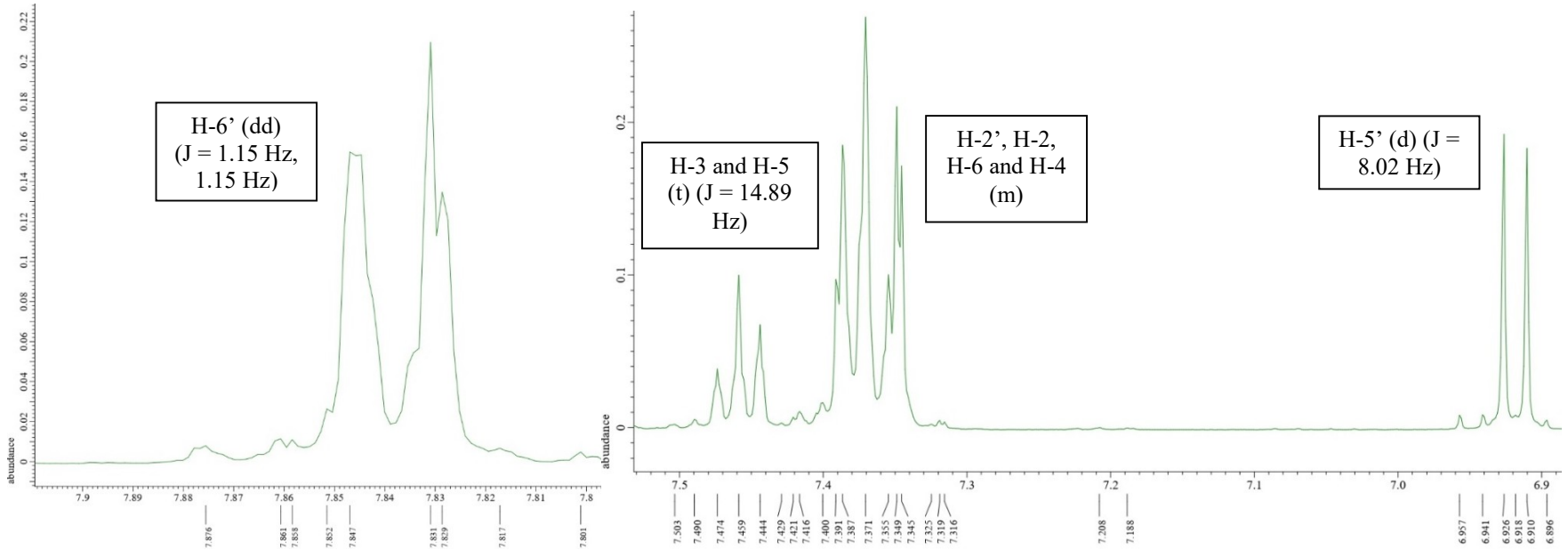
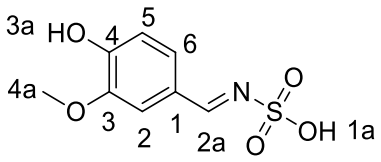


Figure 4.125: Expansion of several sections of ^{1}H NMR of compound (15)

A total of 7 protons were shown by the ^{1}H NMR of compound (17). Table 4.23 summarises the signals shown by all protons of compound (17).

Table 4.23: ^{1}H NMR of compound (17)



Numbers of protons	^{1}H NMR δ (ppm)	Multiplicity	J values (Hz)
1a	10.211	s	-
2a	9.730	s	-
2	7.349, 7.344	d	2.29
5	6.926, 6.918	d	8.02
6	7.390, 7.387, 7.374, 7.371	dd	1.72, 1.72
3a	9.761	s	-
4a	3.799	s	-

Based on Figure 4.126, there were two singlets indicated by the two hydrogens attached to OH groups. The most downfield signal was recorded as a singlet at δ 10.211, which was shown by H-1a of OH group of sulfamic acid structure. The highly electronegative oxygen and sulphur atoms effective deshield the H-1a, thus showing the most downfield peak. The subsequent singlet signal at δ 9.761 was dedicated for H-3a of OH group of vanillin structure. Furthermore, H-2a of imine bond was indicated by the presence of another singlet signal at δ 9.730. A doublet of doublets signal shown at δ 7.390,

δ 7.387, δ 7.374 and δ 7.371 (J = 1.72 Hz, 1.72 Hz), indicative of the coupling constant shown by H-6 to the ortho H-5 and meta H-2. On top of that, doublet signal at δ 7.349 and δ 7.344 (J = 2.29 Hz) was observed due to the meta coupling of H-2 with H-6. Moreover, H-5 was able to show ortho coupling constant with H-6, resulted in formation of a doublet signal at δ 6.926 and δ 6.918 (J = 8.02 Hz). Similarly, the two doublets were differentiated by J values, such that the ortho coupling constant of H-5 to H-6 depicted greater J value than the meta coupling constant of H-2 to H-6. Lastly, H-4a of methoxy group was able to show a singlet signal at δ 3.799 in the spectrum. Apart from Figure 4.126, expansions of the multiplets were illustrated in Figure 4.127.

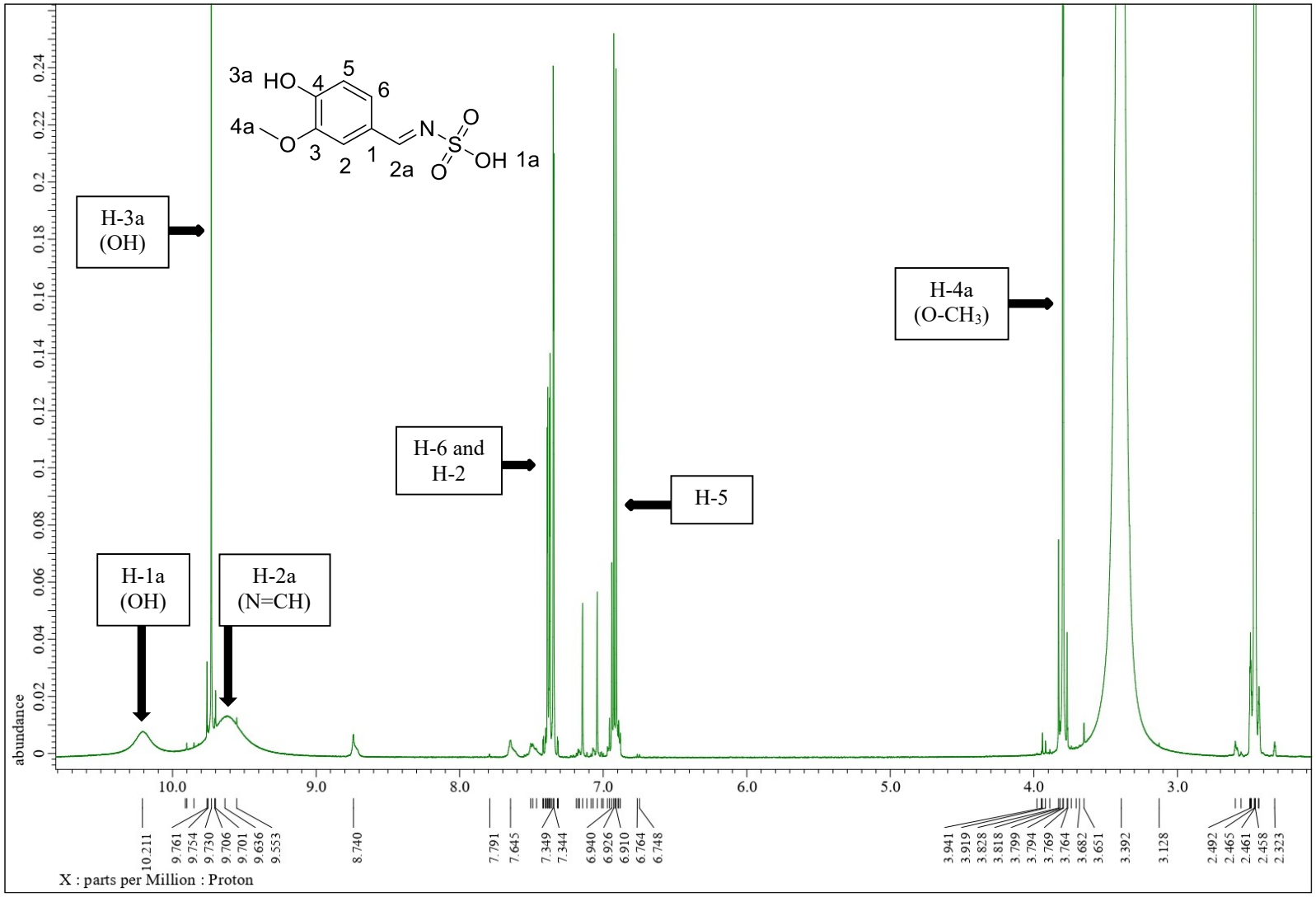


Figure 4.126: ^{1}H NMR of compound (17)

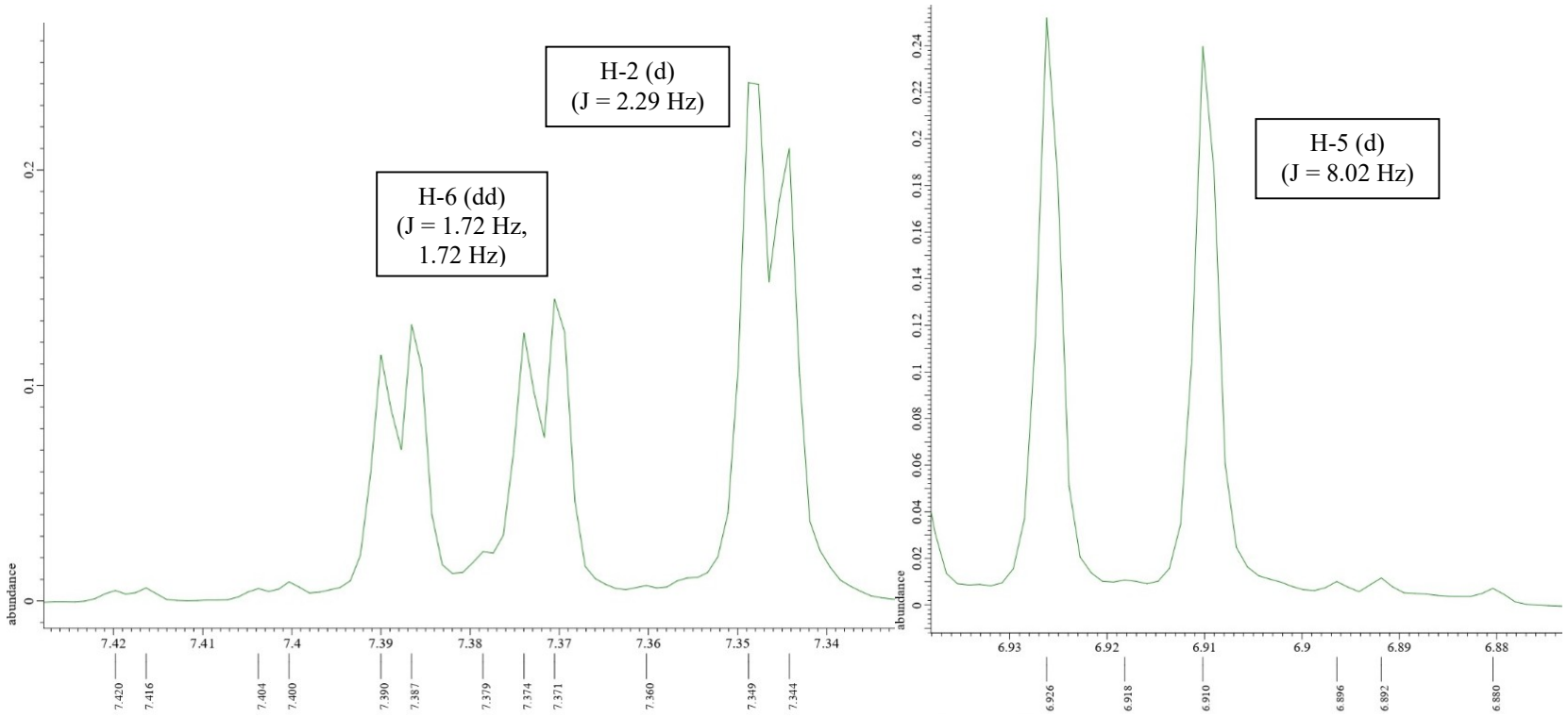
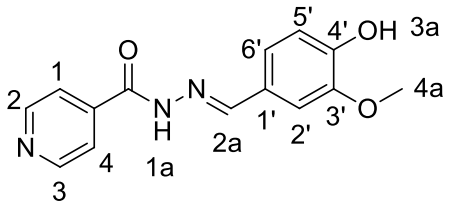


Figure 4.127: Expansion of several sections of ^{1}H NMR of compound (17)

Lastly, the ^{1}H NMR results of compound (21) showed signals of a total of 11 protons, which were summarised as depicted in Table 4.24.

Table 4.24: ^{1}H NMR of compound (21)



Numbers of protons	^{1}H NMR δ (ppm)	Multiplicity	J values (Hz)
1a	12.217	s	-
2a	8.654	s	-
1	7.024, 7.021, 7.008, 7.005	dd	1.15, 1.15
2	7.172, 7.170, 7.156, 7.154	dd	1.15, 1.15
3	7.172, 7.170, 7.156, 7.154	dd	1.15, 1.15
4	7.024, 7.021, 7.008, 7.005	dd	1.15, 1.15
2’	7.593, 7.582	d	5.15
5’	8.762, 8.749	d	6.30
6’	7.807, 7.803, 7.798, 7.795	dd	1.72, 1.15
3a	10.649	s	-
4a	3.782	s	-

Based on the ^{1}H NMR analysis of compound (21), the most downfield signal was recorded as δ 12.217, which was a singlet signal for H-1a attached to a nitrogen atom. Due to the strongly electronegative nitrogen atoms, H-1a was effectively deshielded, thus resulting in formation of signal at the downfield region of the ^{1}H NMR

spectrum. Another singlet signal at δ was observed at δ 10.649, which was indicative for the presence of H-3a from OH group of vanillin part. For the aromatic protons, H-5' was able to show coupling constant with the ortho H-6', hence showing a doublet with signals δ 8.762 and δ 8.749 (J = 6.30 Hz). Similarly, H-2' was able to depict coupling constant with the meta H-6', resulting in presence of a doublet of signals δ 7.593 and δ 7.582 (J = 5.15 Hz). The J value of the ortho coupling of H-5' and H-6' was higher than the meta coupling of H-2' and H-6'. Apart from that, a doublet of doublets signal was shown at δ 7.807, δ 7.803, δ 7.798 and δ 7.795 (J = 1.72 Hz, 1.15 Hz). This was indicated for H-6' which depict coupling constants with the ortho H-5' and meta H-2'. For the aromatic protons of isonicotinic acid hydrazide, H-2 was able to picture coupling constants with ortho H-1 and meta H-3, whereas H-3 was able to form coupling constants with ortho H-4 and meta H-2. This results in the production of a doublet of doublets signal at δ 7.172, δ 7.170, δ 7.156 and δ 7.154 (J = 1.15 Hz, 1.15 Hz). Similarly, coupling constants of H-1 to the ortho H-2 and meta H-4, as well as coupling constants of H-4 to the ortho H-3 and meta H-1 resulted in the doublet of doublet signal at δ 7.024, δ 7.021, δ 7.008 and δ 7.005 (J = 1.15 Hz, 1.15 Hz). Lastly, a singlet signal at δ 3.782 was indicated for H-4a of methoxy group in the vanillin structure. As a whole, the ^{1}H NMR spectrum of compound (21) was as shown in Figure 4.128, whereas Figure 4.129 depict expansions of a few sections of the spectrum.

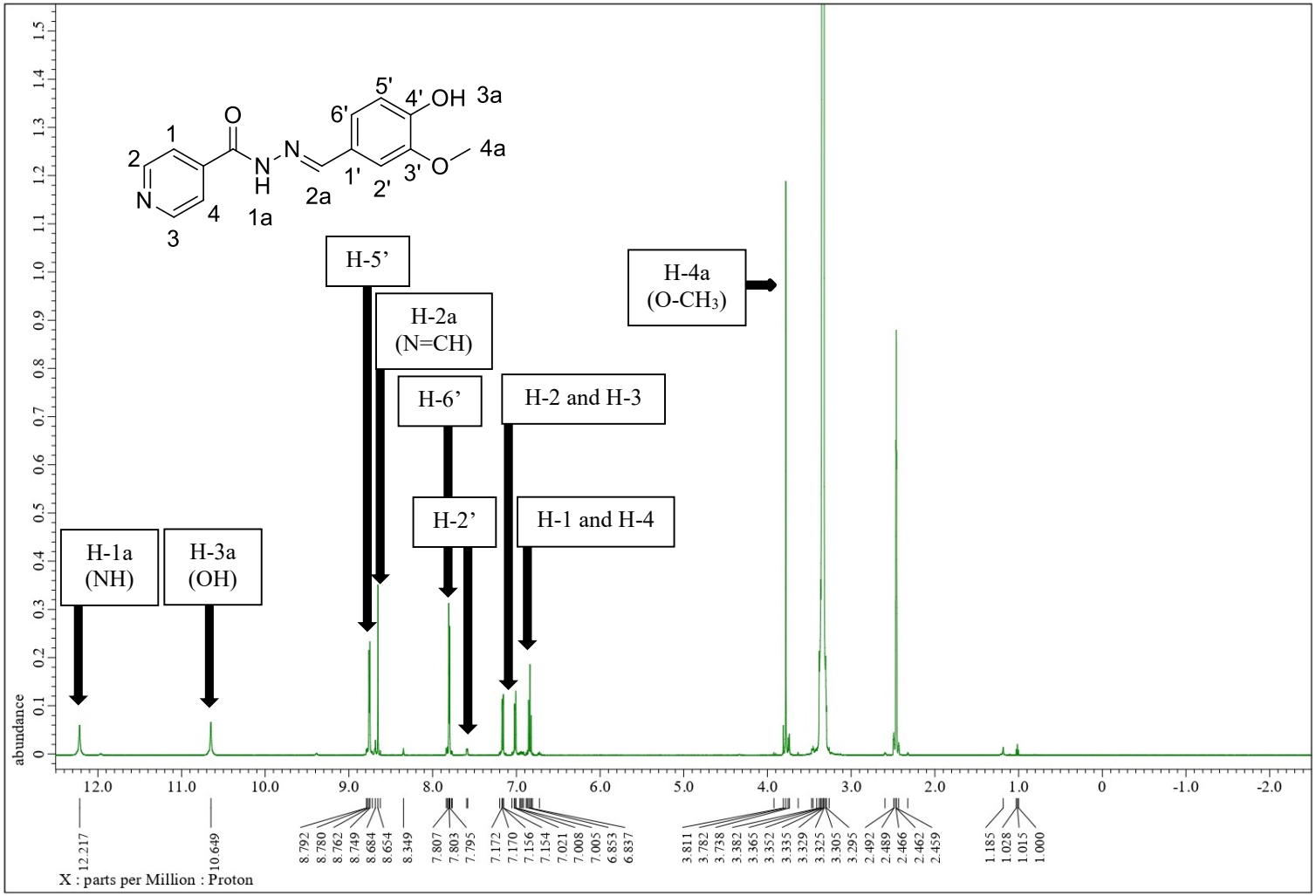


Figure 4.128: ^{1}H NMR of compound (21)

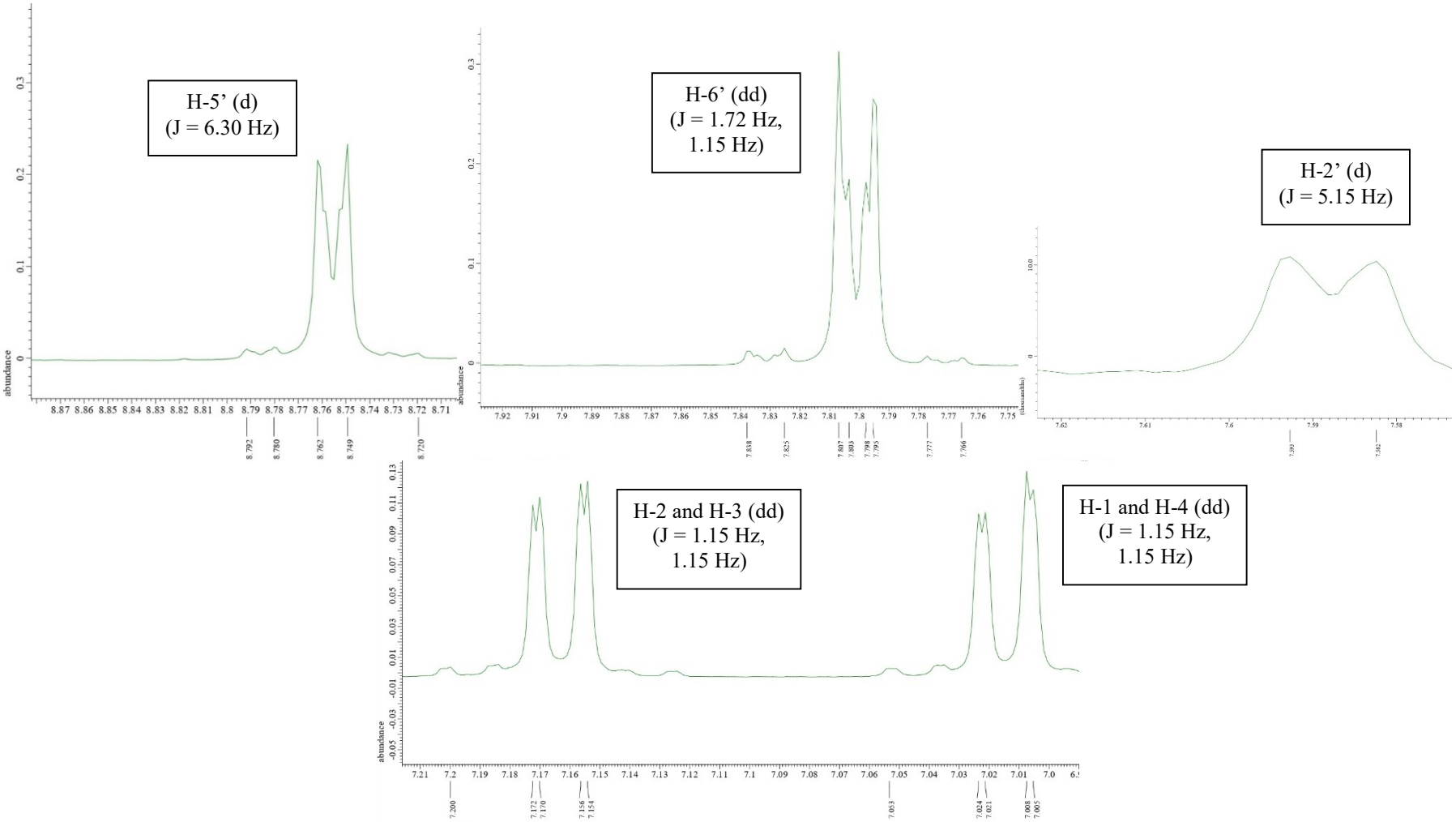


Figure 4.129: Expansion of several sections of ^{1}H NMR of compound (21)

4.7 Antibacterial Assay

The agar diffusion method of antibacterial assay was first performed on the cephalothin positive control and DMSO solvent as negative control. Cephalothin positive control was discovered to depict inhibitory activity towards *S. aureus* by showing an inhibition zone of 15.12 mm. Based on reported literature, cephalothin was reported to illustrate strong inhibitory activity towards *S. aureus* by preventing the growth of the cell wall of the bacteria (del Pilar Zarazaga et al., 2024). Additionally, the 1% DMSO solvent which was used as negative control in a 6 mm well and solvent of Schiff base vanillin derivatives showed no inhibitory activity. DMSO was reported to show only very weak or no antibacterial activity towards *S. aureus* (Arullappan, Zakaria and Basri, 2009). As a result, DMSO was widely utilized as negative control in broad range of antibacterial assays. The result was as shown in Figure 4.130.

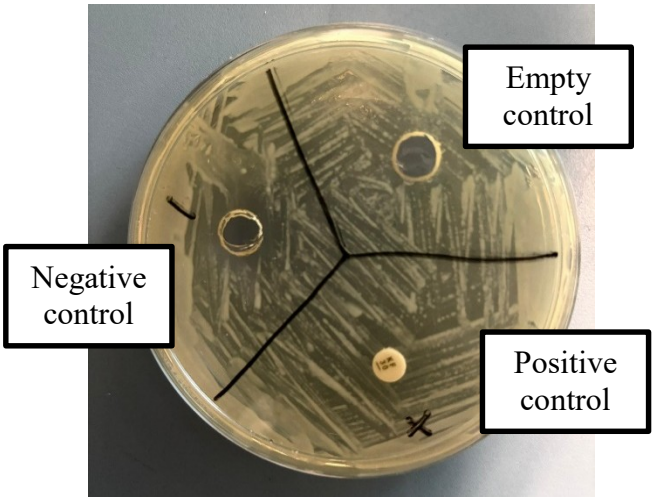
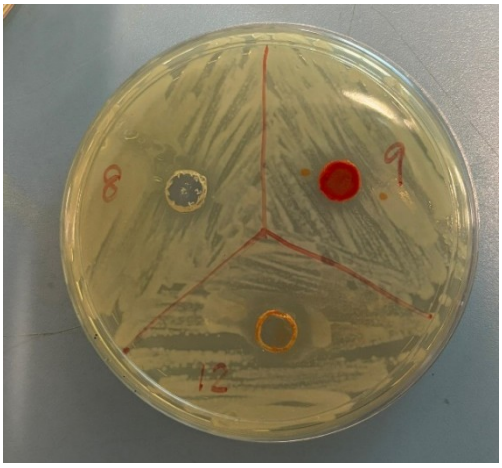


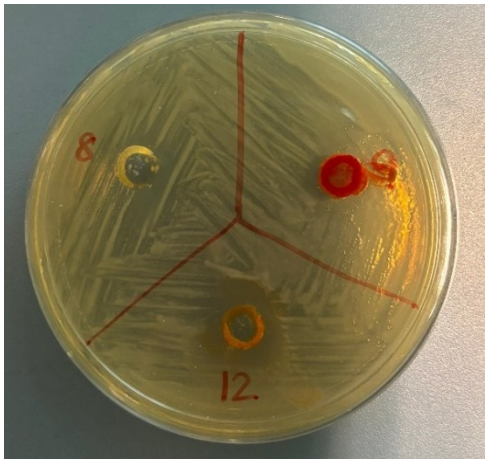
Figure 4.130: Agar diffusion antibacterial assay of positive control, negative control and empty control against *S. aureus*

The 6 Schiff base vanillin derivatives dissolved in DMSO were tested against *S. aureus* in triplicates to obtain an average reading with minimum error. The results were tabulated in Table 4.25 and illustrated in Figure 4.131 and 4.132.

Table 4.25: Antibacterial assay results of positive control, negative control, empty control and Schiff base vanillin derivatives against *S. aureus*

Name of compounds	**Diameter of inhibition zone (mm)**			**Average diameter of inhibition zone (mm)**
(8)	12.25	14.53	12.02	12.93 ± 1.13
(9)	12.06	8.09	9.19	9.78 ± 1.67
(12)	14.64	14.85	15.01	14.83 ± 0.15
(15)	15.02	15.43	15.36	15.27 ± 0.18
(17)	20.22	18.95	22.03	20.40 ± 1.26
(21)	17.55	15.63	15.27	16.15 ± 1.00
Positive control (Cephalothin)	15.12			
Negative control (1% DMSO)	0.00			
Empty control	0.00			

(a) 

(b) 

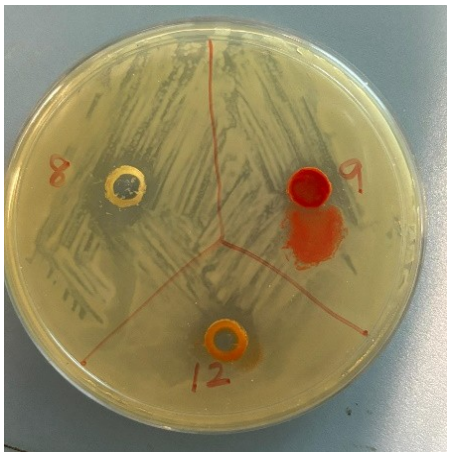
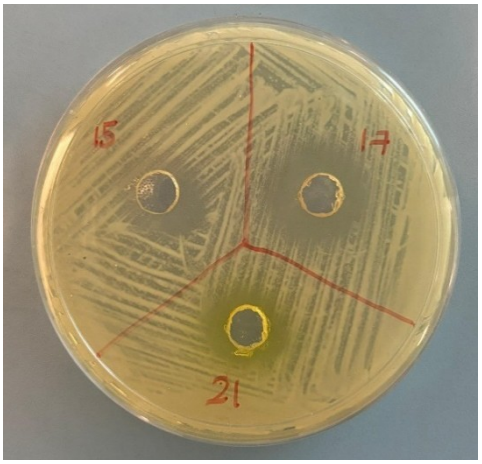
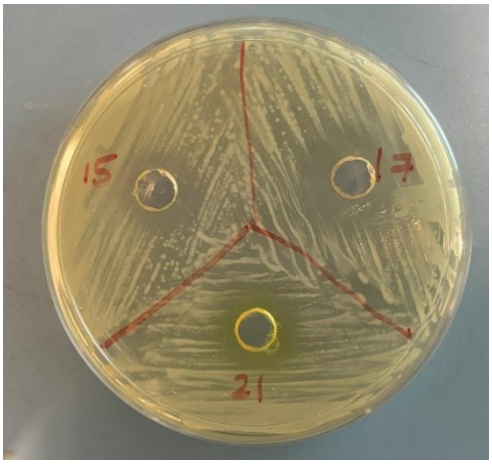
(c) 

Figure 4.131: Agar disk diffusion antibacterial assay of compounds (8), (9) and (12) against *S. aureus* in (a) first replicate (b) second replicate and (c) third replicate

(a) 

(b) 

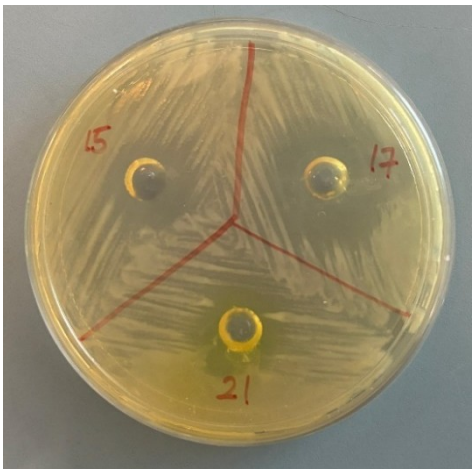
(c) 

Figure 4.132: Agar disk diffusion antibacterial assay of compounds (15), (17) and (21) against *S. aureus* in (a) first replicate (b) second replicate and (c) third replicate

As a whole, all 6 Schiff base vanillin derivatives showed significant inhibition zone, thus essential antibacterial activity against *S. aureus*. The inhibition diameter of the negative control, which is DMSO, served as the baseline or reference point to be compared with the diameters of inhibition zones of the tested vanillin derivatives. Based on the results, all Schiff base vanillin derivatives depicted average diameter of inhibition zone greater than the negative control, thus confirmed for the antibacterial activity against *S. aureus*.

In compared to the cephalothin positive control, compounds (15), (17) and (21) showed inhibition diameter zone greater than the positive control, giving further

fundamental support of the antibacterial activity. Thiobenzamide derivative was reported to show antibacterial activity towards *S. aureus*, particularly as sortase A inhibitors (Ha, Yi and Paek, 2020). Furthermore, derivatives of sulfamic acid were also discovered to show inhibitory activity towards *S. aureus*, specifically as the PlsY inhibitors (Cherian et al., 2012). On top of that, the ATCC 6538 strain of *S. aureus* was reported to be inhibited by the hydrazide-hydrazones of isonicotinic acid (Popiołek, 2021). For depicting fundamental inhibitory activity against *S. aureus*, compounds (15), (17) and (21), which are Schiff base vanillin derivatives of thiobenzamide, sulfamic acid and isonicotinic acid hydrazide, were further and newly discovered to show inhibitory activity towards *S. aureus* through *in silico* and *in vitro* methods.

Compounds (8), (9) and (12) also portrayed essential inhibition diameter zone against *S. aureus*, despite being lower than the positive control, but still greater than the baseline of negative control. 4-hydroxybenzhydrazide derivatives as inhibitors of *S. aureus* were limitedly reported, but were discovered for the inhibitory activity against other bacterial strains such as *Candida glabrata* (Popiołek, 2021). As reported by Hamid et al. (2013), a 2,4-dinitrophenylhydrazine derivative was reported to show strong antibacterial activity towards various bacterial strains, including *S. aureus* but not as strong as other bacterial strains such as *Pasteurella multocida* and *B. subtilis*. Lastly, the antimicrobial activities of transition metal complexes of 4-aminoantipyrine derivatives against *Staphylococci* were also researched and reported (Krishnan et al., 2022). In similar manner, Schiff base vanillin derivatives of the primary amines of 4-hydroxybenzhydrazide, 2,4-dinitrophenylhydrazine and 4-aminoantipyrine, which makes compound (8), (9) and (12) respectively, were further uncovered to possess inhibitory activity towards *S. aureus* through computational study and antibacterial assay despite limited reported studies available.

Additionally, Schiff base derivatives have been reported by Low et al. (2016) to show essentially strong inhibitory activity against *S. aureus*. Simultaneously, vanillin was also reported for the antimicrobial activity against *S. aureus* (Bezerra, 2017). As a result, Schiff base vanillin derivatives of the 6 primary amines, which were compound (8), (9), (12), (15), (17) and (21) showed considerably strong and notable antibacterial activity against Gram-positive bacterium. This result provided fundamental support to the computation confidence of the potential of Schiff base vanillin derivatives as inhibitors of pneumonia-related bacterial strains.

A summary of the overall result in combination of CADD and agar diffusion assay is as depicted in Table 4.26. Based on the tabulated results, 10 out of 21 vanillin derivatives that possessed potential as dual inhibitors of neuraminidase and FtsZ as shown in Table 4.16, showed significant fit values in LBDD and docking values in SBDD. With 6 out of 10 derivatives successfully synthesized, the computational results were further corroborated by the significant inhibition zone against Gram-positive *S. aureus* in agar diffusion assay.

Table 4.26: Summary of overall CADD and agar diffusion assay results

Schiff base vanillin derivatives	**CADD as neuraminidase inhibitors**		**CADD as FtsZ inhibitors**		**Average diameter of inhibition zone (mm)**
	LBDD	**SBDD**	**LBDD**	**SBDD**	
(5)	74.35	-7.60 ± 0.27	85.99	-7.60 ± 0.08	-
(8)	74.12	-6.60 ± 0.32	85.94	-9.60 ± 0.29	12.93 ± 1.13
(9)	73.99	-6.60 ± 0.26	92.98	-9.50 ± 0.11	9.78 ± 1.67
(10)	73.29	-6.20 ± 0.02	83.82	-8.80 ± 0.23	-

Table 4.26 continued

(12)	64.68	-6.20 ± 0.07	103.43	-10.40 ± 0.07	14.83 ± 0.15
(15)	64.58	-7.50 ± 0.14	83.51	-8.50 ± 0.16	15.27 ± 0.18
(16)	64.56	-6.50 ± 0.16	83.51	-8.20 ± 0.20	-
(17)	64.56	-6.70 ± 0.23	85.68	-7.10 ± 0.21	20.40 ± 1.26
(19)	64.55	-7.10 ± 0.28	86.09	-9.80 ± 0.33	-
(21)	64.25	-6.50 ± 0.34	85.60	-8.80 ± 0.07	16.15 ± 1.00

CHAPTER 5

CONCLUSION AND RECOMMENDATIONS

5.1 Conclusion

Out of 21 Schiff base vanillin derivatives, 10 Schiff base vanillin derivatives were concluded as potential inhibitors of *S. pneumoniae* neuraminidase and *S. aureus* FtsZ, whereas 6 of the Schiff base vanillin derivatives were successfully synthesized and depicted inhibition activity against *S. aureus* in antibacterial assay. In computational-aided study, the research was divided into ligand-based pharmacophore modelling, structure-based pharmacophore modelling and structure-based molecular docking.

The first stage of study was evaluation inhibitory activity of Schiff base vanillin derivatives against neuraminidase of *S. pneumoniae*. In ligand-based pharmacophore modelling, upon generation and validation of the reliability of pharmacophore model, all 21 Schiff base vanillin derivatives showed good pharmacophore fit value ranging from 64.25 to 81.50, and 6 to 8 out of 10 matching pharmacophore features in the generated pharmacophore model. In structure-based pharmacophore modelling, compounds that showed good alignment with the oseltamivir carboxylate ligand in 2YA8, 20 out of 21 were able to show good alignment and matching interactions with the ligand of 2YA8. Compound (20) failed to show alignment with the oseltamivir carboxylate ligand due to few possible reasons, including lack of functional groups and suitable conformations. Out of 20 vanillin derivatives, 15 compounds were able to depict matching interactions with the key active site residues, which were compound (2), (3), (4), (5), (6), (8), (9), (10), (12), (15), (16), (17), (18), (19) and (21). Simultaneously, the Schiff base vanillin derivatives showed docking value less than –6.00 kcal/mol, thus depicting strong binding interaction in the active site of

2YA8. This provided further support of the potential of Schiff base vanillin derivatives to show inhibitory activity towards *S. pneumoniae* neuraminidase. As a whole, the 15 Schiff base vanillin derivatives were concluded as potential neuraminidase inhibitors of *S. pneumoniae*.

For analysis of Schiff base vanillin derivatives as potential inhibitors of *S. aureus* FtsZ, 17 out of 21 Schiff base vanillin derivatives were concluded for their potential FtsZ inhibition activity in ligand-based pharmacophore modelling. The tested vanillin derivatives depicted pharmacophore fit value ranging from 66.45 to 104.06, as well as matching with 6 to 10 out of 17 pharmacophore features. Compounds (2), (3), (4) and (11) showed slightly lower fit values and matching interactions in the generated pharmacophore model, thus the remaining 17 Schiff base vanillin derivatives showed considerably satisfied results in ligand-based pharmacophore modelling. In structure-based pharmacophore modelling, 19 out of 21 Schiff base vanillin derivatives showed excellent alignment with the PC190723 ligand of 3VOB, thus depicting matching interactions with important key active site residues. Due to lack of functional groups or suitable conformations to fit in the model, compound (18) failed to show good alignment with PC190723 ligand. Out of the remaining 20 Schiff base vanillin derivatives, 19 of them successfully depicted at least half of the key active site residues towards 3VOB, thus further strengthening their potential inhibitory activity against *S. aureus* FtsZ. Except for compound (6) which only depicted 3 interactions to key active site residues, the other 19 Schiff base vanillin derivatives, including compounds (1), (2), (3), (4), (5), (7), (10), (11), (13), (17), (19), (20) and (21), showed good docking value less than –6.00 kcal/mol. This indicated strong and firm binding interaction in the active site of 3VOB, thus proving greater inhibitory potential against FtsZ of *S. aureus*.

In combination of all results from CADD, a total of 10 Schiff base vanillin derivatives were concluded with potential inhibitory activity against both neuraminidase and FtsZ of *S. pneumoniae* and *S. aureus* respectively. The 10 Schiff base vanillin derivatives were compounds (5), (8), (9), (10), (12), (15), (16), (17), (19) and (21). Among the 10 derivatives, compound (8) showed the best fit value of 74.12 in ligand-based pharmacophore modelling, whereas compound (15) best binding affinity value of -7.50 ± 0.14 kcal/mol in molecular docking respectively as potential neuraminidase inhibitor. Moreover, compound (12) showed the highest fit value and binding affinity in both ligand-based and structure-based study, which were 103.43 and -10.40 ± 0.07 kcal/mol respectively as potential FtsZ inhibitor. As a whole, the first objective to analyse the potential dual inhibitory activity of Schiff base vanillin derivatives targeting *S. pneumoniae* neuraminidase and *S. aureus* FtsZ has been achieved.

Out of 10 Schiff base vanillin derivatives, 6 of them were successfully synthesized by Schiff base synthesis reactions, which were monitored with TLC and FT-IR characterization methods to confirm successful synthesis. Therefore, the second and third objectives are achieved. The 6 Schiff base vanillin derivatives were compounds (8), (9), (12), (15), (17) and (21). These vanillin derivatives were named as follow:

i. **(8)** 4-hydroxy-N'-(4-hydroxy-3-methoxybenzylidene)benzohydrazide

ii. **(9)** 4-((2-(2,4-dinitrophenyl)hydrazono)methyl)-2-methoxyphenol

iii. **(12)** 4-((4-hydroxy-3-methoxybenzylidene)amino)-1,5-dimethyl-2-phenyl-1H-pyrazol-3(2H)-one

iv. **(15)** N-(4-hydroxy-3-methoxybenzylidene)benzothioamide

v. **(17)** (E)-(4-hydroxy-3-methoxybenzylidene)sulfamic acid

vi. **(21)** N'-(4-hydroxy-3-methoxybenzylidene)isonicotinohydrazide

The 6 Schiff base vanillin derivatives were dissolved in DMSO solvent with concentration of 1.0×10^3 μg/mL. The derivatives were lastly subjected to antibacterial assay against *S. aureus* by performing agar diffusion method. In comparison with a cephalothin positive control and 1% DMSO negative control, the 6 Schiff base vanillin derivatives showed significant inhibition diameter zone against *S. aureus*, thus depicting essential inhibitory activity against *S. aureus*. Out of all, compound (17) showed the biggest inhibition diameter zone, which was 20.40 ± 1.26mm, thus exhibiting the strongest antibacterial activity.

Despite the fact that the final objective to prove the antibacterial activity of Schiff base vanillin derivatives against Gram-positive bacterium has been achieved, absence of assay against *S. pneumoniae* is considered a limitation as only one type of bacterial strain, which is *S. aureus*, represents Gram-positive bacteria. Therefore, this result cannot be used to extrapolate other clinically relevant Gram-positive bacteria. Furthermore, assay which does not involve MIC or MBC evaluation is also considered a limitation as evaluations of the therapeutic index and potency of vanillin derivatives are restricted from full assessment. Regardless of the limitations, antibacterial activity of Schiff base vanillin derivatives against Gram-positive bacterium is still proven, and the fourth objective of the research is still achieved. Subsequently, this result further strengthened the computational outcomes of Schiff base vanillin derivatives as potential inhibitors of pneumonia-related bacterial strains.

In conclusion, a total of 6 Schiff base vanillin derivatives were proven as potential inhibitors against neuraminidase of *S. pneumoniae* and FtsZ of *S. aureus*. The novelty of this research is being the first research to apply an integrated ligand- and structure-based

pharmacophore approach targeting both neuraminidase and FtsZ using Schiff base vanillin derivatives. Additionally, the computational methods were specifically studied on dual target, which include neuraminidase of *S. pneumoniae* and FtsZ of *S. aureus* by Schiff base vanillin derivatives. These were new avenues being opened up in the field that have not been performed previously. In conjunction of previously studied methods, such as the binding affinity values, Lipinski's Rule of 5 and the antibacterial assay, the results of the research were considered as atrong, evidenced and novel.

5.2 Recommendations

Throughout the research study, the greatest challenge is the utilisation of LigandScout software. This is due to the limiting numbers of features that can be accessed in demonstration mode. In order to be able to access the activated mode, a license number is required but can only be used for one month. Therefore, the Schiff base vanillin derivatives are recommended to be subjected to other methodologies and computational software, such as quantitative structure-activity relationship (QSAR), virtual screening, Schrödinger software, Discovery Studio software etc., to provide stronger affirmation of their potential inhibitory activities through *in silico* methods.

In ligand-based pharmacophore model, more than 1 pharmacophore model can be created and validated, specifically pharmacophore models with different pharmacophore features and created by training sets of diverse chemical structures to provide stronger fundamental support to the results. On top of that, structure-based pharmacophore modelling can be performed on more than 1 PDB structure to further strengthen the results. Aside from that, structure-based pharmacophore modelling can also be performed on more than 1 surface protein, for example the pneumolysin, choline-binding proteins etc., especially those

that have not been researched in previous literatures. Such method is able to further strengthen the potential antibacterial activity of Schiff base vanillin derivatives against *S. pneumoniae* and *S. aureus*. Besides, selection of primary amines to synthesise Schiff base vanillin derivatives can be done in a more specific way, such as selecting primary amines of a particular functional group or class of compounds to produce more precise explanation and results.

Being promising drug candidates as potential inhibitors of neuraminidase and FtsZ of *S. pneumoniae* and *S. aureus* respectively, the Schiff base vanillin derivatives can be subjected to more assays *via in vitro* and *in vivo*, such as MUNANA assay to confirm their inhibitory activity against *S. pneumoniae* neuraminidase. Although the antibacterial assay against *S. aureus* has provided significant validation to the computational predictions, experimental evaluation against *S. pneumoniae* can be included to further affirmed the findings, provide a more complete assessment and strengthen the potential dual inhibitory activity of vanillin derivatives against both *S. pneumoniae* neuraminidase and *S. aureus* FtsZ. Additionally, broth dilution assay can also be incorporated to determine the MIC and MBC values. Addition of this assay ensures a more quantitative and reproducible evaluation of antibacterial activity, and thus complementary with qualitative results from agar diffusion assay results in stronger support to the fundamental confidence to the potential dual inhibitory activity of Schiff base vanillin derivatives towards both *S. pneumoniae* neuraminidase and *S. aureus* FtsZ.

REFERENCES

Acharya, C., Coop, A., Polli, J. E., & Mackerell, A. D. J. (2011). Recent advances in ligand-based drug design: relevance and utility of the conformationally sampled pharmacophore approach. *Current Computer-Aided Drug Design*, *7*(1), 10–22.

Adams, D. W., & Errington, J. (2009). Bacterial cell division: assembly, maintenance and disassembly of the Z ring. *Nature Reviews. Microbiology*, *7*(9), 642–653.

Agnihotry, S., Pathak, R., Srivastav, A., Shukla, P. K., & Gautam, B. (2020). Molecular docking and structure-based drug design. In *Computer-Aided Drug Design* (Singh, D. B.), pp. 115–131. Singapore: Springer.

Al-Shar'i, N., & Musleh, S. (2020). Identification of CHK1 kinase inhibitors using structure-based pharmacophore modelling and molecular docking. *Indian Journal of Pharmaceutical Sciences*, *82*, 472–482.

American Lung Association. (2024). *What causes pneumonia?* [online] Available at: https://www.lung.org/lung-health-diseases/lung-disease-lookup/pneumonia/what-causes-pneumonia [Accessed on 11 November 2024].

Andreu, J. M., Schaffner-Barbero, C., Huecas, S., Alonso, D., Lopez-Rodriguez, M. L., Ruiz-Avila, L. B., Núñez-Ramírez, R., Llorca, O., & Martín-Galiano, A. J. (2010). The antibacterial cell division inhibitor PC190723 is an FtsZ polymer-stabilizing agent that induces filament assembly and condensation. *The Journal of Biological Chemistry*, *285*(19), 14239–14246.

Anuradha, K., Shyamala, B., & Naidu, M. (2013). Vanilla- its science of cultivation, curing, chemistry, and nutraceutical properties. *Critical Reviews in Food Science and Nutrition*, *53*, 1250–1276.

Arauz, J., Ramos-Tovar, E., & Muriel, P. (2017). Chapter 48 - coffee and the liver. In *Liver Pathophysiology: Therapies and Antioxidants* (Muriel, P.), pp. 675-685. Cambridge: Academic Press.

Arullappan, S., Zakaria, Z., & Basri, D. F. (2009). preliminary screening of antibacterial activity using crude extracts of *Hibiscus rosa sinensis*. *Tropical Life Sciences Research*, *20*(2), 109–118.

Asaruddin, M. R. (2016). *Modelling and syntheses of vanillin derivatives targeting influenza virus neuraminidase*. [e-book] Available through: Universiti Sains Malaysia Institutional Repository <http://eprints.usm.my/id/eprint/45418> [Accessed on 27 March 2023].

Balouiri, M., Sadiki, M., & Ibnsouda, S. K. (2016). Methods for *in vitro* evaluating antimicrobial activity: A review. *Journal of Pharmaceutical Analysis*, *6*(2), 71–79.

Barbuti, M. D., Myrbråten, I. S., Morales Angeles, D., & Kjos, M. (2023). The cell cycle of *Staphylococcus aureus*: An updated review. *MicrobiologyOpen*, *12*(1), 1338.

Basak, P., Dastidar, D. G., Ghosh, D., Chakraborty, T., Sau, S., & Chakrabarti, G. (2024). *Staphylococcus aureus* major cell division protein FtsZ assembly is inhibited by silibinin, a natural flavonolignan that also blocked bacterial growth and biofilm formation. *International Journal of Biological Macromolecules*, *279*, 135252.

Bauer, T. T., Ferrer, R., Angrill, J., Schultze-Werninghaus, G., & Torres, A. (2000). Ventilator-associated pneumonia: incidence, risk factors, and microbiology. *Seminars in Respiratory Infections*, *15*(4), 272–279.

Bezerra, C. F., Camilo, C. J., do Nascimento Silva, M. K., de Freitas, T. S., Ribeiro-Filho, J., & Coutinho, H. D. M. (2017). Vanillin selectively modulates the action of antibiotics against resistant bacteria. *Microbial Pathogenesis*, *113*, 265–268.

Bisson-Filho, A. W., Hsu, Y. P., Squyres, G. R., Kuru, E., Wu, F., Jukes, C., Sun, Y., Dekker, C., Holden, S., Vannieuwenhze, M. S., Brun, Y. V., & Garner, E. C. (2017). Treadmilling by FtsZ filaments drives peptidoglycan synthesis and bacterial cell division. *Science*, *355*(6326), 739–743.

Bjarnason, A., Westin, J., Lindh, M., Andersson, L.-M., Kristinsson, K. G., Löve, A., Baldursson, O., & Gottfredsson, M. (2018). Incidence, etiology, and outcomes of community-acquired pneumonia: a population-based study. *Open Forum Infectious Diseases*, *5*(2), ofy010.

Blanco, A., & Blanco, G. (2017). Chapter 4 - carbohydrates. In *Medical Biochemistry* (Blanco, A., & Blanco, G.), pp. 73–97. Cambridge: Academic Press.

Böhm, H. J. (1992). The computer program LUDI: a new method for the *de novo* design of enzyme inhibitors. *Journal of Computer-Aided Molecular Design*, *6*(1), 61–78.

Booth, S., & Lewis, R. J. (2019). Structural basis for the coordination of cell division with the synthesis of the bacterial cell envelope. *Protein Science: A Publication of the Protein Society*, *28*(12), 2042–2054.

Bottomley, A. L., Kabli, A. F., Hurd, A. F., Turner, R. D., Garcia-Lara, J., & Foster, S. J. (2014). *Staphylococcus aureus* DivIB is a peptidoglycan-binding protein that is required for a morphological checkpoint in cell division. *Molecular Microbiology*, *94*(5), 1041–1064.

Boucher, H. W., & Corey, G. R. (2008). Epidemiology of methicillin-resistant *Staphylococcus aureus*. *Clinical Infectious Diseases*, *46*(5), 344–349.

Briggs, G. S., Smits, W. K., & Soultanas, P. (2012). Chromosomal replication initiation machinery of low-G+C-content firmicutes. *Journal of Bacteriology*, *194*(19), 5162–5170.

Britton, R. A., Lin, D. C., & Grossman, A. D. (1998). Characterization of a prokaryotic SMC protein involved in chromosome partitioning. *Genes & Development*, *12*(9), 1254–1259.

Brooks, L. R. K., & Mias, G. I. (2018). *Streptococcus pneumoniae*'s virulence and host immunity: aging, diagnostics, and prevention. *Frontiers in Immunology*, *9*, 1–29.

Brown, S., Santa Maria, J. P. J., & Walker, S. (2013). Wall teichoic acids of gram-positive bacteria. *Annual Review of Microbiology*, *67*, 313–336.

Bryan, E., Ferrer-González, E., Sagong, H. Y., Fujita, J., Mark, L., Kaul, M., LaVoie, E. J., Matsumara, H., & Pilch, D. S. (2023). Structural and antibacterial characterization of a new benzamide ftsz inhibitor with superior bactericidal activity and *in vivo* efficacy against multidrug-resistant *Staphylococcus aureus*. *ACS Chemical Biology*, *18*(3), 629–642.

Carlson, H. A., Smith, R. D., Khazanov, N. A., Kirchhoff, P. D., Dunbar, J. B. J., & Benson, M. L. (2008). Differences between high- and low-affinity complexes of enzymes and nonenzymes. *Journal of Medicinal Chemistry*, *51*(20), 6432–6441.

Carro, L. (2019). Recent progress in the development of small-molecule ftsz inhibitors as chemical tools for the development of novel antibiotics. *Antibiotics*, *8*(4), 217.

Casiraghi, A., Suigo, L., Valoti, E., & Straniero, V. (2020). Targeting bacterial cell division: a binding site-centered approach to the most promising inhibitors of the essential protein FtsZ. *Antibiotics*, *9*(2), 69.

Celik, S., Ozkok, F., Ozel, A. E., Cakir, E., & Akyuz, S. (2021). Synthesis, FT-IR and NMR characterization, antibacterial and antioxidant activities, and DNA docking analysis of a new vanillin-derived imine compound. *Journal of Molecular Structure*, *1236*, 130288.

Centers For Disease Control and Prevention. (n.d.). *About pneumococcal disease*. [online] Available at: https://www.cdc.gov/pneumococcal/about/index.html [Accessed on 11 November 2024].

Centers For Disease Control and Prevention. (n.d.). *About pneumonia*. [online] Available at: https://www.cdc.gov/pneumonia/about/index.html [Accessed on 11 November 2024].

Centers For Disease Control and Prevention. (2022). *Drug resistance*. [online] Available at: https://www.cdc.gov/pneumococcal/clinicians/drug-resistance.html [Accessed on 11 November 2024].

Centers For Disease Control and Prevention. (2023). *Pneumococcal vaccination*. [online] Available at: https://www.cdc.gov/vaccines/vpd/pneumo/index.html [Accessed on 9 November 2024].

Centers For Disease Control and Prevention. (2024). *Staphylococcus aureus basics*. [online] Available at: https://www.cdc.gov/staphylococcus-aureus/about/index.html [Accessed on 19 November 2024].

Ceramella, J., Iacopetta, D., Catalano, A., Cirillo, F., Lappano, R., & Sinicropi, M. S. (2022). A review on the antimicrobial activity of schiff bases: data collection and recent studies. *Antibiotics*, *11*(2), 191.

Chan, H., Söderström, B., & Skoglund, U. (2020). Spo0J and SMC are required for normal chromosome segregation in *Staphylococcus aureus*. *MicrobiologyOpen*, *9*(4), 999.

Chen, R., Li, L., & Weng, Z. (2003). ZDOCK: An initial-stage protein-docking algorithm. *Proteins: Structure, Function, and Bioinformatics*, *52*(1), 80–87.

Chen, Y., Liu, T., Wang, K., Hou, C., Cai, S., Huang, Y., Du, Z., Huang, H., Kong, J., & Chen, Y. (2016). Baicalein inhibits *Staphylococcus aureus* biofilm formation and the

quorum sensing system *in vitro*. *PloS One*, *11*(4), e0153468.

Cheng, T., Li, X., Li, Y., Liu, Z., & Wang, R. (2009). Comparative assessment of scoring functions on a diverse test set. *Journal of Chemical Information and Modeling*, *49*(4), 1079–1093.

Cherian, P. T., Yao, J., Leonardi, R., Maddox, M. M., Luna, V. A., Rock, C. O., & Lee, R. E. (2012). Acyl-sulfamates target the essential glycerol-phosphate acyltransferase (PlsY) in gram-positive bacteria. *Bioorganic & Medicinal Chemistry*, *20*(16), 4985–4994.

Chou, T.-H., Ding, H.-Y., Hung, W. J., & Liang, C. H. (2010). Antioxidative characteristics and inhibition of α-melanocyte-stimulating hormone-stimulated melanogenesis of vanillin and vanillic acid from *Origanum vulgare*. *Experimental Dermatology*, *19*(8), 742–750.

Cleveland Clinic. (2022). *Pneumonia*. [online] Available at: https://my.clevelandclinic.org/health/diseases/4471-pneumonia [Accessed on 11 November 2024].

Clinical and Laboratory Standards Institute. (2020). *Performance standards for antimicrobial susceptibility testing*. Wayne: CLSI.

Converti, A., Aliakbarian, B., Domínguez, J. M., Vázquez, G. B., & Perego, P. (2010). Microbial production of biovanillin. *Brazilian Journal of Microbiology*, *41*(3), 519–530.

CUSABIO Team. (n.d.). *Streptococcus pneumoniae, a primary cause of pneumonia*. [online] Available at: https://www.cusabio.com/c-20998.html?srsltid=AfmBOoq_RGKxXeDodHuUMRGpRuYXFzW7nRfHk6Jb_OHcQxeXzNjcBhrx#a03 [Accessed on 13 November 2024].

da Silva, C. M., da Silva, D. L., Modolo, L. V, Alves, R. B., de Resende, M. A., Martins, C. V. B., & de Fátima, Â. (2011). Schiff bases: A short review of their antimicrobial activities. *Journal of Advanced Research*, *2*(1), 1–8.

Daniel, R. A., Noirot-Gros, M. F., Noirot, P., & Errington, J. (2006). Multiple interactions between the transmembrane division proteins of *Bacillus subtilis* and the role of FtsL instability in divisome assembly. *Journal of Bacteriology*, *188*(21), 7396–7404.

de Boer, P., Crossley, R., & Rothfield, L. (1992). The essential bacterial cell-division protein FtsZ is a GTPase. *Nature*, *359*(6392), 254–256.

del Pilar Zarazaga, M., Tinti, M. G., Litterio, N. J., Himelfarb, M. A., Andrés-Larrea, M. I. S., Rubio-Langre, S., Serrano-Rodríguez, J. M., & Lorenzutti, A. M. (2024). Dose regimen optimization of cephalothin for surgical prophylaxis against *Staphylococcus aureus* and coagulase negative staphylococci in dogs by pharmacokinetic/pharmacodynamic modeling. *Research in Veterinary Science*, *171*, 105202.

Dhingra, D., & Sharma, A. (2005). Evaluation of antidepressant-like activity of glycyrrhizin in mice. *Indian Journal of Pharmacology*, *37*(6), 390–394.

Diah, I. M. & Aziz, N. (2021). The relative risk estimation of pneumonia in Malaysia using standardized morbidity ratio (sMR). *ASM Science Journal*, *16*, 1–5.

Dion, C. F., & Ashurst, J. V. (2022). *Streptococcus pneumoniae*. [online] Available at: https://www.ncbi.nlm.nih.gov/books/NBK470537/ [Accessed on 9 November 2024].

Doak, B. C., & Kihlberg, J. (2016). Drug discovery beyond the rule of 5 - Opportunities and challenges. *Expert Opinion on Drug Discovery*, *12*(2), 115–119.

Downes, S. G., Owens, R. A., Walshe, K., Fitzpatrick, D. A., Dorey, A., Jones, G. W., & Doyle, S. (2023). Gliotoxin-mediated bacterial growth inhibition is caused by

specific metal ion depletion. *Scientific Reports*, *13*(1), 16156.

Ece, A. (2023). Computer-aided drug design. *BMC Chemistry*, *17*(1), 26.

Erickson, H. P. (1998). Atomic structures of tubulin and FtsZ. *Trends in Cell Biology*, *8*(4), 133–137.

Errington, J., Daniel, R. A., & Scheffers, D. J. (2003). Cytokinesis in bacteria. *Microbiology and Molecular Biology Reviews: MMBR*, *67*(1), 52–65.

Esteban, P., Redrado, S., Comas, L., Domingo, M. P., Millán-Lou, M. I., Seral, C., Algarate, S., Lopez, C., Rezusta, A., Pardo, J., Arias, M., & Galvez, E. M. (2021). *In vitro* and *in vivo* antibacterial activity of gliotoxin alone and in combination with antibiotics against *Staphylococcus aureus*. *Toxins*, *13*(2), 85.

European Committee for Antimicrobial Susceptibility Testing of the European Society of Clinical Microbiology and Infectious Diseases. (2003). Determination of minimum inhibitory concentrations (MICs) of antibacterial agents by broth dilution. *Clinical Microbiology and Infection*, *9*(8), ix–xv.

Fache, M., Boutevin, B., & Caillol, S. (2016). Vanillin production from lignin and its use as a renewable chemical. *ACS Sustainable Chemistry & Engineering*, *4*(1), 35–46.

Fein, A. M., & Niederman, M. S. (1994). Severe pneumonia in the elderly. *Clinics in Geriatric Medicine*, *10*(1), 121–143.

Fleck, O. (2019). *Streptococcus pneumoniae (pneumococcus): Overview*. [online] Available at: https://www.news-medical.net/health/Streptococcus-pneumoniae-%28pneumococcus%29-Overview.aspx [Accessed on 11 November 2024].

Fox, S., Farr-Jones, S., Sopchak, L., Boggs, A., Nicely, H. W., Khoury, R., & Biros, M. (2006). High-throughput screening: update on practices and success. *Journal of*

Biomolecular Screening, *11*(7), 864–869.

Fujita, J., Maeda, Y., Mizohata, E., Inoue, T., Kaul, M., Parhi, A. K., LaVoie, E. J., Pilch, D. S., & Matsumura, H. (2017). Structural flexibility of an inhibitor overcomes drug resistance mutations in *Staphylococcus aureus* FtsZ. *ACS Chemical Biology*, *12*(7), 1947–1955.

Fuqua, C., & Greenberg, E. P. (2002). Listening in on bacteria: acyl-homoserine lactone signalling. *Nature Reviews Molecular Cell Biology*, *3*(9), 685–695.

Gao, B., Li, X., Yang, F., Chen, W., Zhao, Y., Bai, G., & Zhang, Z. (2019). Molecular epidemiology and risk factors of ventilator-associated pneumonia infection caused by carbapenem-resistant enterobacteriaceae. *Frontiers in Pharmacology*, *10*, 262.

Giordano, D., Biancaniello, C., Argenio, M. A., & Facchiano, A. (2022). Drug design by pharmacophore and virtual screening approach. *Pharmaceuticals*, *15*(5), 646. https://doi.org/10.3390/ph15050646

Golos, M., Eliakim-Raz, N., Stern, A., Leibovici, L., & Paul, M. (2019). Conjugated pneumococcal vaccine versus polysaccharide pneumococcal vaccine for prevention of pneumonia and invasive pneumococcal disease in immunocompetent and immunocompromised adults and children. *The Cochrane Database of Systematic Reviews*, *2019*(2), CD012306.

Goodford, P. J. (1985). A computational procedure for determining energetically favorable binding sites on biologically important macromolecules. *Journal of Medicinal Chemistry*, *28*(7), 849–857.

Grabenstein, J. D., & Klugman, K. P. (2012). A century of pneumococcal vaccination research in humans. *Clinical Microbiology and Infection: The Official Publication of the European Society of Clinical Microbiology and Infectious Diseases*, *18*(5), 15–

24.

Grienke, U., Richter, M., Walther, E., Hoffmann, A., Kirchmair, J., Makarov, V., Nietzsche, S., Schmidtke, M., & Rollinger, J. M. (2016). Discovery of prenylated flavonoids with dual activity against influenza virus and *Streptococcus pneumoniae*. *Scientific Reports*, *6*(1), 27156.

Grienke, U., Richter, M., Walther, E., Hoffmann, A., Kirchmair, J., Makarov, V., Nietzsche, S., Schmidtke, M., & Rollinger, J. M. (2016). Discovery of prenylated flavonoids with dual activity against influenza virus and *Streptococcus pneumoniae*. *Scientific reports*, *6*, 27156.

Gualdi, L., Hayre, J. K., Gerlini, A., Bidossi, A., Colomba, L., Trappetti, C., Pozzi, G., Docquier J. D., Andrew, P., Ricci, S., & Oggioni, M. R. (2012). Regulation of neuraminidase expression in *Streptococcus pneumoniae*. *BMC Microbiology*, *12*(1), 200.

Guan, S., Zhu, K., Dong, Y., Li, H., Yang, S., Wang, S., & Shan, Y. (2020). Exploration of binding mechanism of a potential *Streptococcus pneumoniae* neuraminidase inhibitor from herbaceous plants by molecular simulation. *International Journal of Molecular Sciences*, *21*(3), 1003.

Gupta, P. (2023). *What are the 4 stages of pneumonia?* [online] Available at: https://lifemd.com/learn/what-are-the-4-stages-of-pneumonia [Accessed on 11 November 2024].

Gut, H., Xu, G., Taylor, G. L., & Walsh, M. A. (2011). Structural basis for *Streptococcus pneumoniae* NanA inhibition by influenza antivirals zanamivir and oseltamivir carboxylate. *Journal of Molecular Biology. 409*(4), 496 – 503.

Ha, M. W., Yi, S. W., & Paek, S. M. (2020). Design and synthesis of small molecules as

potent *Staphylococcus aureus* sortase A inhibitors. *Antibiotics*, *9*(10), 706.

Hajduk, I. V, Rodrigues, C. D. A., & Harry, E. J. (2016). Connecting the dots of the bacterial cell cycle: Coordinating chromosome replication and segregation with cell division. *Seminars in Cell & Developmental Biology*, *53*, 2–9.

Hamid, A., Sadiq, Z., Yaqub, G., Khan, N., Iqbal, S., Iqbal, K., Ijaz, Z. & Bajwa, A. (2012). Synthesis and bioassay of novel phenylhydrazine and 2,4-dinitrophenylhydrazine substituted carbazoles. *Asian Journal of Chemistry*, *25*(10), 5412–5414.

Han, J., Lin, W. H., Xu, R. S., Wang, W. L., & Zhao, S. H. (1991). Studies on the chemical constituents of *Melia azedarach* L. *Yao Xue Xue Bao = Acta pharmaceutica Sinica*, *26*(6), 426–429.

Hanks, S. K., & Hunter, T. (1995). Protein kinases 6. The eukaryotic protein kinase superfamily: kinase (catalytic) domain structure and classification. *FASEB Journal: Official Publication of the Federation of American Societies for Experimental Biology*, *9*(8), 576–596.

Hemalatha, P. V., Sudha, T., Ravikumar, V. R. & Ganesan, V. (2017). Synthesis, characterization and antimicrobial screening of some salicyl hydrazide schiff bases. *World Journal of Pharmacy and Pharmaceutical Sciences, 7*(1). 1363–1371.

Hissam, M. A., Ngaini, Z., Zamakshshari, N. H., Hejemi, F. N. A. M., Arni, F. S., & Halim, A. N. A. (2024). Synthesis and molecular docking simulation on the antimicrobial effects of halogenated vanillin-azo dyes and schiff base derivatives. *Discover Applied Sciences*, *6*(6), 325.

Hoque, I., Chatterjee, A., Bhattacharya, S., & Biswas, R. (2017). An approach of computer-aided drug design (CADD) tools for *in silico* pharmaceutical drug design and development. *International Journal of Advanced Research in Biological Sciences*,

4(2), 60–71.

Hsiao, Y.-S., Parker, D., Ratner, A. J., Prince, A., Tong, L. (2009). Crystal structures of respiratory pathogen neuraminidases. *Biochemical and Biophysical Research Communications*. *380*(3), 467–471.

Hu, J., Sun, X., Huang, Z., Wagner, A. L., Carlson, B., Yang, J., Tang, S., Li, Y., Boulton, M. L., & Yuan, Z. (2016). *Streptococcus pneumoniae* and *Haemophilus influenzae* type b carriage in Chinese children aged 12-18 months in Shanghai, China: a cross-sectional study. *BMC Infectious Diseases*, *16*, 149.

Hudzicki, J. (2009). *Kirby-Bauer disk diffusion susceptibility test protocol*. [online] Available at: https://asm.org/getattachment/2594ce26-bd44-47f6-8287-0657aa9185ad/Kirby-Bauer-Disk-Diffusion-Susceptibility-Test-Protocol-pdf.pdf [Accessed on 20 November 2024].

Institute for Health Metrics and Evaluation (2024). *Deaths from lower respiratory infections, among individuals aged <5 years per 100,000 people*. [online] Available at: https://vizhub.healthdata.org/gbd-results/ [Accessed on 1 September 2024].

Jain, S., Self, W. H., Wunderink, R. G., Fakhran, S., Balk, R., Bramley, A. M., Reed, C., Grijalva, C. G., Anderson, E. J., Courtney, D. M., Chappell, J. D., Qi, C., Hart, E. M., Carroll, F., Trabue, C., Donnelly, H. K., Williams, D. J., Zhu, Y., Arnold, S. R., Ampofo, K., Waterer, G. W., Levine, M., Lindstrom, S., Winchell, J. M., Katz, J. M., Erdman, D., Schneider, E., Hicks, L. A., McCullers, J. A., Pavia, A. T., Edwards, K. M., and Finelli, L. (2015). Community-acquired pneumonia requiring hospitalization among U.S. Adults. *The New England Journal of Medicine*, *373*(5), 415–427.

Jalil, M. B., & Al Atbee, M. Y. N. (2022). The prevalence of multiple drug resistance *Escherichia coli* and *Klebsiella pneumoniae* isolated from patients with urinary tract

infections. *Journal of Clinical Laboratory Analysis*, *36*(9), e24619.

Jedrzejas, J. M. (2001). Pneumococcal virulence factors: structure and function. *Microbiology and Molecular Biology Reviews*, *65*(2), 187–207.

Jensen, C., Bæk, K. T., Gallay, C., Thalsø-Madsen, I., Xu, L., Jousselin, A., Torrubia, F. R., Paulander, W., Pereira, A. R., Veening, J.-W., Pinho, M. G., & Frees, D. (2019). The ClpX chaperone controls autolytic splitting of *Staphylococcus aureus* daughter cells, but is bypassed by β-lactam antibiotics or inhibitors of WTA biosynthesis. *PLoS Pathogens*, *15*(9), e1008044.

Jorge, A. M., Hoiczyk, E., Gomes, J. P., & Pinho, M. G. (2011). EzrA contributes to the regulation of cell size in *Staphylococcus aureus*. *PloS One*, *6*(11), e27542.

Jorgensen, W. L. (1991). Rusting of the lock and key model for protein-ligand binding. *Science*, *254*(5034), 954–955.

Juan, S., Li, M.-H., Wang, X.-Y., Zhang, Y., Yuan, R.-J., Liu, H.-Y., & Zhu, H.-L. (2014). Vanillin derivatives as the selective small molecule inhibitors of FtsZ. *Medicinal Chemistry Research*, *23*. 2985–2994.

Kadioglu, A., Weiser, J. N., Paton, J. C., & Andrew, P. W. (2008). The role of *Streptococcus pneumoniae* virulence factors in host respiratory colonization and disease. *Nature Reviews Microbiology*, *6*(4), 288–301.

Karathanos, V. T., Mourtzinos, I., Yannakopoulou, K., & Andrikopoulos, N. K. (2007). Study of the solubility, antioxidant activity and structure of inclusion complex of vanillin with β-cyclodextrin. *Food Chemistry*, *101*(2), 652–658.

Kaserer, T., Beck, K. R., Akram, M., Odermatt, A., Schuster, D., & Willett, P. (2015). Pharmacophore models and pharmacophore-based virtual screening: Concepts and applications exemplified on hydroxysteroid dehydrogenases. *Molecules*, *20*(12),

22799 - 22832.

Kazmi, S. Y. (2022). The etymology of microbial nomenclature and the diseases these cause in a historical perspective. *Saudi Journal of Biological Sciences*, *29*(11), 103454.

Khamthong, N., Rukachaisirikul, V., Phongpaichit, S., Preedanon, S., & Sakayaroj, J. (2014). An antibacterial cytochalasin derivative from the marine-derived fungus *Diaporthaceae sp*. PSU-SP2/4. *Phytochemistry Letters*, *10*, 5–9.

Khan, R., Rashid, S., Khan, S., Almutawif, Y. A., & Pari, B. (2024). Synthesis and evaluation of vanillin Schiff bases as potential antimicrobial agents against ESBL-producing bacteria: towards novel interventions in antimicrobial stewardship. *Scientific Reports*, *14*(1), 28007.

Kim, B.-M., Choi, H.-Y., Kim, G.-W., Zheng, C.-J., Kim, Y.-H., & Kim, W.-G. (2017). Madurahydroxylactone, an Inhibitor of *Staphylococcus aureus* FtsZ from *Nonomuraea sp*. AN100570. *Journal of Microbiology and Biotechnology*, *27*(11), 1994–1998.

Kitchen, D. B., Decornez, H., Furr, J. R., & Bajorath, J. (2004). Docking and scoring in virtual screening for drug discovery: methods and applications. *Nature Reviews Drug Discovery*, *3*(11), 935–949.

Krishnan, M. A., Saranyaparvathi, S., Raksha, C., Vrinda, B., Girish, C. G., Kulkarni, N. V, & Kharisov, B. I. (2022). Transition metal complexes of 4-aminoantipyrine derivatives and their antimicrobial applications. *Russian Journal of Coordination Chemistry*, *48*(11), 696–724.

Kumar, M., Mathur, T., Barman, T. K., Chaira, T., Kumar, R., Joshi, V., Pandya, M., Sharma, L., Fujii, K., Bandgar, M., Jadhav, B., Bambal, R., Upadhyay, D., Masuda, N., Verma, A. K., & Bhatnagar, P. K. (2021). Novel FtsZ inhibitor with potent activity against

Staphylococcus aureus. *The Journal of Antimicrobial Chemotherapy*, *76*(11), 2867–2874.

Kumar, R., Sharma, P. K., & Mishra, P. S. (2012). A review on the vanillin derivatives showing various biological activities. *International Journal of PharmTech Research*, *4*(1), 266–279.

Kumar, S., & Kumar, S. (2019). Chapter 6 - molecular docking: a structure-based approach for drug repurposing. In *In Silico Drug Design* (Roy, K.), pp. 161–189. Cambridge: Academic Press.

Kuntz, I. D., Blaney, J. M., Oatley, S. J., Langridge, R., & Ferrin, T. E. (1982). A geometric approach to macromolecule-ligand interactions. *Journal of Molecular Biology*, *161*(2), 269–288.

Kutlushina, A., Khakimova, A., Madzhidov, T., & Polishchuk, P. (2018). Ligand-based pharmacophore modeling using novel 3d pharmacophore signatures. *Molecules*, *23*(12), 3094.

Lavecchia, A., & Di Giovanni, C. (2013). Virtual screening strategies in drug discovery: a critical review. *Current Medicinal Chemistry*, *20*(23), 2839–2860.

Law, W. Y., Asaruddin, M. R., & Bhawani, S. A. (2023). Antiviral study of Schiff base vanillin derivatives against NS2B-NS3 protease of Zika virus based on pharmacophore modelling and molecular docking. *Malaysian Journal of Analytical Sciences*, 27(6), 1300–1325.

Law, W. Y., Asaruddin, M. R., Bhawani, S. A., & Mohamad, S. (2020). Pharmacophore modelling of vanillin derivatives, favipiravir, chloroquine, hydroxychloroquine, monolaurin and tetrodotoxin as MPro inhibitors of severe acute respiratory syndrome coronavirus-2 (SARS-CoV-2). *BMC Research Notes*, *13*(1), 527.

Lee, S. (2022). *A guide to the 4 stages of pneumonia*. [online] Available at: https://healthmatch.io/pneumonia/4-stages-of-pneumonia [Accessed on 11 November 2024].

Lei, J., Hansen, G., Nitsche, C., Klein, C. D., Zhang, L., & Hilgenfeld, R. (2016). Crystal structure of Zika virus NS2B-NS3 protease in complex with a boronate inhibitor. *Science*, *353*(6298), 503–505.

Lengauer, T., & Rarey, M. (1996). Computational methods for biomolecular docking. *Current Opinion in Structural Biology*, *6*(3), 402–406.

Levin, P. A., Kurtser, I. G., & Grossman, A. D. (1999). Identification and characterization of a negative regulator of FtsZ ring formation in *Bacillus subtilis*. *Proceedings of the National Academy of Sciences of the United States of America*, *96*(17), 9642–9647.

Li, H., Dang, C., Tai, X., Xue, L., Meng, Y., Ma, S., & Zhang, J. (2021). VALD-3, a Schiff base ligand synthesized from o-vanillin derivatives, induces cell cycle arrest and apoptosis in breast cancer cells by inhibiting the Wnt/β-catenin pathway. *Scientific Reports*, *11*(1), 14985.

Li, N., Wang, F., Niu, S., Cao, J., Wu, K., Li, Y., Yin, N., Zhang, X., Zhu, W., & Yin, Y. (2009). Discovery of novel inhibitors of *Streptococcus pneumoniae* based on the virtual screening with the homology-modeled structure of histidine kinase (VicK). *BMC Microbiology*, *9*(1), 129.

Li, S., Xi, L., Wang, C., Li, J., Lei, B., Liu, H., & Yao, X. (2009). A novel method for protein-ligand binding affinity prediction and the related descriptors exploration. *Journal of Computational Chemistry*, *30*(6), 900–909.

Lipinski, C. A. (2004). Lead- and drug-like compounds: the rule-of-five revolution. *Drug Discovery Today: Technologies*, *1*(4), 337–341.

Lipinski, C. A., Lombardo, F., Dominy, B. W., & Feeney, P. J. (2001). Experimental and computational approaches to estimate solubility and permeability in drug discovery and development settings1PII of original article: S0169-409X(96)00423-1. *Advanced Drug Delivery Reviews*, *46*(1), 3–26.

Low, M. L., Maigre, L., Tahir, M. I. M., Tiekink, E. R. T., Dorlet, P., Guillot, R., Ravoof, T. B., Rosli, R., Pagès, J.-M., Policar, C., Delsuc, N., & Crouse, K. A. (2016). New insight into the structural, electrochemical and biological aspects of macroacyclic Cu(II) complexes derived from S-substituted dithiocarbazate schiff bases. *European Journal of Medicinal Chemistry*, *120*, 1–12.

Lui, G. C. Y., & Lai, C. K. C. (2025). Community acquired pneumonia due to antibiotic resistant- *Streptococcus pneumoniae*: diagnosis, management and prevention. *Current Opinion in Pulmonary Medicine*, *31*(3), 211–217.

Lund, V. A., Wacnik, K., Turner, R. D., Cotterell, B. E., Walther, C. G., Fenn, S. J., Grein, F., Wollman, A. J., Leake, M. C., Olivier, N., Cadby, A., Mesnage, S., Jones, S., & Foster, S. J. (2018). Molecular coordination of *Staphylococcus aureus* cell division. *eLife*, *7*, e32057.

Lv, Q., Zhang, P., Quan, P., Cui, M., Liu, T., Yin, Y., & Chi, G. (2020). Quercetin, a pneumolysin inhibitor, protects mice against *Streptococcus pneumoniae* infection. *Microbial Pathogenesis*, *140*, 103934.

Ma, Q., Liu, L., Zhao, S., Huang, Z., Li, C., Jiang, S., Li, Q., & Gu, P. (2022). Biosynthesis of vanillin by different microorganisms: a review. *World Journal of Microbiology & Biotechnology*, *38*(3), 40.

Mahal, A., Duan, M., Zinad, D. S., Mohapatra, R. K., Obaidullah, A. J., Wei, X., Pradhan, M. K., Das, D., Kandi, V., Zinad, H. S., & Zhu, Q. (2021). Recent progress in

chemical approaches for the development of novel neuraminidase inhibitors. *RSC Advances*, *11*(3), 1804–1840.

Malaysian Society of Infectious Diseases & Chemotherapy. (2023). *Pneumococcal: available vaccines*. [online] Available at: https://adultimmunisation.msidc.my/pneumococcal/#:~:text=polysaccharide%20is%20protective.-,Vaccines,pneumococcal%20polysaccharide%20vaccine%20(PPV).&text=While%20there%20are%202%20conjugate,is%20approved%20for%20adult%20use [Accessed on 12 November 2024].

Mandell, L. A., Wunderink, R. G., Anzueto, A., Bartlett, J. G., Campbell, G. D., Dean, N. C., Dowell, S. F., File, T. M., Jr, Musher, D. M., Niederman, M. S., Torres, A., & Whitney, C. G. (2007). Infectious Diseases Society of America/American Thoracic Society consensus guidelines on the management of community-acquired pneumonia in adults. *Clinical Infectious Diseases: An Official Publication of the Infectious Diseases Society of America*, *44* (2), S27–S72.

Manikam, L., & Lakhanpaul, M. (2012). Epidemiology of community acquired pneumonia. *Paediatrics and Child Health*, *22*(7), 299–306.

Mathew, S., & Abraham, T. E. (2006). Bioconversions of Ferulic Acid, an Hydroxycinnamic Acid. *Critical Reviews in Microbiology*, *32*(3), 115–125.

Matsui, T., Yamane, J., Mogi, N., Yamaguchi, H., Takemoto, H., Yao, M., & Tanaka, I. (2012). Structural reorganization of the bacterial cell-division protein FtsZ from *Staphylococcus aureus*. *Acta Crystallographica Section D*, *68*(9), 1175–1188.

Mayo Foundation for Medical Education and Research. (2020). *Pneumonia*. [online] Available at: https://www.mayoclinic.org/diseases-conditions/pneumonia/symptoms-causes/syc-20354204 [Accessed on 11 November

2024].

McConkey, B. J., Sobolev, V., & Edelman, M. (2002). The performance of current methods in ligand–protein docking. *Current Science*, *83*(7), 845–856.

Meng, X.-Y., Zhang, H.-X., Mezei, M., & Cui, M. (2011). Molecular docking: a powerful approach for structure-based drug discovery. *Current Computer-Aided Drug Design*, *7*(2), 146–157.

Micoli, F., Romano, M. R., Carboni, F., Adamo, R., & Berti, F. (2023). Strengths and weaknesses of pneumococcal conjugate vaccines. *Glycoconjugate journal*, *40*(2), 135–148.

Midonet, C., & Barre, F.-X. (2014). Xer site-specific recombination: promoting vertical and horizontal transmission of genetic information. *Microbiology Spectrum*, *2*(6).

Migas, P., & Krauze-Baranowska, M. (2015). The significance of arbutin and its derivatives in therapy and cosmetics. *Phytochemistry Letters*, *13*, 35–40.

Mitchell, A. M., & Mitchell, T. J. (2010). *Streptococcus pneumoniae*: virulence factors and variation. *Clinical Microbiology and Infection*, *16*(5), 411–418.

Młynarczyk, A., Młynarczyk, G., & Jeljaszewicz, J. (1998). The Genome of *Staphylococcus aureus*: A review. *Zentralblatt für Bakteriologie: International Journal of Medical Microbiology*, *287*(4), 277–314.

Monteiro, J. M., Pereira, A. R., Reichmann, N. T., Saraiva, B. M., Fernandes, P. B., Veiga, H., Tavares, A. C., Santos, M., Ferreira, M. T., Macário, V., VanNieuwenhze, M. S., Filipe, S. R., & Pinho, M. G. (2018). Peptidoglycan synthesis drives an FtsZ-treadmilling-independent step of cytokinesis. *Nature*, *554*(7693), 528–532.

Musher, D. M. (2003). How contagious are common respiratory tract infections? *The New England Journal of Medicine*, *348*(13), 1256–1266.

Musher, D. M. (2019). *Streptococcus pneumoniae*. [online] Available at: https://www.infectiousdiseaseadvisor.com/home/decision-support-in-medicine/infectious-diseases/streptococcus-pneumoniae/ [Accessed on 11 November 2024].

Neela, M. M. V., & Peram, S. (2025). Computational approaches for drug-protein interaction analysis in cancer: machine learning and structural bioinformatics perspectives. *Journal of Information Systems Engineering and Management*, *10*, 231–247.

Negi, N., & Das, B. (2017). *Streptococcus pneumoniae: An insight into molecular pathogenesis and virulence factors*. [online] Available at: https://www.researchgate.net/publication/320471041_Streptococcus_pneumoniae_An_insight_into_Molecular_Pathogenesis_and_Virulence_Factors [Accessed on 11 November 2024].

Neuhaus, F. C., & Baddiley, J. (2003). A continuum of anionic charge: structures and functions of D-alanyl-teichoic acids in gram-positive bacteria. *Microbiology and Molecular Biology Reviews*, *67*(4), 686–723.

Ngaini, Z., & Mortadza, N. A. (2019). Synthesis of halogenated azo-aspirin analogues from natural product derivatives as the potential antibacterial agents. *Natural Product Research*, *33*(24), 3507–3514.

Nguyen, T. L. A., & Bhattacharya, D. (2022). Antimicrobial activity of quercetin: an approach to its mechanistic principle. *Molecules*, *27*(8), 2494.

Niazi, S. K., & Mariam, Z. (2023). Computer-aided drug design and drug discovery: a prospective analysis. *Pharmaceuticals*, *17*(1), 22.

Nijs, A., Cartuyvels, R., Mewis, A., Peeters, V., Rummens, J. L., & Magerman, K. (2003). Comparison and evaluation of Osiris and Sirscan 2000 antimicrobial susceptibility

systems in the clinical microbiology laboratory. *Journal of Clinical Microbiology*, *41*(8), 3627–3630.

Niu, Y., & Lin, P. (2023). Advances of computer-aided drug design (CADD) in the development of anti-Azheimer's-disease drugs. *Drug Discovery Today*, *28*(8), 103665.

Ogu, C. C., & Maxa, J. L. (2000). Drug interactions due to cytochrome P450. *Baylor University Medical Center Proceedings*, *13*(4), 421–423.

Ohashi, Y., Chijiiwa, Y., Suzuki, K., Takahashi, K., Nanamiya, H., Sato, T., Hosoya, Y., Ochi, K., & Kawamura, F. (1999). The lethal effect of a benzamide derivative, 3-methoxybenzamide, can be suppressed by mutations within a cell division gene, ftsZ, in *Bacillus subtilis*. *Journal of Bacteriology*, *181*(4), 1348–1351.

Oku, Y., Kurokawa, K., Matsuo, M., Yamada, S., Lee, B.-L., & Sekimizu, K. (2009). Pleiotropic roles of polyglycerolphosphate synthase of lipoteichoic acid in growth of *Staphylococcus aureus* cells. *Journal of Bacteriology*, *191*(1), 141–151.

Olatunde, A., Mohammed, A., Ibrahim, M. A., Tajuddeen, N., & Shuaibu, M. N. (2022). Vanillin: A food additive with multiple biological activities. *European Journal of Medicinal Chemistry Reports*, *5*, 100055.

Oliver, F. (2019). *Streptococcus pneumoniae (pneumococcus): Overview*. [online] Available at: https://www.news-medical.net/health/Streptococcus-pneumoniae-(pneumococcus)-Overview.aspx [Accessed on 11 November 2024].

Ouyang, X., Zhou, S., Su, C. T. T., Ge, Z., Li, R., & Kwoh, C. K. (2013). CovalentDock: automated covalent docking with parameterized covalent linkage energy estimation and molecular geometry constraints. *Journal of Computational Chemistry*, *34*(4), 326–336.

Owen, C. D., Lukacik, P., Potter, J. A., Sleator, O., Taylor, G. L., & Walsh, M. A. (2015). *Streptococcus pneumoniae* NanC: structural insights into the specificity and mechanism of a sialidase that produces a sialidase inhibitor. *The Journal of Biological Chemistry*, *290*(46), 27736–27748.

Pahal, P., Rajasurya, V., & Sharma, S. (2023). *Typical bacterial pneumonia*. [online] Available at: https://www.ncbi.nlm.nih.gov/books/NBK534295/ [Accessed on 11 November 2024].

Parker, D., Soong, G., Planet, P., Brower, J., Ratner, A. J., & Prince, A. (2009). The NanA neuraminidase of *Streptococcus pneumoniae* is involved in biofilm formation. *Infection and Immunity*, *77*(9), 3722–3730.

Pasquina-Lemonche, L., Burns, J., Turner, R. D., Kumar, S., Tank, R., Mullin, N., Wilson, J. S., Chakrabarti, B., Bullough, P. A., Foster, S. J., & Hobbs, J. K. (2020). The architecture of the Gram-positive bacterial cell wall. *Nature*, *582*(7811), 294–297.

Pérez-Dorado, I., Galan-Bartual, S., & Hermoso, J. A. (2012). Pneumococcal surface proteins: when the whole is greater than the sum of its parts. *Molecular Oral Microbiology*, *27*(4), 221–245.

Pérez-Rodríguez, N., Pinheiro de Souza Oliveira, R., Torrado Agrasar, A. M., & Domínguez, J. M. (2016). Ferulic acid transformation into the main vanilla aroma compounds by *Amycolatopsis sp*. ATCC 39116. *Applied Microbiology and Biotechnology*, *100*(4), 1677–1689.

Pettigrew, M. M., Fennie, K. P., York, M. P., Daniels, J., & Ghaffar, F. (2006). Variation in the Presence of Neuraminidase Genes among *Streptococcus pneumoniae* Isolates with Identical Sequence Types. *Infection and Immunity*, *74*(6), 3360–3365.

Popiołek, Ł. (2021). Updated information on antimicrobial activity of hydrazide-hydrazones.

International Journal of Molecular Sciences, *22*(17), 9389.

Pradhan, P., Margolin, W., & Beuria, T. K. (2021). Targeting the achilles heel of FtsZ: the interdomain cleft. *Frontiers in Microbiology*, *12*, 732796.

Prakash V. (2017). Applications of vanillin Schiff base ligands and their complexes: A review. *International Journal of Engineering Research & Science*, *3*(2), 36–47.

Qing, X., Lee, X. Y., De Raeymaeker, J., Tame, J. R., Zhang, K. Y., De Maeyer, M., & Voet, A. R. (2014). Pharmacophore modeling: advances, limitations, and current utility in drug discovery. *Journal of Receptor, Ligand and Channel Research*. *70* (5): 1129–1143.

Ramachandra, R. S. and Ravishankar, G. (2000). Vanilla flavour: production by conventional and biotechnological routes. *Journal of the Science of Food and Agriculture*, *80*(3): 289–304.

Rasigade, J. P., & Vandenesch, F. (2014). *Staphylococcus aureus*: a pathogen with still unresolved issues. *Infection, Genetics and Evolution: Journal of Molecular Epidemiology and Evolutionary Genetics in Infectious Diseases*, *21*, 510–514.

Rizvi, S. M. D., Shakil, S., & Haneef, M. (2013). A simple click by click protocol to perform docking: AutoDock 4.2 made easy for non-bioinformaticians. *EXCLI Journal*, *12*, 831–857.

Rohrer, S., & Berger-Bächi, B. (2003). FemABX peptidyl transferases: a link between branched-chain cell wall peptide formation and beta-lactam resistance in gram-positive cocci. *Antimicrobial Agents and Chemotherapy*, *47*(3), 837–846.

Roskoski, R. (2019). Properties of FDA-approved small molecule protein kinase inhibitors. *Pharmacological Research*, *144*, 19–50.

Saber, T., Samir, M., El-Mekkawy, R. M., Ariny, E., El-Sayed, S. R., Enan, G., Abdelatif,

S. H., Askora, A., Merwad, A. M. A., & Tartor, Y. H. (2022). Methicillin- and Vancomycin-Resistant *Staphylococcus aureus* From Humans and Ready-To-Eat Meat: Characterization of Antimicrobial Resistance and Biofilm Formation Ability. *Frontiers in Microbiology*, *12*.

Sadeer, N. B., Sinan, K. I., Cziáky, Z., Jekő, J., Zengin, G., Jeewon, R., Abdallah, H. H., Rengasamy, K. R. R., & Mahomoodally, M. F. (2020). Assessment of the pharmacological properties and phytochemical profile of *Bruguiera gymnorhiza* (L.) Lam using *in vitro* studies, *in silico* docking, and multivariate analysis. *Biomolecules*, *10*(5), 731.

Sanchez, E., & Perloff, S. (2023). *Pneumococcal infections (Streptococcus pneumoniae) Medication*. [online] Available at: https://emedicine.medscape.com/article/225811-medication#:~:text=Penicillin%20and%20its%20derivatives%20are,by%20inhibiting%20cell%20wall%20synthesis [Accessed on 11 November 2024].

Satpati, S., Saha, S. K., Suhasaria, A., Banerjee, P., & Sukul, D. (2020). Adsorption and anti-corrosion characteristics of vanillin Schiff bases on mild steel in 1 M HCl: experimental and theoretical study. *RSC Advances*, *10*(16), 9258–9273.

Sattar, S. B. A., Nguyen, A. D., & Sharma, S. *Bacterial pneumonia*. [online] Available at: https://www.ncbi.nlm.nih.gov/books/NBK513321/ [Accessed on 11 November 2024].

Savoy, M. L. (2024). *Pneumococcal vaccine. MSD Manual*. [online] Available at: https://www.msdmanuals.com/professional/infectious-diseases/immunization/pneumococcal-vaccine [Accessed on 12 November 2024].

Schaduangrat, N., Lampa, S., Simeon, S., Gleeson, M. P., Spjuth, O., & Nantasenamat, C. (2020). Towards reproducible computational drug discovery. *Journal of*

Cheminformatics, *12*(1), 9.

Schlecht, L. M., Peters, B. M., Krom, B. P., Freiberg, J. A., Hänsch, G. M., Filler, S. G., Jabra-Rizk, M. A., & Shirtliff, M. E. (2015). Systemic *Staphylococcus aureus* infection mediated by *Candida albicans* hyphal invasion of mucosal tissue. *Microbiology*, *161*(1), 168–181.

Schneewind, O., & Missiakas, D. M. (2019). Lipoteichoic acid synthesis and function in gram‐positive bacteria. In *Biogenesis of Fatty Acids, Lipids and Membranes* (Geiger, O., 1st ed.), pp. 1–18. Cham: Springer.

Seidel, T., Ibis, G., Bendix, F., & Wolber, G. (2010). Strategies for 3D pharmacophore-based virtual screening. *Drug Discovery Today: Technologies*, *7*(4), 221–228.

Seidel, T., Wieder, O., Garon, A., & Langer, T. (2020). Applications of the pharmacophore concept in natural product inspired drug design. *Molecular Informatics*, *39*(11), e2000059.

Seo, S., Choi, J., Park, S., & Ahn, J. (2021). Binding affinity prediction for protein–ligand complex using deep attention mechanism based on intermolecular interactions. *BMC Bioinformatics*, *22*(1), 542.

Shaikh, S., Gawade, R., Dabke, N., Dash, S., Vanka, K., & Gonnade, R. (2024). Crystal Engineering for Intramolecular π—π Stacking: Effect of Substitution of Electron Donating and Withdrawing Group on Molecular Geometry in Conformationally Flexible Sulfoesters and Sulfonamides. *CrystEngComm*, *26*(26), 3557–3573.

Sham, L.-T., Butler, E. K., Lebar, M. D., Kahne, D., Bernhardt, T. G., & Ruiz, N. (2014). Bacterial cell wall. MurJ is the flippase of lipid-linked precursors for peptidoglycan biogenesis. *Science*, *345*(6193), 220–222.

Sharapova, Y., Švedas, V., & Suplatov, D. (2021). Catalytic and lectin domains in

neuraminidase A from *Streptococcus pneumoniae* are capable of an intermolecular assembly: Implications for biofilm formation. *The FEBS Journal*, *288*(10), 3217–3230.

Shityakov, S., and Förster, C. (2014) *In silico* predictive model to determine vector-mediated transport properties for the blood–brain barrier choline transporter. *Advances and Applications in Bioinformatics and Chemistry*, *7*: 23–36.

Shrestha, S., Acharya, A., Gautam, A., Nepal, H. P., Gautam, R., Ansari, S., & Upadhyay, G. (2013). Lower respiratory tract pathogens and their antimicrobial susceptibility pattern in a medical hospital of central Nepal. *International Journal of Biomedical and Advance Research*, *4*(5), 335–340.

Singh, J. K., Makde, R. D., Kumar, V., & Panda, D. (2008). SepF increases the assembly and bundling of FtsZ polymers and stabilizes FtsZ protofilaments by binding along its length. *The Journal of Biological Chemistry*, *283*(45), 31116–31124.

Sobola, A. (2018). Synthesis, characterization and antimicrobial activity of p-vanillin and vanillin Schiff bases. *Journal of Research and Review in Science*, *5*(1).

Song, F., Ren, B., Chen, C., Yu, K., Liu, X., Zhang, Y., Yang, N., He, H., Liu, X., Dai, H., & Zhang, L. (2014). Three new sterigmatocystin analogues from marine-derived fungus *Aspergillus versicolor* MF359. *Applied Microbiology and Biotechnology*, *98*(8), 3753–3758.

Spassov, D. S. (2024). Binding affinity determination in drug design: insights from lock and key, induced fit, conformational selection, and inhibitor trapping models. *International Journal of Molecular Sciences*, *25*(13), 7124.

Surabhi, S., & Singh, B. K. (2018). Computer aided drug design: an overview. *Journal of Drug Delivery and Therapeutics*, *8*(5), 504–509.

Taylor, T. A. and Unakal, C. G. (2023) *Staphylococcus aureus infection*. [online] Available at: https://www.ncbi.nlm.nih.gov/books/NBK441868/ [Accessed on 19 November 2024].

Tenover, F. C. (2009). Antibiotic susceptibility testing. In *Encyclopedia of Microbiology* (Schaechter, M., 3rd ed.), pp. 67–77. Cambridge: Academic Press.

The Star. (2024). *Pneumonia is top killer in Malaysia for 2023, with over 18,000 fatalities*. [online] Available at: https://www.thestar.com.my/news/nation/2024/10/29/pneumonia-is-top-killer-in-malaysia-for-2023-with-over-18000-fatalities [Accessed on 11 November 2024].

Tiwari, A., & Singh, S. (2022). Chapter 13 - computational approaches in drug designing. In *Bioinformatics* (Singh, D. B. & Pathak, R. J.), pp. 207–217. Cambridge: Academic Press.

Tong, S. Y. C., Davis, J. S., Eichenberger, E., Holland, T. L., & Fowler, V. G. J. (2015). *Staphylococcus aureus* infections: epidemiology, pathophysiology, clinical manifestations, and management. *Clinical Microbiology Reviews*, *28*(3), 603–661.

Trott, O., & Olson, A. J. (2010). AutoDock Vina: improving the speed and accuracy of docking with a new scoring function, efficient optimization, and multithreading. *Journal of Computational Chemistry*, 31(2), 455–461.

Turner, R. D., Ratcliffe, E. C., Wheeler, R., Golestanian, R., Hobbs, J. K., & Foster, S. J. (2010). Peptidoglycan architecture can specify division planes in *Staphylococcus aureus*. *Nature Communications*, *1*, 26.

UNICEF. (2024). *Pneumonia in children: What you need to know*. [online] Available at: https://www.unicef.org/stories/childhood-pneumonia-

explained#:~:text=Pneumonia%20kills%20more%20children%20than%20any%20other%20infectious%20disease.&text=Many%20people%20associate%20pneumonia%20with,pneumonia%20and%20save%20their%20lives [Accessed on 1 September 2024].

van der Poll, T., & Opal, S. M. (2009). Pathogenesis, treatment, and prevention of pneumococcal pneumonia. *The Lancet*, *374*(9700), 1543–1556.

Vemula, D., Jayasurya, P., Sushmitha, V., Kumar, Y. N., & Bhandari, V. (2023). CADD, AI and ML in drug discovery: A comprehensive review. *European Journal of Pharmaceutical Sciences: Official Journal of the European Federation for Pharmaceutical Sciences*, *181*, 106324.

Verma, J., Khedkar, V. M., & Coutinho, E. C. (2010). 3D-QSAR in drug design--a review. *Current Topics in Medicinal Chemistry*, *10*(1), 95–115.

Vhanale, B., Kadam, D., & Shinde, A. (2022). Synthesis, spectral studies, antioxidant and antibacterial evaluation of aromatic nitro and halogenated tetradentate Schiff bases. *Heliyon*, *8*(6), e09650.

Vijayalakshmi, S., Xavier, D., Srivastava, C., & Arun, A. (2019). Vanilla-natural vs artificial: A review. *Research Journal of Pharmacy and Technology*, *12*, 3068.

Vollmer, W., Joris, B., Charlier, P., & Foster, S. (2008). Bacterial peptidoglycan (murein) hydrolases. *FEMS Microbiology Reviews*, *32*(2), 259–286.

von Itzstein, M. (2007). The war against influenza: discovery and development of sialidase inhibitors. *Nature Reviews Drug Discovery*, *6*(12), 967–974.

Wacnik, K., Rao, V. A., Chen, X., Lafage, L., Pazos, M., Booth, S., Vollmer, W., Hobbs, J. K., Lewis, R. J., & Foster, S. J. (2022). Penicillin-binding protein 1 (PBP1) of *Staphylococcus aureus* has multiple essential functions in cell division. *MBio*, *13*(4),

e0066922.

Walther, E., Richter, M., Xu, Z., Kramer, C., von Grafenstein, S., Kirchmair, J., Grienke, U., Rollinger, J. M., Liedl, K. R., Slevogt, H., Sauerbrei, A., Saluz, H. P., Pfister, W., & Schmidtke, M. (2015). Antipneumococcal activity of neuraminidase inhibiting artocarpin. *International Journal of Medical Microbiology. 305*(3), 289–297.

Walton, N. J., Mayer, M. J., & Narbad, A. (2003). Vanillin. *Phytochemistry*, *63*(5), 505–515.

Wang, P. H., Keck, J. G., Lien, E. J., & Lai, M. M. C. (1990). Design, synthesis, testing, and quantitative structure-activity relationship analysis of substituted salicylaldehyde Schiff bases of 1-amino-3-hydroxyguanidine tosylate as new antiviral agents against coronavirus. *Journal of Medicinal Chemistry*, *33*(2), 608–614.

Weiser, J. N., Ferreira, D. M., & Paton, J. C. (2018). *Streptococcus pneumoniae*: transmission, colonization and invasion. *Nature Reviews. Microbiology*, *16*(6), 355–367.

Wermuth, C. G., Ganellin, C. R., Lindberg, P., & Mitscher, L. A. (1998). Glossary of terms used in medicinal chemistry (IUPAC Recommendations 1998). *Pure and Applied Chemistry*, *70*(5), 1129–1143.

Whatmore, A. M., & Reed, R. H. (1990). Determination of turgor pressure in *Bacillus subtilis*: a possible role for K+ in turgor regulation. *Journal of General Microbiology*, *136*(12), 2521–2526.

Whitley, K. D., Jukes, C., Tregidgo, N., Karinou, E., Almada, P., Cesbron, Y., Henriques, R., Dekker, C., & Holden, S. (2021). FtsZ treadmilling is essential for Z-ring condensation and septal constriction initiation in *Bacillus subtilis* cell division. *Nature Communications*, *12*(1), 2448.

Wolber, G., & Langer, T. (2005). LigandScout: 3-D pharmacophores derived from protein-

bound ligands and their use as virtual screening filters. *Journal of Chemical Information and Modeling*, *45*(1), 160–169.

Wolber, G., Dornhofer, A. A., & Langer, T. (2006). Efficient overlay of small organic molecules using 3D pharmacophores. *Journal of Computer-Aided Molecular Design*, *20*(12), 773–788.

World Health Organization. (2022). *Pneumonia in children*. [online] Available at: https://www.who.int/news-room/fact-sheets/detail/pneumonia [Accessed on 1 September 2024].

World Health Organization. (n.d.). *Pneumococcal disease*. [online] Available at: https://www.who.int/teams/health-product-policy-and-standards/standards-and-specifications/norms-and-standards/vaccine-standardization/pneumococcal-disease [Accessed on 12 November 2024].

Wouters, O. J., McKee, M., & Luyten, J. (2020). Estimated research and development investment needed to bring a new medicine to market, 2009-2018. *JAMA*, *323*(9), 844–853.

Xie, Z.-R., & Hwang, M.-J. (2015). Methods for predicting protein-ligand binding sites. *Methods in Molecular Biology*, *1215*, 383–398.

Xu, H., Sullivan, T. J., Sekiguchi, J., Kirikae, T., Ojima, I., Stratton, C. F., Mao, W., Rock, F. L., Alley, M. R., Johnson, F., Walker, S. G., & Tonge, P. J. (2008). Mechanism and inhibition of saFabI, the enoyl reductase from *Staphylococcus aureus*. *Biochemistry*, *47*(14), 4228–4236.

Xu, L., Fang, J., Ou, D., Xu, J., Deng, X., Chi, G., Feng, H., & Wang, J. (2023). Therapeutic potential of kaempferol on *Streptococcus pneumoniae* infection. *Microbes and Infection, 25*(3), 105058.

Yadav, G., Prasad, R. L. A., Jha, B. K., Rai, V., Bhakuni, V. and Datta, K. (2008). Evidence for inhibitory interaction of hyaluronan-binding protein 1 (HABP1/p32/gC1qR) with *Streptococcus pneumoniae* hyaluronidase. *The Journal of Biological Chemistry*, *284*(6), 3897–3905.

Yartsev, A. (2017). *Affinity, association constant and dissociation constant*. [online] Available at: https://derangedphysiology.com/main/cicm-primary-exam/pharmacodynamics/Chapter-121/affinity-association-constant-and-dissociation-constant [Accessed on 17 December 2024].

Yuldasheva, N., Acikyildiz, N., Akyuz, M., Yabo-Dambagi, L., Aydin, T., Cakir, A., & Kazaz, C. (2022). The synthesis of Schiff bases and new secondary amine derivatives of p-vanillin and evaluation of their neuroprotective, antidiabetic, antidepressant and antioxidant potentials. *Journal of Molecular Structure*, *1270*, 133883.

Yusof, H. A. (2020). Inhibition of *Streptococcus pneumoniae* hyaluronidase by honeys of Malaysian origins. *Bioremediation of Science and Technology Research*, *8*(1), 1–6.

Zhang, M.-Q., & Wilkinson, B. (2007). Drug discovery beyond the 'rule-of-five.' *Current Opinion in Biotechnology*, *18*(6), 478–488.

Zhao, Y., Wei, J., Li, C., Ahmed, A. F., Liu, Z., & Ma, C. (2022). A comprehensive review on mechanism of natural products against *Staphylococcus aureus*. *Journal of Future Foods*, *2*(1), 25–33.

Zhou, X., Halladin, D. K., Rojas, E. R., Koslover, E. F., Lee, T. K., Huang, K. C., & Theriot, J. A. (2015). Bacterial division. Mechanical crack propagation drives millisecond daughter cell separation in *Staphylococcus aureus*. *Science*, *348*(6234), 574–578.

Zhou, Y., Tang, S., Chen, T., & Niu, M.-M. (2019). Structure-based pharmacophore modeling, virtual screening, molecular docking and biological evaluation for

identification of potential poly (ADP-Ribose) polymerase-1 (PARP-1) inhibitors. *Molecules*, *24*(23), 4258.

Zou, Y., Wang, H., Fang, J., Sun, H., Deng, X., Wang, J., Deng, Y., & Chi, G. (2023). Isorhamnetin as a novel inhibitor of pneumolysin against *Streptococcus pneumoniae* infection *in vivo*/*in vitro*. *Microbial Pathogenesis*, *185*, 106382.

APPENDICES

Appendix A: Journal Publications

1. **Law, W. Y.**, Asaruddin, M. R., & Bhawani, S. A. (2023). Antiviral study of Schiff Base Vanillin Derivatives against NS2B-NS3 protease of Zika Virus based on pharmacophore modelling and molecular docking. *Malaysian Journal of Analytical Sciences*, 27(6), 1300–1325.